TURBULENT FLOW THROUGH A DEGRADED CHANNEL BED

Mosedul Sarkar

To my parents
Ikdul Sarkar & Rasida Bibi
and
my grandmother
Nurjahan Bewa

Turbulent Flow through a Degraded Channel Bed

Thesis submitted for the award

of the degree

of

Doctor of Philosophy (Ph.D.)
(Science)

By

Mosedul Sarkar

Index No: 145/21/ Maths. /27

Physics and Applied Mathematics Unit
Indian Statistical Institute, Kolkata, India

to the
Jadavpur University
Kolkata-700032, India

March 2025

© 2025, Mosedul Sarkar. All rights reserved.

INDIAN STATISTICAL INSTITUTE

Physics & Applied Mathematics Unit
203 Barrackpore Trunk Road
Kolkata 700 108
West Bengal
INDIA

Dr. Sankar Sarkar
Assistant Professor
Phone: +91 33 25753026 (Office), +919002268806 (Mobile)
Email: sankar_s@isical.ac.in, sankar.iitkgp@gmail.com

CERTIFICATE FROM THE SUPERVISOR

This is to certify that the thesis entitled "**TURBULENT FLOW THROUGH A DEGRADED CHANNEL BED**" Submitted by **Sri MOSEDUL SARKAR** got his name registered on 8th December, 2021 for the award of Ph. D. (Science) Degree of Jadavpur University, is absolutely based upon his own work under the supervision of **Dr. Sankar Sarkar**, Assistant Professor, Physics and Applied Mathematics Unit (PAMU), Indian Statistical Institute, Kolkata, India and that neither this thesis nor any part of it has been submitted for either any degree / diploma or any other academic award anywhere before.

Place: Kolkata
Date: 25.03.2025

.....
(Signature of the Supervisor date with official seal)

Dr. Sankar Sarkar
Assistant Professor
Physics and Applied Mathematics Unit
Indian Statistical Institute
Kolkata-700108, India

सहायक प्राध्यापक / Assistant Professor
भौतिकी एवं अनुप्रयुक्त गणित यूनिट
Physics and Applied Mathematics Unit
भारतीय सांख्यिकीय संस्थान
INDIAN STATISTICAL INSTITUTE
203, बैरकपुर ट्रंक रोड, कोलकाता-700108
203, Barrackpore Trunk Road, Kolkata-700108

Declaration

I certify that

a. The work contained in this thesis is original and has been done by me under the guidance of my supervisor.
b. The work has not been submitted to any other Institute for any degree or diploma.
c. I have followed the guidelines provided by the Institute in preparing the thesis.
d. I have conformed to the norms and guidelines given in the Ethical Code of Conduct of the Institute.
e. Whenever I have used materials (data, theoretical analysis, figures, and text) from other sources, I have given due credit to them by citing them in the text of the thesis and giving their details in the references. Further, I have taken permission from the copyright owners of the sources, whenever necessary.

Kolkata
Date: 25-03-2025

Mosedul Sarkar

Mosedul Sarkar

Acknowledgements

I take this opportunity to express my deep sense of heartfelt gratitude and indebtedness to my supervisor Dr. Sankar Sarkar, Physics and Applied Mathematics Unit, Indian Statistical Institute, Kolkata, India, for his inspiration, incredible and scholarly guidance at all the stages of my investigation. This work would not have been possible without his invaluable mentorship, encouragement, and assistance.

I am fortunate to have connected with many renowned national and international researchers to participate in many collaborative efforts throughout my doctoral studies. I sincerely thank them for their insightful suggestions, which have significantly enriched my knowledge. I also extend my heartfelt appreciation to Prof. Asis Mazumdar, Director, School of water resources engineering and other members of my Doctoral Advisory Committee for their constructive feedback and valuable guidance throughout this study.

I would like to express my deepest gratitude to my parents, Mr. Ikdul Sarkar and Mrs. Rasida Bibi, and my grandmother, Nurjahan Bewa, whose years of sacrifice have made me who I am today. I also wish to thank my wife, Merina Yeasmin; my sister, Dr. Renuka Khatun; and my brother, Raju Sarkar for their unconditional love and constant encouragement. Additionally, I am profoundly grateful to all the teachers and mentors who have guided me throughout my educational journey, from my early schooling to university education. I extend my appreciation to my friends and well-wishers for their moral support during this period. I pray to the Almighty for their lifelong good health and happiness.

I would also like to acknowledge the Indian Statistical Institute, Kolkata, for its support and the Department of Science and Technology (DST), Innovation in Science Pursuit for Inspired Research (INSPIRE), Government of India, for providing financial assistance in the form of a research fellowship to carry out this work.

Finally, I humbly bow before the Almighty, who has made everything possible.

Kolkata
Date: 25-03-2025

Mosedul Sarkar
Mosedul Sarkar

List of Journal Publications

Sarkar M., Maurya S. K., Gopmandal P. P., Sarkar S. (2021). Hydrodynamics of flow through a degraded channel bed. ***Journal of Turbulence***, 22(12), 814-842. https://doi.org/10.1080/14685248.2021.2007256

Sarkar M., Sarkar S. (2023). Structure functions of turbulence through a degraded channel bed. ***European Journal of Mechanics-B/Fluids***, 98, 292-318. https://doi.org/10.1016/j.euromechflu.2022.12.012

Samanta A., **Sarkar M.,** Mondal H., Das R., Sarkar S. (2023). Turbulence anisotropy in a wall-wake flow downstream of two horizontal cylinders. ***Flow Measurement and Instrumentation***, 94, 102456. https://doi.org/10.1016/j.flowmeasinst.2023.102456

Sarkar M., Samanta A., Sarkar D., Das R., Sarkar S. (2024). Turbulence in a wall wake flow downstream of two horizontal cylinders. ***Marine Georesources & Geotechnology***, 42(7), 878-897. https://doi.org/10.1080/1064119X.2023.2234361

Sarkar M., Radice A., Gopmandal P. P., Sarkar S. (2024). Quadrant analysis of turbulence over a degraded channel-bed of bimodal sediment, with a definition framework for averaging methods. ***Environmental Fluid Mechanics***, 1-33. https://doi.org/10.1007/s10652-024-10010-4

List of Symbols

b_{ik} = Reynolds stress anisotropy tensor [= $\overline{u_i' u_k'}$ /(2q) – (δ_{ik}/3)] ($M^0L^0T^0$);

d = representative sediment diameter (M^0LT^0);

d_{16} = 16 % finer sediment size (M^0LT^0);

d_{50} = median diameter of sand and gravel (M^0LT^0);

$(d_{50})_1$ = median size of sand (M^0LT^0);

$(d_{50})_2$ = median size of gravel (M^0LT^0);

d_{84} = 84 % finer sediment size (M^0LT^0);

d^q = Mean durations of the bursting events in an q^{th} quadrant (M^0L^0T);

$E(k)$ = energy spectra with respect to wave number [$M^0L^3T^{-2}$]

E_D = normalized turbulent dissipation [= $\varepsilon h/ u_*^3$] ($M^0L^0T^0$);

F = invariant function [= (1 + 9II + 27III)] ($M^0L^0T^0$);

F = flow Froude number [= $\bar{U}$ /(gh)$^{0.5}$] ($M^0L^0T^0$);

F_{ku} = normalized streamwise flux of turbulent kinetic energy, f_{ku}/u_*^3 ($M^0L^0T^0$);

F_{kw} = normalized vertical flux of turbulent kinetic energy, f_{kw}/u_*^3 ($M^0L^0T^0$);

f_E = normalized mean frequency of ejections ($M^0L^0T^0$);

f_{ku} = streamwise flux of turbulent kinetic energy, $0.5(\overline{u'u'u'} + \overline{u'v'v'} + \overline{u'w'w'})$ ($M^0L^3T^{-3}$);

f_{kw} = vertical flux of turbulent kinetic energy, $0.5(\overline{u'u'w'} + \overline{v'v'w'} + \overline{w'w'w'})$ ($M^0L^3T^{-3}$);

f^q = frequency of the bursting events in an q^{th} quadrant ($M^0 L^0T^{-1}$);

f_S = normalized mean frequency of sweeps ($M^0L^0T^0$);

g = acceleration due to gravity (M^0LT^{-2});

H = hole-size parameter ($M^0L^0T^0$);

h = flow depth (M^0LT^0);

q = quadrant number ($M^0L^0T^0$);

I_{av} = turbulence indicator ($M^0L^0T^0$);

i_E = mean interval between ejections (M^0L^0T);

i_S = mean interval between sweeps (M^0L^0T);

k	=	wave number ($M^0L^{-1}T^0$);
k	=	turbulent kinetic energy [= $0.5(\overline{u'u'} + \overline{v'v'} + \overline{w'w'})$] ($M^0L^2T^{-2}$);
k_s	=	equivalent roughness height (M^0LT^0);
$\overline{k'u'}/u_*^3$	=	nondimensional stream-wise flux of TKE ($M^0L^0T^0$);
$\overline{k'w'}/u_*^3$	=	nondimensional vertical flux of TKE ($M^0L^0T^0$);
$\overline{k'u'}_{quad}^{q}$	=	quadrant-averaged conditional stream-wise TKE flux of bursting events in a q^{th} quadrant ($M^0L^3T^{-3}$);
$\overline{k'w'}_{quad}^{q}$	=	quadrant-averaged conditional vertical TKE flux of bursting events in a q^{th} quadrant ($M^0L^3T^{-3}$);
L	=	streamwise distance from the of initiation of bed degradation ($M^0L^0T^0$)
P_D	=	normalized pressure energy diffusion, [= $p_D h/ u_*^3$] ($M^0L^0T^0$);
p, q	=	order of scaling exponents in mixed-order structure functions($M^0L^0T^0$);
p	=	time-averaged hydrostatic pressure ($ML^{-1}T^{-2}$);
p'	=	pressure fluctuations ($ML^{-1}T^{-2}$);
p^q	=	percentage occurrence of the bursting events in a q^{th} quadrant ($M^0L^0T^0$);
p^H	=	percentage of fluctuations out of the hole ($M^0L^0T^0$);
$p^{H,q}$	=	percentage of fluctuations out of the hole for a certain quadrant ($M^0L^0T^0$);
$p^{q,H}$	=	percentage of fluctuations in a quadrant among those out of the hole. ($M^0L^0T^0$);
p_D	=	pressure energy diffusion [= $\partial(\overline{p'w'/\rho})/\partial z$] ($M^0L^2T^{-3}$);
k	=	the average turbulent kinetic energy in tensor form [= $\overline{u_i'u_i'}/2$] ($M^0L^{-2}T^{-2}$);
q_s	=	transport rate of sediment ($ML^{-1}T^{-1}$);
R	=	flow Reynolds number, [= $4h\overline{U}/\upsilon$] ($M^0L^0T^0$);
R_D	=	wake Reynolds number ($M^0L^0T^0$);

R_u = autocorrelation function of u-component ($M^0L^0T^0$);

R_* = shear-particle Reynolds number, [= $d_{50}u_*/\upsilon$] ($M^0L^0T^0$);

R = spatial separation distance ($M^0L^1T^0$);

r_{uw} = correlation coefficient, [= $-\overline{u'w'}/(\overline{u'u'} \times \overline{w'w'})^{0.5}$] ($M^0L^0T^0$);

S_h = relative submergence, [= d_{50}/h] ($M^0L^0T^0$);

s = relative density of sediments ($M^0L^0T^0$);

S_n = structure function of order n ($M^0L^nT^n$);

S_n^{pq} = tensorial mixed $n^{\text{-th}}$ order structure function ($M^0L^nT^n$);

t = instantaneous time(M^0L^0T);

T = sampling time (M^0L^0T);

T_D = normalized turbulent energy diffusion, [= t_Dh/u_*^3] ($M^0L^0T^0$);

T_E = normalized mean-time duration of ejections ($M^0L^0T^0$);

T_P = normalised turbulent production [= t_Ph/u_*^3] ($M^0L^0T^0$);

T_S = normalized mean-time duration of sweeps ($M^0L^0T^0$);

t_D = turbulent energy diffusion, [= $\partial f_{kw}/\partial z$] ($M^0L^2T^{-3}$);

t_E = mean-time duration of ejections (M^0L^0T);

t_P = turbulent production, [= $-\overline{u'w'}(\partial u/\partial z)$] ($M^0L^2T^{-3}$);

t_S = mean-time duration of sweeps (M^0L^0T);

$U(z)$ = the time-average approach velocity at an elevation z (M^0LT^{-1});
for plane wall-wake flows (M^0LT^{-1});

$\overline{U}$ = depth-averaged approach velocity (M^0LT^{-1});

U_1 = Resultant velocity from three-dimensional velocity components (M^0LT^{-1});

u = streamwise velocity component (M^0LT^{-1});

u' = fluctuations of streamwise velocity (M^0LT^{-1});

u^+ = non dimensional velocity [= u/u_*] ($M^0L^0T^0$)

uw^+ = normalized Reynolds shear stress [= $-\overline{u'w'}/u_*^2$] ($M^0L^0T^0$);

u_* = shear velocity (M^0LT^{-1});

u_{*c} = critical shear velocity (M^0LT^{-1});

u_{*1} = shear velocity determined from the bed slope [= $(ghS)^{0.5}$] (M^0LT^{-1});

u_{*2}	=	shear velocity obtained from the Reynolds shear stress (M^0LT^{-1});
$\overline{u}^q_{quad}$	=	quadrant-averaged conditional stream-wise velocity of bursting events in a q^{th} quadrant (M^0LT^{-1});
$\overline{k'w'}^q_{quad}$	=	quadrant-averaged conditional vertical TKE flux of bursting event
	=	in aq^{th} quadrant ($M^0L^3T^{-3}$);
$\overline{u}^q_{tot}$	=	total-averaged conditional stream-wise velocity of bursting events in a q^{th} quadrant (M^0LT^{-1});
$\overline{u'u'}/u_*^2$	=	nondimensional stream-wise Reynolds normal stress ($M^0L^0T^0$);
$\overline{u'u'}^q_{quad}$	=	quadrant-averaged conditional stream-wise Reynolds stress (discarding ρ) of bursting events in a q^{th} quadrant ($M^0L^2T^{-2}$);
$\overline{u'w'}/u_*^2$	=	nondimensional Reynolds shear stress ($M^0L^0T^0$);
$\overline{u'u'}^q_{tot}$	=	total-averaged conditional stream-wise Reynolds stress (discarding ρ) of bursting events in an q^{th} quadrant ($M^0L^2T^{-2}$);
$\overline{u'w'}^q_{quad}$	=	quadrant-averaged conditional Reynolds stress (discarding ρ) of bursting events in an q^{th} quadrant ($M^0L^2T^{-2}$);
$\overline{u'w'}^q_{tot}$	=	total-averaged conditional Reynolds stress (discarding ρ) of bursting events in an q^{th} quadrant ($M^0L^2T^{-2}$);
$\overline{u'w'}^H_{tot}$	=	mean Reynolds shear stress(discarding ρ) for all the fluctuations out of the hole, considering all events as the sample size ($M^0L^2T^{-2}$);
$\overline{u'w'}^H_{hole}$	=	mean Reynolds shear stress(discarding ρ) for all the fluctuations out of the hole, considering the events out of the hole as the sample size ($M^0L^2T^{-2}$);
$\overline{u'w'}^{q,H}_{tot}$	=	mean Reynolds shear stress(discarding ρ) for all the fluctuations out of the hole and in a certain quadrant, considering all events as the sample size ($M^0L^2T^{-2}$);
$\overline{u'w'}^{q,H}_{quad}$	=	mean Reynolds shear stress(discarding ρ) for all the fluctuations out of the hole and in a certain quadrant, considering the events in that quadrant as the sample size ($M^0L^2T^{-2}$);
$\overline{u'w'}^{q,H}_{hole}$	=	mean Reynolds shear stress(discarding ρ) for all the fluctuations out of the hole and in a certain quadrant, considering the events out of the hole as the sample size ($M^0L^2T^{-2}$);
$\overline{u'w'}^{q,H}_{quad,hole}$	=	mean Reynolds shear stress(discarding ρ)for all the fluctuations out of the hole and in a certain quadrant, considering the events in that quadrant and out of the hole as the sample size ($M^0L^2T^{-2}$);
$\overline{w'w'}/u_*^2$	=	nondimensional vertical Reynolds normal stress ($M^0L^0T^0$);

$\overline{w}^{q}_{quad}$	=	quadrant-averaged conditional vertical velocity of bursting events in a q^{th} quadrant (M^0LT^{-1});
$\overline{w}^{q}_{tot}$	=	total-averaged conditional vertical velocity of bursting events in a q^{th} quadrant (M^0LT^{-1});
$\overline{w'w'}^{q}_{quad}$	=	quadrant-averaged conditional vertical Reynolds stress (discardingρ) of bursting events in a q^{th} quadrant ($M^0L^2T^{-2}$);
$\overline{w'w'}^{q}_{tot}$	=	total-averaged conditional vertical Reynolds stress (discarding ρ) of bursting events in a q^{th} quadrant ($M^0L^2T^{-2}$);
v	=	transverse velocity component (M^0LT^{-1});
v'	=	fluctuations of transverse velocity component (M^0LT^{-1});
v_D	=	viscous diffusion [$= -\upsilon(\partial^2 k/\partial z^2)$] ($M^0L^3T^{-4}$) ;
w	=	vertical velocity component (M^0LT^{-1});
w^+	=	[$= (\overline{w'w'})^{0.5}/u_*$] ($M^0L^0T^0$);
w'	=	fluctuations of vertical velocity component (M^0LT^{-1});
x, y, z	=	streamwise, vertical and transverse distances, respectively (M^0LT^0);
$\hat{x}$	=	nondimensional streamwise distance, [$= x/d_{50}$] ($M^0L^0T^0$);
z^+	=	normalized vertical distance [$= z/d_{50}$] ($M^0L^0T^0$);
I, II, III	=	independent invariants, ($M^0L^0T^0$);
α	=	an exponent ($M^0L^0T^0$);
β	=	nondimensional parameter ($M^0L^0T^0$);
γ	=	specific weight of water ($ML^{-3}T^0$);
Δu	=	velocity defect ($M^0L^1T^{-1}$);
δ_{ik}	=	Kronecker delta function ($M^0L^0T^0$);
ε	=	turbulent dissipation in turbulent energy budget ($M^0L^2T^{-3}$);
$\langle\varepsilon\rangle$	=	spatially-averaged turbulent dissipation ($M^0L^2T^{-3}$);
ζ_n^u	=	isotropic streamwise scaling exponent of order n ($M^0L^0T^0$);
ζ_n^w	=	isotropic vertical scaling exponent of order n ($M^0L^0T^0$);
ζ_n^{pq}	=	anisotropic scaling exponents of order n ($M^0L^0T^0$);
η	=	Kolmogorov microscale ($M^0L^1T^0$);
Θ	=	Shields parameter ($M^0L^0T^0$);

Θ_c = critical Shields parameter ($M^0L^0T^0$);

$\bar{\theta}$ = time-averaged quantity;

κ = von Karman constant ($M^0L^0T^0$);

λ = the nondimensional transverse distance (= y/y_1)

λ = Taylor microscale (M^0LT^0);

λ_i^q = clipping function for quadrant(M^0LT^0);

λ_i^H = quadrant-averaged conditional vertical TKE flux of bursting events in a q^{th} quadrant ($M^0L^3T^{-3}$);

Λ = correlation length (M^0LT^0);

Λ_c = critical correlation length (M^0LT^0);

$\lambda_{i,H}$ = detection function ($M^0L^0T^0$);

μ = Coulomb friction factor ($M^0L^0T^0$);

ξ = fraction of particles entrained per unit area ($M^0L^0T^0$) (Chapter 4);

ρ = mass density of fluid ($ML^{-3}T^0$);

ρ_0 = porosity of sediments ($M^0L^0T^0$);

σ = nondimensional pressure ($M^0L^0T^0$);

σ_g = geometric standard deviation of particle size ($M^0L^0T^0$);

$\hat{\sigma}_u$ = σ_u/u_* ($M^0L^0T^0$);

$\hat{\sigma}_w$ = σ_w/u_* ($M^0L^0T^0$);

τ_0 = bed shear stress ($ML^{-1}T^{-2}$);

$\hat{\tau}$ = nondimensional Reynolds shear stress [= $-\tau/(\rho u_*^2)$] ($M^0L^0T^0$);

τ_c = critical bed shear stress ($ML^{-1}T^{-2}$);

τ_s = bed shear stress of sediment particle ($ML^{-1}T^{-2}$);

τ_t = total shear stress ($ML^{-1}T^{-2}$);

τ_{uw} = Reynolds shear stress ($ML^{-1}T^{-2}$);

τ_{vis} = viscous shear stress ($ML^{-1}T^{-2}$);

υ = kinematic viscosity of fluid ($M^0L^2T^{-1}$);

$\psi(k)$ = Taylor's Coefficient ($M^0L^0T^0$);

Abbreviations

ADV	Acoustic Doppler velocimeter
AIF	Anisotropy Invarient Function
AIM	Anisotropy Invarient Map
LDA	Laser Doppler anemometry
LDV	Laser Doppler velocimetry
PIV	Particle Image velocimetry
PSD	Power Spectral Density
SF	Structure Functions
MSF	Mixed Structure Functions
TKE	Turbulent kinetic energy

Abstract

This study examines the turbulent flow characteristics in a degraded channel bed based on experimental data. The experiments were performed in the Fluvial Mechanics Laboratory of the Indian Statistical Institute, Kolkata. A Vectrino velocimeter was used to capture the three-dimensional velocity components over a degraded channel bed under equilibrium condition at different spatial locations. The data were further analyzed to investigate structure functions of turbulence, turbulence anisotropy, intermittency, and turbulent bursting phenomena etc.

The streamwise velocity, Reynolds shear and normal stresses, turbulent kinetic energy (TKE), and TKE fluxes were examined and compared with existing literature. For the advancement of the knowledge of flow over a degraded channel bed, the study explored the laws of turbulence and the TKE budget. In pursuit of this, velocity structure functions of turbulence were applied. Second- and third-order streamwise velocity structure functions, along with mixed third-order velocity structure functions, revealed the existence of an inertial subrange. The TKE dissipation rate was estimated using Kolmogorov's 4/5-law and Monin–Yaglom's 4/3-scaling laws of turbulence. The TKE budget analysis showed that near the bed, at the maximum equilibrium depth of degradation, TKE dissipation exceeds TKE production and turbulent diffusion, whereas pressure diffusion exhibits larger negative values. The distributions of anisotropic invariant maps and invariant functions indicated anisotropic turbulence near the bed, while above the initial bed level (measured before degradation takes place), turbulence tended toward three-dimensional isotropy.

Furthermore, the velocity data were processed to examine the vertical distributions of turbulence indicators and turbulence length scales at different locations of flow through a degraded channel bed. The primary focus of this study was to investigate the influence of bed degradation on flow intermittency and turbulence anisotropy using high-order structure functions and their scaling exponents. The extended self-similarity (ESS) technique was employed to estimate the scaling exponents of high-order structure functions. The results showed that below the initial bed level, the scaling exponents deviated significantly from the theoretical (K41) values, indicating enhanced intermittency. Moreover, data were analyzed to determine the scaling exponents of mixed higher-order structure functions. In this regard, $SO(3)$ symmetry decomposition was utilized to differentiate between the isotropic and anisotropic components of the scaling exponents. The anisotropic scaling exponents obtained from high-order mixed structure functions exhibited higher values than that of their isotropic parts, demonstrating flow anisotropy.

Finally, an in-depth analysis was conducted on the conditional statistics of streamwise and vertical velocity components, Reynolds stresses, and turbulent kinetic energy fluxes. Additionally, the percentage occurrence, mean duration, and frequency of bursting events within each quadrant were examined. The primary objective of this analysis was to establish a definition framework for averaging methods of quadrant analysis of turbulence over a degraded channel bed and the results were compared systematically. The findings revealed the presence of a top layer where flow properties closely resembled those of the incoming flow, as well as a mixing layer near the initial bed elevation. Near the bed, sweeps were dominant, whereas ejections became more prevalent at higher elevations.

Keywords: Turbulent flow characteristics; Open channel flow; Laws of turbulence; Structure functions; Turbulence anisotropy; Intermittency; Degraded bed flow; Bursting phenomena.

Mosedul Sarkar
Signature of Student 25-03-2025

Signature of Supervisor 25.03.2025

सहायक प्राध्यापक / Assistant Professor
भौतिकी एवं अनुप्रयुक्त गणित यूनिट
Physics and Applied Mathematics Unit
भारतीय सांख्यिकीय संस्थान
INDIAN STATISTICAL INSTITUTE
203, बैरकपुर ट्रंक रोड, कोलकाता-700108
203, Barrackpore Trunk Road, Kolkata-700108

Contents

Chapter 1

Introduction

1.1 General

Fluid flows either in a smooth and orderly manner or in a random and swirling manner based on several criteria starting from the medium though which it flows to the properties of the fluid itself. The first category of the flow mentioned above is the laminar flow that involves particles moving along predictable distinct paths, which can be straight or curved. In contrast, the second one is the turbulent flow which is characterized by irregular fluctuations in velocity and other properties, making it unpredictable and highly sensitive to initial conditions. The transition between laminar and turbulent flow depends on the generation methods and the flow parameters themselves.

Since the turbulent flow is unpredictable in nature, earlier works does not adequately define its precious definition. However, they highlighted the key characteristics such as strong mixing, high velocity fluctuation, non-linearity, dissipative, and sensitivity to initial conditions, distinguishing turbulence from laminar flow. Hinze (1959) described turbulence as an irregular flow state with random variations in time and space, allowing statistically identifiable averages. Modern research describes incompressible turbulence as a spatially complex pattern of vortices that appears randomly in space and time, making it a multiscale, non-linear process (Davidson, 2015). However, turbulence is ubiquitous in nature, influences several features in rivers, atmosphere, oceans, engineering devices, and astrophysical phenomena, etc. For example, stirring a liquid, smoke from chimneys, and ocean currents all demonstrate turbulence’s extensive nature. Despite its ubiquity and importance, turbulence remains a challenging phenomenon to model and analyze due to its complexity and non-linear behavior. Consequently, its study is vital in fields like hydrodynamics, fluvial processes, aerodynamics, geophysics, astrophysics, and so on requiring sophisticated mathematical tools for understanding and predictions.

Natural flow, such as flow through open-channel streams is turbulent in character due to high velocity and low viscosity of water, bed roughness of the channel, changes in the bed topography, presence of bluff-bodies of different size and shapes, etc. Since the river morphology and river-training works largely depend on the flow characteristics, flow through natural rough-bed streams remains a topic of continuing interest to the scientific communities. These natural stream-beds are often made up of sand and gravel of uniform and non-uniform sizes and shapes which make the near-bed spatially heterogeneous. Flow over fixed and weakly mobile rough beds, water-worked gravel beds, dunal beds, and aggraded and degraded beds, etc, are quite common phenomena in natural rivers.

The degraded bed and aggraded beds refer to the distinct morphological adjustments of the channel bed in response to sediment transport processes and flow conditions in an open channel. A degraded bed occurs when sediment is moved from the channel bed at a rate faster than it is replenished. This typically happens due to sediment deficit, where the transport capacity of the flow exceeds the sediment supply. Due to amplified flow velocity or discharge that enhances sediment entrainment, decreases sediment supply from upstream. This often happens due to dam construction or sediment trapping or channel steepening etc., which increases erosive power being some common reasons of bed degradation. Over the time, as degradation continues, the channel bed may reach an equilibrium condition. In this state, sediment transport capacity aligns with the available sediment supply, halting further erosion. On the other hand, an aggraded bed results from sediment deposition when the sediment supply exceeds the transport capacity of the flow. In contrast to the degraded bed conditions, the factors leading to aggradations include low flow velocity, often caused by channel widening, meandering, or reduced discharge, excessive sediment input from upstream sources, such as landslides, bank erosion, or human activities and deposition zones, where sediment-laden flows face obstacles or changes in slope and so on. When sediment deposition stabilizes, the channel reaches a new equilibrium condition where sediment transport out of the reach equals sediment supply into it.

The equilibrium condition represents a dynamic balance in sediment transport processes, where neither significant degradation nor aggradation occurs. At equilibrium state, the

channel bed maintains a relatively stable form over the time, where sediment input becomes equal to sediment output, minimizing long-term morphological changes and flow energy is optimally distributed between sediment transport and resisting forces. In both natural and engineered systems, achieving equilibrium is essential for sustainable channel management, as long-term degradation can damage structures and harm habitats, while continued aggradations can block the channel and increase flooding risk.

A degraded bed immediately downstream of a solid apron is very common in open-channel flow and therefore, has vast practical applications in sediment transport, bank-erosion and river training works, etc. Specifically, it has wide applications in scour downstream of an apron of a sluice gate, energy dissipater, different shapes of bridge pier, spur dikes, and various shapes and types of the bluff body and abutments, etc. Due to its significant applications in geology, open-channel hydraulics, and sediment transport phenomena, understanding the statistics of turbulence over a degraded bed is crucial. However, numerous aspects of turbulence over degraded beds remain insufficiently explored. Therefore, further research is necessary for an extensive knowledge of flow through both uniform and bimodal degraded beds. Given the above-mentioned conditions, this research work presents a rigorous study of the flow properties through degraded channel beds.

1.2 Scope of the Present Work

Laws of turbulence (Kolmogorov's 2/3, Kolmogorov's 4/5, and Monin-Yaglom's 4/3-laws) and estimation of turbulent kinetic energy (TKE) dissipation rates were analyzed based on structure function technique. In addition, time-averaged turbulent flow statistics, spectral analysis, turbulent kinetic energy, energy budget were observed for degraded channel-bed. The turbulence anisotropy analysis using anisotropy invariants map (AIM) and anisotropy invariant function (AIF) were performed through degraded channel bed under equilibrium condition.

High-order structure functions were extensively explored together with the distributions of velocity vector profile, turbulence indicator, and turbulent length scales in the flow over degraded channel bed. With the help of extended self-similarity (ESS) technique in

the inertial subrange, scaling exponents of high-order structure functions were estimated. The intermittency behavior of the flow was analyzed using intermittency parameter which can be defined using scaling exponents of the higher order structure functions. In addition to the high-order single component structure functions, mixed structure functions and the related scaling exponents were also computed using the *SO*(3) decomposition method. The anisotropy of the scaling exponents based on these mixed high-order structure functions were estimated for different sediment bed under different flow conditions.

Finally, turbulent bursting phenomena were extensively explored using quadrant analysis of conditional turbulent characteristics such as streamwise and vertical velocity components, Reynolds shear and normal stresses, and TKE fluxes in flows over an equilibrium degraded channel bed. The conditional averaging of turbulent characteristics can be defined in two different approaches, namely, total- and quadrant-averaging, and the results were systematically compared.

1.3 Objectives of the Present Investigation

- To investigate the laws of turbulence, turbulence kinetic energy (TKE) dissipation rate, energy budget along with Reynolds stress anisotropy in a degraded channel bed under equilibrium condition.

- To examine the impact of bed degradation on turbulence anisotropy and intermittency using high-order and mixed high-order structure functions, with their scaling exponents estimated through extended self-similarity (ESS) in flows over a degraded channel bed.

- To explore turbulence bursting phenomena through quadrant analysis of conditional turbulent characteristics, employing different frameworks of averaging methods over a degraded channel bed, with a detailed assessment of hole size implications.

1.4. Structure of the Thesis

The thesis is structured into seven chapters. Chapter 1 provides an introduction to turbulence characteristics in unidirectional flow over a degraded bed under equilibrium conditions, highlighting its relevance to environmental systems. Chapter 2 presents theoretical background and a review of relevant literature. Chapter 3 described the experimental setup and procedures for different conditions. Chapter 4 discusses fundamental experimental results including turbulence laws, structure functions, energy budget, and Reynolds stress anisotropy in a degraded channel bed. Chapter 5 explores turbulence intermittency and anisotropy using high-order structure functions and their scaling exponents. Chapter 6 examines turbulence bursting phenomena through quadrant analysis, introducing a definition framework for averaging methods. Finally, Chapter 7 summarizes the conclusions drawn from this investigation.

Chapter 2

Background and Review of Literature

2.1 General

This chapter presents a comprehensive literature review on turbulent flow statistics over a degraded channel bed comprised of uniform and bimodal grades of sediment. The review begins with the fundamental turbulent characteristics, including velocity, Reynolds stresses, turbulent kinetic energy (TKE), TKE fluxes, etc. Next, the review covers turbulence anisotropy utilizing the anisotropy invariant map (Lumley triangle) and anisotropy invariant function through a degraded channel bed. After that the chapter delves into the study of structure functions, the application of extended self-similarity (ESS) technique and the calculation of scaling exponents based on high-order structure functions. The evidences for existence and behavior of intermittency in the flow, as revealed by these scaling exponents, were also reviewed. Furthermore, the review explored mixed high-order structure functions as well as their scaling exponents and the effects of anisotropy on the exponents over both the uniform and bimodal degraded channel beds. Finally, the studies on bursting phenomena in turbulent flow, utilizing quadrant analysis were reviewed.

2.2 Turbulent flow

The fluid flows are broadly divided into two categories, namely laminar and turbulent. Whilst the laminar flow are characterized by a well-defined path of the fluid particle while is in motion, turbulent flow is considered as a random, highly unpredictable, diffusive and chaotic one with strong mixing properties. For highly chaotic behavior of flow parameters, turbulent flow remains a matter of interest to the scientific communities. However, they can be predicted, if not fully calculated using different statistical techniques. For instance, turbulent flow in open channels is characterized by turbulent eddies, vortices, and rapid fluctuations in velocity and pressure. This type of flow is

common in rivers, streams, and artificial channels where the flow conditions are in favor of turbulence, making it directly relevant to applications in river engineering, environmental studies, and hydraulic design. In turbulent flow, hydrodynamic quantities like velocity and pressure at a specific point in space fluctuate irregularly over time. Visualization of turbulent flow shows that these fluctuations are caused by the continuous formation and breakdown of eddies. To describe these hydrodynamic quantities statistically, it is useful to separate the time-averaged value from the fluctuating component, known as Reynolds decomposition (Reynolds 1985). We obtain three-dimensional time-averaged velocity components along with their corresponding fluctuations by applying Reynolds decomposition to the Navier-Stokes equations. The product of these fluctuations gives additional stresses known as turbulent stresses or Reynolds stresses, which consequently lead to the calculation of other turbulent characteristics. In the next sections and sub-sections, some basic understanding of the calculation procedure and some terminologies are presented.

2.2.1 Reynolds averaging and decomposition

In turbulent flow, any stochastic quantity can be presented as the sum of its average and fluctuation. For velocity components, Reynolds proposed the following (Reynolds 1985):

$$u_x = \overline{u}_x + u'_x;\;\; u_y = \overline{u}_y + u'_y;\;\; u_z = \overline{u}_z + u'_z \tag{2.1}$$

Where $u'_x,\; u'_y,\; u'_z$ are the deviations of the velocity components u_x, u_y, u_z in the *x*, *y*, and *z* directions respectively. The Reynolds averaged velocity components are given by

$$\overline{u}_x = \lim_{T\to\infty} \frac{1}{T}\int_0^T u_x dt;\quad \overline{u}_y = \lim_{T\to\infty} \frac{1}{T}\int_0^T u_y dt;\quad \overline{u}_z = \lim_{T\to\infty} \frac{1}{T}\int_0^T u_z dt \tag{2.2}$$

where T is the total time of observation.

Now the Reynolds averaging method has the following characteristics:

(i) The averaged fluctuations of the quantities are zero i.e.,

$$\overline{h} = 0$$

(ii) The averaged of the average quantity is equal to the once averaged i.e.,

$$\overline{\overline{h}} = \overline{h}$$

(iii) The averaged of the sum is equal to the sum of the averaged i.e.,

$$\overline{h+g} = \overline{h} + \overline{g}$$

(iv) Operators of averaging and differentiation are commutative i.e.,

$$\overline{\frac{\partial y}{\partial t}} = \frac{\partial \overline{y}}{\partial t}; \quad \overline{\frac{\partial y}{\partial x}} = \frac{\partial \overline{y}}{\partial x}$$

(v) Averaged of two fluctuating quantities product is not zero and so on i.e.,

$$\overline{hf} \neq 0, \quad \overline{\overline{h}f} = \overline{hf}$$

$$\overline{\overline{h}f} = \overline{hf}$$

2.2.2 Equation of motion in turbulent flow (Reynolds-Averaged Navier-Stokes equations)

The Navier-Stokes equations for viscous incompressible fluid flow in Cartesian coordinate system in the tensorial form such that the velocity components *u*, *v*, and *w* in *x*, *y*, *z*-directions, respectively noted by u_i, i = 1, 2, 3 is written as:

Continuity Equation (Conservation of Mass):

$$\nabla u_i = 0 \tag{2.3}$$

Momentum Equation (Conservation of Momentum):

$$\frac{Du_i}{Dt} = \frac{-1}{\rho}\frac{\partial p}{\partial x_i} + \upsilon \nabla^2 u_i, \tag{2.4}$$

Where $\frac{D}{Dt} = \frac{\partial}{\partial t} + u_j \frac{\partial}{\partial x_j}$, is the material derivative obeying the neighboring fluid particles

$$\frac{\partial u_i}{\partial t} + u_j \frac{\partial u_i}{\partial x_j} = \frac{-1}{\rho}\frac{\partial p}{\partial x_i} + \upsilon \nabla^2 u_i, \tag{2.5}$$

The equation can be written as

$$\frac{\partial u_i}{\partial t} + \frac{\partial u_i^2}{\partial x_j} + \frac{\partial u_i u_j}{\partial x_j} = \frac{-1}{\rho}\frac{\partial p}{\partial x_i} + \upsilon \nabla^2 u_i, \tag{2.6}$$

Where u_i,u_j are the velocity components in the *i*-th and *j*-th directions, respectively. The x_i represents the spatial coordinates, *t* is time, ρ is density and *p* is the pressure.

Now, according to the Reynolds decompositions, the flow variables u_i and *p* can write as the sum of their averaged and fluctuating part as $u_i = \overline{u_i} + u_i'$; $p = \overline{p} + p'$, the continuity equations become

$$\nabla \cdot (\overline{u_i} + u_i') = 0, \tag{2.7}$$

and the momentum equation becomes

$$\frac{\partial(\overline{u_i}+u_i')}{\partial t} + \frac{\partial(\overline{u_i}+u_i')^2}{\partial x_i} + \frac{\partial(\overline{u_i}+u_i')(\overline{u_j}+u_i')}{\partial x_j} = -\frac{1}{\rho}\frac{\partial(\overline{p}+p')}{\partial x_i} + \upsilon\nabla^2(\overline{u_i} + u_i') \tag{2.8}$$

$$\text{or, } \frac{\partial(\overline{u_i}+u_i')}{\partial t} + \frac{\partial\left(u_i^2+u'^2_i+\overline{u_i}u_i'\right)}{\partial x_i} + \frac{\partial\left(\overline{u_iu_j}+u_i'u_j'+u_i'\overline{u_j}+\overline{u_i}u_j'\right)}{\partial x_j} = \frac{-1}{\rho}\frac{\partial(\overline{p}+p')}{\partial x_i} + \upsilon\nabla^2(\overline{u_i} + u_i') \tag{2.9}$$

Taking averaged in time of both continuity and momentum equations and using the Reynolds averaging characteristics that is, $\overline{u} = \overline{u}$, $\overline{p} = \overline{p}$ and $\overline{u_i'} = \overline{p'} = 0$. Also,$\overline{\frac{\partial\overline{p}}{\partial x_i}} = \frac{\partial\overline{p}}{\partial x_i}$, $\overline{\nabla \cdot u_i} = \nabla \cdot \overline{u_i}$, $\overline{\nabla^2 u_i} = \nabla^2 \cdot \overline{u_i}$ and $\overline{\frac{\partial\overline{p'}}{\partial x_i}} = 0$, $\overline{\frac{\partial\overline{u'}}{\partial t}} = 0$, $\overline{\frac{\partial\overline{u'}}{\partial x_i}} = 0$, $\overline{\frac{\partial\overline{u_i'u_j}}{\partial t}} = 0$, $\overline{\frac{\partial\overline{u_iu_j'}}{\partial t}} = 0$ $\nabla^2\overline{u_i'} = 0$,

The followings equations become

$$\nabla \cdot \overline{u_i} = 0, \nabla \cdot u_i' = 0, \tag{2.10}$$

$$\frac{\partial\overline{u_i}}{\partial t} + \frac{\partial\overline{u_i^2}}{\partial x_i} + \frac{\partial\overline{u'^2_i}}{\partial x_i} + \frac{\partial\overline{u_iu_j}}{\partial x_j} + \frac{\partial\overline{u_i'u_j'}}{\partial x_j} = \frac{-1}{\rho}\frac{\partial\overline{p}}{\partial x_i} + \upsilon\nabla^2\overline{u_i} \tag{2.11}$$

Using the equation of continuity, substituting $\frac{\partial\overline{u_j}}{\partial x_j} = \frac{-\partial\overline{u_i}}{\partial x_i}$ the momentum equation becomes

$$\frac{\partial\overline{u_i}}{\partial t} + \overline{u_i}\frac{\partial\overline{u_i}}{\partial x_i} + \frac{\partial\overline{u'^2_i}}{\partial x_i} + \overline{u_j}\frac{\partial\overline{u_i}}{\partial x_j} + \frac{\partial\overline{u_i'u_j'}}{\partial x_j} = \frac{-1}{\rho}\frac{\partial\overline{p}}{\partial x_i} + \upsilon\nabla^2\overline{u_i} \tag{2.12}$$

$$\text{or, } \frac{\partial\overline{u_i}}{\partial t} + \overline{u_i}\frac{\partial\overline{u_i}}{\partial x_i} + \overline{u_j}\frac{\partial\overline{u_i}}{\partial x_j} = \frac{-1}{\rho}\frac{\partial\overline{p}}{\partial x_i} + \upsilon\nabla^2\overline{u_i} - \left(\frac{\partial\overline{u'^2_i}}{\partial x_i} + \frac{\partial\overline{u_i'u_j'}}{\partial x_j}\right) \tag{2.13}$$

Now the momentum equations in component form can be written as

$$\frac{\partial \overline{u}}{\partial t} + \overline{u}\frac{\partial \overline{u}}{\partial x} + \overline{v}\frac{\partial \overline{u}}{\partial y} + \overline{w}\frac{\partial \overline{u}}{\partial z} = \frac{-1}{\rho}\frac{\partial \overline{p}}{\partial x} + \upsilon\nabla^2\overline{u} - \left(\frac{\partial \overline{u'u'}}{\partial x} + \frac{\partial \overline{u'v'}}{\partial y} + \frac{\partial \overline{u'w'}}{\partial z}\right) \quad (2.14)$$

$$\frac{\partial \overline{v}}{\partial t} + \overline{u}\frac{\partial \overline{v}}{\partial x} + \overline{v}\frac{\partial \overline{v}}{\partial y} + \overline{w}\frac{\partial \overline{v}}{\partial z} = \frac{-1}{\rho}\frac{\partial \overline{p}}{\partial y} + \upsilon\nabla^2\overline{v} - \left(\frac{\partial \overline{v'u'}}{\partial x} + \frac{\partial \overline{v'v'}}{\partial y} + \frac{\partial \overline{v'w'}}{\partial z}\right) \quad (2.15)$$

$$\frac{\partial \overline{w}}{\partial t} + \overline{u}\frac{\partial \overline{w}}{\partial x} + \overline{v}\frac{\partial \overline{w}}{\partial y} + \overline{w}\frac{\partial \overline{w}}{\partial z} = \frac{-1}{\rho}\frac{\partial \overline{p}}{\partial z} + \upsilon\nabla^2\overline{w} - \left(\frac{\partial \overline{w'u'}}{\partial x} + \frac{\partial \overline{w'v'}}{\partial y} + \frac{\partial \overline{w'w'}}{\partial z}\right) \quad (2.16)$$

These equations are called Reynold averaged Navier-Stokes equations (RANS) [Pope (2000), and Schlichting and Gersten (2001)]. Due to the deviations of the velocity components, RANS exhibit six additional stress terms such as three shear and three normal stresses, which are explicitly known as Reynolds stresses. The Reynolds stresses are given in the matrix form as

$$\begin{pmatrix} -\rho\overline{u'u'} & -\rho\overline{u'v'} & -\rho\overline{u'w'} \\ -\rho\overline{v'u'} & -\rho\overline{v'v'} & -\rho\overline{v'w'} \\ -\rho\overline{w'u'} & -\rho\overline{w'v'} & -\rho\overline{w'w'} \end{pmatrix} \quad (2.17)$$

Due to the symmetry characteristics, the Reynolds shear stresses are $-\overline{u_i u_j} = -\overline{u_j u_i}$ i.e., $-\overline{u'v'} = -\overline{v'u'}$, $-\overline{v'w'} = -\overline{w'v'}$, $-\overline{u'w'} = -\overline{w'u'}$, and the normal stresses are $-\overline{u'u'}$, $-\overline{v'v'}$, and $-\overline{w'w'}$ respectively.

It is clear that the flow system consists of four equations: three momentum equations and one continuity equation with ten unknowns, three averaged velocity components, the averaged pressure, and the six Reynolds stresses. Since the number of variables are more than the number of equations, it is not possible to solve the system explicitly. As a result, additional equations related to the system are required to express the Reynolds stresses over the velocity and pressure. In 1925, Ludwig Prandtl introduced the mixing length hypothesis which describes a direct relation between mixing length and turbulent eddy viscosity. Later, several researchers and scientists proposed different model equations at different times for Reynolds stress terms. Nevertheless, the model equations of the system are always flow-dependent and require experimental data for their accuracy and validation. This indeterministic characteristic of the system demonstrated that there is no exact classical and statistical model theory of turbulence. This problem is called as closure problem of turbulence.

2.3 Reynolds stress anisotropy

The Reynolds stress anisotropy tensor, initially introduced by Rotta in 1951 to assess the nature and degree of turbulence anisotropy, was significantly improvised in hydraulics by Lumley and Newman in 1977 [as further explored by Frohnapfel et al. (2007), Dey et al. (2019), and Penna et al. (2020)]. A key benefit of tensor anisotropy analysis is providing a comprehensive picture of turbulent flow anisotropy, without any external normalization of turbulent parameters.

Based on the directions in tensor coordinate systems, the Reynolds stress anisotropy tensor (a_{ik}) can be defined according to Rotta (1951) as

$$a_{ij} = \overline{u_i' u_k'} - \frac{2}{3} q \delta_{ik}, \tag{2.18}$$

where q is the average turbulent kinetic energy ($\overline{u_i' u_i'}/2$) and δ_{ik} is 0 if $i \neq k$, or 1 if $i = k$.

The anisotropy tensor can be normalized using the turbulent kinetic energy as

$$b_{ik} = \frac{a_{ik}}{2q} = \overline{u_i' u_k'}/(2q) - (\delta_{ik}/3) \tag{2.19}$$

Each component of the tensor b_{ik} is symmetric and traceless, with values ranging from –1/3 to 2/3. The anisotropy of turbulence can be assessed using a cross-plot of two principal invariants: *II* (= $– b_{ik}b_{ik}/2$) and *III* (= $b_{ij}b_{jk}b_{ki}/3$). This cross-plot, known as the Anisotropic Invariant Map (AIM), visualizes turbulence anisotropy, where – *II* indicates the degree and *III* describes the nature of anisotropy.

The AIM forms a triangular shape, often called the Lumley triangle, which has three limiting states that define the boundaries of the map. The bottom cusp of the triangle, where *II* = *III* = 0 is the 3D isotropic turbulence, is also known as the three-component (3C) limit. The one-component (1C) limit, representing rod-like or cigar-shaped turbulence, is located at the triangle's apex, while the left curved boundary indicates the two-component (2C) limit, corresponding to "pancake" turbulence.

2.4 Turbulent kinetic energy cascade (Classical and modern views on turbulence)

Esteemed British fluid dynamicist, Lewis Fry Richardson (1881–1953) was the first to carry out numerical computations of turbulence in the early 20th century. According to Richardson's assumptions, turbulence is a dissipative dynamical process, leading to a cascading energy transfer across the scales. The turbulent kinetic energy cascade describes the process by which energy is transferred across different scales in a turbulent flow. Energy is usually input at larger scales in a turbulent system, and it cascades down to smaller and smaller scales until it is transformed into thermal energy at the molecular level by viscous forces.

2.5 Turbulent length scales

Turbulent flow spans a wide range of eddy sizes, categorized into three regions based on length scales. The energy-containing range consists of the largest eddies (integral length scale), where kinetic energy is generated by external or gravitational forces, making this region non-universal. In the inertial subrange**,** energy cascades from larger to smaller eddies without dissipation, following universal turbulence laws. Finally, in the dissipation range, the smallest eddies convert into heat through molecular viscosity. Among these, the inertial subrange is particularly significant for understanding turbulence due to its universal scaling behavior.

2.5.1 Integral length scale

To measure the integral length scale, energy spectral and correlation functions are the well-accepted methodologies. However, the calculation using the correlation function is one of the most robust methods. The autocorrelation functions can be calculated as: $R(x, \Delta t) = u'(x, t + \Delta t)u'(x, t)$, where x is the point of location on the (x, z) plane, u' is the temporal velocity fluctuation in the streamwise direction, and t is time. With the transformation from time lag (Δt) to spatial increment (i.e., $R(x, \Delta t) = R(x, r)$), the correlation length can be defined as:

$$\Lambda(x, r) = \frac{1}{R(x,0)} \int_0^\infty R(x, r)\, dr \tag{2.21}$$

in the case of statistical convergence. Here r represents the spatial increment obtained using Taylor hypothesis $r(x,r) = |\bar{u}(x,\Delta t)|\Delta t$.

2.5.2 Taylor microscale

The Taylor microscale is an intermediate length scale used to characterize turbulent flow, where viscosity significantly influences the dynamics of turbulent eddies. Mathematically, It is defined by

$$\lambda = \left(\frac{15\upsilon\sigma_u}{\varepsilon}\right)^{0.5} \tag{2.22}$$

where σ_u is the streamwise Reynolds normal stress and ε is the dissipation rate. Taylor microscale is much smaller than the integral length scale. For isotropic homogeneous turbulence, they can be related via

$$\frac{\lambda}{\Lambda} \sim Re_{\Lambda}^{-1/2} \tag{2.23}$$

Here Re_Λ is the Reynolds number, that depend on the integral length scale Λ. Hence, the Reynolds number based on the Taylor microscale is given by

$$Re_{\Lambda} = (\sigma_u)^{1/2}\lambda/\nu \tag{2.24}$$

2.5.3 Kolmogorov dissipation scale

In the energy cascade process, viscosity dominates within the dissipation range, where turbulent kinetic energy (TKE) is converted into heat at the smallest length scales. The Kolmogorov dissipation scale is used to determine the size of these smallest eddies and can be estimated using the TKE dissipation rates. According, to Kolmogorov's first hypothesis (discussed later), the dissipation rate in small scale at high Reynolds number depends on the kinematic viscosity, velocity and length scale that is $\varepsilon \sim \nu u^{\alpha}/\eta^{\beta}$. Using the dimensional analysis, we have $D[\varepsilon] = D[\nu]D[u]^{\alpha}D[\eta]^{\beta}$, where D represents the dimension of the quantity. This gives

$L^2T^{-3}=L^2T^{-1}(LT^{-1})^{\alpha}L^{\beta}$ which implies that $\alpha + 1 = 3$ and $\alpha + \beta = 0$, $\alpha = 2$, $\beta = -2$

which gives $\varepsilon \sim \nu u^2/\eta^2$. Similarly smallest velocity scale u with ν and ε as $u \sim (\nu\varepsilon)^{1/4}$ and time scale t as $t \sim (\nu/\varepsilon)^{1/2}$. Finally, the Kolmogorov dissipation scale η can be written as

$$\eta = (\varepsilon/\nu)^{-1/2} u = (\nu^3/\varepsilon)^{1/4} \tag{2.25}$$

2.6 Kolmogorov hypothesis (1941)

In 1941, Russian mathematician and probabilist, A. N. Kolmogorov (1903–1987) inspired by Richardson's idea of energy cascade, postulated that the cascade process in turbulent flow. This suggests that statistical behavior of eddy exhibits self-similarity and is constant across different range of sizes. Thus, Kolmogorov introduced two major assumptions to explain this behavior and offered the scientific basis for the fundamental mechanism of turbulence as:

Hypothesis 1: In the turbulent flow at sufficiently high Reynolds number, statistics of small-scale motions ($l << \Lambda$) are isotropic and have a universal form that is uniquely determined by viscosity ν and the rate of dissipation ε.

From the dimensional analysis, we can show the dissipation law at small scales is according to the first hypothesis is $\varepsilon \sim \nu\, u^2/l^2$.

Hypothesis 2: In turbulent flow at sufficiently high Reynolds number, the statistics of the motions in the inertial subrange have a universal form that is uniquely determined by ε and independent of ν.

Mathematically, the dissipation law in the inertial subrange is given by $\varepsilon \sim l^{\alpha} u^{\beta}$. From the dimensional analysis, we have $L^2T^{-3} = L^{\alpha} (LT^{-1})^{\beta}$, which implies that $\alpha = -1$ and $\beta = 3$. This gives

$$\varepsilon = C_{\varepsilon} u^3/l \text{ with } C_{\varepsilon} = \text{Kolmogorov constant.} \tag{2.26}$$

2.7 Structure functions and laws of turbulence

The structure function analysis has been extensively employed to predict the scaling laws and to quantify the behavior of scaling exponents in turbulent flows (Kolmogorov 1941).

The general form of structure functions of order p can be written as:

$$S_p(\mathbf{r}) = \langle u(\mathbf{x} + \mathbf{r}) - u(\mathbf{x}))^p \tag{2.27}$$

for any $p > 0$, where $\mathbf{x}$, $\mathbf{x} + \mathbf{r}$ are two points in the flow field, u is the velocity component in the $\mathbf{r}$ direction, r is the length $|\mathbf{r}|$ of $\mathbf{r}$, and the angle brackets denote an ensemble average

Kolmogorov proposed several scaling laws based on his hypotheses, known as Kolmogorov's –5/3, 2/3, and 4/5-laws (Frisch 1995). Among these laws, the widely accepted power law within the inertial subrange is expressed as:

$$E(k_w) = C\varepsilon^{2/3}{k_w}^{-5/3} \tag{2.28}$$

where $E(k_w)$ is the energy spectrum, C is the Kolmogorov constant, ε is the turbulent kinetic energy dissipation rate, k_w is the wave number of the eddies of sizes l (i.e., $k_w = 2\pi/l$).

Furthermore, according to Kolmogorov's second similarity hypothesis, second-order velocity structure functions within the inertial subrange can be represented as:

$$\langle \Delta u \rangle^2 = C_2\varepsilon^{2/3}r^{2/3} \tag{2.29}$$

This is known as Kolmogorov's 2/3-law and applies under conditions of steady, homogeneous, and isotropic turbulence.

where C_2 is a universal constant, with a recommended value of 2.12.

Moreover, the TKE dissipation rate and the third-order velocity structure functions are connected by the law, known as Kolmogorov's 4/5-law, which was derived from the von Karman-Howarth equation and expressed as

$$\langle \Delta u \rangle^3 = 6\nu\frac{\partial\langle \Delta u \rangle^2}{\partial r} - \frac{4}{5}\varepsilon r \tag{2.30}$$

Now, within the inertial subrange, according to Kolmogorov's second hypothesis, the kinematic viscosity ν is negligible ($\rightarrow 0$) and ε is constant. Hence, the equation (2.30) can be rewritten as

$$\langle \Delta u \rangle^3 = -\frac{4}{5}\varepsilon r \tag{2.31}$$

which is known as Kolmogorov's 4/5-law.

However, for anisotropic turbulence, the third-order mixed structure function, well-known as Monin-Yaglom 4/3-law is also applicable in open-channel flow which is expressed as:

$$\langle \Delta u[(\Delta u)^2 + (\Delta v)^2 + (\Delta w)^2] \rangle = -\frac{4}{3}\varepsilon r \tag{2.32}$$

The third-order moments of velocity increments presented in Kolmogorov 4/5-law and Monin-Yaglom 4/3-law are used from the assumptions of homogeneous isotropic turbulence. These exact laws offer unique insights within the inertial subrange, including length scales and the dissipation rate. The isotropy is often not applicable in realistic flows, such as in open channel turbulence where physical factors like rotation and shear layers can affect the flow behavior, disrupt isotropy, and introduce anisotropy.

2.8 Estimation of TKE dissipation rate

The extensive application of the laws of turbulence and the structure functions lies in estimating the turbulent kinetic energy dissipation rate ε.

One of the primitive methods to measure the turbulent kinetic energy dissipation rate as described by Irwin (1973) and Krogstad and Antonia (1999) is

$$\varepsilon = (15\upsilon/u^2)\overline{(\partial u'/\partial t)^2}, \tag{2.33}$$

where ν is the kinematic viscosity of water and u' is the deviation of the time-averaged streamwise velocity component.

ε can also be estimated from the velocity power spectra by applying Kolmogorov's −5/3 power law (Kolmogorov 1941 a, b) as

$$E(k_w) = C_1 \varepsilon^{2/3} k_w^{-5/3}\,, \tag{2.34}$$

where $E(k_w)$ denotes the energy spectrum, while C_1 and k_w represent the Kolmogorov constant and wave number, respectively.

Later in 1962, Kolmogorov proposed that the second-order structure function could provide a more robust approach for estimating the turbulent kinetic energy dissipation rate. This approach aligns with Kolmogorov's 2/3-law, wherein ε is derived by the equation

$$\langle \varepsilon \rangle = (1/r)\, \overline{(\langle \Delta u \rangle^2 / C_2)^{3/2}} \tag{2.35}$$

where C_2 is a universal constant equal to 2.12.

Furthermore, according to the Kolmogorov's 4/5-law, ε can be determined from the relation based on the von Kármán–Howarth equation (Kármán and Howarth 1938) which can be expressed as:

$$\langle \varepsilon \rangle = (-5/4r)\langle \overline{\Delta u^3} \rangle \tag{2.36}$$

This equation enables a more precise estimation of ε.

The dissipation rate ε, can also be estimated using the third-order mixed structure function, commonly known as Monin-Yaglom's 4/3-law (Karman and Hawarth 1938) as:

$$\langle \varepsilon \rangle = (-4/3r)\, \langle \overline{\Delta u[(\Delta u)^2 + (\Delta v)^2 + (\Delta w)^2]} \rangle \tag{2.37}$$

It is important to note that, Monin-Yaglom's 4/3-law is derived under the assumption of isotropic turbulence, which is considered applicable across both high and low Reynolds numbers.

2.9 Some of the notable works in open-channel flow and structure functions

Nikora and Goring (2000) investigated the properties of turbulence structures in quasi-uniform, two-dimensional flows over a fully rough bed. Their study involved collecting velocity data under various flow conditions such as at a high flow rate on a weekly mobile bed and two lower flow rates on a fixed bed. They showed that the mean velocity

profile for the weakly mobile bed flow (WMBF) does not indicate the wake region, unlike in the fixed bed flows (FBF) where wake regions are observable. In WMBF, the von Kármán constant was notably lower than in FBF, while the roughness length was comparatively higher. Additionally, the roughness sublayer in WMBF is thicker, and the correlation coefficient is reduced, indicating a weaker coherence structure in the turbulent flow. As for the relative turbulence intensities, they increase from the water surface towards the bed, but this increase is less pronounced in WMBF. The normalized durations of ejections and sweeps are slightly extended in WMBF compared to FBF. Furthermore, there is indication of turbulence anisotropy in WMBF, suggesting directional variations in the turbulent flow. Whereas turbulence intensities, higher order moments, velocity auto and co-spectra appeared to be similar among all flows.

Shvidchenko and Pender (2001) explored the general turbulent structures and the turbulence-driven mechanisms in open channel flow over a mobile gravel bed. They described the turbulent flow as a sequence of long-lasting, three-dimensional turbulent eddies. The size of these eddies was predicted to be close to the flow depth in the vertical direction, and approximately 4 and 2 times the flow depth in the streamwise and transverse directions, respectively. These eddies move downstream at the same speed as the bulk flow, generating quasi-periodic fluid motions. These motions include high-speed downward “sweeps” and burst-like upward “ejections” that occur throughout the flow depth, resulting in quasi-periodic fluctuations in the flow's direction and speed. The up-and-down movement of the fluid particles caused by these eddies produces lift and drag forces on the bed particles, which were strong enough, can cause the particles movement or displaced.

Banerjee et al. (2007) employed the Barycentric map to examine the turbulence anisotropy in the flow. They presented an expression of anisotropic invariants derived from the Reynolds stress tensor’s eigenvalue, dealing with the restrictions of the nonlinear anisotropic invariant function suggested by Lumley and Newman (1977). The barycentric coordinates within the map, estimated using eigenvalues, gives a precise measurement of the weighting of the limiting states. This method allows for the assessment of anisotropy in various flow conditions using scalar metrics. The capability

of these barycentric metrics lies in their representation on a barycentric map, an equilateral triangle with vertices depicting the three limiting states. By plotting the metrics in 2D, the characteristics of anisotropic stress at specific locations is clearly illustrated addressing these limiting states.

Mignot et al. (2009) utilized spatial-averaging techniques to explored rough-bed turbulence statistics over gravel beds in open-channel flows. Their study express that macro-roughness particles in the bed notably influence the turbulent kinetic energy budget in rough bed circumstances. For flows over smooth and uniformly rough beds without macro-roughness, TKE production peaks very close to the bed. In contrast, for fully rough beds with macro-roughness elements, maximum turbulence activity and TKE production occur at the crest of the gravel. At this height, turbulent diffusion also reaches its peak. Above twice the height of the roughness crest level, TKE production and dissipation approximately balance each other, similar to the log-law region in smooth boundary layers, where turbulent diffusion is generally minimal. In the region between half of the crest level and twice of the roughness crest level, TKE production surpasses dissipation, and turbulent diffusion is at its highest. This intense diffusion effectively spreads the turbulence production around the crest level.

Jain et al. (2015) carried out an experiment to measure the three-dimensional velocity components, turbulence intensity, and Reynolds stress over a degraded sand-gravel bed formed due to the transport of the bed particles. They also examined the impact of sweep and ejection events in sediment transport using quadrant analysis. Their observations revealed that the highest turbulence intensity and Reynolds stress occurred close to the initial bed level, before the detachment of the bed material takes place, with both values decreasing as the vertical distance increased. Moreover, as the flow moved spatially downstream along the degraded bed, the turbulence intensities and Reynolds stresses diminished, indicating a weakening of vortex structures due to bed degradation. This trend demonstrates a significant decline in the frequency of turbulent events as the flow moved downstream to the degraded region. Additionally, ejection and sweep events were found to be more dominant than inward and outward interactions, with sweep and

ejection events exhibit the highest occurrence probabilities. However, these probabilities decreased with increasing hole size, arriving close to zero for larger hole sizes.

Ferraro et al. (2016) examined the characteristics of turbulence over heterogeneous sediment beds, such as pebbles and gravel, considered as natural bed flow. The study deeply discussed the laws of turbulence, including Kolmogorov's 4/5-law and Monin-Yaglom's 4/3-law. The Taylor frozen-in approximation was implemented to convert the data from time increment into spatial increments before using the structure functions methodlogy. Fundamental turbulent characteristics, such as velocity, Reynolds normal stresses, and shear stress, were examined to validate the results. Applying the structure functions methodology, the study observed that Kolmogorov's –5/3-law was not completely satisfied due to the presence of large-scale coherent structures and turbulent anisotropy in the flow. However, within the inertial subrange, where the third and mixed third-order structure functions followed their respective laws, the turbulent kinetic energy dissipation rate was measure more accurately within this region. Near the crest level of the natural bed, the Taylor coefficients surpassed a magnitude of 1, violating the validity of Taylor's hypothesis. Finally, the study detected a two-fifteenth law related to the cascade of helicity distribution, providing a new perspective in the study of turbulence through a highly rough bed flow.

Padhi et al. (2018) comprehensively studied the scaling law and turbulent kinetic energy dissipation rate through water-worked gravel beds (WGB) and screeded gravel beds (SGB) using the structure functions methodology. To better understand the influence of shear Reynolds number on WGB, they performed experiments under three different shear Reynolds number conditions. They observed that the water flow causes the surface gravels in the WGB to be more spatially organized, whereas in the SGB, the gravels are arranged more randomly. This spatial arrangement generates the higher roughness in the WGB compared to the SGB. The second and third-order structure functions exhibited larger values in the WGB than in the SGB and followed the Kolmogorov's 2/3 and 4/5 scaling laws within the inertial subrange. By utilizing these scaling laws, they determined the TKE dissipation rate, which was observed to be higher near the bed due to the influence of bed roughness. Finally, they found the values of TKE, TKE dissipation rate,

and structure functions all increased or decreased in proportion to the shear Reynolds number.

Padhi et al. (2019) further carried out an extensive study on the influence of coherent structures in near-bed turbulent flow over screeded gravel beds (SGB) and water-worked gravel beds (WGB). Using 2-D particle image velocimetry (PIV) under identical flow conditions, they investigate the behavior and characteristics of coherent structures in these different bed configurations. In the near-bed flow zone, the presence of roughness elements leads to turbulence production, resulting in consistently high turbulence levels that gradually decrease with increasing vertical distance from the bed. Due to the greater roughness height of the WGB compared to the SGB, the spatially averaged turbulence indicators, second and third order moments, and turbulent kinetic energy budget parameters are all found to have higher magnitudes in the WGB. The water-worked gravel bed (WGB) features a more organized and structured roughness, generating from the natural rearrangement of sediment particles under the influence of water flow. In contrast, the SGB presents a randomly distributed roughness structure, as it is typically formed without the influence of water-driven processes.

Penna et al. (2020) conducted an experiment to statistically analyze the turbulence characteristics over a water-worked gravel bed. They applied the laws of turbulence and invariant anisotropic stress tensor, along with the anisotropy invariant map (AIM), Lumley triangle, and anisotropy invariant function, to assess the flow structure. By using the Taylor hypothesis, the acoustic Doppler velocimeter (ADV) collected velocity data in time increments, which were then converted into spatial increments. The structure functions methodology was applied to understand the scaling laws of turbulence for the experimental condition. These data were then utilized to generate energy spectra, confirming the existence of an inertial subrange that aligns with Kolmogorov's −5/3-law. The presence of this inertial subrange was further supported by second and third-order statistical analyses. Within this subrange, third-order statistics were used to accurately calculate the turbulent kinetic energy (TKE) dissipation rate. However, when the Monin-Yaglom four-thirds law was applied to estimate the TKE dissipation rate, the results were different, indicating the influence of anisotropic effects throughout the flow depth. The

anisotropy invariant map within the Lumley triangle demonstrated that turbulent anisotropy was predominant near the gravel bed but gradually transitioned to three-dimensional isotropy with increasing vertical distance towards the free surface. Additionally, the anisotropy invariant function revealed confined streamwise variations, which were attributed to the regular arrangement of the gravel bed's roughness structure.

Dey et al. (2020) experimentally investigated the turbulence structure in flows over and within the interface of a series of continuous dunes. Their results showed that the velocity field and vorticity contour highlighted a decelerated flow zone downstream of the dune crest. This zone, marked by reduced flow speed, is linked to the formation of a recirculation zone, starting right after the dune crest where the flow separates from the bed, creating reverse flow and low-velocity regions. This behavior is common in areas with prominent topographical features like dunes, resulting in localized zones of reduced velocity and flow reversal. Additionally, the time-averaged vertical velocity profile indicated a velocity defect line above the crest, coinciding with the peak in shear stress. The turbulence indicator revealed high turbulence in the interfacial sublayer below the crest, peaking at half the dune height, with moderate turbulence levels above the crest. Third-order correlations showed rapid fluid motion with downward-downstream stress diffusion in the interfacial sublayer, and slower fluid motion with upward-upstream diffusion above the crest. The TKE flux followed a similar pattern. The TKE budget showed significant form-induced diffusion, which was negative in the form-induced sublayer and positive in the interfacial sublayer, with peaks near the crest. Sweep events were prominent in the interfacial sublayer, and quadrant analysis showed energetic fluctuations within the roughness sublayer.

Penna et al. (2021) investigated the interactions between turbulent flow structures and a naturally rough gravel bed, highlighting its connection to sediment transport using conditional turbulent statistics and high-order velocity structure functions. They observed variations in the flow field and turbulence anisotropy near the bed, attributed to the presence of coherent structures generated by the rough pebble surface. The turbulence intensity (level) was found to be highest close to the bed, gradually decreasing with increasing vertical distance. At the roughness crest, sweep and ejection events had

comparable effects this suggests that the impact of low-speed fluid parcels rising from the near-bed flow zone is diminished by the arrival of high-speed fluid parcels descending from the upper flow zone, while sweep events dominated the region above this level. In contrast, outward and inward interactions consistently had a minimal influence on the turbulence statistics. Within the scaling region, the scaling exponents of high-order velocity structure functions revealed the multifractal nature of the flow.

Rathore et al. (2022) studied turbulent characteristics over an open channel where the bed changed abruptly from smooth to rough. Downstream of the smooth-to-rough interface, Reynolds shear and normal stresses, along with bed shear stress, increase with longitudinal flow development. The Reynolds shear stress reaches its peak at one-fifth of the flow depth in the rough bed zone. Third-order correlations show that the upstream flow is mainly influenced by the arrival of slower-moving fluid streaks, accompanied by outward Reynolds stress diffusion. In contrast, the near-bed flow over the downstream coarser bed is driven by faster-moving fluid streaks associated with inward diffusion of Reynolds stresses. In terms of the turbulent kinetic energy (TKE) budget, peak values of TKE production and dissipation rates are greater near the downstream coarser bed than in the upstream region. In the wall-shear layer, TKE production exceeds dissipation, while in the near-bed flow of the downstream zone, negative TKE diffusion enhances TKE levels. Conditional statistics of Reynolds shear stress confirm that sweep events dominate the near-bed flow in the downstream coarser bed, whereas ejection events control the upstream flow.

2.10 High-order structure functions

More detailed information on the turbulence structures can be obtained through the analysis of high-order generalized structure functions $S_p(r)$ defined by the equation (2.27). For homogenous isotropic turbulence, the scaling behavior of $S_p(r)$ is described as (Kolmogorov 1941)

$$S_p(r) \sim r^{\xi p} \tag{2.40}$$

Where ξ_p are scaling exponents of p^{th} order structure functions. According to the Kolmogorov theory, in the inertial subrange, the structure function of order p exhibits the exponents as $\xi_p = p/3$, corresponding to a mono-fractal behavior. However, the presence of intermittency, characterized by intense changes of turbulence fluctuations, causes deviations of scaling exponents from the Kolmogorov hypothesis that is $\xi_p \neq p/3$, leading to multi-fractal behavior of turbulence. Over recent decades, high-order structure function analysis has become a crucial tool for quantifying intermittency in turbulent flows.

2.11 Extended self-similarity

In 1983 Roberto Benzi was introduced the concept of Extended self-similarity (ESS) to estimate the scaling exponents of high-order structure functions. In ESS technique to identify the scaling exponents, the structure functions were plotted against those of another order. Mathematically,

$$S_n(r) \sim S_m(r)^{\bar{\zeta}_{m,n}}, \bar{\zeta}_{m,n} = \frac{\zeta_n}{\zeta_m} \tag{2.41}$$

where $\bar{\zeta}_{m,n}$ is the relative scaling exponents of order n (i.e., ζ_n) with respect to a particular order m (i.e., ζ_m).

In turbulent flow, based on Kolmogorov (1941) theory, the exact exponent $\zeta_3 = 1$, for $n = 3$ was used in the ESS technique. Consequently, equation (2.41) take the form, $S_n(r) \sim S_3(r)^{\zeta_n}$, i.e., the structure functions of order n, $S_n(r)$ can be relatively evaluated from $S_3(r)$.

2.12 High-order mixed structure functions

The mixed structure functions of order n in tensorial form following Frisch (1995), Dhruva et al. (1997) and Arad et al. (1998) can be written as:

$$S_n^{pq} = \langle [u(x+r) - u(x)]^p [w(x+r) - w(x)]^q \rangle, \tag{2.42}$$

where $n = p + q$ is the order of the mixed structure functions, u and w are the velocity components in streamwise and vertical directions. According to the $SO(3)$ decomposition introduced by Kurien and Sreenivasan (2000) in turbulent flow, the scaling exponents for isotropy and anisotropy can be derived from high-order unidirectional and mixed structure functions. The scaling exponents of mixed structure functions are referred to as anisotropic scaling exponents, while those obtained from unidirectional structure functions are termed as isotropic scaling exponents.

2.13 Some of the notable works on high-order structure functions in open-channel flow

Benzi et al. (1993 a, b) provided numerical and experimental evidence for the Extended Self-Similarity (ESS) technique, demonstrating its effectiveness in calculating the scaling exponents of high-order structure functions over a range that extends beyond the inertial subrange. They showed that in high Reynolds number turbulence, the scaling exponents of high-order structure functions are observed not only within the inertial subrange but across a broader range, including large-scale and dissipation regions. This technique reveals that the self-similar properties of structure functions persist in both high and low Reynolds number cases, encompassing the inertial, large-scale, and dissipation ranges. ESS offers a more precise method for determining the scaling exponents of high-order velocity increments, enhancing accuracy across the full range of turbulence, such as inertial and dissipation scales, for both high and low Reynolds number turbulence.

Protas et al. (1996) and Gaudin et al. (1998) numerically and experimentally explored the spatial behavior of the scaling exponents of high-order structure functions in wake flows downstream of bluff bodies. The Extended Self-Similarity (ESS) technique was extensively employed to calculate the scaling exponents of these structure functions at various locations near and far from the wake flows. It was found that the wake flows near bluff bodies exhibited shorter scaling regions compared to the far wake flows. Additionally, the scaling exponents showed greater deviations near the wake, while in the far wake, they displayed an asymptotic trend with the K41 assumptions, highlighting the

effects of intermittency and inhomogeneity in the near-wake region. Specifically, for the second-order structure function, the exponents asymptotically approached Kolmogorov 1941 theory from higher values, whereas for the fourth, sixth, and eighth-order structure functions, the exponents approached the asymptotes from lower values.

Arad et al. (1998) analytically derived second-order structure functions using two-directional velocity data at high Reynolds numbers and experimentally validated their findings with atmospheric surface layer turbulence velocity data. Based on the magnitude of the scaling exponents, they observed that the purely longitudinal structure function is less sensitive to anisotropy, whereas the finite θ structure function, which involves velocity differences in directions other than the flow direction, is more influenced by anisotropy. They proposed this method as a fundamental way to quantify the degree of anisotropy using scaling exponents.

Kurien and Sreenivasan (2000) aimed to determine the scaling exponents for the anisotropic components of high-order structure functions. To ensure that these anisotropic components were not mixed with their isotropic counterparts at each order, they exclusively utilized tensor components that are fully anisotropic. This was achieved by focusing on the isotropic sector corresponding to $j = 0$ in the $SO(3)$ decomposition of each tensor, and then constructing components that are explicitly zero within the isotropic sector. The anisotropic scaling exponents obtained were consistently larger than those corresponding to the isotropic components across all orders. This provides strong evidence that anisotropy diminishes as the scale decreases. However, the rate at which anisotropy decreases is slower than predicted by dimensional analysis.

Warhaft and Shen (2002) described the high-order longitudinal and transverse structure functions, and investigating their relationship with mixed high-order structure functions in high Reynolds number shear flow. They found that the scaling exponents of mixed high-order structure functions were consistently larger than those of single-component structure functions. Additionally, the ratio of anisotropic to isotropic scaling exponents tended to decrease with increasing order, indicating a persistent anisotropy even at the smallest turbulence scales for higher-order structure functions. They also noted a significant difference between the scaling exponents of the longitudinal and transverse

structure functions, and used the arithmetic mean of these values when calculating the ratio of anisotropic to isotropic exponents. Similar to kurien and sreenivasan (2000), they also found that the effect of anisotropy diminishes with decreasing scale more gradually than anticipated. The inequality of anisotropic and isotropic exponents weakens progressively as order increases, indicating that at higher orders, isotropy may not be fully restored based on this measure.

Shen and Warhaft (2002) conducted an extensive study on the scaling exponents of longitudinal and two types of transverse structure functions which are included in measurements of the longitudinal velocity in the transverse direction and the transverse velocity in the streamwise direction. The experiment was performed in both uniform sheared and nonsheared flows, at low and high Reynolds numbers turbulence. In high Reynolds number turbulence, for both sheared and nonsheared cases the scaling exponents were nearly identical for the longitudinal velocity measured in both the streamwise and transverse directions. However, at low Reynolds numbers, significant differences emerged between the exponents. The scaling exponents for the longitudinal velocity in the transverse direction were consistently smaller than those for the longitudinal velocity in the streamwise direction. Notably, the exponents for the transverse velocity measured in the streamwise direction were always smaller than those for the longitudinal velocity, in both high and low Reynolds number turbulence, and in both sheared and nonsheared flows. A minor difference between shear and nonshear flows was that the scaling exponents were slightly higher in nonshear flows.

Aberle and Nikora (2006) experimentally analyzed the statistical characteristics of armored pebble bed surfaces using high-order structure functions. They used six different armoring discharges across six separate runs. Their findings showed that, as the armoring discharge increased, the distribution of bed elevations became more diverse, with fewer data points near the zero-mean elevation. This was evident in the probability density functions (PDFs), which revealed increased geometric roughness due to the accumulation of coarser particles on the bed surface during the progressive development of the armor layer. Additionally, they observed that similar to second-order structure functions, higher-order structure functions could be divided into scaling, transition, and saturation

regions. Notably, the scaling region was influenced by armoring discharge. The scaling exponents of the structure functions calculated for the scaling region suggested that initial beds elevation exhibit simple scaling behavior, while water-worked beds elevation tends to display multiscaling behavior.

Coscarella et al. (2020) conducted an experimental study investigating turbulence anisotropy and intermittency over a channel bed composed of sediments of different sizes, leading to different roughness levels. Using particle image velocimetry to measure flow velocity, they divided the flow region vertically into two zones based on the viscous shear stress. Zone 1, near the bed, exhibited very small velocity derivatives, while Zone 2 was located above this region. From the contour plots of the second-order structure function, they observed that anisotropy became more pronounced near the grain crests in Zone 1, while in Zone 2, the flow tended toward isotropy. The analysis of anisotropy angle gives small-scale turbulence exhibited more isotropy, whereas large-scale turbulence near the rough bed was more anisotropic. Additionally, flows over beds with larger sediment sizes showed more isotropy. The scaling exponents from higher-order structure functions in the inertial subrange revealed multifractal behavior, with intermittency occurring near the bed.

2.14 Turbulent bursting process

Studies from the 1960s and 1970s (Kline et al., 1967; Corino and Brodkey, 1969; Grass, 1971) identified the bursting process in turbulent boundary layers, where alternating low- and high-speed streaks interact through ejections and sweeps. Ejections occur when low-speed fluid lifts into the main flow, while sweeps bring high-speed fluid downward, forming a turbulent shear layer with small-scale vortices.

Quadrant analysis quantifies these events by measuring their duration, mean cluster time, and frequency of transitions. A hole threshold is applied to isolate strong bursts, though increasing hole size complicates conditional averaging. To address this issue, conditional means are defined based on the denominator and hole size for a more accurate representation of turbulent bursting events.

2.15 Quadrant analysis

Turbulent events in the boundary layer can be effectively characterized using quadrant analysis, a method introduced by Willmarth and Lu (1972). This approach divides local flow behavior into four quadrants based on the signs of the streamwise (u') and normal (w') velocity fluctuations. The four quadrants are defined as follows:

i) Q_1, first-quadrant $(u'w')_1$, signifies outward interactions where $u'>0$ and $w'>0$, denoting an event in which high speed fluid moves toward the centre of the flow field;

ii) Q_2, second-quadrant $(u'w')_2$, signifies ejections where $u'<0$ and $w'>0$, denoting an event in which low-speed fluid moves toward the centre of the flow field, away from the wall;

iii) Q_3, third-quadrant $(u'w')_3$, signifies inward interactions where $u'<0$ and $w'<0$, denoting an event in which low-speed fluid moves toward the wall; and

iv) Q_4, fourth-quadrant $(u'w')_4$, signifies sweeps where $u'>0$ and $w'<0$, denoting an event in which low-speed fluid moves toward the wall.

In open channel flow, events in the second and fourth quadrants are important. Near the wall, sweep events are more dominant, while farther from the wall, ejection events become more significant. These events play a major role in generating Reynolds stresses and maintaining the turbulent structures within the boundary layer.

2.15 Some of the notable works on bursting phenomena in open-channel flow

Kline et al. (1967) were among the first to investigate the flow structure in a turbulent boundary layer. Using a hydrogen bubble visualization technique, they revealed that the near-bed region exhibits a highly complex structure, organizing into alternating, unsteady patterns of high-speed ($+u'$) and low-speed ($-u'$) regions relative to the mean streamwise

velocity. Fluid migrates laterally from areas of high speed to those of low speed. This streaky structure in the boundary layer interacts with the outer flow through a sequence of gradual outflow, lift-up, sudden oscillation, and eventual breakup.

Grass (1971) examined the structural characteristics of turbulent flow over both smooth and rough beds. Near the boundary, he identified two distinct intermittent flow features: sweep and ejection, present in both types of beds. Through conditional averaging, he found that these events are strongly correlated with significant contributions to Reynolds stress, which drives maximum turbulence production close to the boundary.

From their experimental results, Lu and Willmarth (1973) concluded that a burst occurs when the streamwise velocity at the edge of the viscous sub-layer becomes low and decreases, while a sweep happens when the streamwise velocity becomes high and increases. Across the turbulent boundary layer, ejection events are the primary contributors to Reynolds shear stress production, with sweep events being the second largest contributors. They also determined the characteristic mean time intervals for ejection and sweep events, finding that these intervals were approximately equal and remained constant throughout most of the turbulent boundary layer.

Raupach (1981) investigated turbulent structures over smooth and rough surfaces under zero pressure gradient conditions. Quadrant analysis revealed that sweep events dominate stress generation near rough surfaces, with their relative contribution increasing both with surface roughness and proximity to the surface. In the remaining portions of the inner and outer layers, the flow adhered closely to established similarity laws concerning surface roughness. Furthermore, the disparity between sweep and ejection events was found to be closely associated with the third-order moments of the streamwise and vertical velocity fluctuations throughout the flow field.

Cellino and Lemmim (2004) conducted an experiment under three different flow conditions, measuring turbulent characteristics in both clear water and particle-laden open channel flow with varying suspension concentrations. Quadrant analysis was employed to examine turbulent features, focusing on conditional averages of velocity, root mean square (RMS) values of streamwise and vertical fluctuations, and turbulent kinetic energy (TKE) fluxes. Notably, quadrant-based averaging was applied only to the

streamwise velocity, while total averages were used for the RMS values of the streamwise and vertical fluctuations, as well as the TKE fluxes, to capture all bursting events. The results revealed that ejection and sweep events are the most significant contributors to sediment suspension and transport. In the near-bottom layer, ejections and sweeps exhibited comparable influences, while across the remaining water depth, ejections dominated the flow dynamics.

Balachandar and Bhuiyan (2007) investigated the influence of surface roughness on higher-order velocity moments in turbulent open channel flow with pronounced bottom roughness. They examined flow over two types of rough beds and compared the results to those from a smooth open channel. Their study included the analysis of higher-order velocity fluctuation moments, conditional statistics using quadrant analysis, and turbulent kinetic energy production. The findings revealed that third-order moments were highly sensitive to wall conditions, with significant effects observed throughout the flow depth. Comparisons between rough and smooth beds indicated that the impact of bed roughness extended beyond the near-bed region. The authors also highlighted that higher-order moments provide valuable insights into the coherent structures within the flow.

Padhi et al. (2019) explicitly explore the contributions of bursting events to the total turbulent characteristics in water-worked and screeded gravel bed flows. All bursting events of turbulent characteristics have been computed using quadrant-based average. Vertical profiles of turbulent bursting events and total turbulent quantity gives that within the roughness layer sweep is the most dominating and give highest contributions to produce the total turbulent quantities. Moreover, above the roughness layer ejection governs the flow.

Dey et al. (2020) demonstrated the effectiveness of bursting events in flow over a series of two-dimensional dunes. Quadrant-based turbulent characteristics namely streamwise velocity, Reynolds shear and normal stresses and TKE fluxes has been analyzed explicitly. Below the crest level of the dunes sweep dominates the flow whereas ejection dominates and contributes most above the crest level in the remaining flow region.

Matsumoto et al. (2024) performed quadrant analysis of Reynolds Shear stress using total averaged bursting events. According to a quadrant analysis of the conditional Reynolds

stresses, the near-bed flow's Reynolds shear stress production is primarily caused by sweeps and ejections, while the sweeps acting as the governing event close to the bed level.

However different researchers used different averaging methods to demonstrate the bursting process using Quadrant analysis of turbulent quantities, although we assert that conditional properties require a well-defined framework. For that, we introduce a definition framework incorporating two averaging methods: total-averaging and quadrant-averaging. Total-averaged quantities, which always use the total sample size in the denominator, have the advantage that their sum across all four quadrants equals the mean quantity before conditioning. However, they may not accurately capture the dynamics within a specific quadrant, which could be more relevant for understanding flow interactions with surrounding bodies. This limitation may encourage the use of quadrant-averaged quantities.

Chapter 3

Experimental Setup and Procedure

3.1 General

This chapter presents the experimental facilities in the Fluvial Mechanics Laboratory of Physics and Applied Mathematics Unit (PAMU), Indian Statistical Institute, Kolkata, India. A detailed description of the experimental setup, experimental design, experimental procedure, and measurement techniques are discussed here.

3.2 Experimental facilities

All the experiments related to this research work were conducted in a hydraulic flume of the Fluvial Mechanics Laboratory of Indian Statistical Institute, Kolkata. The flume measured 20 m in length, 0.5 m in depth, and 0.5 m in width. To facilitate clear visualization of the flow, the sidewalls were constructed from transparent Perspex sheets, allowing for direct observation. Water was supplied to the flume using two high-power centrifugal pumps. Flow rate monitoring and regulation were achieved using an electromagnetic flow meter and a control valve, respectively. To minimize initial disturbances caused by turbulence, waves, or external influences, a pair of honeycomb structures was installed at the flume inlet.

3.2.1 Additional Attachments

An instrument carriage with a main unit and an auxiliary unit was used to mount the instruments over the flume. The main unit spanned the flume and moved along two parallel rails in the streamwise direction. The auxiliary unit, which held instruments like the point gauge and Vectrino and others, could be adjusted across the flume. This setup allowed the Vectrino to take measurements at different vertical, transverse, and streamwise positions.

3.3 Scheme of Experiments

The whole experimental programme was divided into two phases. At first, a number of experiments were performed over a degraded bed made up of bimodal (a 1: 1 mixture of two different sizes of uniformly graded) noncohesive sediments. The second set of experiments was preformed over a degraded bed created by uniform grade of sediments. The details of the experimental parameters are also presented in the respective chapters.

3.3.1 Uniform and Bimodal gravel

The Indian Standard sieves were used to prepare various sediment samples. To determine the values of d_{16} and d_{84} of the sediment samples sieve analysis was perform using grain size distribution curves. Here, d_{16} and d_{84} represent the sediment sizes for which 16 percent and 84 percent of the sample, respectively, are finer. The degree of uniformity in the particle size distribution of a sediment sample was assessed using the geometric standard deviation σ_g, defined as $(d_{84}/d_{16})^{0.5}$ According to Dey and Raikar (2007), a sediment sample is considered uniform if σ_g is less than 1.4. Based on this criterion, uniform sediment samples were prepared. Similarly, for the bimodal bed, gravel with the required d_{50} value was selected.

3.3.2 Final Preparation of Sample

All sediment samples were thoroughly washed to remove any greasy material, dust, or other foreign particles. After cleaning, they were dried completely and carefully stored in labeled containers for proper identification.

3.4 Method of Measurement

3.4.1 Discharge

The discharges were measured using two electromagnetic discharge meters. The discharge meters are attached to the delivery pipe of the pumps. Total discharge capacity of the pumps is approximately 0.25 m^3/s. The valves of the pumps can be regulated manually to fix the discharge according to the requirement of the experiments. An indirect measurement of discharge was also carried out by integrating the measured

velocity distribution profiles along different vertical lines across the flume as a cross-verification.

Figure 3.2: Photograph of the electromagnetic discharge meter installed in the Fluvial Mechanics Laboratory, Indian Statistical Institute, Kolkata, India.

3.4.2 Bed and Water Surface Levels

The bed and water surface levels were measured using a Vernier point gauge with an accuracy of ±0.1 mm. The gauge was mounted on an instrument carriage, allowing movement in both the streamwise and transverse directions. Additionally, a transparent graph sheet was affixed to one side of the glass panel in the data collection zone, enabling water surface profiles to be visually recorded directly from the graph sheet.

3.4.3 Velocity and Flow Field

A 5 cm downward-facing Acoustic Doppler Velocimeter (ADV) probe, Vectrino, manufactured by Nortek, was employed to capture instantaneous velocity components. This high-resolution acoustic velocimeter is widely used for measuring three-dimensional (3D) water velocity in both laboratory and field applications. The instrument operated at an acoustic frequency of 10 MHz with a sampling rate of 100 Hz, which could be increased to 200 Hz. However, tests indicated that a 100 Hz sampling rate minimized noise in the recorded signals.

The sampling volume of the Vectrino probe was cylindrical, with a 6 mm diameter and an adjustable height ranging from 1 mm to 9.1 mm. The sensor system comprised one transmitting transducer and four receiving transducers, with the addition of the fourth receiver enhancing turbulence measurements and providing redundancy. As the measurement volume was located 5 cm below the probe, the instrument's presence had negligible influence on the recorded velocity data.

The Vectrino also featured an adjustable transmit pulse length ranging from 0.3 mm to 2.4 mm. Increasing the transmit pulse length improved the signal-to-noise ratio (SNR), whereas a shorter pulse length was used near boundaries to reduce the sampling volume. The processing module executed digital signal processing to determine Doppler shifts, and the data acquisition software provided a real-time graphical and tabular display of the measurements.

During the experiments, no external seeding was required, as the ambient particles in the flow ensured that the SNR remained at or above 17. Uncertainty analyses were conducted to assess the accuracy of the velocity data. Furthermore, velocity power spectra from unfiltered Vectrino data confirmed that the measurements were free from spikes. The lowest vertical resolution of the Vectrino measurements was 0.3 cm, with a minimum sampling length of 1 mm.

Figure 3.3: Vectrino probe in the flume at Fluvial Mechanics Laboratory, Indian Statistical Institute, Kolkata, India.

(a)

(b)

Figure 3.4: (a) Uniform (unimodal) fine sediment with d_{50} = 0.25mm, (b) Gravel with d_{50} = 3.5mm in the flume at Fluvial Mechanics Laboratory, Indian Statistical Institute, Kolkata, India.

Chapter 4

Hydrodynamics of flow through a degraded channel bed

4.1 General

The work of the present chapter was devoted to the experimental study of turbulent flow through a degraded channel-bed comprised of bimodal sediment.

The study of turbulent flow through natural rough-bed streams has remained a subject of scientific interest for several decades due to its practical implications. These streambeds typically consist of sand and gravel with varying sizes and shapes, creating a heterogeneous near-bed environment. Natural erosional processes lead to the detachment of bed particles, resulting in deformed surfaces known as degraded beds in the fields of geology, hydraulics, and sediment transport. However, due to experimental limitations, degraded sedimentary beds have received less attention compared to rigid beds. While extensive experimental research has been conducted in recent years on sediment entrainment thresholds, fixed and weakly mobile gravel beds, water-worked gravel beds, dunal beds, and aggraded beds, relatively few studies have focused on the turbulent flow characteristics over degraded channel beds. Given the complexity of natural streambeds, a comprehensive understanding of flow dynamics requires studying beds composed of bimodal or, more specifically, polymodal gravels.

The flow over mobile and degraded gravel beds is quite different from the rigid sedimentary beds of uniformly graded sand or gravels. For instance, based on the rigid and weakly mobile gravel bed experiments, Nikora and Goring (2000) observed that the hydrodynamics of mobile granular beds are significantly different than those of rigid bed streams. One of the most important findings of their study was the reduction of von Kãrmãn constant due to bed mobility for the weakly mobile bed. Shvidchenko and Pender (2001) experimentally studied the turbulent structures over mobile gravel beds with different size of gravels. The experimental data showed that lift and drag forces generated due to eddy motion of fluid is responsible for movement of fluid particles.

Wilcock et al. (2001) measured transport rates of sediment particles during a laboratory experiments on various sand and gravel mixtures. They also calculated the bed shear stress for a bed of sand-gravel mixture. They observed that due to sand content, sediment transport gets isolated by using the same gravel population. Based on the experiments carried out over a bed of immobile coarse sediments feeded with fine sand, Grams and Wilcock (2007) reported that the proportion of a gravel bed stream covered by the sand strongly affects the amount of sediment transportation. Partial filling of grain interstices were observed over a narrow range of flow and transport rates indicating a sharp threshold between no interstitial sand storage and a sand-covered bed. The relationship between bed coverage, transport rate, and bed shear stress were also observed. However, in their studies the turbulent flow characteristics were not fully understood. Later, using an acoustic Doppler velocimeter, Wren et al. (2011) studied turbulent flow field over an immobile coarse gravel bed into which sand was added gradually. The additions of sand over gravel-bed lead to remarkable changes in the bulk flow and turbulent characteristics. It was evident from the experimental findings that because of changes in the rough nature of the sedimentary bed, individual velocity profiles varied significantly. Also, an increase in the elevation of sand layer relative to that of the gravel resulted in lowering the bed shear stress and the Reynolds stress. They also observed the raising of the relative turbulence intensity and a near-bed shift toward the sweep-dominated turbulence. Jain et al. (2015) performed an experimental study on the turbulent flow over degraded bed comprised of sand-gravel mixture. They observed that the Reynolds shear and normal stresses attain their respective maximum values at the initial bed-level and their values reduce as one moves towards the downstream along the degraded bed signifying the weakening of vortex structure by bed degradation. The bursting analysis results suggest that sweep and ejections are the most important bursting events in comparison to those of inward and outward interactions. However, the study of turbulent flow over bimodal degraded gravel beds are mainly confined within the flow characteristics like, velocity, Reynolds shear and normal stresses, turbulent kinetic energy (TKE), etc. where there is no precise information of the velocity structure functions, scaling laws of turbulence, TKE budget, Reynolds stress anisotropy, etc. Note that such information is certainly important parameters to have a precise understanding of the flow characteristics. The

present problem is therefore aimed at to the following objectives: Comparing with the flow properties like, velocity, Reynolds stresses, TKE, TKE fluxes with the existing literatures and investigates other essential characteristics which are yet to be explored.

Turbulence characteristics such as scaling laws of turbulence, TKE dissipation rates, length scales, and anisotropy can be understood more lucidly by applying the structure functions method which was introduced and pioneered by Kolmogorov (1941a, b). The method is in principle combination of some theories based on the energy spectrum and second and third-order velocity structure functions (Kolmogorov and Obukhov 1941). However, the structure function methods have been widely accepted in predicting the dissipation rate of turbulent flow in open channel. It is important to mention here that Kolmogorov (1941a, b) formulated his scaling theory of turbulence based on the second- and third-order structure functions. Later, the theory of Kolmogorov was challenged by several researchers (Landau, 1959) and therefore modified (Kolmogorov and Obukhov 1962) and extended beyond third-order (Anselmet et al. 1984, Boschung et al. 2017). In this regard, it is important to admire some recent studies on open-channel turbulence. For instance, Ferraro et al. (2016) conducted a laboratory experiment in a natural pebble-bed channel and observed that the velocity power-spectra follow Kolmogorov's 5/3rd power law (1941a, b) which reveals the presence of inertial subrange. The experimental data were also verified with Kolmogorov's 4/5-law and Monin-Yaglom's 4/3-law (Yaglom 1949, Monin and Yaglom 1975). TKE dissipation was estimated by using different laws and they concluded that these scaling laws are best suited to estimate the value of dissipation rate accurately. Kolmogorov's 4/5-law was also used by Coscarella et al. (2017) for a satisfactory estimation of ε values for flow over a highly rough bed. Later, Padhi et al. (2019) calculated TKE dissipation rate ε over water-worked and screeded gravel bed using Particle Image Velocimetry (PIV) in laboratory experiments using the spatial-averaging methodology. The second- and the third-order velocity structure functions revealed the evidence of an inertial subrange where Kolmogorov's 2/3rd and 4/5-laws were preserved for both the experimental conditions. They estimated the value of ε using Kolmogorov's 2/3rd and 4/5-laws. Quite recently, Penna et al. (2020) estimated the value of ε using Kolmogorov's 4/5-law and Monin–Yaglom's 4/3-law

experimentally for flow over a water-worked gravel bed. The results of their study showed that there can be differences in the values of ε estimated by these Kolmogorov's 4/5- and Monin–Yaglom's 4/3-laws. The Reynolds stress anisotropy was also studied in details using tensor analysis. Kurien et al. (2000) studied the variation of scaling exponents for the anisotropic components of structure functions of high-order. The scaling behaviour of high-order structure functions for a variety of turbulent flow was observed by Water et al. (1999). Importantly, Coscarella et al. (2020) analyzed the turbulence anisotropy based on second-order structure functions and anisotropy angle. The scale-dependent anisotropy level was quantified based on high-order structure function to examine the tendency of the system from large-scale anisotropy to small-scale isotropy. However, the experimental setup of the present study is substantially different from that of Padhi et al. (2019) and Penna et al. (2020). It is therefore well-understood that there remains enough scope to understand the hydrodynamics of flow through degraded channel beds with sand-gravel mixtures using the scaling laws of turbulence. The present problem is therefore aimed at to observe scaling laws of turbulence, TKE budget and Reynolds stress anisotropy along with the streamwise velocity, Reynolds shear and normal stresses, TKE and fluxes, etc. It is pertinent to mention here that the present study was confined within the third-order structure functions and its applications.

4.2 Description of experimentation

A total number of six experiments were performed in the Flume Laboratory of Indian Statistical Institute, Kolkata, India. The laboratory is equipped with a hydraulic flume of 20 m long, 0.5 m wide and 0.5 m depth and a pair of centrifugal pumps to supply water into the flume with a capacity of 0.25 m^3/s. Its Perspex-made transparent side-walls ease the visual observation of the flow. The flow rate can be observed and controlled by using an electromagnetic flow meter and a regulatory valve, respectively. A 6 m × 0.5 m × 0.5 m test section was fixed at a distance of 5 m from the entrance of the flume. To reduce the initial disturbances created by turbulence, wave etc. a pair of honeycomb structures were placed at the entrance of the flume inlet.

At first, a bimodal sediment mixture was prepared by mixing uniformly graded natural sand with a median diameter of d_{50} = 0.25 mm (uniformity coefficient σ_g = 1.25 and relative density s = 2.65, d_{84} and d_{16} are the particle size at which 84 percent and 16 percent of the sediment particle were smaller) and gravel with a median diameter of D_{50} = 3.5 mm (σ_g = 1.2 and s = 2.65) in equal proportions by weight. The sand-gravel mixture was then spreaded on the floor of the flume to create a sedimentary bed 0.2 m thickness with a predetermined slope. The bed surface was leveled from upstream to downstream end of the test section maintaining a thickness of 0.2 m throughout and was measured using a Vernier point gauge with an accuracy of ± 1 mm. An approximately 10 hour time was given each time to drench the sedimentary bed so as to make them void-free. Then water was drained out and the bed level was checked again and the necessary adjustment was made to maintain the required slope. Once the bed became fully saturated and bed slope was ensured, the centrifugal pump was employed to supply water and the pre-calculated discharge was applied to the bed to achieve the required flow depth.

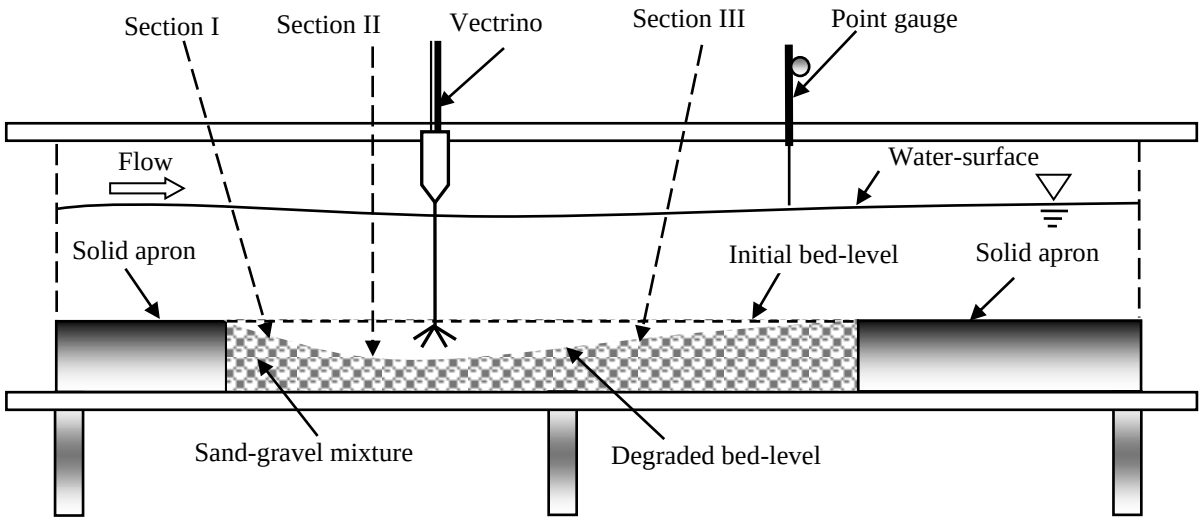

Figure 4.1: Schematic of the experimental arrangements in the Fluvial Mechanics Laboratory, Indian Statistical Institute, Kolkata, India.

Two solid aprons each of 1 m length were used at the upstream and downstream of the test sections. Measurements were taken after one hour since the bed reaches the equilibrium condition. After completion of one run, the bed was removed, the mixture

was again prepared and the bed was made ready for a new set of experiment. All the experiments were conducted under shallow depths with aspect ratio $b/h < 2$ (where, b refers the width of the channel and h is the flow depth above the bed-level before detachment of the sediments measured by a Vernier point gauge). Figure 4.2 shows the graphical presentation of the degraded bed profile in normalized form. In the figure, z^+ (= z/d, where d is the maximum equilibrium depth of degradation) is the normalized vertical distance, and x/L (L is the longitudinal distance between sections I and II) is the normalized streamwise distance. Velocities were measured at three different sections for each run. Section I was chosen at $x/L \leq 0.4$, whereas Section II was located at $x/L = 1$, and Section III was at $x/L \geq 1.8$. The location of sections I was at a streamwise distance of more than 6 m from the entrance of the flume where the flow was observed to be fully developed according to the velocity profiles measured at different steamwise locations before starting the experimental runs. It was therefore assured that all the measurements were taken within the fully-developed turbulent flow zones. As the experiments were conducted under the shallow depth conditions, there was no side-wall effect in the measurement. Figure 4.1 presents the schematic of the experimental set up.

A four-beam Vectrino velocimeter was used to collect instantaneous velocity components in three dimensions, such as u (streamwise), v (lateral), and w (vertical) in the x, y, and z-directions, respectively. A sampling duration $t = 180$ s was adequate to achieve the time-independent averaged velocity components. The velocity fluctuations u', v', and w' in x, y, and z-directions were obtained by subtracting $\overline{u}$, $\overline{v}$, and $\overline{w}$ from the corresponding time-averaged values u, v, w respectively. The Vectrino was operated with a data collecting frequency of 100 Hz and an acoustic frequency of 10 MHz. The signal-noise ratio (SNR) value was above 18 and the correlation coefficient was more than 70 which established that sufficient care was taken in collecting the readings. For all the runs, the shear Reynolds number $R_* > 70$ ($R_* = u_* D_{50}/\upsilon$, where u_* is the shear velocity and υ is the kinematic viscosity of water) indicated that experiments were conducted under hydraulically rough bed conditions. Near the bed, at some locations data were contaminated by the spikes which were filtered and replaced by using phase-space thresholding method and by the median of the neighbouring samples, respectively as was

suggested by Goring and Nikora (2002). However, in most of the cases, the unfiltered data were used so that the natural turbulence properties were not destroyed.

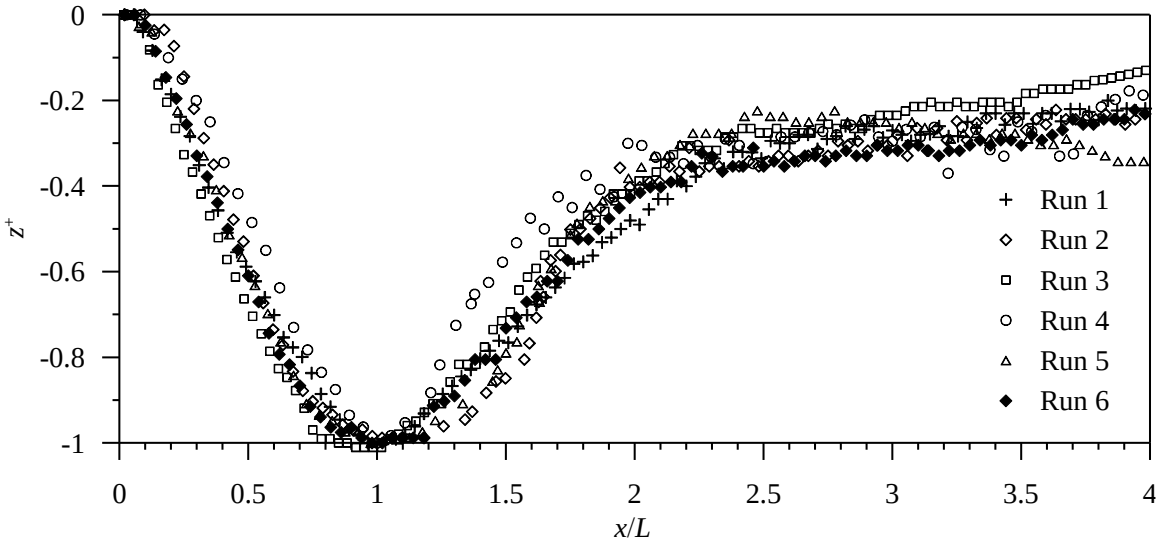

Figure 4.2: Degraded bed profile. In the figure, zero-line shows the initial bed level i.e., the level before the detachment took place

TABLE 4.1: Experimental parameters

Run	d_{50} (mm)	D_{50} (mm)	d (m)	h(m)	S	U (m/s)	u_* (m/s)	Time for equilibrium (hr)
1	0.25	3.5	0.09	0.1	0.0035	0.47	0.06	12
2	0.25	3.5	0.082	0.13	0.004	0.64	0.072	12
3	0.25	3.5	0.098	0.105	0.0045	0.65	0.068	10
4	0.25	3.5	0.04	0.115	0.0033	0.62	0.061	10
5	0.25	3.5	0.076	0.12	0.0045	0.61	0.073	12
6	0.25	3.5	0.082	0.1	0.005	0.68	0.07	12

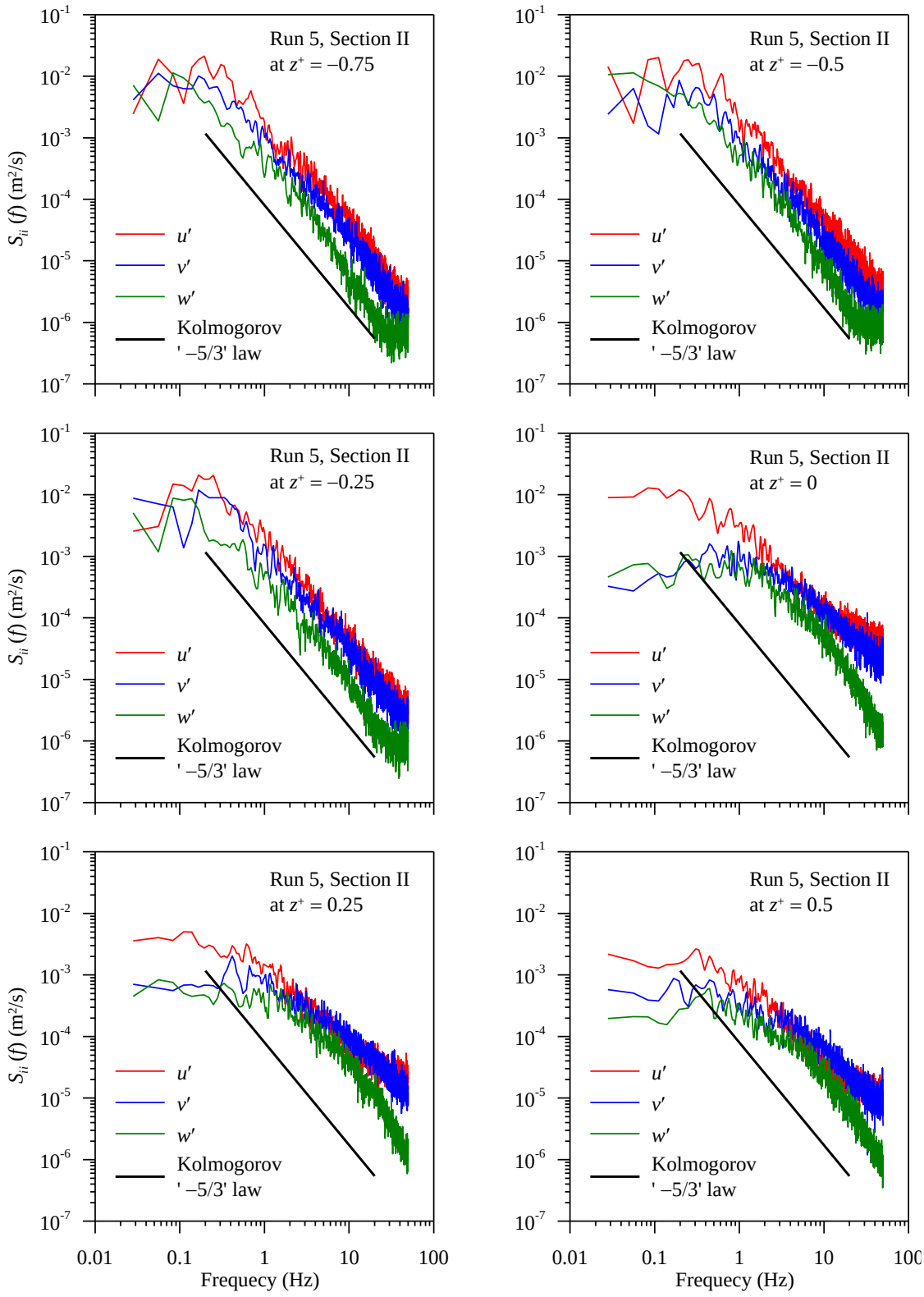

Figure 4.3: Velocity power spectra for Run 5, Section II data at z+ = –0.75, –0.5, –0.25, 0, 0.25, and 0.5.

4.3 Spectral analysis and validation of turbulent data

Figure 3 presents the velocity power spectra at Section II for Run 5 at the vertical distance z^+ = –0.75, –0.5, –0.25, 0, 0.25, and 0.5. In general, all the velocity power-spectra shown here followed $f^{-5/3}$-slope within the inertial subrange. It was observed from the power spectra that they obey the relation $F_{uu} > F_{vv} > F_{ww}$ below the degraded bed-level $z^+ = 0$. However, above $z^+ = 0$, the velocity power spectra follow $F_{uu} \approx F_{vv} > F_{ww}$ indicating closer to the three-dimensional isotropy toward water-level. However, for a clear understanding of anisotropy, the anisotropic invariant map and invariant functions will be used later. Table 1 shows the details of the experimental parameters. The depth averaged-velocity U for the runs were in the ranges of 0.48 to 0.68 m/s. The corresponding Froude numbers F [= $U/(gh)^{0.5}$, g is the acceleration due to gravity] of the experimental runs 1–6 were 0.5, 0.57, 0.64, 0.58, 0.56, 0.68 confirming that all the experiments were conducted under subcritical conditions. The Reynolds numbers were R [= 4 Uh/υ] were 2 × 105, 3.3 × 105, 2.73 × 105, 2.85 × 105, 2.9 × 105, 2.72 × 105 for Run 1, 2, 3, 4, 5 and 6, respectively.

4.4 Time-averaged streamwise velocity

Figure 4.4 presents the vertical profiles of normalized time-averaged streamwise velocity u^+ at sections I, II, and III for runs 1–6. Note that the time-averaged streamwise velocity $\bar{u}$ was scaled by the shear velocity u_* (i.e., $u^+ = \bar{u}/u_*$) obtained from the slope of bed that was measured before the detachment of the bed took place (i.e., $u_* = (ghS)^{0.5}$, S is the bed slope) and the vertical distance z was scaled by the maximum equilibrium depth of degradation d (i.e., $z^+ = z/d$) for a run.

It is quite evident from the experimental data that irrespective of the streamwise locations, u^+ starts with a small value near the bed which goes on increasing with increase in the vertical distance until it attains the maximum value at $z^+ \approx 0.6$. Above $z^+ = 0.6$, u^+ becomes almost invariant with depth. Above $z^+ = 0$, the profiles of u^+ are almost similar at different sections for a run except small differences in their values. Below $z^+ = 0$, there are considerable differences in the values of u^+. It was observed that except Run 1, the

values of u^+ is the smallest at Section I than Sections II and III below $z^+ = 0$ which indicates that the maximum retardation in the streamwise velocity took place at the upstream side of the maximum equilibrium depth of degradation. Interestingly, negative streamwise velocity was found in the vicinity of the bed surface at Section I that clearly signify the reversal of flow which may be a strong contribution to form vortex structure. This is in conformity with the findings of Jain et al. (2015). However, no negative streamwise velocity was observed in sections II and III although their values are very small near the bed which indicates that no significant reversal flow took place as one move towards downstream. It can therefore be concluded that the degradation has a considerable impact in the streamwise velocity over a degraded bed.

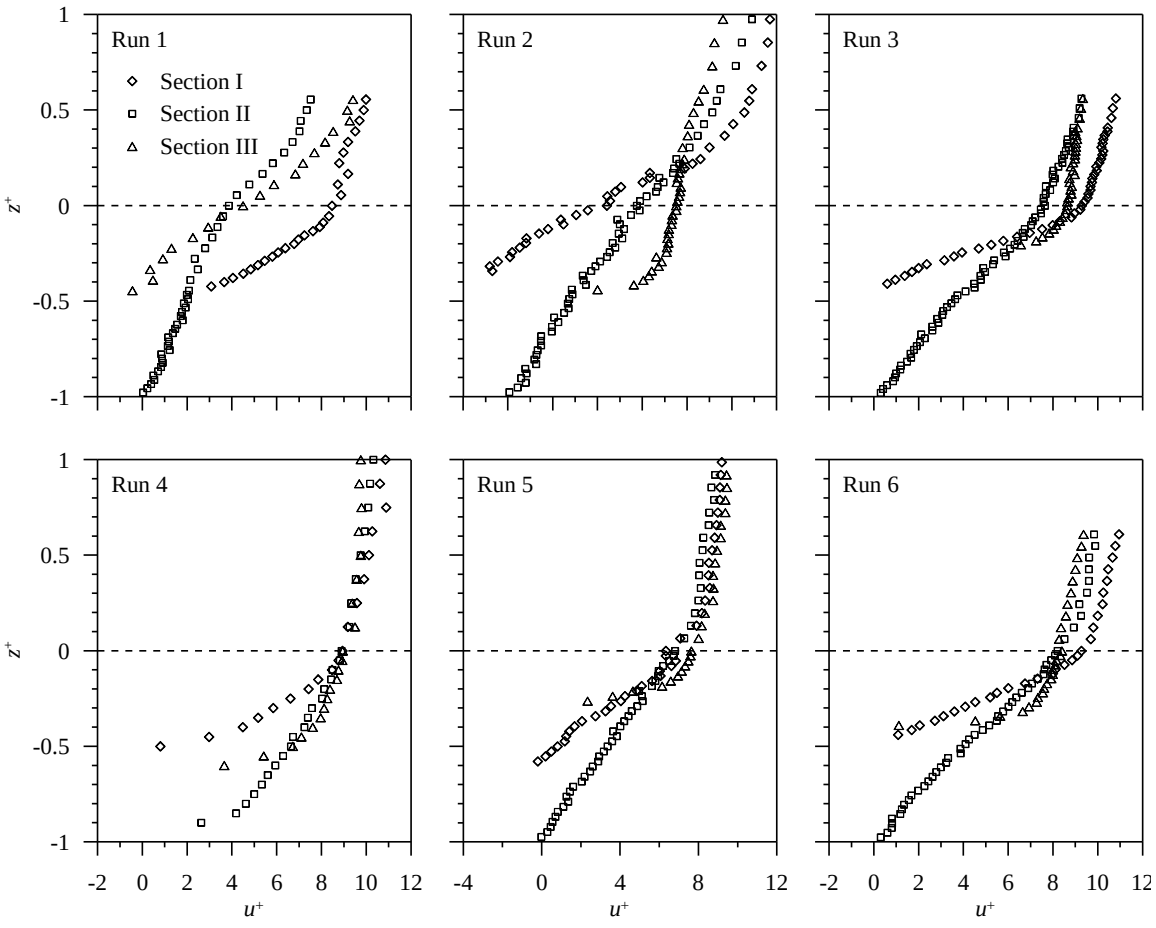

Figure 4.4: Vertical profiles of mormalized time-averaged streamwise velocity u^+ at sections I, II, and III for runs 1–6.

4.5 Time-averaged Reynolds shear and normal stresses

The vertical distributions of normalized Reynolds shear stress (RSS) for different locations under different experimental runs were depicted in the Figure 4.5. The Reynolds shear stresses were scaled by square of the shear velocities ($uw^+ = -\rho\overline{u'w'}/u_*^2$, where $-\rho\overline{u'w'}$ is the RSS and ρ is the mass density of fluid). In general, the normalized RSS uw^+ for an open channel flow follows the traditional gravity line of uw^+-distribution (i.e., $uw^+ = 1$ at $z^+ = 0$ and $uw^+ = 0$ at $z^+ = 1$) with permissible scatter in values occurred due to the laboratory measurements. However, it is understood form Figure 4.5 that due to the degradation in the bed, the RSS-profiles were shifted from the gravity line which was more prominent at sections I and II than Section III. Near the bed at Section I, the RSS starts with a small value that goes on increasing with an increase in the vertical distance until it attains the maximum value near $z^+ \approx 0$. Beyond that, uw^+ decreases with increase in vertical distance. The RSS-profile for Section II is almost similar to that of Section I with difference in values. On the other hand, the RSS-profile for Section III is quite different from that of sections I and II. At Section II, uw^+ starts with a value that increases very little with an increase in the vertical distance and attains the maximum value at $z^+ \approx 0$ and above that uw^+ decreases with increase in z^+. However, the maximum value of uw^+ was found around $z^+ \approx 0$ irrespective of the sections and runs. In this regard, it is important to mention that Jain et al. (2015) also found similar profiles of RSS. For some cases it was at the bed-level and for some cases it was slightly below the bed-level. However, the uw^+ in the present study is quite different from that of Jain et al. (2015). The differences in the values of uw^+ are attributed to the differences in values of shear velocities and the bed roughness. The amplification in the RSS-values signifies maximum turbulent mixing at the bed level before start of detachment. It was also observed that as one move further downstream from the maximum degraded depth, the RSS decreases throughout the depth. Interestingly, the magnitude of RSS attains maximum value at Section I than that of sections II and III indicating more prominent vortex structure at the upstream of the degraded bed which then reduce as one move towards the downstream direction indicating the weakening of the vortex structure along the degraded bed.

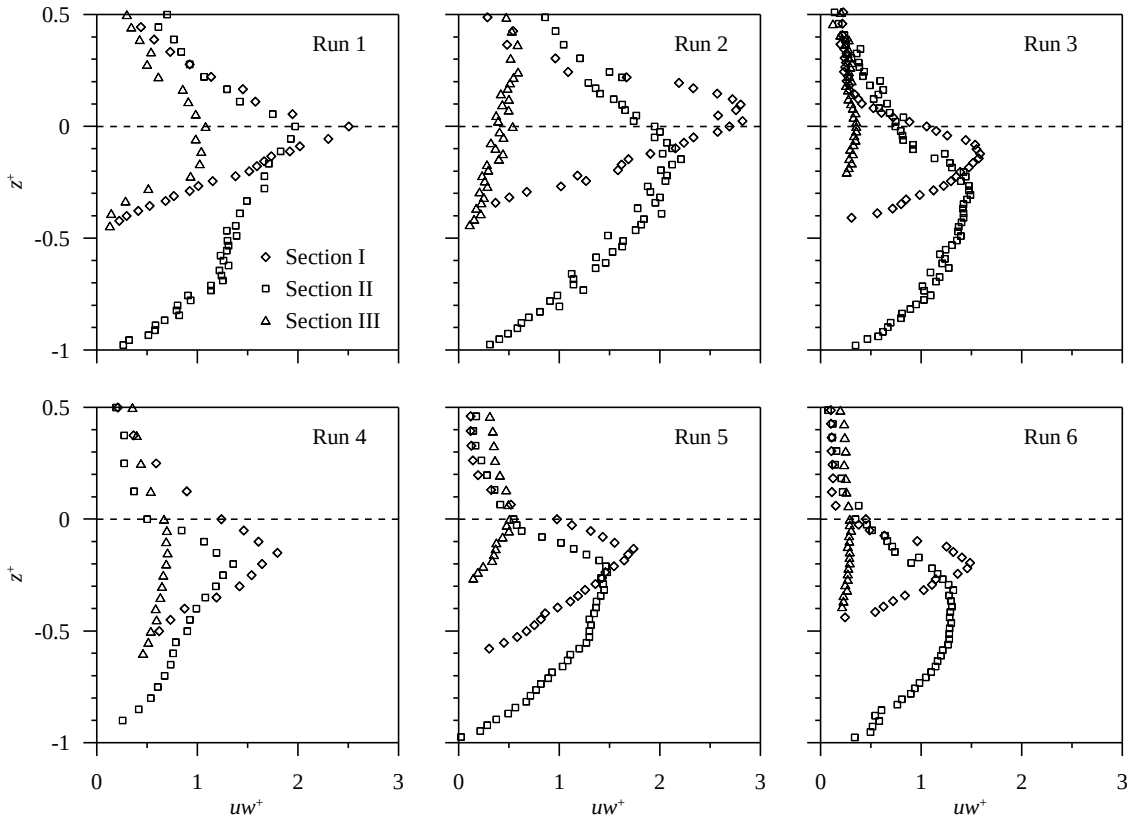

Figure 4.5: Vertical profiles of normalized RSS uw^+ at sections I, II, and III for runs 1–6.

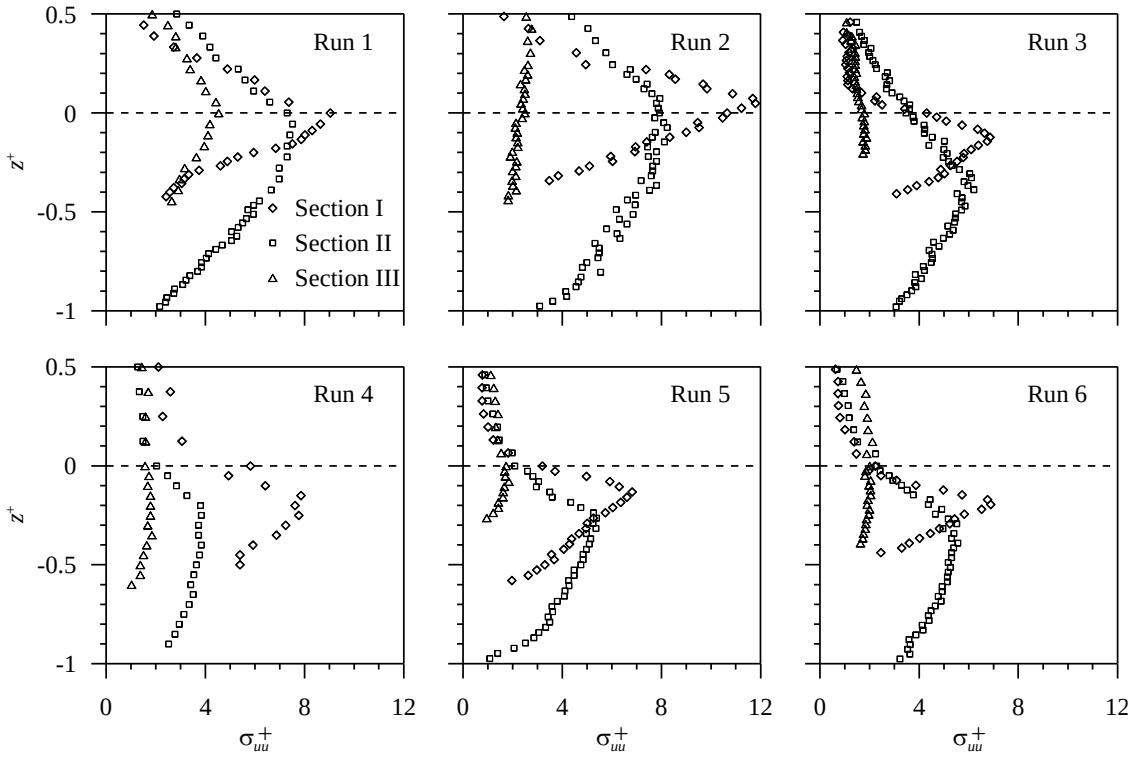

Figure 4.6: Vertical profiles of normalized Reynolds normal stress in streamwise direction σ_{uu}^+ at sections I, II, and III for runs 1–6.

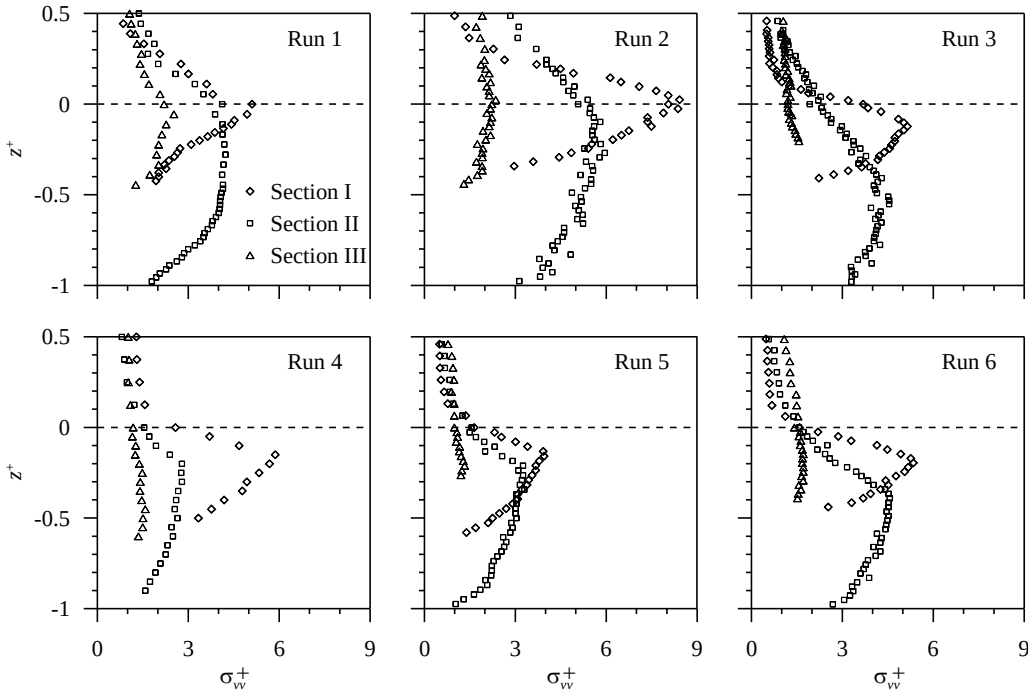

Figure 4.7: Vertical profiles of normalized Reynolds normal stress in lateral direction σ_{vv}^+ at sections I, II, and III for runs 1–6.

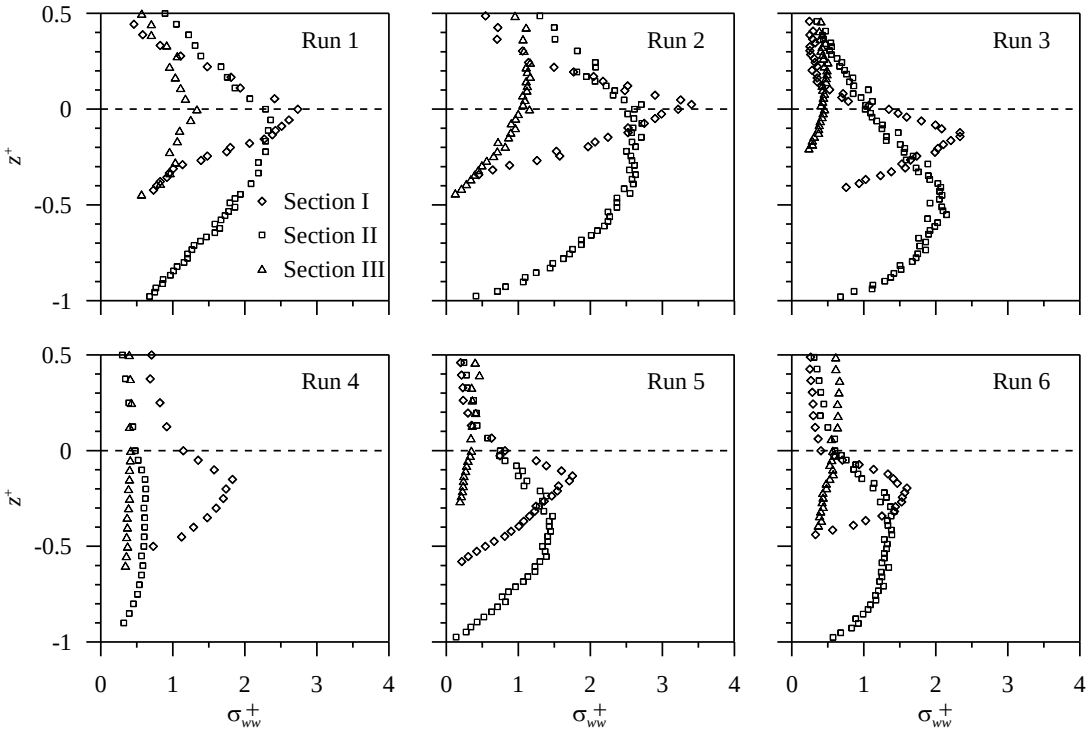

Figure 4.8: Vertical profiles of normalized Reynolds normal stress in vertical direction σ_{ww}^+ at sections I, II, and III for runs 1–6.

The Reynolds normal stresses (RNS) in streamwise, lateral and vertical directions are calculated by $\sigma_{uu} = -\rho\overline{u'u'}$, $\sigma_{vv} = -\rho\overline{v'v'}$ and $\sigma_{ww} = -\rho\overline{w'w'}$, respectively. The normalized form of σ_{uu}, σ_{vv}, and σ_{ww} are: σ_{uu}^+, σ_{vv}^+, $\sigma_{ww}^+ = (\sigma_{uu}, \sigma_{vv}, \sigma_{ww})/(\rho u_*^2)$. The vertical distributions of σ_{uu}^+, σ_{vv}^+, and σ_{ww}^+ at different locations are shown in Figure 4.6 – 4.8. The overall behavior of σ_{uu}^+, σ_{vv}^+, and σ_{ww}^+ are similar i.e., $\sigma_{uu}^+ > \sigma_{vv}^+ > \sigma_{ww}^+$ irrespective of the experimental runs and locations. They start with a lower value in the vicinity of the bed that increases with an increase in the vertical distance until attains the maximum value at the bed-level or slightly below the initial bed-levels. The reason behind this is that the maximum turbulent mixing takes place at this level. However, below and above this level, their values decrease, although for runs 5 and 6 the peak value occurs slightly below the bed-level showing the effect of intense turbulent mixing even slightly below the bed-level. However, below further downward, the effect of turbulent mixing reduces and values of fluctuations in the velocity components decrease that dampens the values of

the σ_{uu}^{+}, σ_{vv}^{+}, and σ_{ww}^{+}. Moreover, for an isotropic turbulence, the value of $\sigma_{ww}^{+}/\sigma_{uu}^{+}$ is unity whereas, for the anisotropy of the turbulence $\sigma_{ww}^{+}/\sigma_{uu}^{+}$ is less than unity. According to the figures 4.6 and 4.7, the basic trend of $\sigma_{ww}^{+}/\sigma_{uu}^{+}$ indicates that the turbulence is strongly anisotropic in nature as $\sigma_{ww}^{+}/\sigma_{uu}^{+} < 1$ irrespective of experimental runs and locations.

4.6 Turbulent kinetic energy

Figure 4.9 shows the vertical distributions of normalized turbulent kinetic energy (TKE) at different locations for runs 1 – 6. The TKE is defined as the mean kinetic energy per unit mass of fluid associated with the eddies in a turbulent flow and calculated by summing up half of the three-dimensional RNS components as

$$k = 0.5(\overline{u'u'} + \overline{v'v'} + \overline{w'w'}) \tag{4.1}$$

where, $\overline{u'u'}$, $\overline{v'v'}$ and $\overline{w'w'}$ are the RNS in the streamwise, lateral and vertical directions, respectively. The normalized TKE is calculated by $k^{+} = k/u_{*}^{2}$. It is quite predictable from the RNS-profiles that in the vicinity of the degraded bed, the turbulent kinetic energy starts from a smaller value which increases with an increase in the vertical distance and attains the peak value on or slightly below $z^{+} = 0$ signifying the maximum turbulent mixing at the initial bed level. Above $z^{+} = 0$, the k^{+} decreases with an increase in the vertical distance. This is the general tendency of the TKE-profiles irrespective of the streamwise location along the degraded bed. Interestingly, the peak value of k^{+} at section I is more than that of the values at sections II and III. It can therefore be concluded that as one moves downstream, the peak value of k^{+} decreases and at section III the k^{+} decreases for throughout the depth. The turbulent kinetic energy is indeed responsible to detach the bed particles from the bed and its effect minimizes as the bed starts to be free from detachment of the particles.

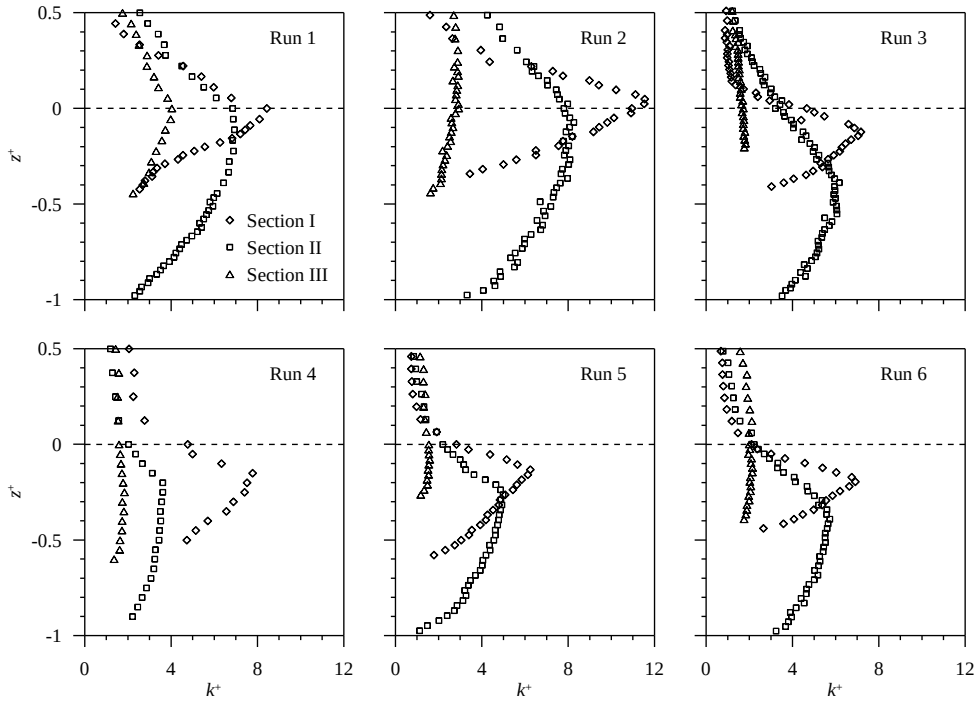

Figure 4.9: Vertical profiles of normalized turbulent kinetic energy k^+ at sections I, II, and III for runs 1–6.

4.7 Turbulent kinetic energy fluxes

Figure 4.10 shows the vertical distributions of normalized streamwise and vertical TKE fluxes, F_{ku} and F_{kw}, respectively. The TKE fluxes are calculated from the third-order moments of velocity fluctuations. The streamwise TKE flux, f_{ku} is calculated by the equation:

$$f_{ku} = 0.5(\overline{u'}^3 + \overline{u'}\overline{v'}^2 + \overline{u'}\overline{w'}^2) \tag{4.2}$$

and the vertical TKE flux, f_{kw} is calculated by the equation:

$$f_{kw} = 0.5(\overline{u'}^2\overline{w'} + \overline{v'}^2\overline{w'} + \overline{w'}^3) \tag{4.3}$$

and normalized as F_{ku} and F_{kw} (i.e., $F_{ku} = f_{ku}/u_*^3$ and $F_{kw} = f_w/u_*^3$), respectively. It is understood from the equations of f_{ku} and f_{kw} that the positive values of F_{ku} indicate the streamwise TKE flux transport towards the downstream whereas; negative values of F_{ku} indicate the streamwise TKE flux transport towards the upstream. Also, the positive values of F_{kw} indicate the vertical TKE flux in the upward direction and the negative

values of F_{kw} indicate the vertical TKE flux in the downward direction. Most importantly, the TKE fluxes give an indication of the predominance of turbulent bursting events (Lu and Willmarth 1973) due to their sign conventions.

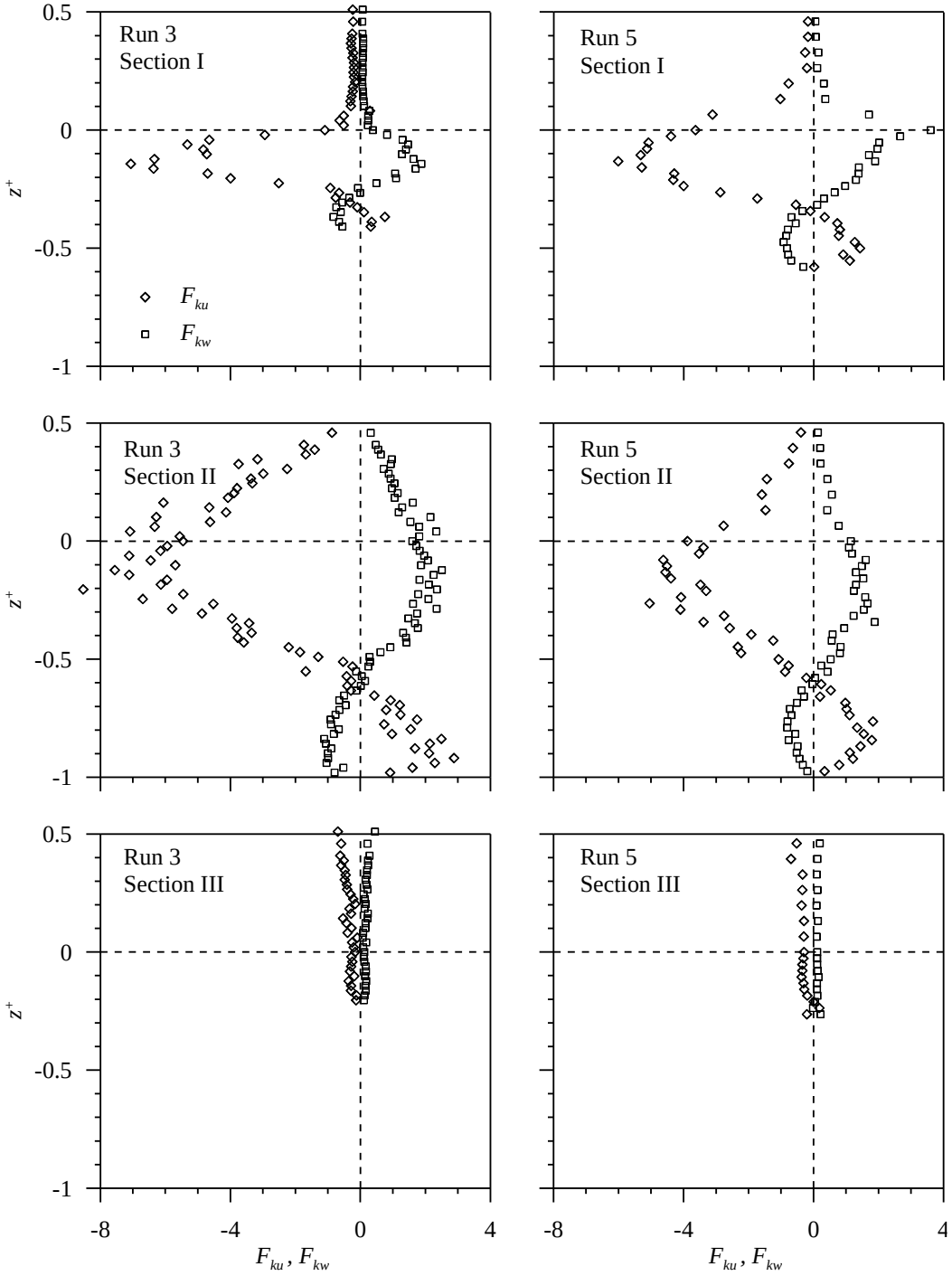

Figure 4.10: Variations of normalized streamwise and vertical turbulent kinetic energy fluxes F_{ku} and F_{kw} with normalized vertical distance z^+ at different locations. Data were shown from Run 3 and Run 5.

The $+u'$ that makes positive F_{ku} and $-w'$ that makes negative F_{kw} together gives the indication of the predominance of the sweep events in the vicinity of degraded bed. On the contrary, $-u'$ that makes negative F_{ku} and $+w'$ that makes positive F_{kw} together give rise to the ejection events that were observed with an increase in the vertical distance. The present findings are in confirmation with Jain et al. (2015) who also observed that sweep is predominating in the near-bed and above that ejection is predominating, whereas inward ($+u'$, $+w'$) and outward interactions ($-u'$, $-w'$) are the least important events throughout the vertical distance.

It is evident from the figures that although the values of F_{ku} and F_{kw} are different at different locations, their overall behaviors are similar above $z^+ = 0.2$ for both the runs. However, below $z^+ = 0.2$, the enhancement in the values of F_{ku} and F_{kw} was noticed. The values of F_{ku} and F_{kw} are in comparison with Dey et al. (2012), Dey et al. (2011), Bigillon et al. (2006) and Mignot et al. (2009). The experimental data of López and García (1999), Hurther and Lemmin (2000), and Bigillon et al. (2006) showed that irrespective of the roughness of the bed $F_{kw} \approx 0.3$ within $0.2 < z^+ < 0.5$ at large Reynolds numbers. For the flow regions other than $0.2 < z^+ < 0.5$, the F_{kw} decreases both towards the bed and towards the free-surface. Mignot et al. (2011) also found that above the crest level of the gravel-bed, $F_{ku} = -0.7$ and $F_{kw} = 0.2–0.3$. According to Bigillon et al.(2006), the values of F_{kw} may vary depending upon the bed roughness and Reynolds numbers, whereas Mignot et al. (2011) believes that the disparity of the F_{ku} and F_{kw} is due to the normalizing parameter (u_*) that is used to scale the f_{ku} and f_{kw}. In addition, Sarkar and Dey (2011) argued that due to the changes in the bed roughness, F_{ku} and F_{kw} can vary significantly. However, the values of F_{ku} and F_{kw} in the present study is more than that of the values of López and García (1999), Hurther and Lemmin (2000), and Bigillon et al. (2006), and Mignot et al. (2009) which suggests that degradation of the sedimentary bed is also responsible to get amplified values of F_{ku} and F_{kw}.

4.8 Scaling in turbulence

In the energy cascading process, scaling of turbulence is one of the most fascinating aspects in characterizing open channel flow which can more perfectly be understood by

using the structure functions analysis. Since the pioneering work of Kolmogorov (1941a, b) which is popularly termed as K41, structure function analysis has been extensively used to predict the scaling behaviour in turbulent flow.

The general form of structure functions of any order can be written as:

$$S_p(\mathbf{r}) = \langle (u(\mathbf{x} + \mathbf{r}) - u(\mathbf{x}))^p \rangle, \tag{4.4}$$

for any $p > 0$, where $\mathbf{x}$, $\mathbf{x} + \mathbf{r}$ are points in a turbulent flow field, u is the component of the velocity in the direction of $\mathbf{r}$, r is the length $|\mathbf{r}|$ of $\mathbf{r}$, and the angle brackets denote an average. However, due to the measuring limitations of the velocity measuring methods by ADV, it was necessary to transform the time lags into spatial increment r using the Taylor hypothesis i.e., $r(x, z) = |\bar{u}(x, z)|\Delta t$, where Δt is the time lag.

4.9 Taylor hypothesis and Taylors Coefficient

As in the present study, the time lag was transformed into the spatial increment following the Taylor frozen-in hypothesis, it was important to verify its validity. To this end, the relation that should be satisfied for the Taylor approximation is $2\pi\sqrt{kE(k,z)} << \bar{u}(z)$. It was therefore required to estimate the energy spectra E_u with respect to the wave number k. While performing so, the energy spectra $E_u(f, x)$ was estimated applying the discrete fast Fourier transform of the autocorrelation functions $R_u(x, \Delta t) = \overline{u'(x,t+\Delta t)u'(x,t)}$ of the streamwise velocity and plotted them on a frequency f-scale (as shown in Figure 4.2) , with a resolution frequency defined by F_s/n, where n is the total number of samples captured for a sampling duration and F_s is the sampling frequency. Once the $E_u(f, x)$ was estimated, they were transformed into $E_u(k, x)$ by using $k = f/\bar{u}$ according to the Taylor hypothesis. The energy spectra $E_u(k, x)$ are in agreement with Kolmogorov's 5/3-law where the $E_u(k, x)$ follow $k^{-5/3}$-slope within the inertial subrange. The energy spectra $E_u(k, x)$; and the graphical verification of the Taylor hypothesis taken at different vertical distances of Section II of Run 5 are shown below:

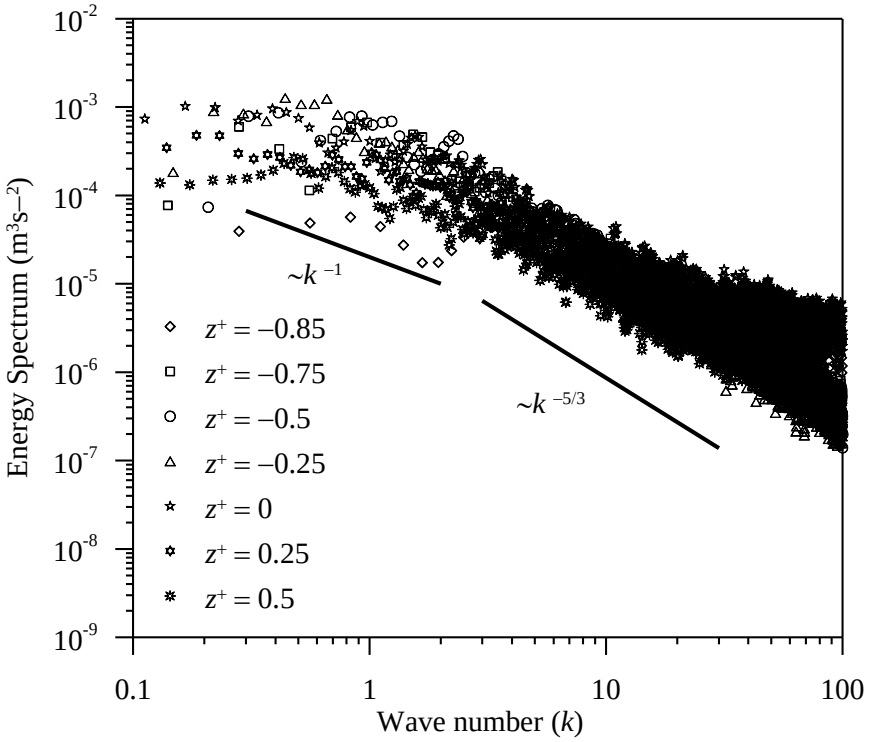

Figure 4.11: Energy spectra $E_u(k)$ (using Taylor hypothesis) at different normalized vertical distance z^+ = –0.85, –0.75, –0.5, –0.25, 0, 0.25, and 0.5. Data were shown from Section II of Run 5.

It is evident from Figure 4.11 that the Taylor coefficient $2\pi\sqrt{kE(k,z)}/\bar{u}(z) = \psi(k, z)$ close to the degraded bed, in the injection region (or rough region) of small-scale turbulence, the Taylor hypothesis is partially violated which was also observed by Ferraro et al. (2016) in the vicinity of the pebble bed. In fact, Penna et al. (2020) and Ferraro et al. (2016) truly pointed out that it is not uncommon to be violated the Taylor hypothesis in some cases, for example, wall-bounded flow and in the vicinity of the permeable pebble bed flow. In the present problem, the main reason for such thing may be due to the fact that $\bar{u}(z)$-values are very small in the vicinity of the degraded bed as shown in figure 4.12.

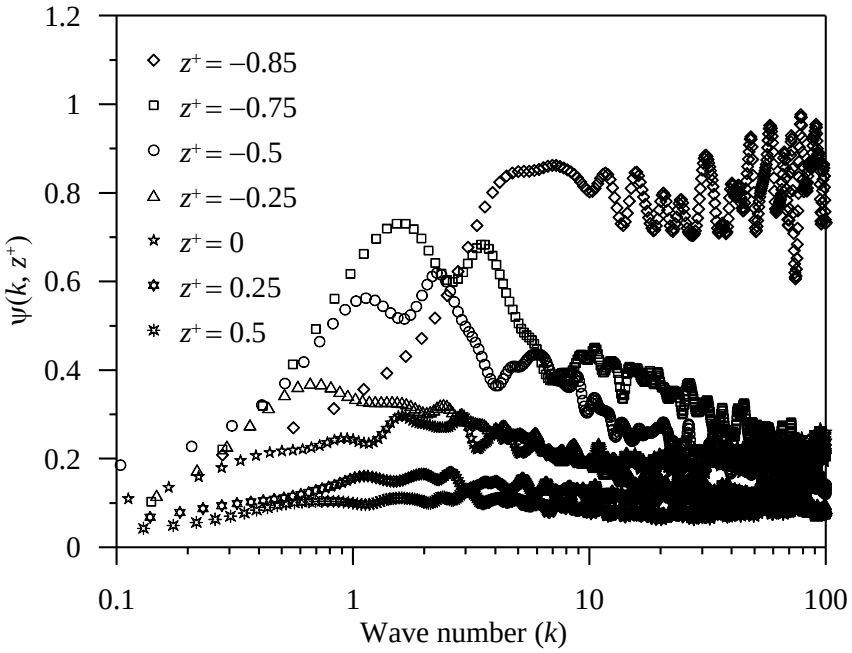

Figure 4.12: Taylor coefficient $\psi(k, z^+)$ as a function of k at normalized vertical distance $z^+ = –0.85, –0.75, –0.5, –0.25, 0, 0.25,$ and 0.5. Data were shown from Section II of Run 5.

4.10 Second-order structure functions

Figure 4.13 presents the variations of second-order velocity structure function with time lag at different sections I, II, and III at different vertical distances for Run 3 and 5. It is important to note that the $\overline{\Delta u^2}$ is presented here with respect to time lag which is different from that of Padhi et al. (2018) because of taking the advantage of showing them on a same horizontal axis. A careful observation of $\overline{\Delta u^2}$ data reveals that the $\overline{\Delta u^2}$ follows the 2/3-law within the shorter span of time lags. Interestingly, for Section I, the $\overline{\Delta u^2}$ follows 2/3-slope for a shorter time lags than those for Section II and III. The possible reason for this is that due to the initialisation of the degrading, the second-order structure function losses its validity with 2/3-slope and the length of inertial subrange decreases. However, as the streamwise distance increases the length of inertial subrange increases and the second-order structure function follows the 2/3-slope for a longer span of time lags. It

was also observed that in the vicinity of the bed, the second-order structure function follows 2/3-slope for a shorter span of time lags than the depths above $z^+ = -0.75$. However, at higher values of time lags, the significance of the second-order structure function is lost and

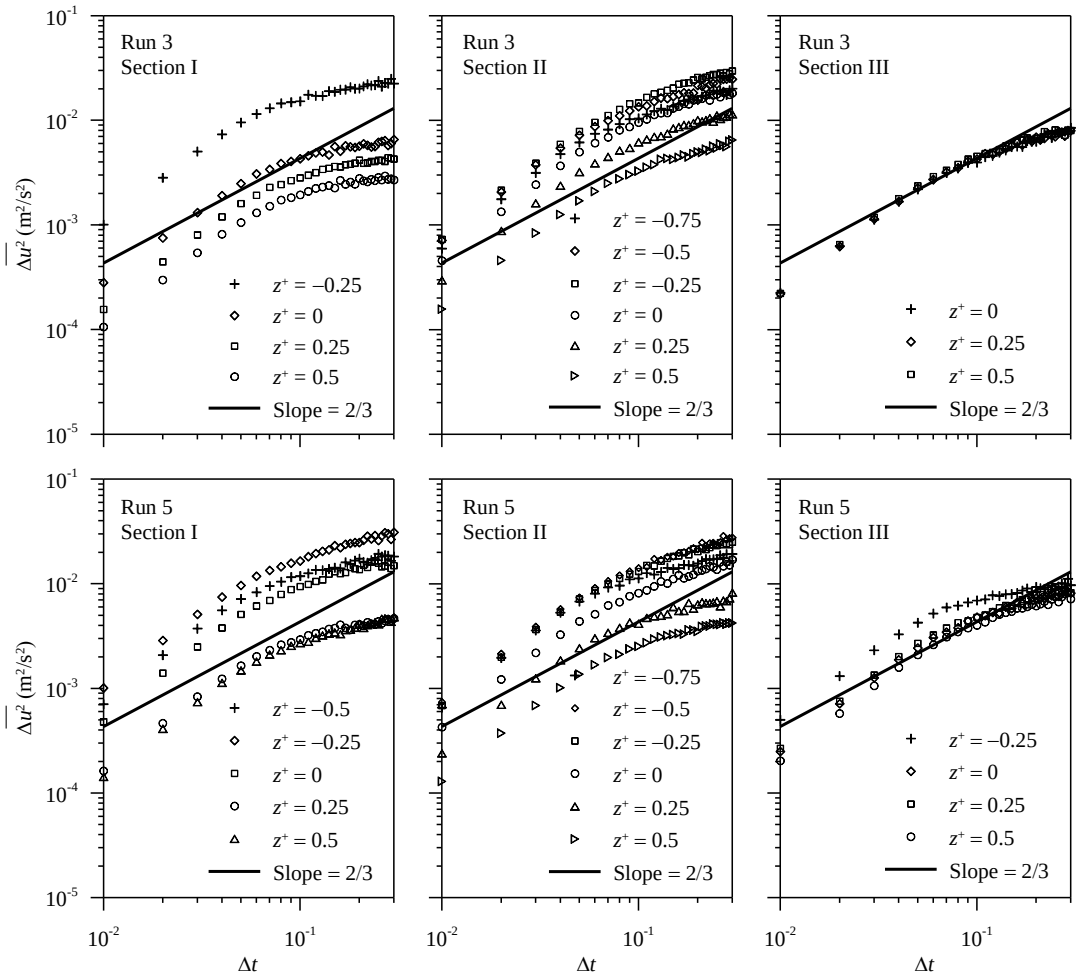

Figure 4.13: Variations of second-order velocity structure function with time lag at sections I, II, and III at different vertical distances. Data of runs 3 and 5 are presented.

$\overline{\Delta u^2}$ becomes almost asymptotic. However, there were no significant changes of the $\overline{\Delta u^2}$ -profiles for other runs and therefore data were plotted here for Runs 3 and 5 only.

4.11 Third-order structure functions

Figure 4.14 presents the variations of third-order velocity structure function with time lag at different sections I, II, and III at different vertical distances. Data were plotted with respect to time-lag to show them on a same horizontal axis. The general observation of the plots are that within a shorter span of time-lag, the third-order statistics follow Kolmogorov's 4/5-law and losses its significance at a higher values of time lags. Interestingly, in the vicinity of the bed for Section I, the third-order structure functions stops following 4/5-slope than sections II and III which suggests that the third-order statistics are influenced by the degradation of the bed. In addition, the near-bed third-order structure functions losses its validity with the slope for a shorter time lag than that for the remaining depth of the flow. It is pertinent to mention here that Padhi et al. (2018) also observed the similar behavior at near-bed zone for screeded gravel beds. However, a direct comparison between the present work and Padhi et al. (2018) is not done here because Padhi et al. (2018) have presented the nondimensional values of $\overline{\Delta u^3}$ with respect to nondiemensional separation distance which were calculated from the measuring locations on the bed, whereas in the present study the separation distance was approximated by multiplying the time-lag with the point-averaged streamwise velocity.

4.12 Mixed third-order structure functions

The velocity data were further processed for mixed third-order structure function which is expressed as $\overline{\Delta u[(\Delta u)^2+(\Delta v)^2+(\Delta w)^2]}$ is shown in Figure 4.15. Like the second- and third-order structure functions, mixed third-order structure functions follow 4/3-solpe for quite a shorter time-lag span in the vicinity of the bed. However, as the time lag increases, the mixed third-order structure function shows less validity with 4/3-slope.

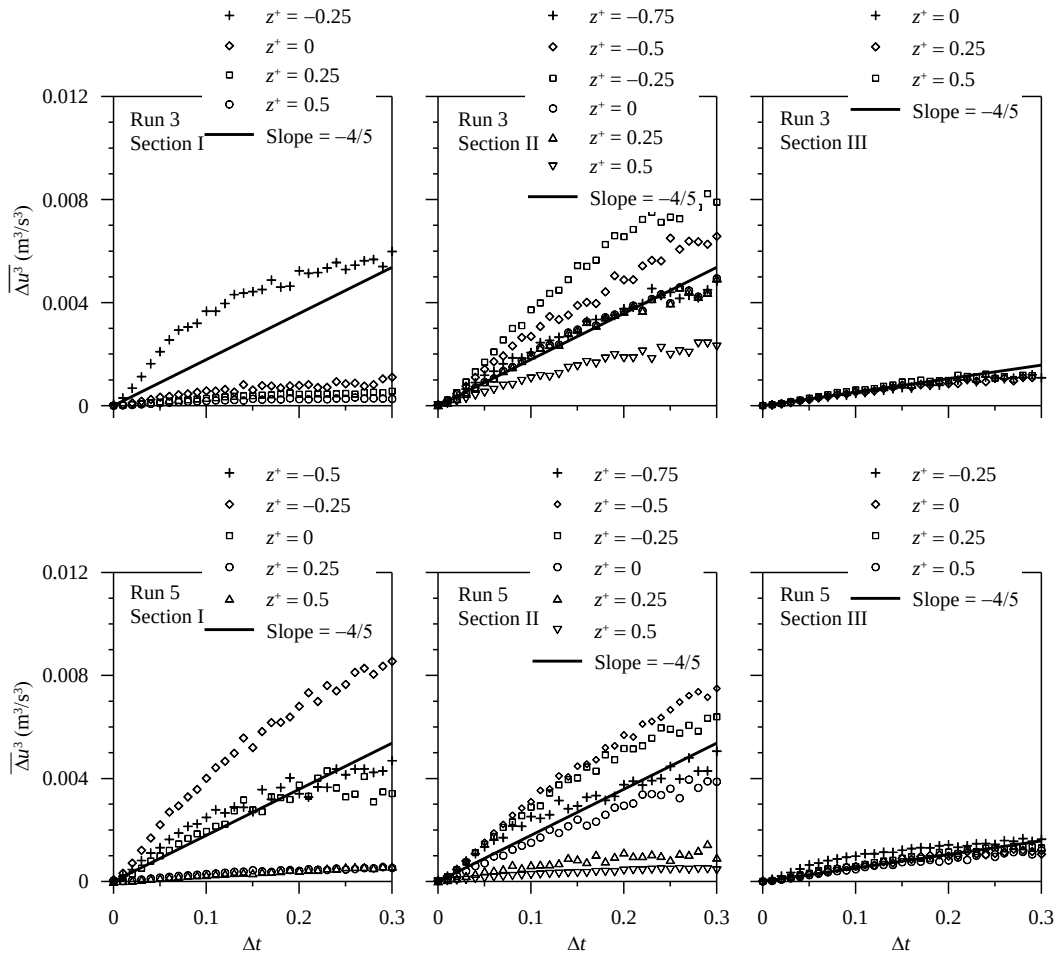

Figure 4.14: Variations of third-order velocity structure function with time lag at sections I, II, and III at different vertical distances. Data of runs 3 and 5 are presented.

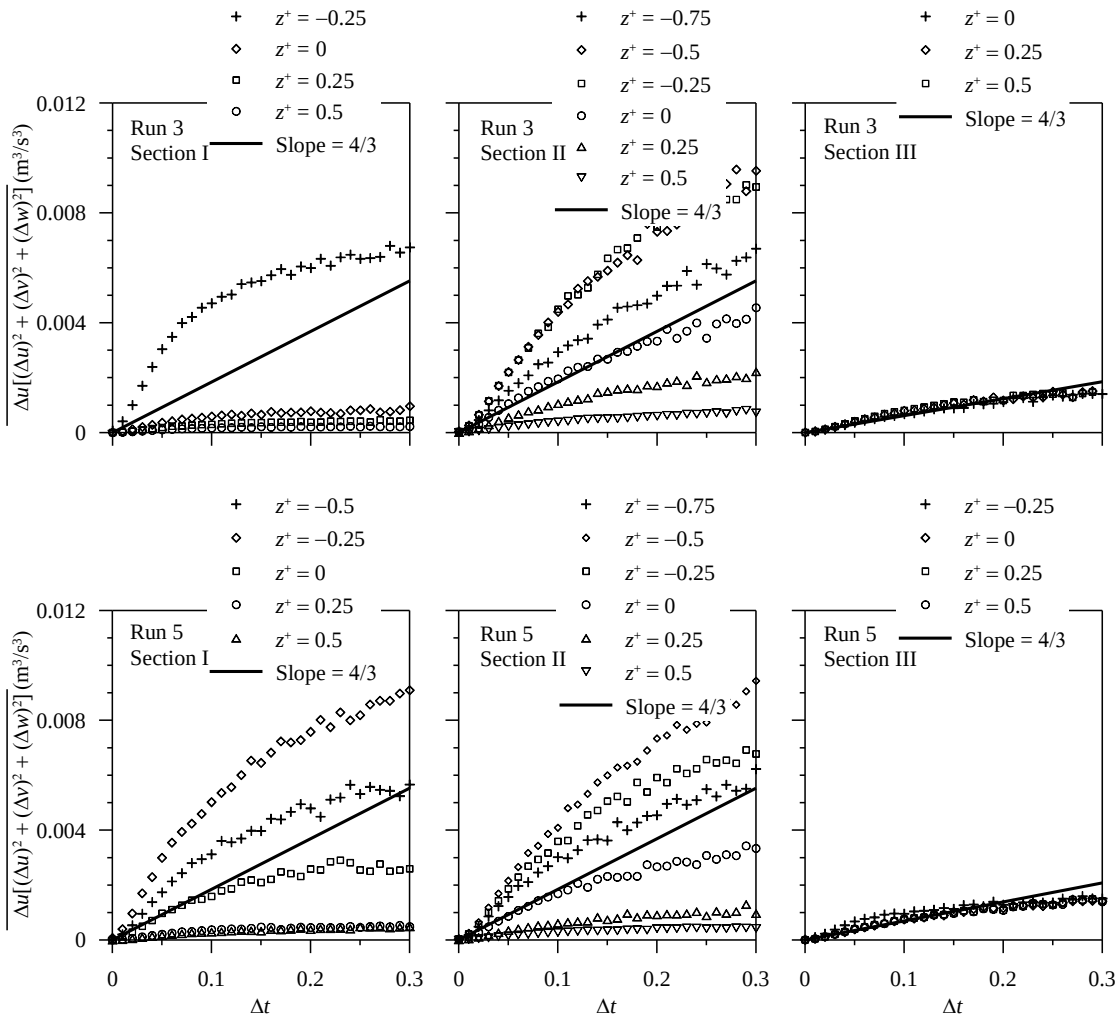

Figure 4.15: Variations of third-order mixed structure function with time lag at sections I, II, and III at different vertical distances. Data of runs 3 and 5 are presented.

4.13 Estimation of TKE dissipation rate with Kolmogorov 4/5-law and Monin-Yaglom 4/3-law

One of the most important applications of structure functions is the estimation of the turbulent kinetic energy dissipation rate ε. According to the literature, there are several methods to estimate the TKE dissipation rate.

For instance, according to Irwin (1973) and Krogstad and Antonia (1999), the ε may be calculated from the equation:

$$\varepsilon = (15\upsilon/u^2)\,\overline{(\partial u'/\partial t)^2}\,, \tag{4.5}$$

where ν is the kinematic viscosity of water and u' is the fluctuation of the time-averaged streamwise velocity component.

The ε can also be estimated from the velocity power spectra using the Kolmogorov's 5/3rd power law (Kolmogorov 1941) based on the expression

$$E(k_w) = C_1 \varepsilon^{2/3} k_w^{-5/3}, \tag{4.6}$$

where $E(k_w)$ represents one-dimensional energy spectrum, C_1 and k_w represent the Kolmogorov constant and wave number of the eddies ($2\pi/l$, l = size of the eddies), respectively (Zhu et al. (2006), Wan et al. (2010), Singh et al. (2014), Sarkar et al. (2016), Han et al. (2017), etc.). However, the value of ε obtained from 5/3rd power law is biased by the value of Kolmogorov universal constant C_1 that varies from 1.5 to 2.

It is important to mention here since Kolmogorov's pioneering work, it has been modified by Kolmogorov and several researchers. Kolmogorov (1962) and Padhi et al. (2018) suggested that second-order structure function could be more useful in estimating the ε value which is analogous to Kolmogorov's 2/3rd law where the ε is estimated from the second-order structure function that follows 2/3-line within the inertial subrange. However, the ε may also be biased by the universal constant used in the equation:

$$\langle \varepsilon \rangle = (1/r)\,(\langle \Delta u \rangle^2 / C_2)^{3/2}, \tag{4.7}$$

where C_2 is an universal constant value of which is 2.12 (Sreenivasan 2019).

For large Reynolds number, Kolmogorov derived 4/5-law using the von Kármán–Howarth equation (Ferraro et al. 2016) which is written as:

$$\langle \overline{\Delta u^3} \rangle = (-5/4 \langle \varepsilon \rangle r), \tag{4.8}$$

where $\langle \overline{\Delta u^3} \rangle$ represents third-order streamwise velocity structure function. Using this equation, the ε can be estimated more accurately for flow with high Reynolds number. The third-order structure functions can be plotted in a log-log scale and the values of ε can be estimated from a constant value of $(-5/4r)\,\langle \overline{\Delta u^3} \rangle$ in the inertial subrange.

In the present study, third-order and mixed third-order structure functions were used to estimate the ε. It is important to note that the angle bracket $\langle\rangle$ used here is to show the

results with respect to spatial increment. According to figure 4.16, the r versus $(-5/4r)\langle\overline{\Delta u^3}\rangle$ presents the value of ε where the $(-5/4r)\langle\overline{\Delta u^3}\rangle$ has nearly a constant value within $r \leq 0.1$ m signifying the length of inertial subrange. Beyond that, the $(-5/4r)\langle\overline{\Delta u^3}\rangle$ decrease and do not follow any constant value any more. In the figure 4.14, Section II data of Run 5 have presented only as it was experienced that for other runs and sections also they follow the same trend with different values. However, at the near-bed the $(-5/4r)\langle\overline{\Delta u^3}\rangle$-values are little bit inconsistent than those of the remaining vertical distances.

The ε can also be estimated from the third-order mixed structure function also known as Monin-Yaglom's 4/3-law (Karman and Howarth 1938, Antonia et al. 1997). From third-order mixed structure function, ε can be calculated from the equation

$$\langle\varepsilon\rangle = (-4/3r)\langle\overline{\Delta u[(\Delta u)^2 + (\Delta v)^2 + (\Delta w)^2]}\rangle, \tag{4.9}$$

considering that the third-order mixed structure function follows 4/3-slope within the inertial subrange located within $r \leq 0.7$ m. However, Monin–Yaglom's 4/3-law is based on the assumption of isotropic turbulence at low Reynolds number. The procedure of estimating the value of $\langle\varepsilon\rangle$ using Monin-Yaglom's 4/3-law is as same as that using the third-order structure function.

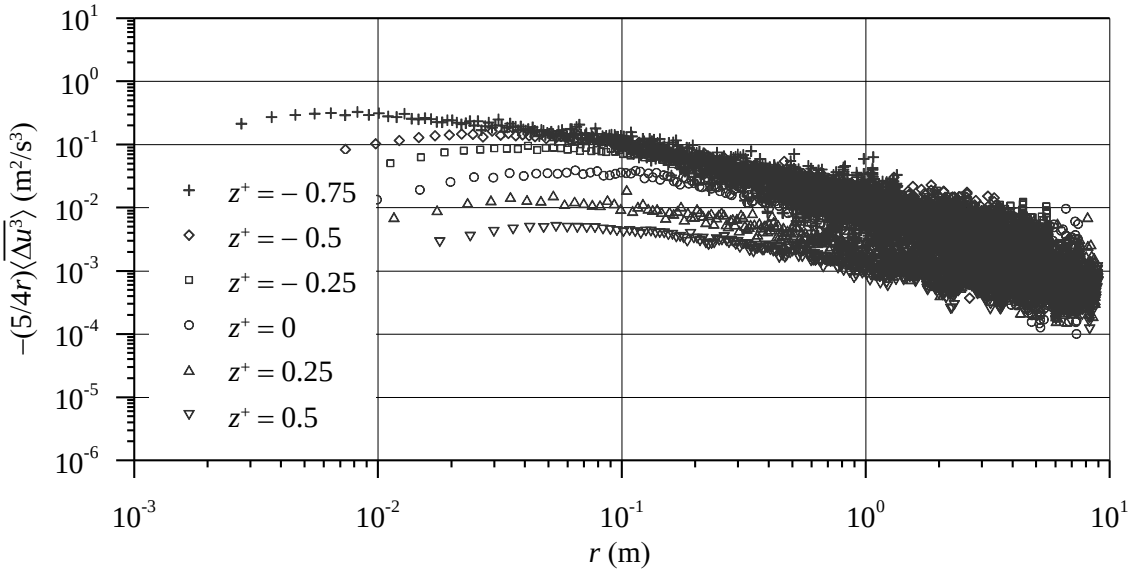

Figure 4.16: Kolmogorov's 4/5-law at different vertical distances z^+ = –0.75, –0.5, –0.25, 0, 0.25 and 0.5. Section II data of Run 5 are presented.

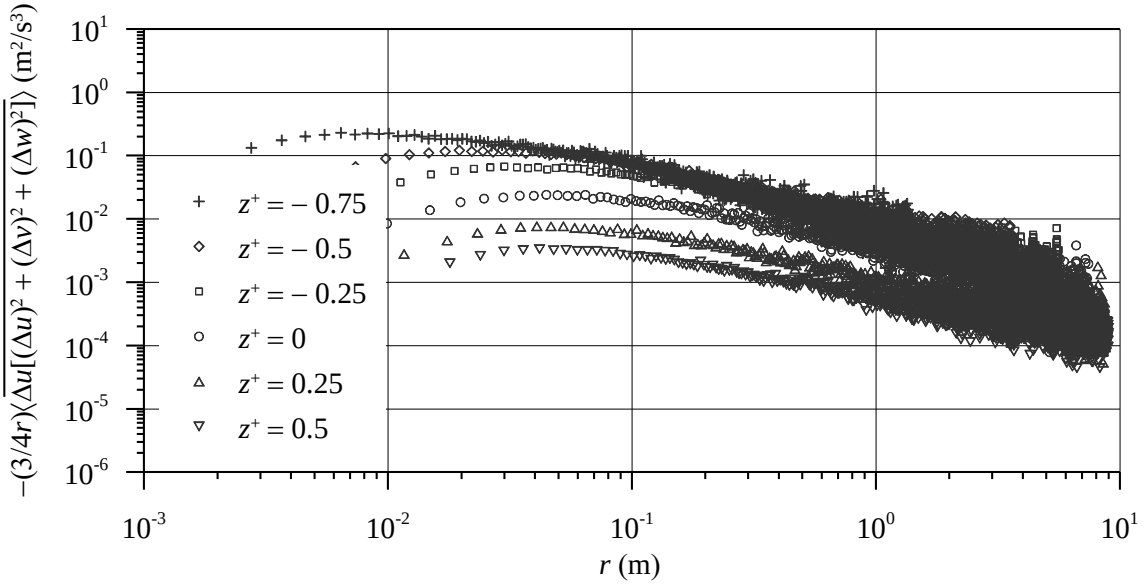

Figure 4.17: Monin–Yaglom's 4/3-law at different vertical distances z^+ = –0.75, –0.5, –0.25, 0, 0.25 and 0.5. Section II data of Run 5 are presented.

The $\langle\varepsilon\rangle$ estimated from Monin-Yaglom's 4/3-law gives lesser value (0.65 to 0.75 times that of Kolmogorov's 4/5-law). The discrepancies in the values of ε are due to the fact that the Kolmogorov's 4/5-law is based on the assumptions of flow to be anisotropic in nature for high Reynolds numbers, whereas the Monin-Yaglom's 4/3-law is based isotropic turbulence at low Reynolds number. However, for flow over plane rough-bed and water-worked gravel beds, Ferraro et al. (2016) and Penna et al. (2020) also experienced the similar discrepancies in the values of $\langle\varepsilon\rangle$. However, in the cases stated earlier, the discrepancies were more than that of the present study that may be due to the differences in flow and bed conditions. However, Penna et al. (2020) concluded that the due to the anisotropic turbulence at large scales, $\sigma_{uu}^+ > \sigma_{vv}^+ > \sigma_{ww}^+$ was observed that was responsible to give lesser values of $\langle\varepsilon\rangle$ based on Monin-Yaglom's 4/3-law.

The third-order structure functions and the mixed structure functions data were compared and shown in figure 4.18. It was found that the third-order structure function data are

higher than that of the mixed structure function below the initial bed level. However, above the bed-level, their differences are less. Below the bed-level, the values of ε from third-order structure functions are approximately 0.75 times of the values from mixed structure functions. However, for the remaining part, the $\langle\varepsilon\rangle$ estimated from the third-order structure functions were used as it was suggested by Penna et al. (2020) that for an anisotropic data, the third-order structure function is more appropriate than the mixed structure function. However, the near-bed and above $z^+ = 0.2$, the data becomes isotropic in nature and therefore the third-order and mixed structure function both are valid. However, the anisotropy will be discussed in details afterwards.

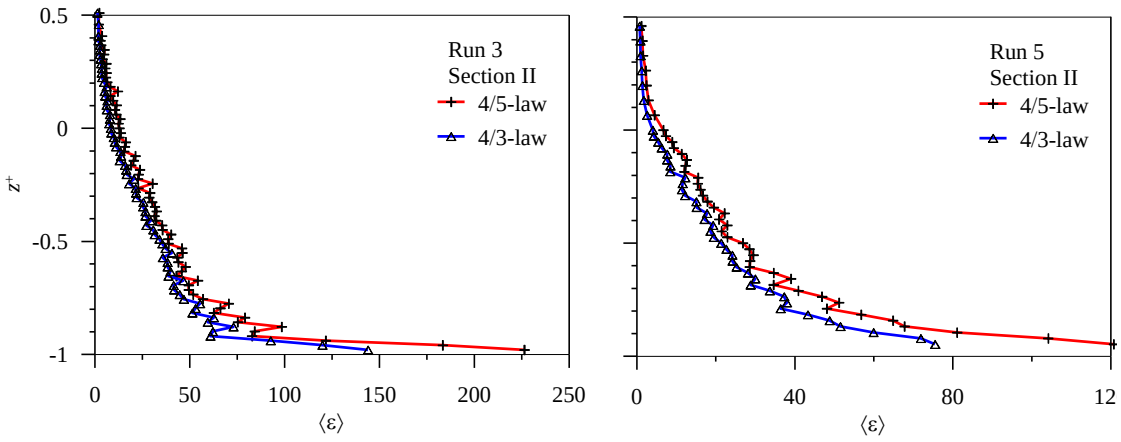

Figure 4.18: Comparison the $\langle\varepsilon\rangle$-values estimated from the third-order mixed structure function and mixed structure function. Data of Run 3 and Run 5 at section II are presented.

4.14 Turbulent kinetic energy budget

Turbulent kinetic energy budget includes different energy terms and their balance in a turbulent fluid flow. These energy terms are: the turbulent production t_P, the turbulent dissipation ε, turbulent energy diffusion t_D, pressure energy diffusion p_D and viscous diffusion. For a uniform two-dimensional open-channel flow, TKE budget is calculated by Nezu and Nakagawa (1938) written as

$$t_p = \varepsilon + (\partial f_{kw}/\partial z) + (1/\rho)(\partial \overline{p'w'}/\partial z) - \upsilon(\partial k/\partial z^2) \quad (4.10)$$

According to Nezu and Nakagawa (1938), in turbulent energy budget, t_P is calculated from the Reynolds shear stress and velocity gradient in vertical directions as $t_P = -\overline{u'w'}(\partial u/\partial z)$. In TKE budget of the present study, the TKE dissipation rate ε estimated from third-order structure functions $\langle\varepsilon\rangle$ was used. The turbulent energy diffusion t_D is calculated from the formula: $\partial f_{kw}/\partial z$, where f_{kw} vertical flux of TKE.

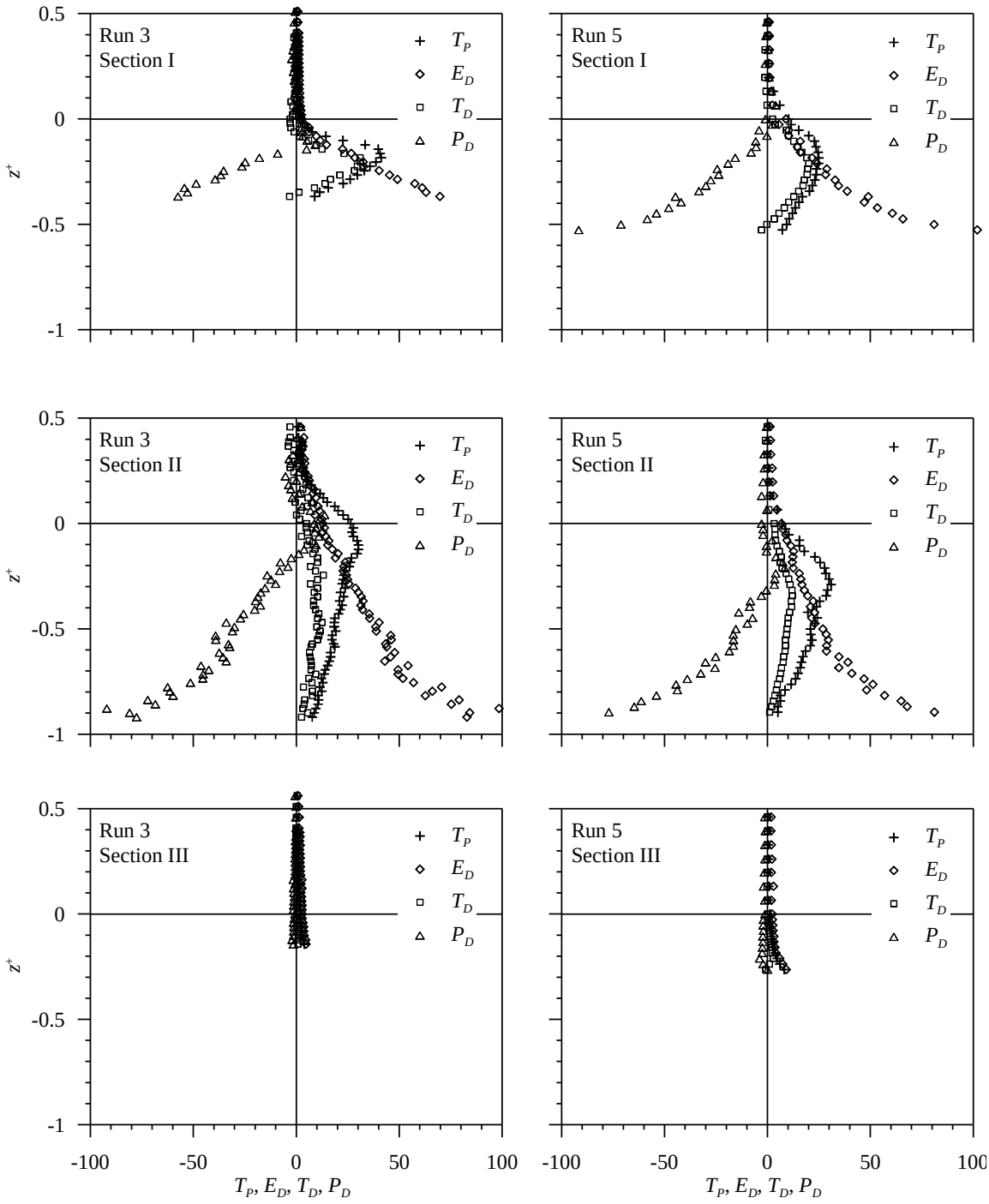

Figure 4.19: Vertical distribution of T_P, E_D, T_D and P_D. Data are shown here for runs 3 and 5 at sections I, II, and III.

The viscous diffusion term v_D was estimated from $-\upsilon(\partial^2 k/\partial z^2)$. The pressure energy diffusion may be estimated from $p_D = \partial(\overline{p'w'/\rho})/\partial z$, where p' is the pressure fluctuation. However, in the present study it was not feasible to measure the p' and therefore it was

calculated from the balancing equation of the TKE budget. Importantly, for all the measuring locations, the viscous diffusion υ_D was negligibly small as found in the open channel turbulence. The pressure energy diffusion p_D is thus obtained from the energy budget relationship, as an unknown, as $p_D = t_P - \varepsilon - t_D$. The normalized form of these parameters are expressed as $T_P, E_D, T_D, P_D = (t_P, \varepsilon, t_D, p_D) \times (d/u_*^3)$. The TKE budget at sections I, II and III for Runs 3 and 5 are shown in Figure 4.19. It was observed from the figure that below $z^+ = 0$, over the degraded bed show that at Sections I and II, E_D is greater than T_P and T_D which continues till $z^+ \approx 0$ where T_P and E_D crosses each other. Above this level, T_P is more than all other TKE budget parameters for the remaining depths. Importantly, above $z^+ \approx 0$, the values of T_P decrease with increase in depth and attain the lowest value slightly above $z^+ \approx 0.3$. Beyond that, the T_P becomes very low and almost invariant with respect to depth. The profile of TKE budget at Section II is almost similar to that of Section I. However, TKE budget at Section III is quite different in which throughout the depth T_P maintains the maximum values than the remaining terms, whereas P_D is significantly small throughout the depth which is very common for flow over plane rough bed.

4.15 Reynolds stress anisotropy

Reynolds stress anisotropy tensor introduced by Rotta (1951) is one of the preeminent tools to examine the degree and nature of turbulence anisotropy, and fully developed in hydraulics by Lumley and Newman (1977). Since the work of Lumley and Newman (1977), Reynolds stress anisotropy has become an important aspect to explain the turbulent flow characteristics (Banerjee et al. (2007), Frohnapfel et al. (2007), Sarkar and Dey (2015), Sarkar and Dey (2015), Dey et al. (2019) , Sarkar et al. (2019), and Penna et al. (2020)). The main advantage of the tensor anisotropy analysis is that it does not require any additional or external component to normalize the turbulent parameters but it gives a complete idea of the turbulent flow characteristics in the form of anisotropy.

Based on the directions in tensor coordinate systems, the Reynolds stress anisotropy tensor a_{ik} can be defined according to Rotta (1951) as

$$a_{ij} = \overline{u_i' u_k'} - \frac{2}{3} q \delta_{ik} , \tag{4.11}$$

where q is the average turbulent kinetic energy ($\overline{u_i' u_i'}/2$) and δ_{ik} is the Kronecker delta function, the value of which is 0 if $i \neq k$, or 1 if $i = k$.

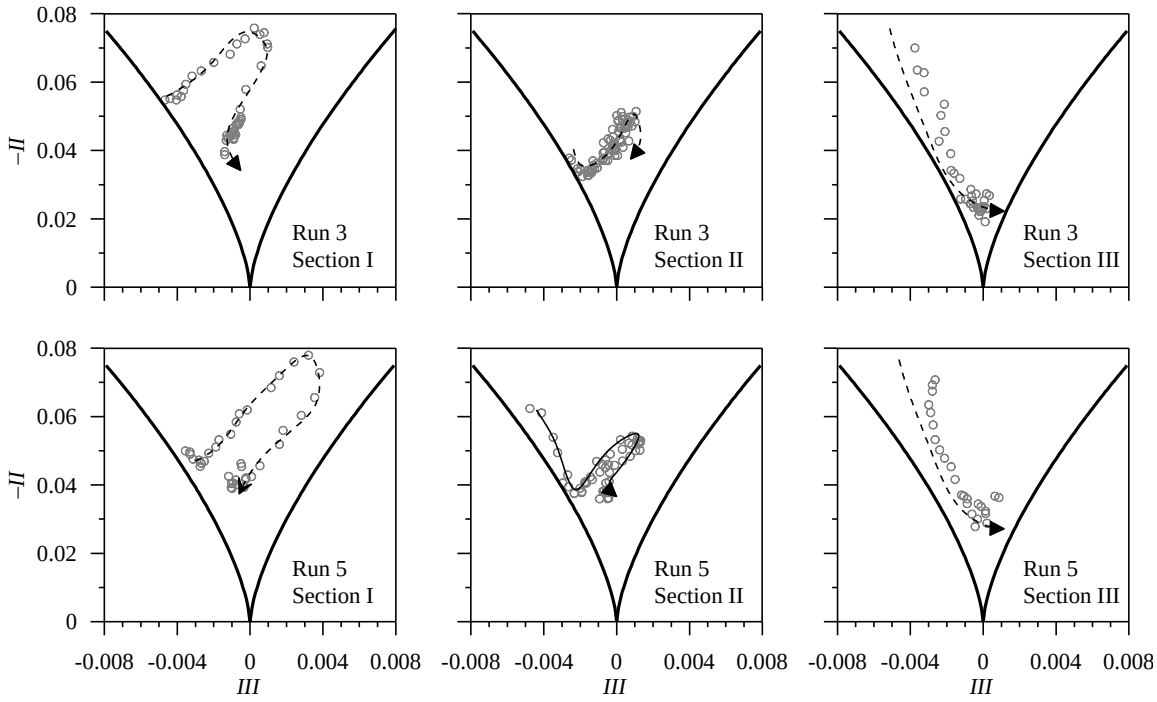

Figure 4.20: AIM for runs 3 and 5 at section I, II, and III are presented.

The anisotropy tensor then normalized by the turbulent kinetic energy q as

$$b_{ik} = \frac{a_{ik}}{2q} = \overline{u_i' u_k'}/(2q) - (\delta_{ik}/3) \tag{4.12}$$

Each term of b_{ik} is symmetric and traceless tensor and their values ranges from –1/3 to 2/3. The anisotropy of turbulence can be estimated and described by using a cross-plot of two principal independent invariants *II* (= $-\ b_{ik}b_{ik}/2$) and *III* (= $b_{ij}b_{jk}b_{ki}/3$). The cross-plot is termed Anisotropic invariant map (AIM), in which *–II* represents the degree and *III* represents the nature of anisotropy. The AIM forms a triangle known as Lumley triangle. The triangle has three limiting states that define the boundaries of the map. In the map, *– II = III* = 0 belongs to the bottom cusp represents the 3D isotropic turbulence also called

as 3-component limit (3C). All other locations within the triangle represent anisotropic turbulence. The 1-component limit (1C) indicates a rod like or cigar shape turbulence, whereas the left curved boundary represents 2-component limit (2C) and referred to as pancake turbulence.

Figure 4.20 presents AIM at different locations for runs 3 and 5 data. It was observed that near the bed, the anisotropy tends to reduce to 2D isotropy as data plots move toward the left-curved boundary. With increase in the vertical distances, data plots show a tendency to move toward bottom cusp signifying three-dimensional isotropy. It is important to mention here that Sarkar et al. (2019) also observed that turbulence at far downstream of a bluff-body starts from two-dimensional isotropy and with increase in vertical distance; turbulence has a tendency to reduce to three-dimensional isotropy.

Use of the invariant function F is another easy and satisfactory method to determine the state of turbulence: whether it is two- or three-dimensional and is calculated as

$$F = 1 + 9II + 27III \tag{4.13}$$

The value of $F = 0$ for two-dimensional turbulence and $F = 1$ for a three-dimensional isotropic state.

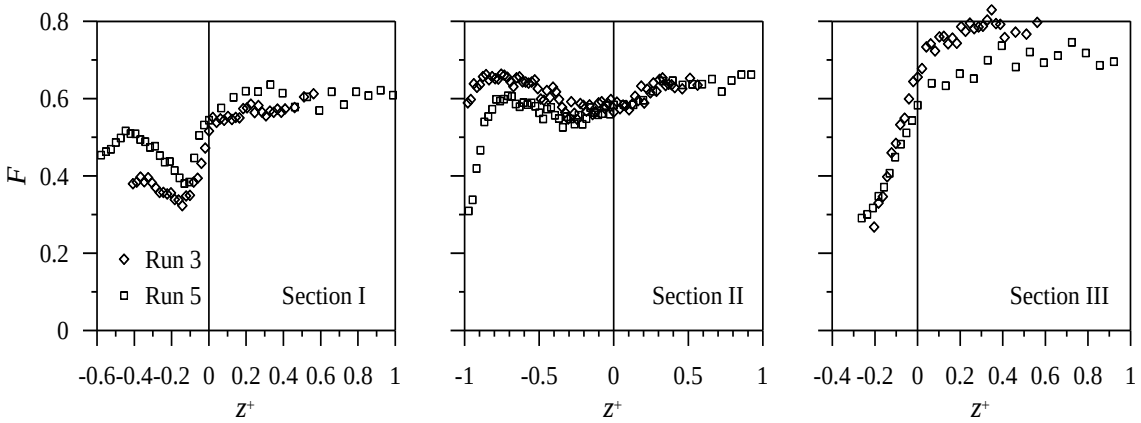

Figure 4.21: Vertical distribution of Invariant function F for Run 3 and Run 5 at Section I, II, and III are presented.

Figure 4.21 shows the distribution of F with flow depths. Near the bed at section I, F starts with values in the ranges of 0.3–0.45 which increases with z^+ and again decreases from $z^+ \approx -0.4$ and attains the lowest value at $z^+ \approx 0$. Beyond that F increases and at $z^+ \approx 0.4$, F becomes almost invariant with z^+. The profile is almost same for F of Section II. However, at Section III, value of F starts from 0.3 which increases with z^+ until attains

the maximum value at $z^+ = 0.3$. After that F becomes invariant with z^+. However, below $z^+ = 0$, the value of F for all the cases evidences that the anisotropy starts from the two-dimensional state and with increase in depth they show an affinity to follow a three-dimensional isotropic state.

4.12 Concluding remarks

This paper presents experimental findings for flow over a degraded bed made up of sand-gravel mixture. Data were analyzed to observe time-averaged streamwise velocity, Reynolds shear and normal stresses, TKE, TKE fluxes, TKE budget and Reynolds stress anisotropy, etc. The streamwise velocity indicated that the degradation has a considerable impact in the streamwise velocity over a degraded bed. A reversal flow takes place in the vicinity of the degraded bed whereas above the initial bed level, streamwise velocity does not show any significant changes. The Reynolds shear and normal stresses attain maximum value around the initial bed-level, whereas their values decrease with an increase and decrease in vertical distances. Near the bed, the streamwise TKE flux becomes positive and the vertical TKE flux becomes negative which indicate the sweep as the governing event in the vicinity of the degraded bed; whereas ejection is predominating throughout the depth of the flow. Second-, third-, and mixed third-order velocity structure function indicate the existence of inertial subrange for lower values of time lags irrespective of the measuring sections. However, their values decrease with increase in the vertical distances. Data were further analyzed to estimate the turbulent kinetic energy dissipation rate using the third-order and mixed third-order statistics of turbulence. The estimated results were used to observe TKE budget. Below the initial bed-level, the value of turbulent production is more than the turbulent kinetic energy dissipation and TKE diffusion; whereas pressure energy diffusion is negative throughout the depth at the maximum degraded bed location. The anisotropy analysis suggested anisotropic turbulence in the near-bed which tends to become three-dimensional isotropic towards the free water-surface. However, the effect of bed-degradation lowers as one move towards further downstream from the maximum depth of degradation. The present study was exclusively confined within the third-order structure functions and its applications. High-order structure functions and scaling exponents may be explored for

similar kind of experimental setup in future. As future scope, turbulent flow characteristics over a degraded bed can be examined over a bimodal gravel-bed under wave-current interactions. Data of the present study may also be useful to simulate the turbulent flow through a bimodal scoured bed.

Chapter 5

High-order Structure functions of turbulence through a degraded channel bed

5.1 General

So far, the fundamental turbulence characteristics over a bimodal degraded channel-bed were studied in Chapter 4 where the bed was made up of bimodal type of sediment. Several turbulence characteristics, like TKE dissipation rates, scaling laws of turbulence in open-channel and TKE budget were estimated using the structure functions data up to 3rd order. However, the structure functions have several applications in turbulent flow study. Therefore, the study was further extended for high-order structure functions. Moreover, it was assumed that the turbulence properties may be different if the characteristics can be observed for uniform as well as bimodal gravel bed under degraded conditions. In view of addressing the above-mentioned parameters, in the present chapter the high-order structure functions were applied over the uniform and degraded channel-bed.

The flows within natural stream beds that contain different types of sediment particles, from fine sand to larger coarse gravel and mixtures of both, are characterized by the transport of sediments and the flow of water they carry. Based on particle size, stream beds are generally classified as either sand beds or gravel beds. However, there is also a third type, called bimodal, which contains a mix of both sand and gravel in significant amounts (Smith, 1996). Due to the sediment transport occurring in streams, the bed particles detach which eventually deform the natural sediment bed and convert it to degraded-, aggraded-, and scoured-beds, etc. The bed degradation is in principle a result of the bed erosion or localized scouring, whereas the bed aggradation is the opposite phenomenon occurred due to the sediment deposition in a natural stream bed. It is therefore imperative to gain a proper understanding of flow through degraded channel-beds to solve various problems on bank erosion, sedimentation, river morphology, and so on. Bed degradation in open channel flow also involves the safety of hydraulic structures

like apron downstream of a sluice gate and energy dissipater, bridge piers, spur dikes and abutments, etc. (Dey and Sarkar 2006). In view of this, in recent years, a significant number of research works have been carried out in open-channel flow to understand the turbulence behavior under different flow and sedimentary bed conditions. For instance, turbulent flow over armored gravel bed, mobile bed, water-worked bed, aggraded bed, scoured bed, bedforms, etc. have been studied extensively during last few decades. However, the flow through a uniform and bimodal degraded bed has not been paid enough attention in comparison to that of others. Although a number of attempts have been made on this topic in recent years by several researchers like Shvidchenko and Pender (2001), Wilcock et al. (2001), Grams and Wilcock (2007), Wren et al. (2011), Jain et al. (2015), and Pandey et al. (2019) on various parameters of flow through uniform and bimodal bed, there remain some more issues to execute. In this context, it is important to note that Shvidchenko and Pender (2001) studied the turbulent flow over heterogeneous gravel mobile beds and observed that lift and drag forces generated due to the eddy motion of fluid is responsible for the movement of fluid particles. In a laboratory experiment on flow over various sand-gravel mixtures, Wilcock et al. (2001) estimated transport rates of sediment particles and the bed shear stress. In another experimental study for flow over immobile coarse sediments feeded with fine sand, Grams and Wilcock (2007) observed the effect of addition of sand over a gravel bed. Based on the experimental data, they established relationship among the bed coverage, transport rate, and bed shear stress, etc. Later, Wren et al. (2011) studied turbulent flow over an immobile coarse gravel bed and found significant changes in the turbulence characteristics when the bed is subjected to a gradual addition of sand. Jain et al. (2015) performed an experimental study to understand the flow characteristics like streamwise velocity, Reynolds shear and normal stresses and bursting events for flow over a degraded channel bed and found considerable changes of all these turbulence parameters particularly in the vicinity of the degraded bed. In the work of scouring around spur dike in sand-gravel mixture bed, Pandey et al. (2019) pointed out that the rivers in upper reaches or hilly streams are mainly composed of different sediment mixtures or non-uniform sediments, whereas the uniform sediments are generally found in rivers in lower reaches. Significantly, Sarkar et al. (2021) studied the hydrodynamics of flow through a

degraded channel bed experimentally. It was evident from the results that the streamwise velocity, Reynolds shear and normal stresses, turbulent kinetic energy (TKE), TKE dissipation rates, and Reynolds stress anisotropy change significantly due to the bed degradation. All the above-mentioned turbulence parameters show maximum amendment at the utmost equilibrium depth of the degradation. Streamwise and mixed structure functions up to third-order were studied in detail along with the related scaling laws of turbulence. Notably, the study of Sarkar et al. (2021) was confined up to third-order structure functions and there was no information about scaling exponents obtained from higher order structure functions. However, some recent works in fluvial hydrodynamics suggest that due to the differences in the bed profiles, the scaling exponents based on higher order structure functions change extensively from the predicted values, particularly in the near-bed flow zone (Penna et al. 2022).

The estimation of scaling exponents in open-channel turbulence is in principle based on the scaling theory introduced by Kolmogorov (1941a, b) that is popularly called as K41 and their extension to higher order structure functions. In the introductory works of Kolmogorov, the structure functions were confined up to second- and third-order which was used by several researchers to understand the laws of turbulence quite successfully. The laws are known as two-third power law and four-fifths power law based on the second and third-order structure functions of single-component velocity fluctuations. Later, the scaling theory was modified for mixed third-order (Monin -Yaglom 1975, Frish 1995) which is known as four-third laws of turbulence. However, the structure functions methodology remains very popular and so more research works have been carried out on it and now higher order structure functions is a matter of great interest to several researchers for estimating the scaling exponents and intermittency in open-channel flow. For instance, Benzi et al. (1993, 1995), Protas et al. (1996) Gaudin et al. (1998) Jimenez (1998), Kurien and Sreenivasan (2000), Warhaft and Shen (2002), and Shen and Warhaft (2002) etc. have done significant works on this topic and found that the scaling exponents are not fully universal but they can be modified based on different conditions and the ranges of the Reynolds number. However, their applications in open-channel flow were fully realized by Nikora and Walsh (2004), Coscarella et al. (2020), Penna et al. (2022), etc. Interestingly, in Coscarella et al. (2020), and Penna et al. (2022), the analyses were

based on the data captured in an open-channel flow with different types of rough beds made up of gravels, pebbles, etc. In those problems, sediment movement or changes in the bed-elevations were not studied. However, in the present problem, the sediment beds are made up of uniform sand particles and sand-gravel mixtures, respectively in which degradation of the sediment bed took place. It is important to mention here that such sedimentary beds and flow conditions are very common in open-channel flow and therefore possess a vast practical application in sediment transport, bank-erosion and river training works, etc. To be more explicit, the problem has a wide application in scour downstream of an apron of a sluice gate, energy dissipator, etc. It also has a great theoretical insight. Based on its wide application in open-channel hydraulics, the present experimental setup was chosen and the analyses were focused on to observe the effect of bed-degradation on the scaling exponents of higher order streamwise and mixed structure functions. The velocity vector in (x, z) plane, turbulence indicator and length scales were also included in this chapter as references to understand the physics of the flow behind the bed-degradation.

Rest of the chapter was arranged as follows: Experimental setup and methodology was discussed in a section, Physics of flow behind the bed degradation was discussed in another section, the main results of the chapter in terms of the higher order scaling exponents, and finally conclusion was drawn from the present observation.

5.2 Description of the Experimentation

The experiments (designated herein as Run 1, Run 2, Run 3 and Run 4) were carried out in a rectangular flume fabricated in the Fluvial Mechanics laboratory of Indian Statistical Institute, Kolkata, India. The flume is 20 m long, 0.5 m deep and 0.5 m wide. The visual observation to the flow is provided by its transparent side-walls. For the experimental Runs 1 and 2, the bed was made up of river-borne sand of uniform size d_{50} = 1.2 mm with σ_g = 1.1. For Runs 3 and 4, bimodal bed was used that was made up of a mixture of river-borne sand of uniform size $(d_{50})_{sand}$ = 0.25 mm (uniformity coefficient $\sigma_g = d_{84}/d_{16}$ = 1.25 and relative density s = 2.65, d_{84} and d_{16} are the particle size at which 84 percent and 16 percent of the sediment particle were smaller) and gravel with a median diameter of

(d_{50})$_{gravel}$ = 3.5 mm (σ_g = 1.2 and s = 2.65), respectively. Hence, the mean sediment size of the mixture d_{50} was considered as the mean of (d_{50})$_{sand}$ and (d_{50})$_{gravel}$ = 1.875 mm. For all the runs, two solid aprons each of 1 m length × 0.5 m wide × 0.2 m height were installed at the upstream (5 m from the entrance of the flume) and downstream ends of the test section. The dimension of the test section was 6 m × 0.5 m × 0.5 m. Figure 5.1 shows the photograph of one experimental setup. For Runs 1 and 2, the initial bed slope of 0.00075 was made using the uniform sand particles. However, to attain comparable depths of degradation for bimodal sediment beds, higher values of initial bed slopes and discharges were used. For bimodal beds, the sand and gravel were mixed in equal proportions (by weight) and laid them on the flume to create a slope of 0.0045 and 0.005 for Run 3 and Run 4, respectively. Once the sediment bed was prepared, water was supplied on it very slowly to check and adjust the initial bed-slope more accurately. Once all the conditions were satisfied, one centrifugal pump was employed finally to supply the water over the bed to achieve a predetermined uniform free surface elevation. The constant discharges for the experimental runs were 0.027, 0.024, 0.037 and 0.034 m^3/s for Runs 1, 2, 3, and 4, respectively. During the experiment, bed-degradation took place immediately after the solid apron placed upstream. It is important to note that, although Run 4 was not much different from Run 3 with respect to the flow and bed conditions, it was conducted to support the findings of Run 3. On the other hand, Runs 1 and 2 were conducted to compare the bimodal bed data with that of uniform sediment degraded bed. The velocity measurement was started under the equilibrium condition that was reached after 16 hours for Runs 1 and 2 since the experimental run was initiated. For Runs 3 and 4, approximately 12 hours time was required to achieve the equilibrium condition. The equilibrium condition of the degraded bed was ensured by observing no movement of the sediment particles and no further changes in the bed profiles within the test section. Figure 5.2 presents the evolution of the bed degradation with time for Runs 1–4. The value of maximum degraded depth (d_{max}) in cm with respect to time (s) was shown in the Figure 5.2. However, after achieving the equilibrium degraded-bed condition, measurements of the three-dimensional velocities were conducted using a Nortek-manufactured Vectrino velocimeter. Relied upon the earlier experiences, the data were collected throughout the middle line of the channel cross-section with the sampling

frequency of 100 Hz, acoustic frequency of 10 MHz, signal-noise ratio (SNR) of 18 and above, and the correlation coefficient of 70 and above. Unless it was very much essential, the raw data were used directly for the turbulence analysis to keep the natural turbulence properties undisturbed. However, close to the bed, at some locations data were filtered using phase-space thresholding method and replaced by the median of the neighbouring samples, following Goring and Nikora (2002). The details of working with Vectrino and measurement techniques, pre- and post-processing of data, filtering the spurious data were described elaborately in Sarkar et al. (2021).

Figure 5.3 presents the normalized equilibrium degraded bed profile where z^+ represents the normalized vertical distance measured with respect to the maximum equilibrium depth of degradation d (i.e., $z^+ = z/d$) and x/L represents the normalized streamwise distance measured with respect to the streamwise distance L from where the degradation was initiated. In Figure 5.3, locations of the measurements indicate that one of the measuring locations were at the upstream of the maximum degraded-depth (Section I), at the maximum degraded-depth (Section II) and downstream of the maximum depth of degradation (Section III). Although, Section III seems much closer to the maximum scour cross section in Runs 1 and 2, than in Runs 3 and 4, it was due to the non-dimensionalising of the streamwise distance. To be more explicit, due to larger values of L for uniform sediment beds, location of Section III looks closer. Based on the issuing experimental parameters, the Froude number F [$= \overline{U}/(gh)^{0.5}$, where $\overline{U}$ = depth-averaged velocity, g = acceleration due to gravity, h = depth of water above bed-level] was calculated and the values were 0.41 for Run 1, 0.40 for Run 2, 0.56 for Run 3 and 0.68 for Run 4. Accordingly, the Reynolds numbers R [$= 4\overline{U}h/\upsilon$, υ = kinematic viscosity of water = 10^{-6} for water at 20°C] were also calculated based on the issuing velocity and flow depth. Their values for were 2.11×10^5, 1.68×10^5, 2.9×10^5 and 2.72×10^5, for Runs 1, 2, 3, and 4 respectively.

Table 1 shows the experimental parameters based on the initial conditions of the experiments for Runs 1–4. The critical shear velocity u_{*c} for each case was calculated using the van Rijn (1984) equations and Shields diagram (1936). The relative density of the sediment particles were 2.65 for all the sediment particles and so, $\Delta = s - 1 = 1.65$,

where s = relative density of sediment particles, that is ρ_s/ρ; ρ_s = mass density of sediment; and ρ = mass density of fluid.

Figure 5.1: Photograph of the experimental setup at the fluvial mechanics laboratory of Indian Statistical Institute, Kolkata, India.

Table 5.1:

Experimental parameters based on the initial conditions of the experiments

Run	Q (m^3/s)	d_{50} (mm)	d (m)	h (m)	S	$\bar{U}$ (m/s)	u_* (m/s)	u_{*c} (m/s)	F	R	L (m)
1	0.027	1.2	0.098	0.12	0.00075	0.44	0.029	0.0237	0.41	211200	0.71
2	0.024	1.2	0.1	0.1	0.00075	0.42	0.027	0.0237	0.42	168000	0.79
3	0.036	1.875	0.076	0.12	0.0045	0.61	0.073	0.035	0.56	292800	0.39
4	0.034	1.875	0.082	0.1	0.005	0.68	0.07	0.035	0.68	272000	0.51

Note: In the above, u_* is the shear velocity calculated from the bed slope before the degradation took place u_{*c} is the critical shear velocity obtained from the Shields diagram. (Sheilds 1936, van Rijn 1984, Dey 2014).

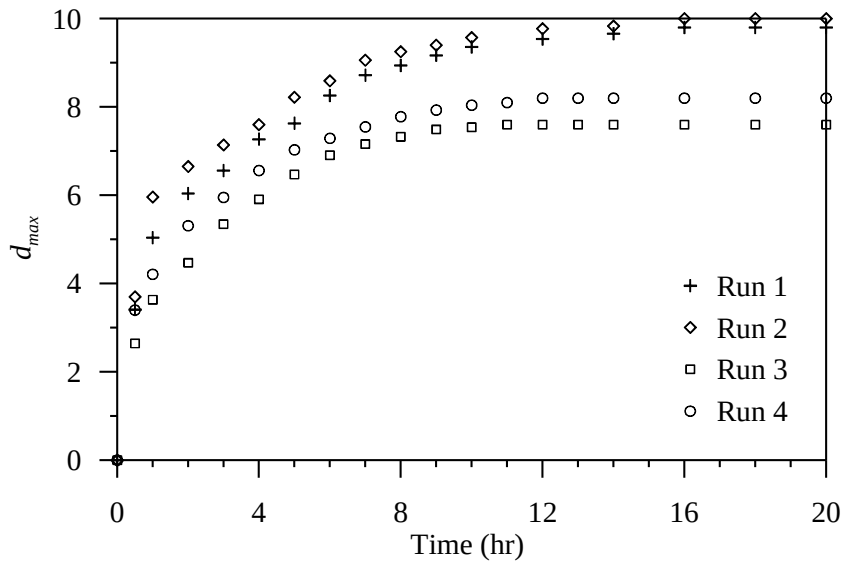

Figure 5.2: Evolution of the bed degradation (in cm) with time (in hr) for Runs 1–4.

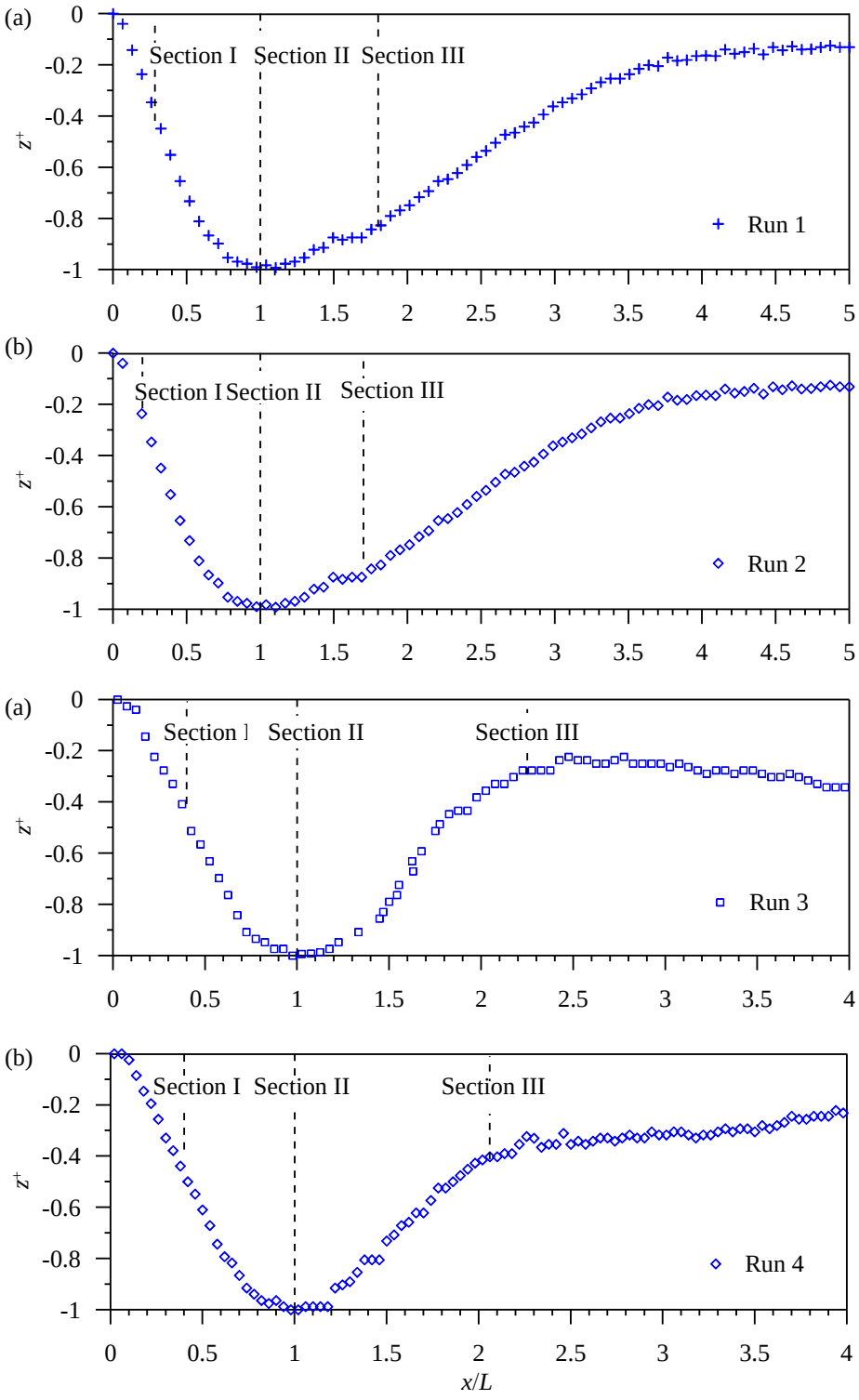

Figure 5.3: Degraded bed profile in equilibrium conditions for Runs 1–4.

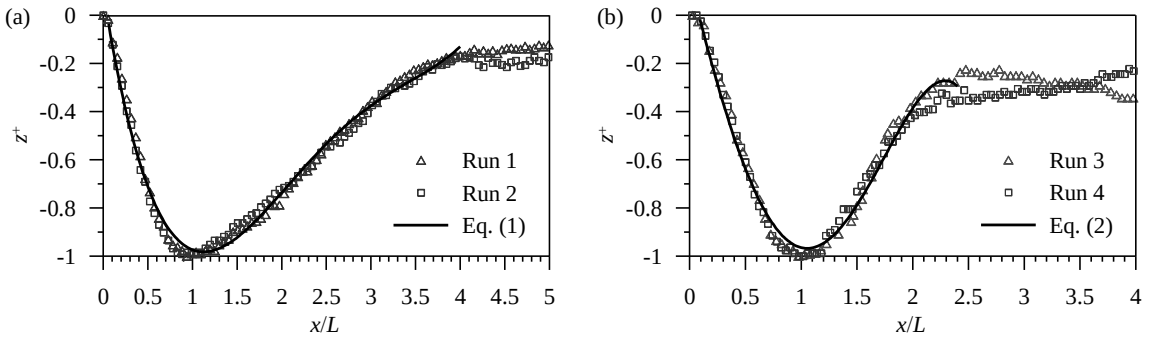

Figure 5.4: Similarity of the degraded bed profiles for (a) Runs 1–2, and (b) Run 3–4.

A close observation of the equilibrium degraded bed profiles (Figure 5.3) gave an indication of the existence of similarity. To establish the similarity, degraded bed profiles of Runs 1 and 2; and Runs 3 and 4 were plotted in nondimensional forms. Figure 4 shows nondimensional depth of degradation under equilibrium condition with respect to nondimensional streamwise distance originated from the origin of the degradation for (a) Runs 1–2, and (b) Runs 3–4, respectively. The data plots show a clear existence of the similarity of the degradation profiles within the scour holes. For Runs 1 and 2 the uniform degraded bed profiles can be described by Eq. (1), whereas the scour profiles for Runs 3 and 4 can be described by Eq. (2) given below:

$$z^+ = 0.10 - 2.36\,(x/L) + 1.68\,(x/L)^2 - 0.44\,(x/L)^3 + 0.04\,(x/L)^4 \quad (5.1)$$

$$z^+ = 0.15 - 1.84\,(x/L) + 0.24\,(x/L)^2 + 0.70\,(x/L)^3 - 0.21\,(x/L)^4 \quad (5.2)$$

It was observed that for both the uniform and bimodal bed cases, the equations (5.1) and (5.2) are of fourth-order polynomial. Additionally, the profiles of Runs 1 and 2 are quite different from that of Runs 3 and 4. This is due to the differences in the sediment beds. For uniform sediment beds, degraded zones after the maximum equilibrium depth of degradation were much wider than that of bimodal sediment beds. Notably, in the scour study downstream of an apron due to submerged horizontal jets, Dey and Sarkar (2006) observed that the scour profiles can essentially be represented by third-order polynomial which is different from the present cases. However, the difference is quite obvious as the present experimental setup is different from Dey and Sarkar (2006).

Furthermore, due to the bed degradation, the initial flow parameters like slopes of the bed and flow depths were changed. It was therefore required to measure the Froude, Shields and Reynolds numbers again at the downstream end where uniform bed was reformed to get the final values of uniform slope, Froude number, Reynolds number, shear velocity, etc. The final values of the experimental parameters are given below in Table 2. In the Table 2, L_f represents the location of the streamwise distance from where the degradation was initiated to the distance where the uniform bed slope was started at far downstream the degraded depth.

Table 5.2:

Final experimental parameters (measured at a location of uniform slope) after achieving the equilibrium condition

Run	L_f (m)	h_f (m)	S_f	$\bar{U}_f$ (m/s)	k_s (m)	u_{*f} (m/s)	u_{*c} (m/s)	F_f	R_f
1	3.2	0.125	0.00063	0.40	0.0022	0.026	0.027	0.38	184000
2	3.5	0.113	0.00056	0.42	0.0025	0.024	0.027	0.40	188160
3	1.25	0.133	0.00099	0.58	0.0020	0.034	0.035	0.51	308560
4	1.87	0.118	0.00125	0.60	0.0022	0.035	0.035	0.56	283200

Note: In the above, u_{*f} is the shear velocity calculated from the bed slope after the degradation took place. The subscript *f* in Table 2 refers to the final values after achieving the equilibrium conditions.

Literature also suggests that the bed roughness has significant effect on bed degradation. To understand the bed roughness, the equivalent roughness of the bed (k_s) was estimated from the time-averaged streamwise velocity distributions. To this end, the equations of time-averaged streamwise velocities were used which are given as follows:

$$\frac{u}{u_*} = \frac{1}{\kappa} ln\left(\frac{z}{z_0}\right), \tag{5.3}$$

where $z_0 = k_s/30$ for $R_* \geq 70$ and $z_0 = 0.11(\upsilon/u_*) + (k_s/30)$ for $5 < R_* < 70$, κ is the von kármán constant = 0.41. In the equation, u_* was calculated from the slope, u value was taken from the section where the uniform bed-slope was restored, and k_s was calculated from the Eq. (5.3). The values of k_s for Runs 1–4 are shown in Table 2 along with other

parameters. The Data plots of time-averaged streamwise velocity distributions for Run 1–4 overlapping on theoretical curve obtained from Eq. (5.3) were shown in Figure 5.2 below. It is pertinent to mention here that the k_s-values can be estimated more accurately by using statistical analysis of the bed topography (Penna et al. 2022).

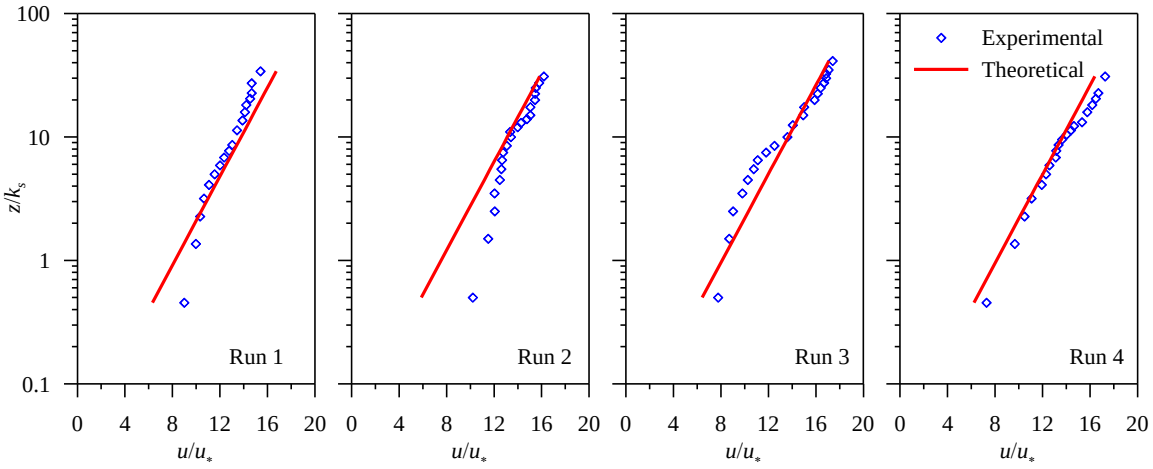

Figure 5. 5: Data plots of time-averaged streamwise velocity distributions at L_f = 3.2, 3.5,1.25, and 1.87 m for Run 1, 2, 3, 4 and overlapping on theoretical curve obtained from Equation (5.3).

5.3 Physics of the flow through degraded channel bed

5.3.1. Velocity vector field

Figure 5.6 presents the spatial distribution of the velocity vector in the (x, z) plane for flow over a degraded channel bed at sections I, II, and III for Runs 1–4. The magnitudes and directions of the velocity vectors were calculated by $\widehat{U} = (\overline{u}^2 + \overline{w}^2)^{0.5}/\overline{U}$ and arctan $\overline{w}/\overline{u}$, respectively, where $\widehat{U}$ is the normalized resultant velocity obtained from the time-averaged streamwise and vertical velocity components $\overline{u}$ and $\overline{w}$, respectively. The vector plots indicated that irrespective of the streamwise locations x/L, $\widehat{U}$ starts with a small value in the vicinity of the bed which goes on increasing with increase in the vertical distance until it becomes almost invariant with depth signifying the depth-averaged velocity $\overline{U}$. Above $z^+ = 0$, the profiles of $\widehat{U}$ are almost similar at different

sections for a run except small differences in their values. Below $z^+ = 0$, considerable differences in the values of $\widehat{U}$ were observed. The smaller values of $\widehat{U}$ in the near-bed indicate that the maximum retardation in the streamwise velocity took place at the upstream side of the maximum equilibrium depth of degradation. This is in conformity with the findings of Jain et al. (2015).

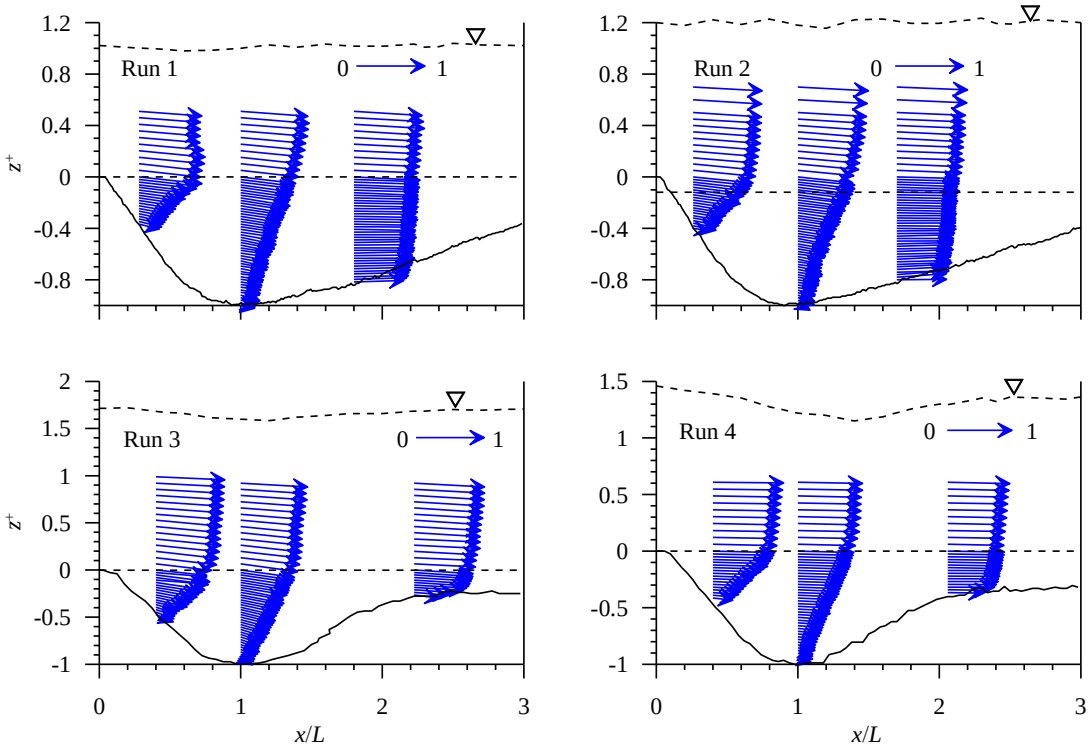

Figure 5.6: Spatial distributions of velocity vectors for flow over a degraded channel bed for Runs 1–4.

The $\widehat{U}$-values change more rapidly within the degraded bed than that above the bed-level. It can therefore be concluded that the bed degradation has a considerable impact on the velocity particularly below the initial bed-level. So far, no significant differences in the velocity vectors were observed for different experimental runs. The results therefore indicate that the similar velocity vectors are valid for bimodal and uniform degraded beds. However, the details of the streamwise velocity over a degraded bed were described in Sarkar et al. (2021).

5.3.2 Turbulence indicator

The average turbulence intensity I_{av}, also known as turbulence indicator was measured based on the experimental data to quantify the local turbulence level. Mathematically, it is expressed as $I_{av} = (2k/3)^{0.5}/\bar{U}_1$, where k is the turbulent kinetic energy (TKE) [$= 0.5(\overline{u'u'} + \overline{v'v'} + \overline{w'w'})$]; and $\overline{u'u'}$, $\overline{v'v'}$, $\overline{w'w'}$ are the Reynolds normal stresses relative to ρ in streamwise, spanwise and vertical directions, respectively, and $\bar{U}_1$ represents the local time-averaged resultant velocity calculated from three-dimensional velocity components as $[(\bar{u}^2 + \bar{v}^2 + \bar{w}^2)^{0.5}]$, where $\bar{v}$ is the time-averaged lateral velocity component. The I_{av} is a useful parameter that was introduced to describe turbulence in pipe flow, where the ranges I_{av} = 0.05–0.2, 0.01–0.05 and <0.01 represent the high-, medium-, and low-turbulence, respectively (Russo and Basse 2016, Dey and Sarkar 2020). However, it was later used by Sarkar and Dey (2020) to quantify the local turbulence for flow downstream of a dunal bedform, by Penna et al. (2022), etc. to describe the local turbulence over a water-worked gravel-bed, and Rathore et al. (2022) for open-channel flow subjected to a sudden change from smooth to rough bed, etc.

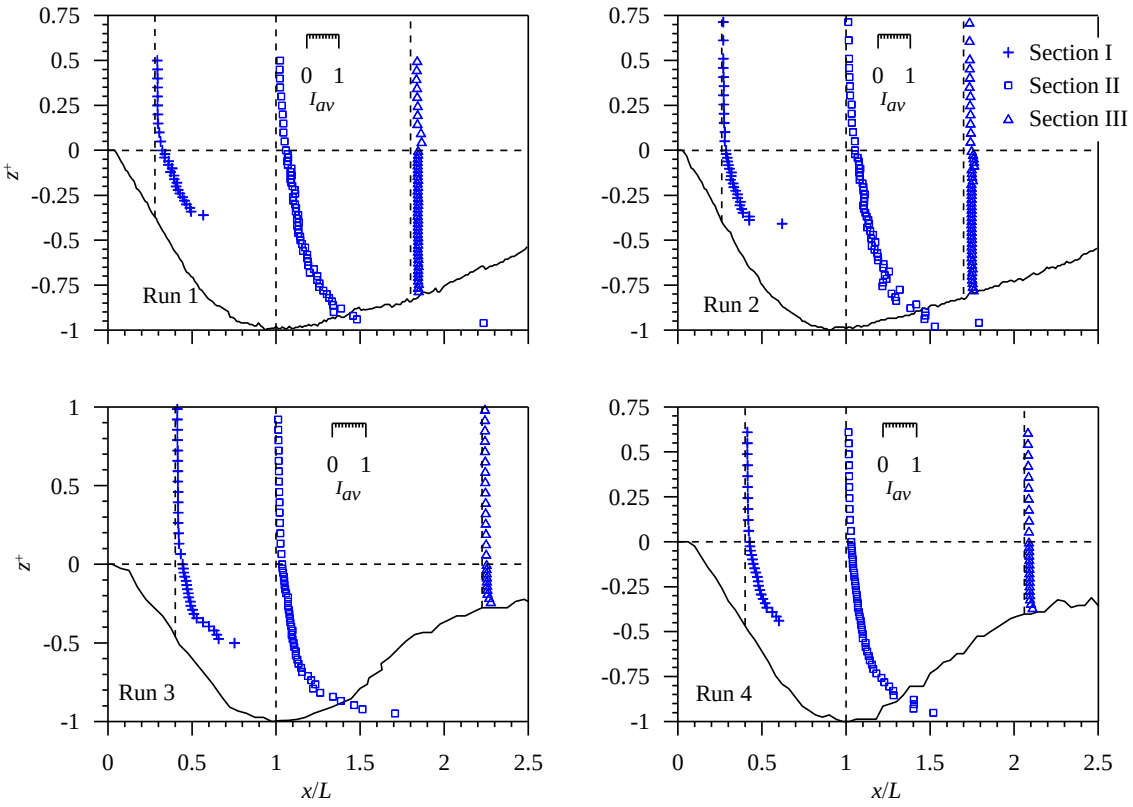

Figure 5.7: Vertical profiles of the time-averaged turbulence indicator I_{av} for flow over a degraded channel bed at Section I, II and III for Runs 1–4.

Figure 5.7 shows the vertical profiles of the time-averaged turbulence indicator I_{av} at sections I, II and III over a degraded bed for Runs 1–4. From Figure 5.7, it was observed that below the bed-level ($z^+ = 0$), the turbulence level is very high which continues up to a very little distance over the bed. However, above $z^+ \approx 0$, the I_{av} decreases quite significantly indicating a medium to low-level of local turbulence for all the sections and both the runs. Although not so significant, some differences were found in the values of I_{av} that are quite obvious because of the differences in the flow and sediment parameters. In this context, it be concluded that the bed degradation can increase the local turbulence behavior of a sedimentary bed.

5.4 Turbulent Length Scales

The turbulent length scale is a physical parameter that describes the size of large energy-containing eddies present in a fluid flow. These eddies are of different sizes that vary continuously from the largest scale to the smallest one. The largest size of the eddies is known as integral length scale that can be estimated from the correlation functions or energy spectra and the smaller eddies can be determined by the fluid viscosity regarded as the Taylor microscale and the Kolmogorov length scale. According to the literature reviewed, these scales have significant impact on turbulence and they depend on types of the experimental setup and bed topography, etc. However, their effects on degraded bed were not verified and so, based on the present experimental data, they were presented below.

5.4.1 Correlation Length (Integral length scale)

The size of the biggest eddies in a turbulent flow is determined by the correlation length of the velocity components. There are several methods to estimate the correlation length of turbulence (Ferraro et al. 2016, Matzler 2017, Trush et al. 2022). However, calculation based on the correlation function which is one of the most sophisticated and accurate methods of calculating the correlation length was used in the present study following Ferraro et al. (2016) and Penna et al. (2020). To do so, the autocorrelation functions were calculated using the formula: $R(x,\Delta t) = \overline{u'(x,t+\Delta t)u'(x,t)}$, where x is a point of location on the *xz* plane, u' is the temporal velocity fluctuation in the streamwise direction, and t is time. With the transformation from time lag to spatial increment i.e., $R(x, \Delta t) \rightarrow R(x, r)$, in the case of statistical convergence, it is possible to define the correlation length as:

$$\Lambda(x, r) = \frac{1}{R(x,0)} \int_0^\infty R(x,r)\, dr, \tag{5.4}$$

where r is the spatial increment obtained by applying the Taylor hypothesis $r(x,z) = |\bar{u}\,(x,z)|\Delta t$ and Δt = time lag.

It is important to mention here that such a transformation requires a validation checkup using the condition, ψ (k, z^+) [$= 2\pi\sqrt{k\langle E(k,z)\rangle}/\langle\bar{u}(z)\rangle$] <<1, where ψ is the Taylor coefficient, and $E(k, z)$ is the energy spectra with respect to wave number k. The details of the procedure were explained in Ferraro et al. (2016), Penna et al. (2020) and Sarkar et al. (2021). Figure 5.8(a–d) given below presents the validation of the Taylor hypothesis tested at different vertical locations of section II for Runs 1–4 data set.

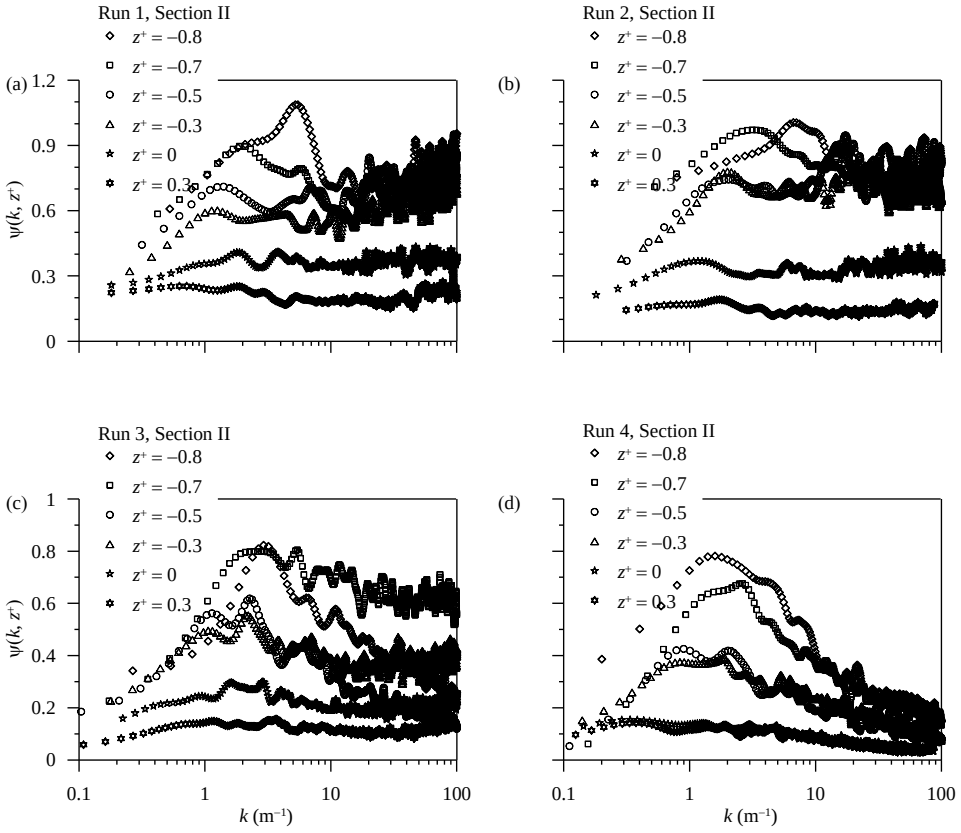

Figure 5.8: Taylor coefficient $\psi(k, z^+)$ (using Taylor hypothesis) at different vertical distances over a degraded channel bed at Section II for (a) Run 1, (b) Run 2, (c) Run 3, and (d) Run 4.

Now, while estimating the correlation length, there are several methods available in the literature to choose the truncation point for the integration of eq. (4). For instance, according to Trush et al. (2022), if the autocorrelation function has a negative region, the integration can be done: (i) over the entire available domain, or (ii) only up to the value

where the autocorrelation function is a minimum, or (iii) up to the first zero-crossing, namely zero-crossing method. However, for the present experimental data, the zero-crossing method was applied and the first zero-crossing was observed nearly within time lag 0.5 s for most of the present experimental data sets.

The vertical distribution of normalized correlation length Λ/d_{50} for Runs 1–4 are shown in Figure 5.9. The general observation from Figure 5.9 is that irrespective of the experimental runs, Λ/d_{50} starts with a smaller value in the vicinity of the bed which goes on increasing with increase in the vertical distance. However, the rate of increasing in the values Λ/d_{50} with respect to vertical distance is lower above than below the undisturbed bed level. Interestingly, towards the free-surface the Λ/d_{50}-profile attains a nearly asymptotic nature and increases quite slowly. In addition, in the vicinity of the maximum equilibrium degraded depth (Section II), the Λ/d_{50} falls significantly for all the runs. The vertical distributions of the autocorrelation length can be described by using a third-order polynomial irrespective of the experimental conditions. For the data set of Run 1, the normalized correlation length may be calculated by using the equation:

$$z^+ = 0.0000045(\Lambda/d_{50})^3 - 0.00049(\Lambda/d_{50})^2 + 0.0312(\Lambda/d_{50}) - 1.035, \text{ with } R^2 = 0.85 \quad (5)$$

and that of Run 2 may be described by another third-order polynomial equation:

$$z^+ = 0.0000015(\Lambda/d_{50})^3 - 0.00012(\Lambda/d_{50})^2 + 0.0157(\Lambda/d_{50}) - 0.893, \text{ with } R^2 = 0.91 \quad (6)$$

However, when data were considered for both the experimental Runs 1 and 2, they can be described further by using another third-order polynomial equation:

$$z^+ = 0.0000014(\Lambda/d_{50})^3 - 0.00012(\Lambda/d_{50})^2 + 0.018(\Lambda/d_{50}) - 0.921, \text{ with } R^2 = 0.86 \quad (7)$$

On the other hand, the normalized correlation length for Run 3 may be calculated by using the equation:

$$z^+ = 0.000055(\Lambda/d_{50})^3 - 0.0037(\Lambda/d_{50})^2 + 0.095(\Lambda/d_{50}) - 1.209, \text{ with } R^2 = 0.86 \quad (8)$$

and the normalized correlation length for Run 2 may be calculated by using the equation:

$$z^+ = 0.000032(\Lambda/d_{50})^3 - 0.0024(\Lambda/d_{50})^2 + 0.071(\Lambda/d_{50}) - 1.067, \text{ with } R^2 = 0.89 \quad (9)$$

Runs 3 and 4 can be described by another third-order polynomial equation:

$$z^+ = 0.000032(\Lambda/d_{50})^3 - 0.0022(\Lambda/d_{50})^2 + 0.067(\Lambda/d_{50}) - 1.067, \text{ with } R^2 = 0.84 \quad (10)$$

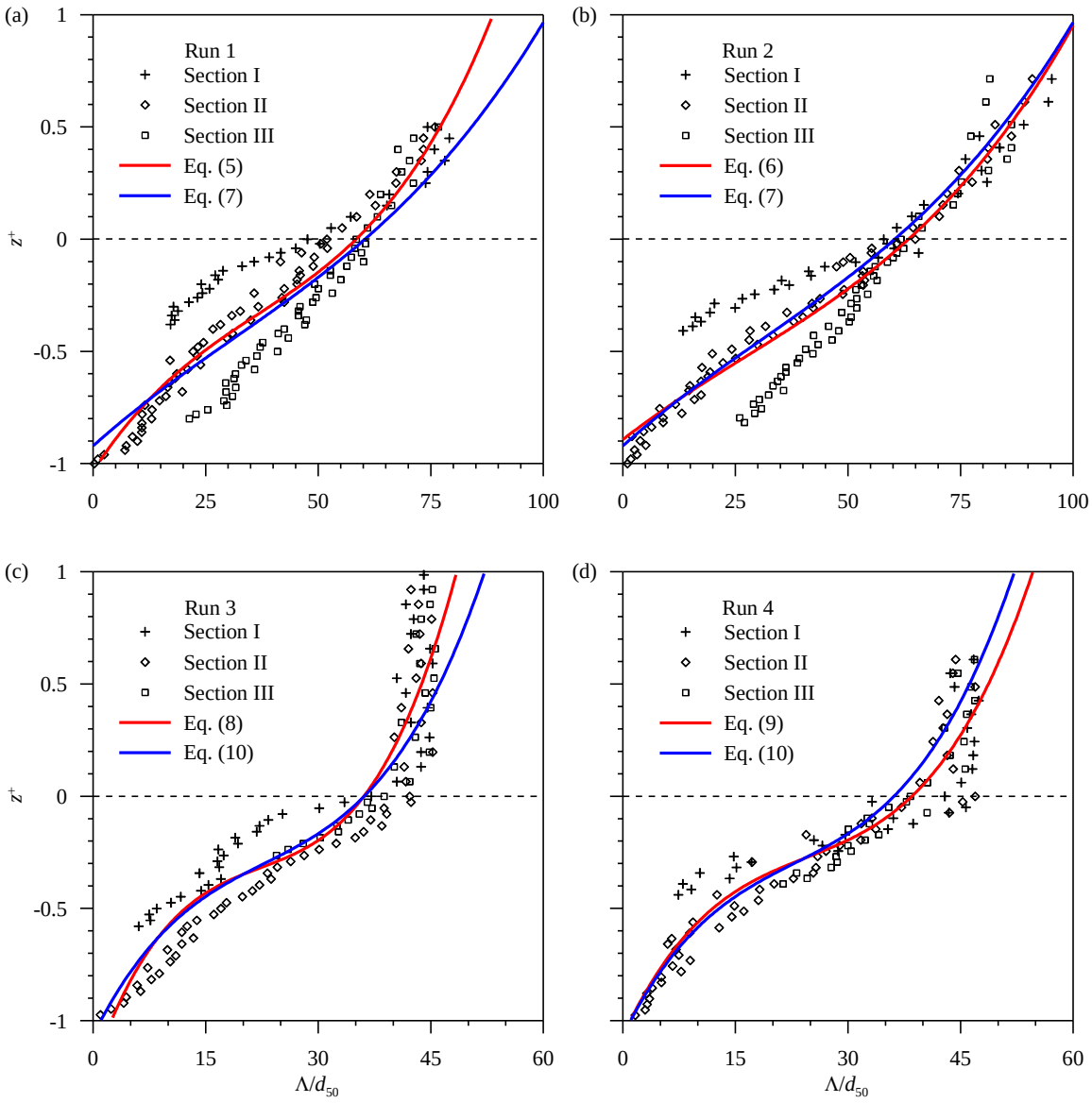

Figure 5.9: Vertical profiles of the normalized energy-containing scale.

The observation of the present study is in good agreement with Penna et al. (2020), who observed that towards the free surface, the correlation length remains almost constant. Beyond $z^+ \approx 0.5$, it remains almost constant where $\Lambda \approx 0.08$ for Runs 1 and 2, and $\Lambda \approx 0.09$ m for Runs 3 and 4, that can be taken as the critical value of the correlation length Λ_c (measured at the vertical distance from and above which the value of Λ remains almost constant). The present profile is also in confirmation with Sukhodolov et al.

(1998) who observed a growth of scales towards the free surface for natural rivers. It is important to mention here that for Runs 3 and 4, the length scales were nondimensionalised by the diameter of the coarser sediment based on the idea that within the degraded bed zone, the bed-surface was dominated by the coarser particles due to armoring effect. It was also observed from Figures. 5.9(a–d) that the rate of increasing of the Λ/d_{50}-values are quite faster (varying almost linearly with depth) in case of uniform sediment degraded beds than that of the bimodal sediment bed.

In this context, it is important to add that Ferraro et al. (2016) observed the value of Λ_c is approximately equal to the average size of pebbles used in the laboratory experiments. However, based on their results and comparing them with the literature, Ferraro et al. (2016) concluded that the integral scales of turbulence in rivers may be as large as the flow depth. From the results of present experiments, it was therefore re-verified that the value of Λ_c may be different due to differences in the bed topography and flow conditions. Based on the present data, it can further be concluded that bed degradation takes active role in lowering the Integral length scale quite significantly. Also, below the bed-level, the distributions of Λ/d_{50} are almost similar which indicates that, correlation lengths follow similar trends within the degraded depth.

5.4.2 Taylor microscale

Taylor microscale is the intermediate length scale used to characterize the turbulent fluid flow at which viscosity significantly affects to the dynamics of turbulent eddies. Taylor microscale λ defines a typical eddy size in the inertial subrange and is the relevant length scale of turbulence. It is calculated by using the following formula:

$$\lambda = \left(\frac{15\upsilon\sigma_u}{\varepsilon}\right)^{0.5}, \tag{5.11}$$

where σ_u is the streamwise Reynolds normal stress divided by ρ, that is $\overline{u'u'}$, and ε is the TKE dissipation rate. The ε-distributions are obtained from the relationship used by Irwin (1973) and Krogstad and Antonia (1999) and also adopted by Kurien and Srinivasan (2000) as:

$$\varepsilon = (15\upsilon/u^2)\overline{(\partial u'/\partial t)^2}\,, \tag{5.12}$$

The vertical distributions of normalised Taylor microscale were shown in Figures. 5.10(a), 5.10(c), 5.10(e), and 5.10(g) for Runs 1, and 2, 3, and 4 respectively. It was observed from Figures. 5.10(a), 5.10(c), 5.10(e), and 5.10(g) that λ/d_{50} starts with a smaller value that goes on increasing with an increase in vertical distance. However, the rate of change of increasing is much higher below the bed-level than that above the bed level and at $z^+ > 0.3$, it becomes almost invariant with vertical distances. Importantly, below the bed-level, the Taylor microscale attains the lowest value at Section I at $z^+ \approx -0.5$ than that of Sections II and III, which attains higher values as one moves towards downstream achieving the highest value at the furthest downstream. It was therefore concluded that the Taylor microscale values get significantly affected where the bed degradation initiates and starts increasing with increase in the streamwise distance. In addition, within the degraded bed, their rate of decreasing is more than that above the bed-level.

5.4.3 Kolmogorov length scale

In an energy cascade process, the viscosity dominates within the dissipation range and the TKE is dissipated into heat at the smallest length scale. Kolmogorov microscale is used to determine the size of the smallest eddies which can be estimated from the TKE dissipation rates. Mathematically, it is expressed as:

$$\eta = (\upsilon^3 / \varepsilon)^{0.25} \tag{5.13}$$

Figures 5.10(b), 5.10(d), 5.10(f), and 5.10(h) show the vertical distributions of normalized Kolmogorov length scale η/d_{50} at different sections over the degraded bed for Runs 1, 2, 3, and 4, respectively. In principle, there was no significant differences between the Taylor and Kolmogorov length scales, except the ranges of the values which was approximately 1/20 times of that of the values of Taylor microscale. It was observed that Integral length scales become invariant above the bed level, but Taylor microscale and Kolmogorov length scales increase linearly above the bed level (only their growth rate is invariant). The profiles of Taylor microscale and Kolmogorov length scale above the bed-level are in confirmation with the findings of Sarkar and Dey (2015), and Sarkar et al. (2016), for flow downstream of a sphere, and flow past a protruding array, etc.

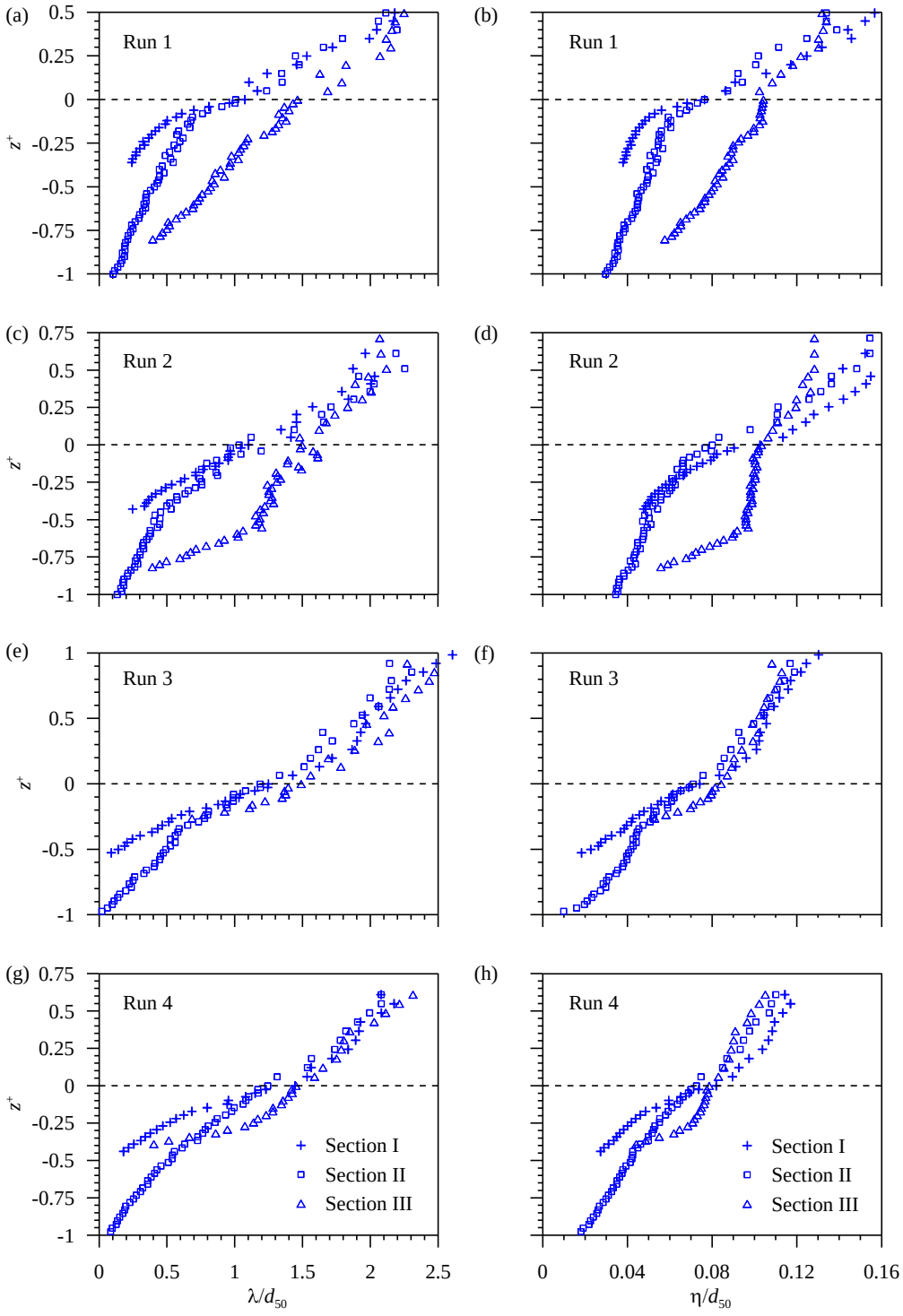
(a)
Run 1
(b)
Run 1
(c)
Run 2
(d)
Run 2
(e)
Run 3
(f)
Run 3
(g)
Run 4
(h)
Run 4
z^+
Section I
Section II
Section III
λ/d_{50}
η/d_{50}

Figure 5.10: Vertical profiles of the normalized Taylor microscale λ/d_{50}), and Kolmogorov length scale η/d_{50}: (a–b) for Run 1, (c–d) for Run 2, (e–f) for Run 3 and (g–h) for Run 4, respectively.

It is very clear that in the present case below $z^+ = 0$, the vertical distances at Section II behave like the downstream of a bluff body which is responsible for the Kolmogorov length scales to be sufficiently lower. However, above the bed-level there may be little changes in the values that are due to measurement limitations only. However, no significant changes were found for Run 3 and Run 4 data with respect to the Taylor and Kolmogorov length scales. On the contrary, for Runs 1 and 2, the trend is almost similar with Runs 3 and 4 but the differences of the values of Section I, II and III are more prominent in case of uniform sediment beds. The possible reason for that, the locations in the streamwise distances are different for the experimental run and the uniform beds are more affected by the degradation than that for bimodal bed. However, the differences in the values of η/d_{50} and λ/d_{50} are affected by the nondimensionalising of the length scales. Therefore, a direct comparison between bimodal and uniform degraded beds is not possible.

5.5 High-order structure functions

The main findings of the present paper are discussed in this section. Scaling exponents based on single-component and higher order mixed structure functions were illustrated here. However, validation of the Taylor hypothesis was examined before using it at different vertical distances as was shown in Figure 5.8.

The general equation of structure functions of any order n for a single-component of velocity u can be defined by the equation:

$$S_n(\mathbf{r}) = \langle (u(\mathbf{x} + \mathbf{r}) - u(\mathbf{x})) \rangle^n, \tag{5.14}$$

for any positive value of n, $\mathbf{x}$, $\mathbf{x} + \mathbf{r}$ are points in a turbulent flow field, u is the component of the velocity in the direction of $\mathbf{r}$, r is the length $|\mathbf{r}|$ of $\mathbf{r}$ called the separation distance between two measuring locations, and the angle brackets denote an average (Arenas and Chorin 2006). In calculating the structure functions, the spatial

increment was estimated from the time lag using the Taylor hypothesis that was explained earlier section.

5.6 Determination of scaling exponents and estimation of the intermittency

One of the most interesting features in the study of fully developed turbulent flow is its statistical property like intermittency. To this end, the data were analyzed for higher order structure functions $S_n(r)$ up to eighth-order using equation (5.14) for streamwise component for Runs 1–4 data sets.

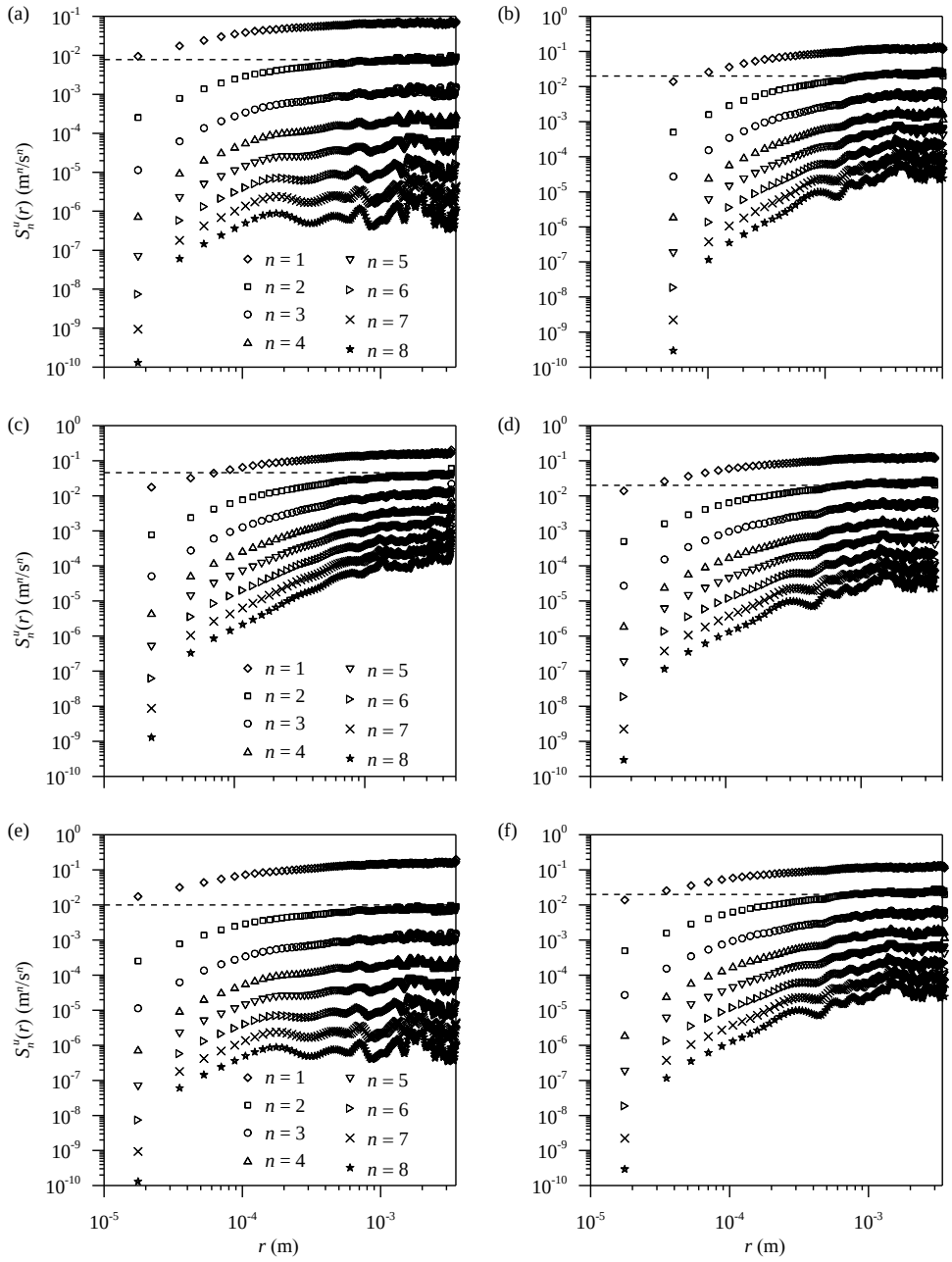

Figure 5.11: Streamwise structure functions upto eighth-order vs. spatial distance r at z^+ = –0.8, –0.7, –0.5, –0.3, 0 and 0.3 for Run 3 data. The dotted lines indicate the saturation level in the second-order structure function.

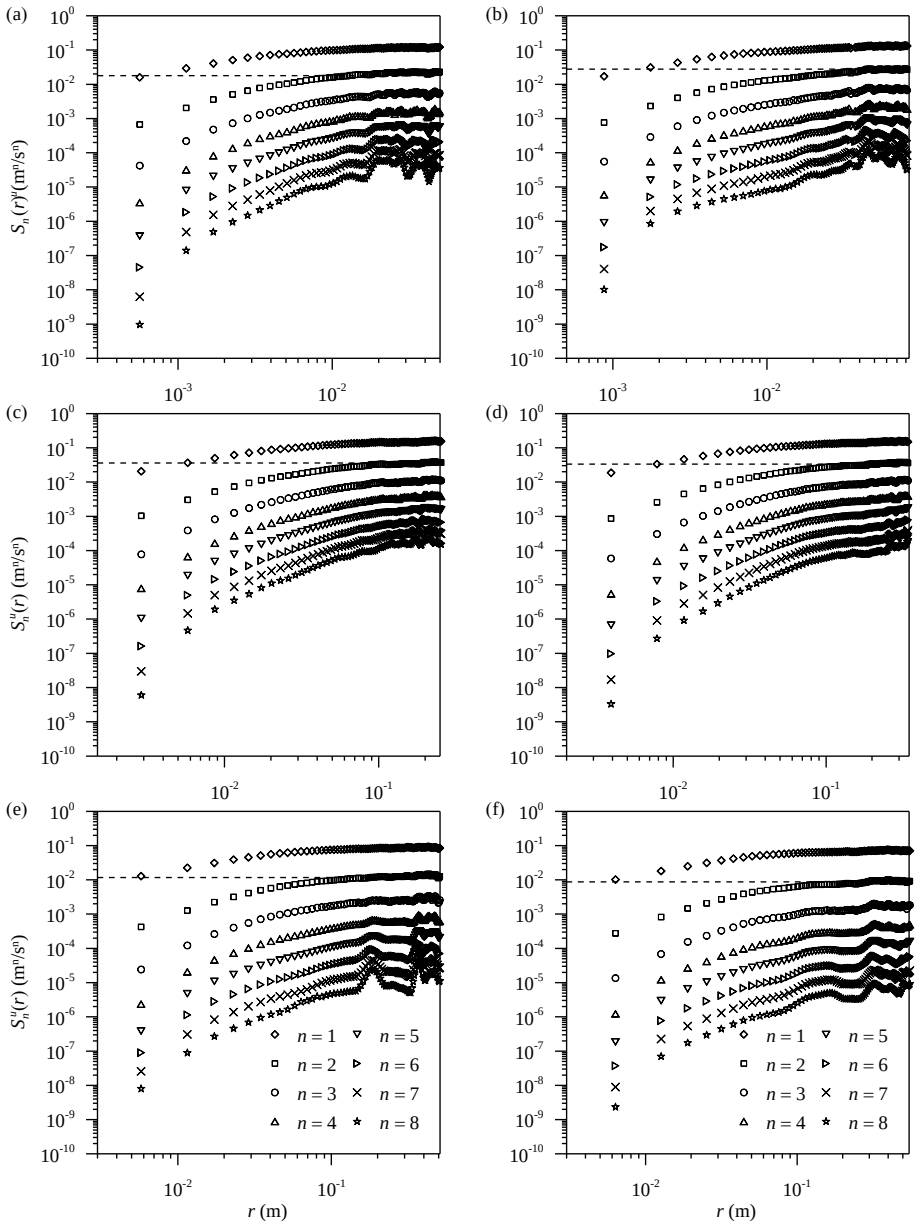

Figure 5.12. Streamwise structure functions upto eighth-order vs spatial distance r at z^+ = –0.8, –0.7, –0.5, –0.3, 0 and 0 for Run 4 data. The dotted lines indicate the saturation level in the second-order structure function.

The $S_n(r)$ vs. r results for the vertical distances z^+ = –0.8, –0.7, –0.5, –0.3, 0 and 0.3 of Section II were shown in Figures 5.11 and 5.12 for Runs 3 and 4, respectively. It was

evident from Figures. 5.11 and 5.12 that all the structure functions possess three distinct regions namely scaling, transition, and saturation. The scaling region exists within small values of r, after that the saturation region exists where the value of $S_n(r)$ is approximately constant [$S_n(r)$~ constant] and this region exists after a fixed value of r, which indicates about the inertial sub range, between this two regions transition region exists. Actually, transition region represents the lower and upper boundaries between saturation and scaling regions.

A careful observation also shows the influence of the bed degradation in the inertial subrange irrespective of the experimental runs. In the vicinity of the maximum equilibrium depth of degradation i.e., $z^+ = -0.8$, the range of r values for inertial subrange was quite narrow, that goes on increasing with increase in the vertical distance until it becomes invariant with respect to vertical distance nearly $z^+ = 0$. The findings confirm a narrowing of the inertial subrange due to the bed degradation. The Figures 5.11 – 5.12 also suggest that as the order of structure functions and the separation distance r increase, the structure functions data contain some fluctuations irrespective of the locations. Above $z^+ = 0$, the similar findings were observed for Section I and III which suggest that the influence of the bed degradation is predominating in the vicinity of the degraded bed only and above the bed-level they are almost similar with a little changes in their values. It is important to mention here that the structure functions up to eighth-order for Run 3 and 4 shown here for presentation purpose. The same methodology was used for Runs 1 and 2 data also and the similar observations are valid for them.

5.7 Extended Self-Similarity (ESS)

Since the pioneering work of Kolmogorov for structure functions, it has been used and extended by many researchers. Later, it was observed that the values of scaling exponents ζ_n deviates substantially from the predictions of K41 at higher order structure functions in many occasions. The main reason for the anomaly was due to the fact that Kolmogorov's theory of turbulence was based on the homogeneous and isotropic turbulence which can be changed depending on the flow parameters. However, to overcome the anomalies and to estimate the scaling exponents more accurately, the

concept of *extended self-similarity* (ESS) was introduced. In principle, it states that the scaling exponent for any order of structure functions data is more prominent once it is plotted against another one.

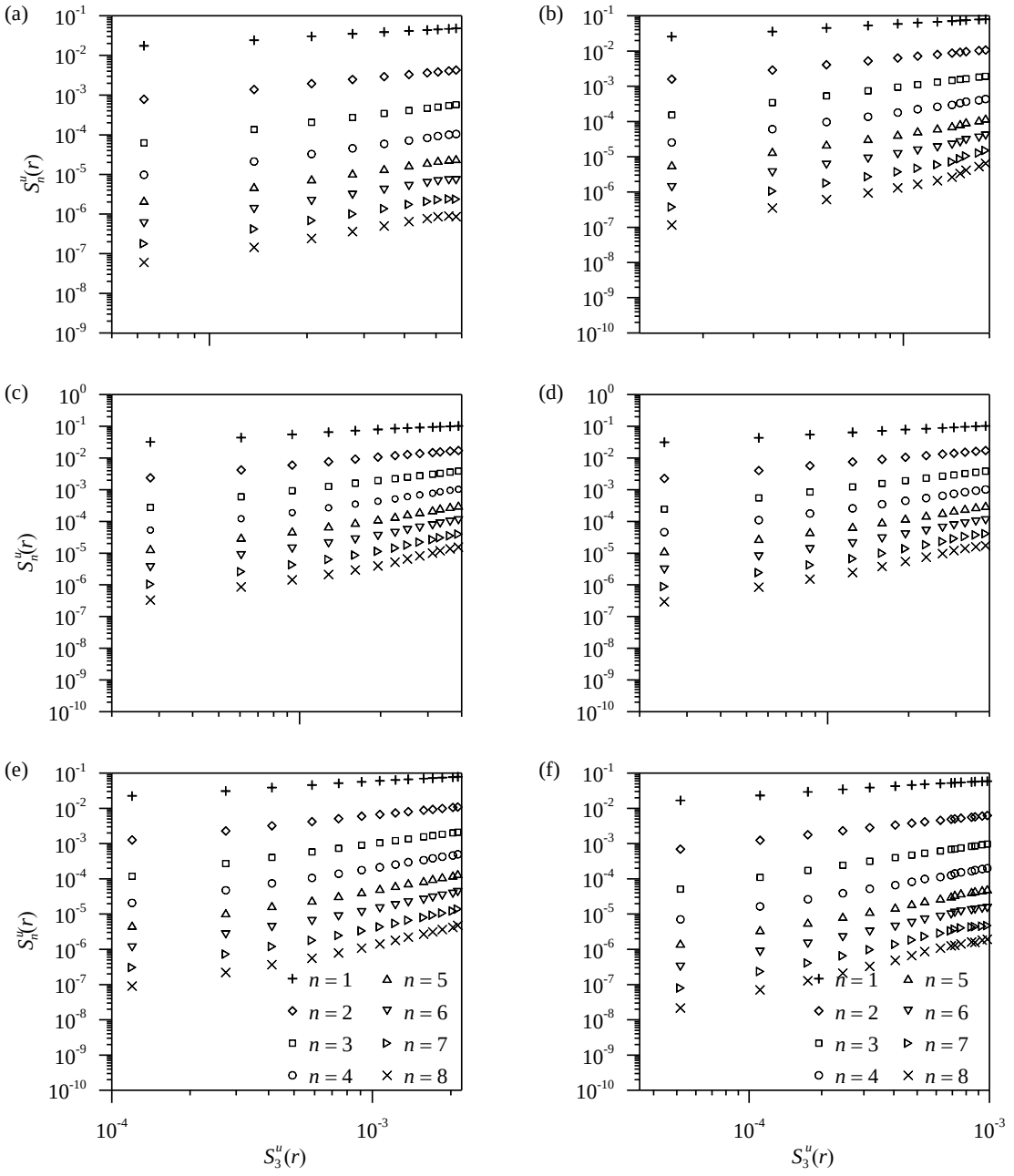

Figure 5.13: Structure functions of order 1 to 8 as a function of third-order structure functions at (a) $z^+ = -0.8$, (b) $z^+ = -0.7$, (c) $z^+ = -0.5$, (d) $z^+ = -0.3$, (e) $z^+ = 0$ and (f) $z^+ = 0.3$ for Run 3.

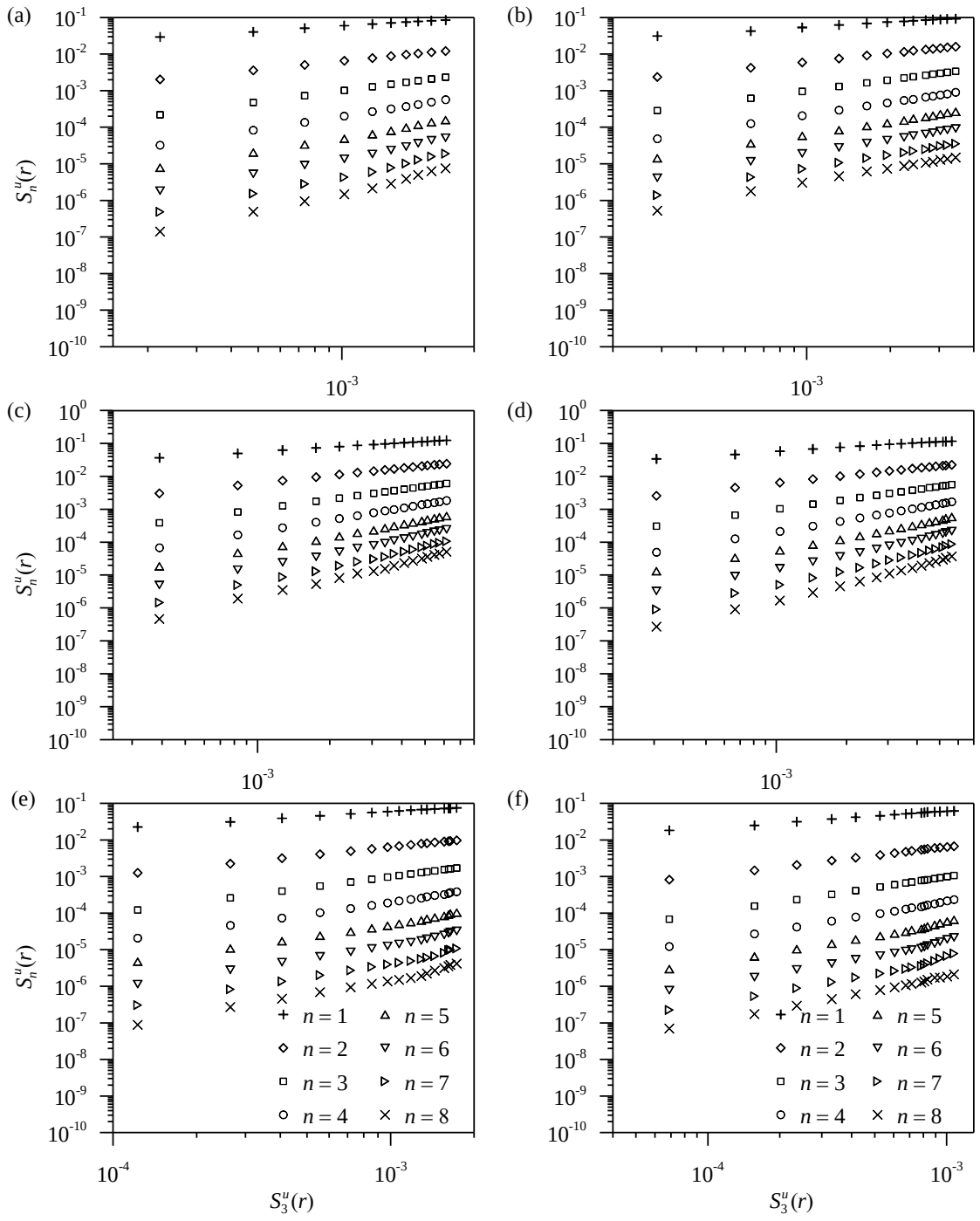

Figure 5.14: Structure functions of order 1 to 8 as a function of third-order structure functions at (a) $z^+ = -0.8$, (b) $z^+ = -0.7$, (c) $z^+ = -0.5$, (d) $z^+ = -0.3$, (e) $z^+ = 0$ and (f) $z^+ = 0.3$ for Run 4.

Mathematically, ESS is presented by the equation given by Protas et al. (1996) as:

$$S_n(r) \sim S_m(r)^{\bar{\zeta}_{m,n}}, \bar{\zeta}_{m,n} = \frac{\zeta_n}{\zeta_m} \tag{5.15}$$

where $\bar{\zeta}_{m,n}$ is the relative scaling exponents of any order n (i.e., ζ_n) with respect to a particular order m (i.e., ζ_m).

It is important to mention that for ESS, the exact exponent $\zeta_3 = 1$,for $n = 3$ was considered according to Kolmogorov (1941) and the others order structure functions can be comparatively executed from $S_3(r)$ i.e. $S_n(r) \sim S_3(r)^{\zeta n}$ as shown above in Figures 5.13 and 5.14.

Figures. 5.13 and 5.14 illustrate the structure functions of order 1 to 8 as a function of third-order structure functions for the vertical distances $z^+ = –0.8, –0.7, –0.5, –0.3, 0$ and 0.3 at Section II for Runs 3 and 4, respectively. All the plots indicate that there exists a range of data within which the ratios of the structure functions hold with same exponents indicating extended self-similarity. Interestingly, the number of data obeying the ESS was less in the vicinity of the degraded bed which increases as one moves vertically upward. It is important to mention here that only the graphical presentations for Section II are presented here, although the same was performed for Section I and III as well. Notably, the same methodology was applied for the data sets of Runs 1 and 2, and they were used for further processing of the scaling exponents. To avoid the repetition of the similar plots, all of them were not shown here.

Using the ESS methodology, the streamwise and vertical scaling exponents ζ_n^u and ζ_n^w were estimated from higher order structure functions and compared with the theoretical values of K41 for different vertical distances of Section I, II and III as shown in Figure 5.15. Although no significant changes were noticed between the profiles of streamwise scaling exponents of Run 3 and Run 4, both of them certainly deviate from the theoretical values of K41 at higher order of structure functions indicating intermittency. Interestingly, scaling exponents of Run 3 data have slightly lesser values than that of scaling exponents of Run 4 irrespective of the order and location of measurement. This may be due to the differences in the experimental parameters and nondimensionalisation of the depth of degradation. Moreover, it was clear from the scaling exponents of both

Run 3 and Run 4 at different vertical locations that the flow zone in the vicinity of the degraded bed was more intermittent than that above the bed-level, which was similar to the findings of Coscarella et al. (2020) who found that in the near-bed region of rough bed, the flow was more intermittent which lessens as one moves vertically upward. In addition, other turbulence parameters like turbulence indicators, velocity vector and length scales, etc. also show that flow in the vicinity of the degraded bed are significantly different than rest of the flow depths. Interestingly, no significant changes were found at $z^+ \geq -0.3$ of Section I, II and III for Runs 3 and 4 that indicates the intermittency is more predominating in the vicinity of the degraded bed and lessens as one moves vertically upward irrespective of the streamwise locations. It is important to mention here that the similar trends of ζ_n^u values were observed for Runs 1 and 2 but due to the overlapping of data, they were not presented here. However, in Figure 5.16, their values were shown graphically for Section II considering that Section II gives the overall picture of the bed degradedness.

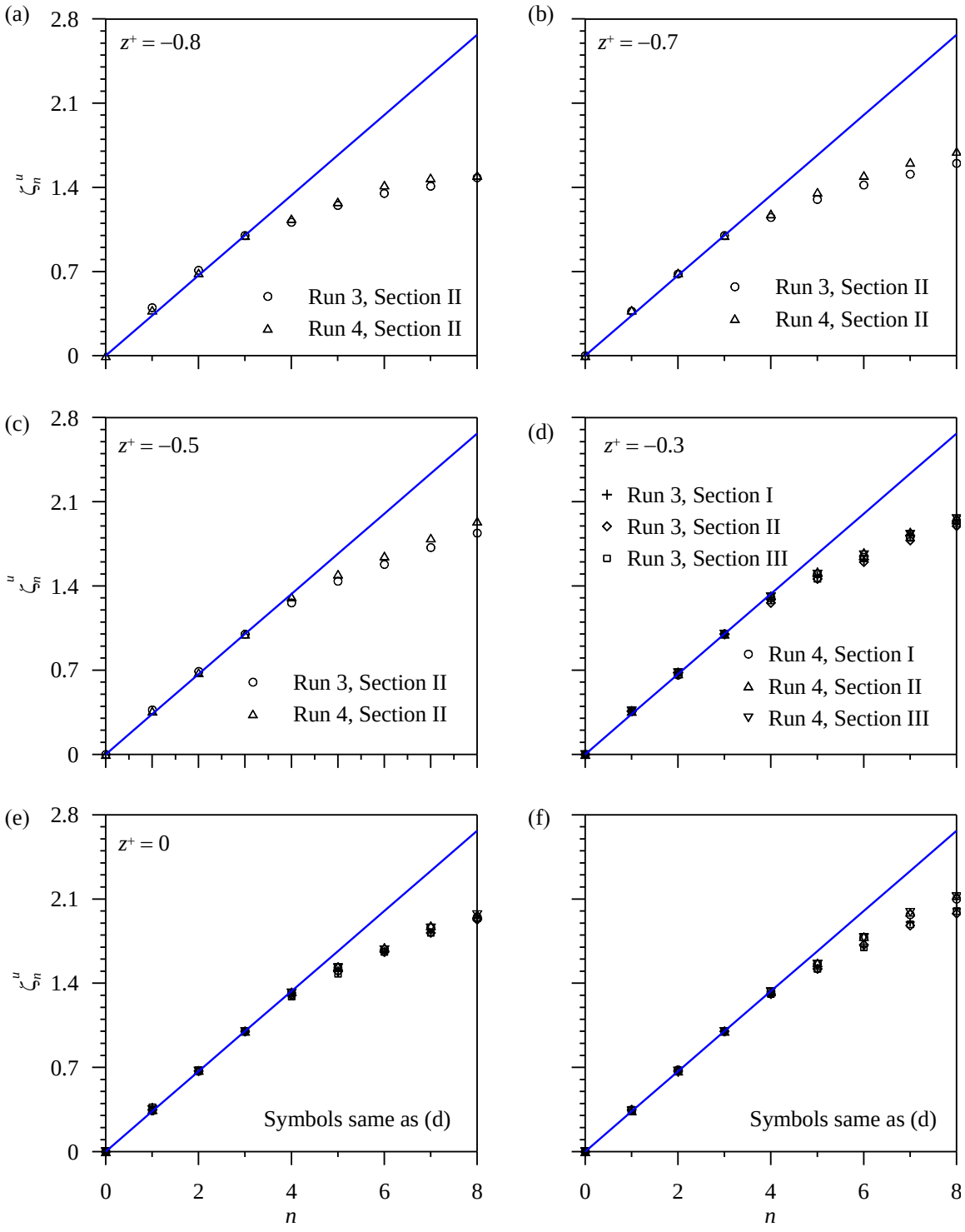

Figure 5.15: The values of Scaling exponents using ESS methodology with respect to order n at $z^+ = -0.8$, -0.7, -0.5, -0.3, 0 and 0.3 for Sections I, II, and III of Run 3 and Run 4. Blue solid line indicates scaling exponents based on Kolmogorov (1941).

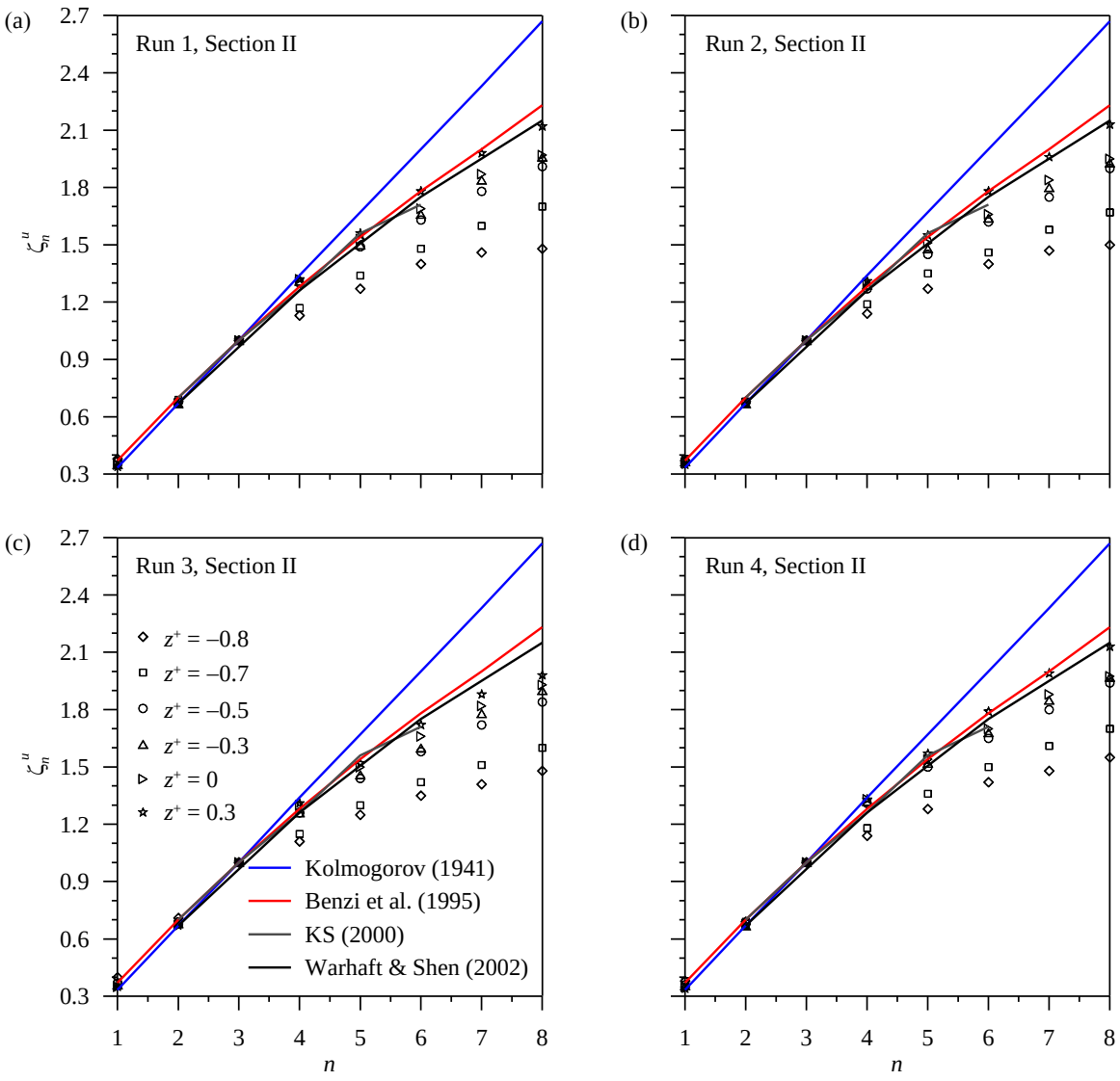

Figure 5.16: Streamwise scaling exponents with respect to order n at z^+ = –0.8, –0.7, –0.5, –0.3, 0 and 0.3 and their comparisons with literature for (a) Run 1, Section II, (b) Run 2, Section II, (c) Run 3, Section II, and (d) Run 4, Section II, data sets.

Figure 5.16(a–b) and 5.16(c–d) show the streamwise scaling exponents (ζ_n^u) with respect to order n at section II for Runs 1–2 and Runs 3–4, respectively and their comparisons with values observed by different researchers under different conditions. It was evident from Figure 5.16 that the values of ζ_n^u of the present study are quite different from those of K41, Benzi et al. (1995), Kurien and Sreenivasan (2000) and Warhaft and Shen

(2002). Particularly, the values of ζ_n^u of the present study within $z^+ \leq 0$ are lowest among all. It is important to mention here that K41 is based on the theoretical data calculated based on the dimensional analysis, wheres Benzi et al. (1995) estimated scaling exponents under a moderate and low Reynolds number flow conditions downstream of a cylinder and a jet. On the other hand, Kurien and Sreenivasan (2000) estimated the value based on wind flow data collected at high-Reynolds number turbulence, and Warhaft and Shen (2000) data were based on the wind-tunnel turbulence data generated by a variable solidity screen followed by flow straighteners at high-Reynolds number experiments with and without shear. It can therefore be concluded that the near-bed zone within the degraded bed shows a considerable intermittency, although intermittency was present throughout the depth. The findings of the present study was almost similar to that of Penna et al. (2021), who found that in the vicinity of the rough bed, the effect of intermittency was more which decreases with increase in the vertical distance and become almost invariant as one moves towards the free-surface. However, the technique used by Penna et al. (2022) was different from that of the present study which probably was responsible to get higher differences in the values of scaling exponents in Penna et al. (2022) than that of the present study. Penna et al. (2022) calculated Hurst exponent for the calculation of high-order scaling exponents. However, although no significant differences were observed in the ζ_n^u-profiles of Run 1–4, differences were obviously there in their values. Importantly, the differences are more prominent when they were compared with the values obtained from the literature.

One more difference between Penna et al. (2022) and the present study was due to the fact that due to committing the third-order structure functions as the standard one, in the present study no significant changes in the values of scaling exponents were noticed for $n \leq 3$.

In addition, the anomalous characteristics of the scaling exponents function can be parameterized as a polynomial given by Penna et al. (2022):

$$\zeta_n = (1/3 - C)\, n \tag{5.16}$$

where C represents the intermittency parameter. Multifractal characteristics is occurred if the parameter C is not equal to zero. Actually this intermittency parameter C is

responsible for the deviation of exponents from Kolmogorov (1941) predicted value (n/3) i.e., violate the self similar characteristics. However, values of C and R^2 for Runs 1–4 in the present study are given below in Table 3. At the maximum degraded region near the bed the parameter C is higher than those above the bed irrespective of the vertical and streamwise locations of the measurement and experimental runs. On the other hand, no significant changes in their values were noticed at $z^+ \geq 0.3$ confirming no major changes in the scaling exponents above the bed-level at different streamwise locations.

Table 3: The values of C and R^2 for Runs 1–4

	Run 1						Run 2					
z^+	Section I		Section II		Section III		Section I		Section II		Section III	
	C	R^2	C	R^2	C	R^2	C	R^2	C	R^2	C	R^2
–0.8			0.11	0.92					0.11	0.94		
–0.7			0.09	0.93					0.10	0.95		
–0.5			0.07	0.95					0.07	0.96		
–0.3	0.08	0.95	0.06	0.96	0.08	0.95	0.07	0.94	0.07	0.95	0.07	0.95
0	0.07	0.96	0.06	0.96	0.06	0.96	0.06	0.96	0.06	0.96	0.06	0.96
0.3	0.05	0.97	0.05	0.97	0.05	0.97	0.05	0.97	0.05	0.98	0.05	0.97

	Run 3						Run 4					
z^+	Section I		Section II		Section III		Section I		Section II		Section III	
	C	R^2	C	R^2	C	R^2	C	R^2	C	R^2	C	R^2
–0.8			0.11	0.92					0.10	0.94		
–0.7			0.10	0.92					0.09	0.94		
–0.5			0.04	0.93					0.06	0.95		
–0.3	0.06	0.95	0.07	0.95	0.06	0.92	0.06	0.95	0.06	0.96	0.06	0.93
0	0.06	0.95	0.06	0.95	0.06	0.94	0.06	0.95	0.05	0.97	0.06	0.94
0.3	0.05	0.96	0.05	0.96	0.05	0.94	0.04	0.96	0.04	0.98	0.04	0.95

5.8 High-order mixed structure functions

According to Arad et al. (1998); Kurien and Sreenivasan (2000); and Warhaft and Shen (2002); the experimentally measured structure functions are considered to be a mixture of the isotropic and higher order anisotropic parts. To obtain the scaling exponents for the anisotropic parts, mixed structure functions up to eighth-order was attempted here. The isotropic part was extracted by projecting the measured structure functions onto the

isotropic sector of the *SO*(3) decomposition (2002). Here, only the tensor components of structure functions that were explicitly zero in the isotropic sector were considered, so that their measurements derive their contribution entirely from the anisotropic sector. This method allowed us to examine anisotropic effect in structure function tensors of order two and above.

We adopted here the tensorial mixed n^{th}-order structure functions following Frisch (1995), Dhruva et al. (1997) and Arad et al. (1998) as:

$$S_n^{pq} = \langle [u(x+r) - u(x)]^p [w(x+r) - w(x)]^q \rangle, \tag{5.17}$$

where $n = p + q$ is the order of the structure functions, u and w are the velocity components in streamwise and vertical directions, r is the separation distance between the two positions where u and w measured, $\langle . \rangle$ denotes ensemble average. For conversion of temporal (Δt) to spatial (r) scale, we used the same aforementioned technique which was taken for single-component structure functions i.e., $r(x,z) = |\bar{u}(x,z)|\Delta t$.

The isotropic part of the scaling exponent S_n^{pq}, was denoted by ζ_n^u and ζ_n^w corresponding to streamwise and vertical components, whereas the anisotropic part was denoted by ζ_n^{pq} (Dhruba 1997, Arad 1998).

5.9 Isotropic and anisotropic scaling exponents

Figure 5.17 shows the second-order structure functions and their compensated form corresponding to u, w, and uw at vertical distances $z^+ = -0.5$ and -0.3 for Run 4 at Section II data. The second -order mixed structure functions were calculated using the formula: $S_2^{11} = \langle [u(x+r) - u(x)]^1 [w(x+r) - w(x)]^1 \rangle$. All the structure functions give a clear indication of the existence of inertial sub range within lower ranges of r. The magnitude of w-structure function (S_2^w) value was always smaller than that of u-structure functions (S_2^u). On the other hand, the uw-structure functions (S_2^{11}) start with the lowest value within short ranges of r. As the separation distance r increases, the uw-structure function values start increasing and cross the w-structure function value and stays

between *u* and *w*-structure functions and moves towards the saturation region. In addition, at the vertical distance z^+= –0.5 for Run 4 at Section II, the isotropic scaling exponents from *u* and *w*-structure functions were 0.68 and 0.61, and at z^+= –0.3 for Run 4 at Section II, they were 0.67 and 0.60, respectively. On the other hand, the anisotropic scaling exponents ζ_2^{11}, corresponding to *uw*-structure functions S_2^{11} were 0.96 and 0.97 at z^+= –0.5 and –0.3 for Run 4 at Section II, respectively which are quite smaller than the *uw*-scaling exponent 4/3 according to the dimensional consideration. Now, the higher order mixed functions will be studied.

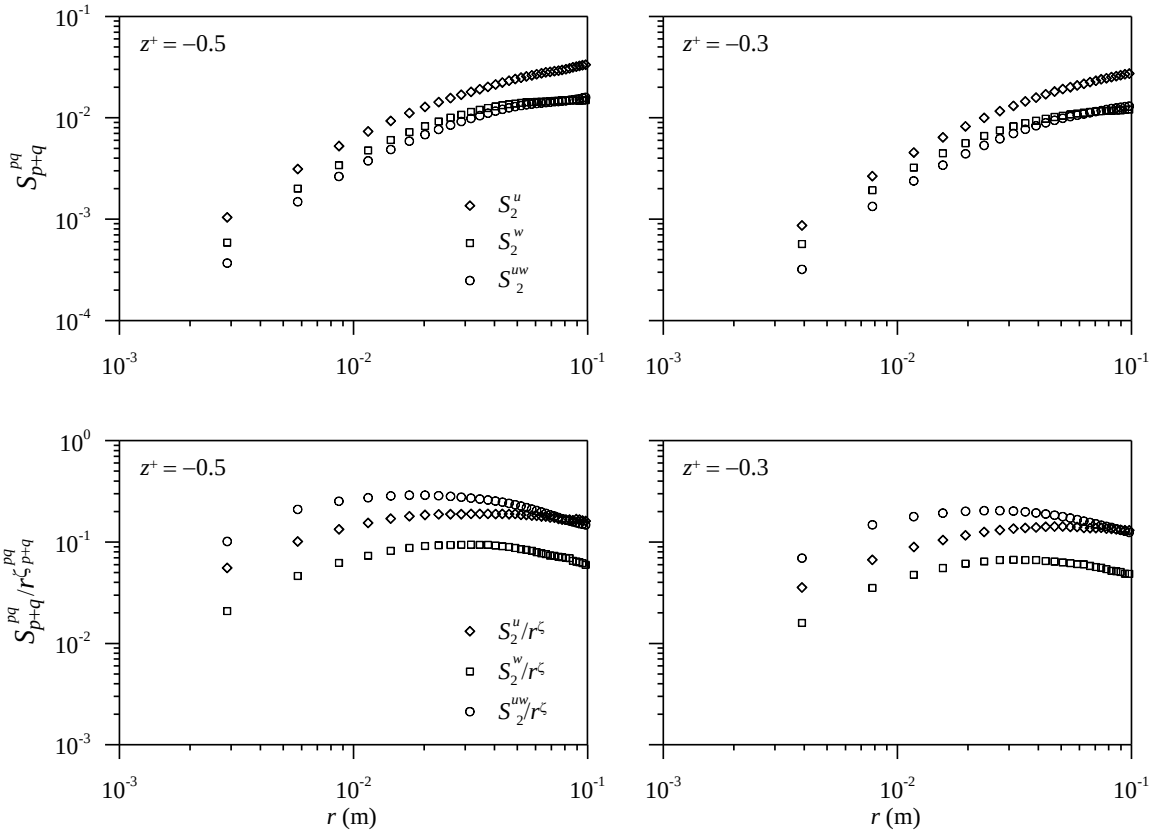

Figure 5.17: The second-order mixed structure functions S_2^u, S_2^w, and S_2^{uw} and their compensated form at z^+ = –0.5 and –0.3 of Section II of Run 4 data.

For the higher order mixed structure functions, we observed all even order anisotropic scaling exponents up to eighth-order. The modulus values of all order structure functions

were taken into account to obtain their better convergence. Now, according to Kurien and Sreenivasan (2000), the higher even order anisotropic structure functions using the equations (18a – 18c) components are:

for $n = 4$: S_4^{31}, S_4^{13} (18a)

for $n = 6$: S_6^{51}, S_6^{33}, S_6^{15} 18b)

for $n = 8$: S_8^{71}, S_8^{53}, S_8^{35}, S_8^{17} (18c)

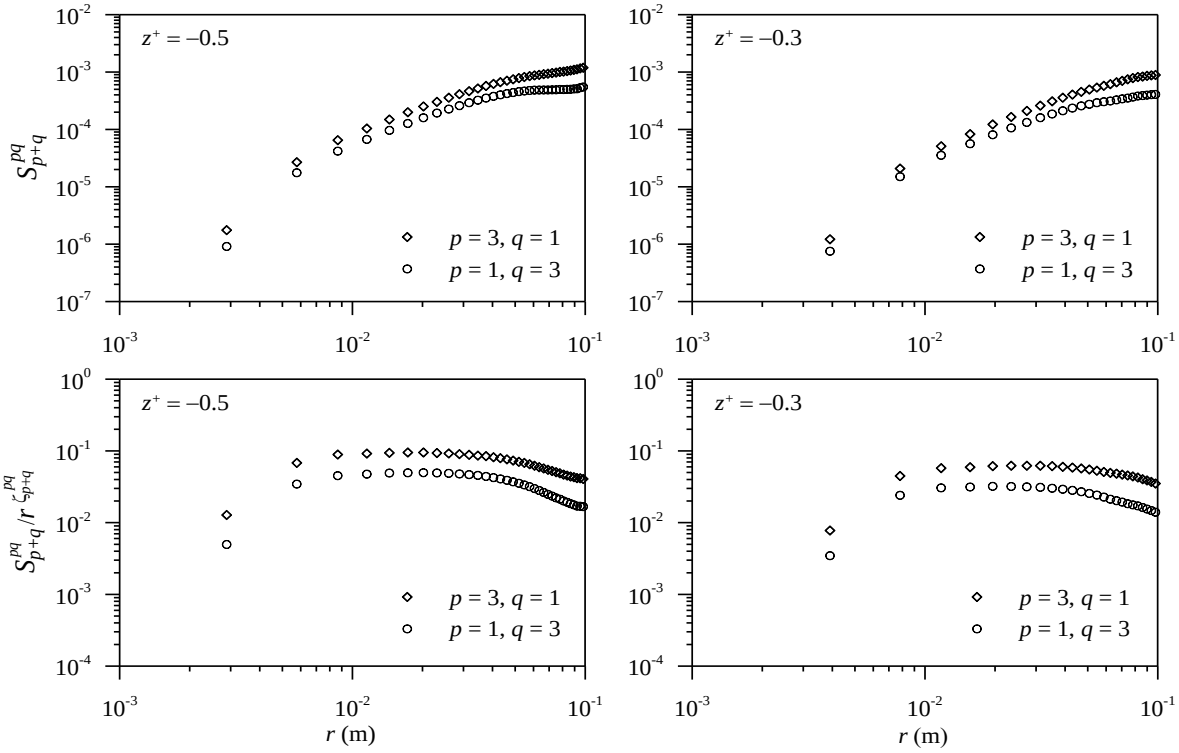

Figure 5.18: The fourth-order mixed structure functions and their compensated form at $z^+ = -0.5$ and -0.3 of Section II of Run 4 data.

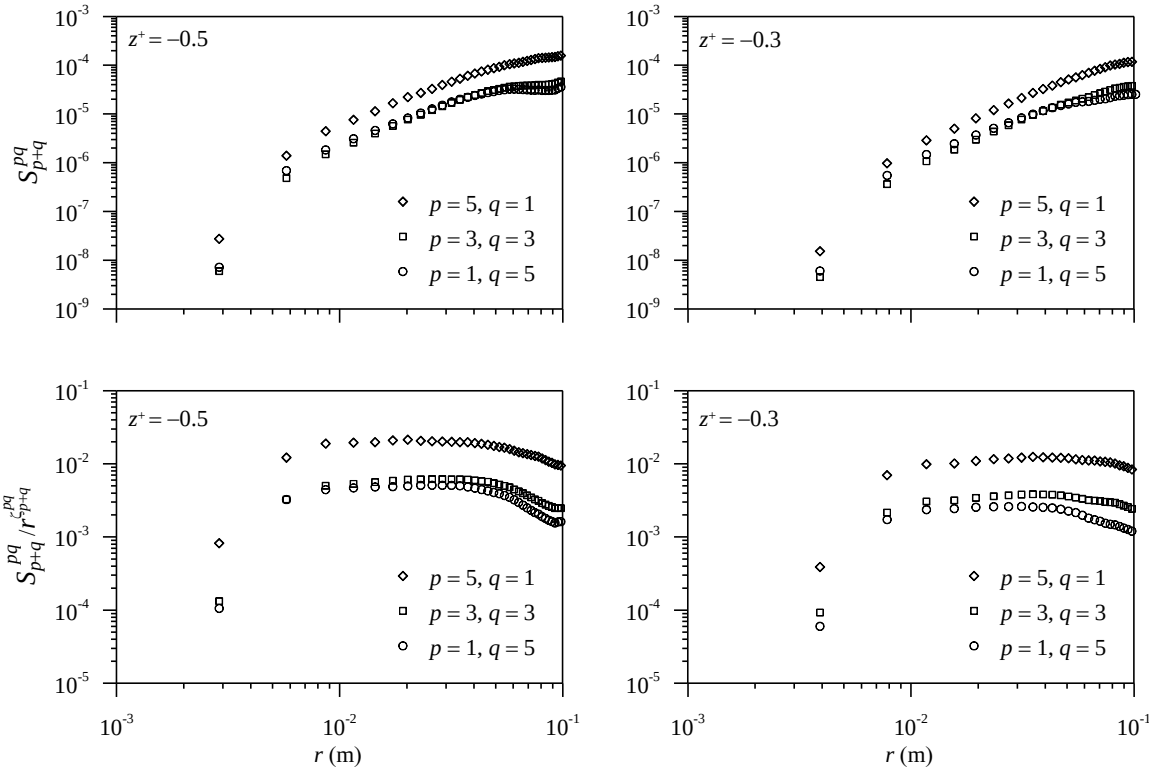

Figure 5.19: The sixth-order mixed structure functions and their compensated form at $z^+ = -0.5$ and -0.3 of Section II of Run 4 data.

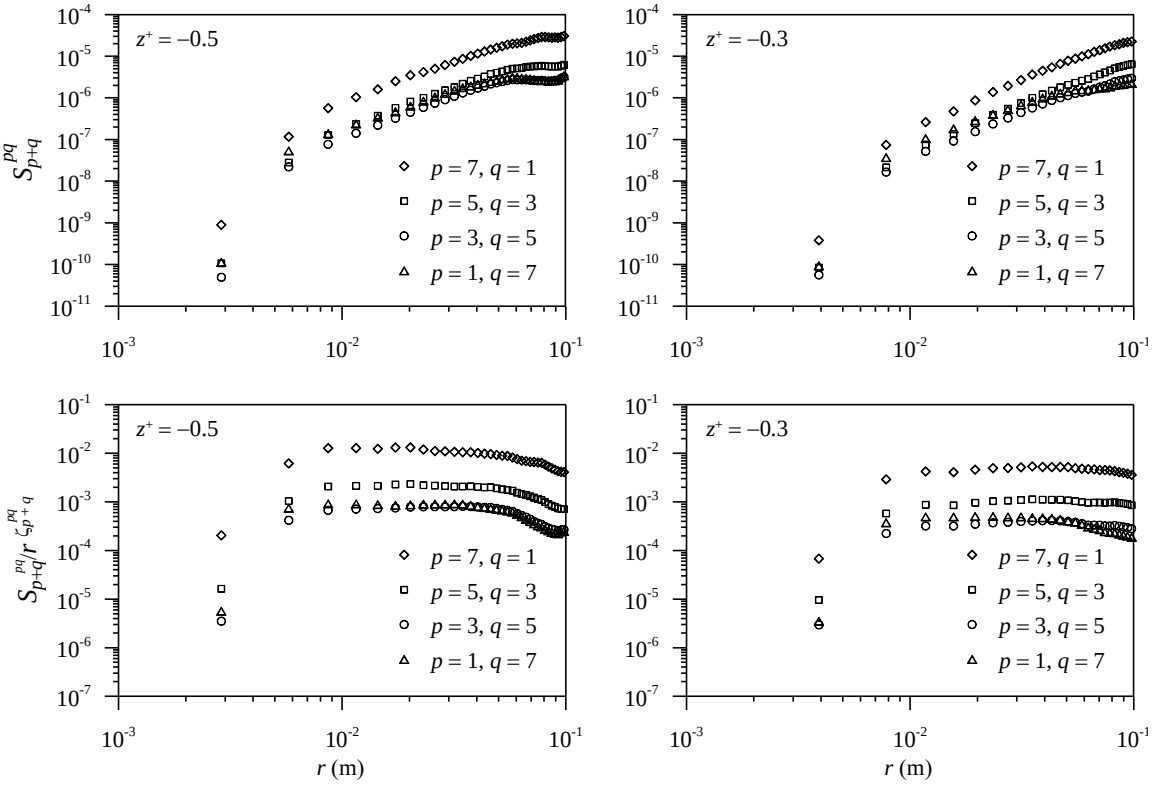

Figure 5.20: The eighth-order mixed structure functions and their compensated form at $z^+ = -0.5$ and -0.3 of Section II of Run 4 data.

Figures 5.18 – 5.20 show the fourth-, sixth-, and eighth-order mixed structure functions and their compensated form for $z^+ = -0.5$ and -0.3 of Section II for Run 4 data, which have zero values in the isotropic sector. It is important to mention here that the same was performed for Sections I and III for all the Runs 1–4 datasets. All the higher order mixed structure functions and their compensated forms give a clear indication of the existence of the inertial subrange within a lower ranges of separation distance. In addition, the scaling exponents estimated from them indicated that the values of scaling exponents increase with increase in the order of structure functions irrespective of the vertical distances. The graphical presentations of the anisotropic scaling exponents from the higher order mixed structure functions are given below in Figures 5.21 and 5.22 for Run 3 and Run 4, respectively. Although Runs 1 and 2 data sets are not shown here graphically, their values were shown in Table 4 along with the values of Runs 3 and 4.

From the values of anisotropic scaling exponents for instance, ζ_8^{71}, ζ_8^{53}, ζ_8^{35}, ζ_8^{17} for a particular value of order $n(n = 8)$, the structure functions give a clear understanding of the variations of scaling exponent values in a particular pattern i.e. if the structure function is more *u* (streamwise velocity components) dominated that gives higher scaling exponents and if *w* (vertical velocity components) dominated that gives comparatively lower scaling exponents.

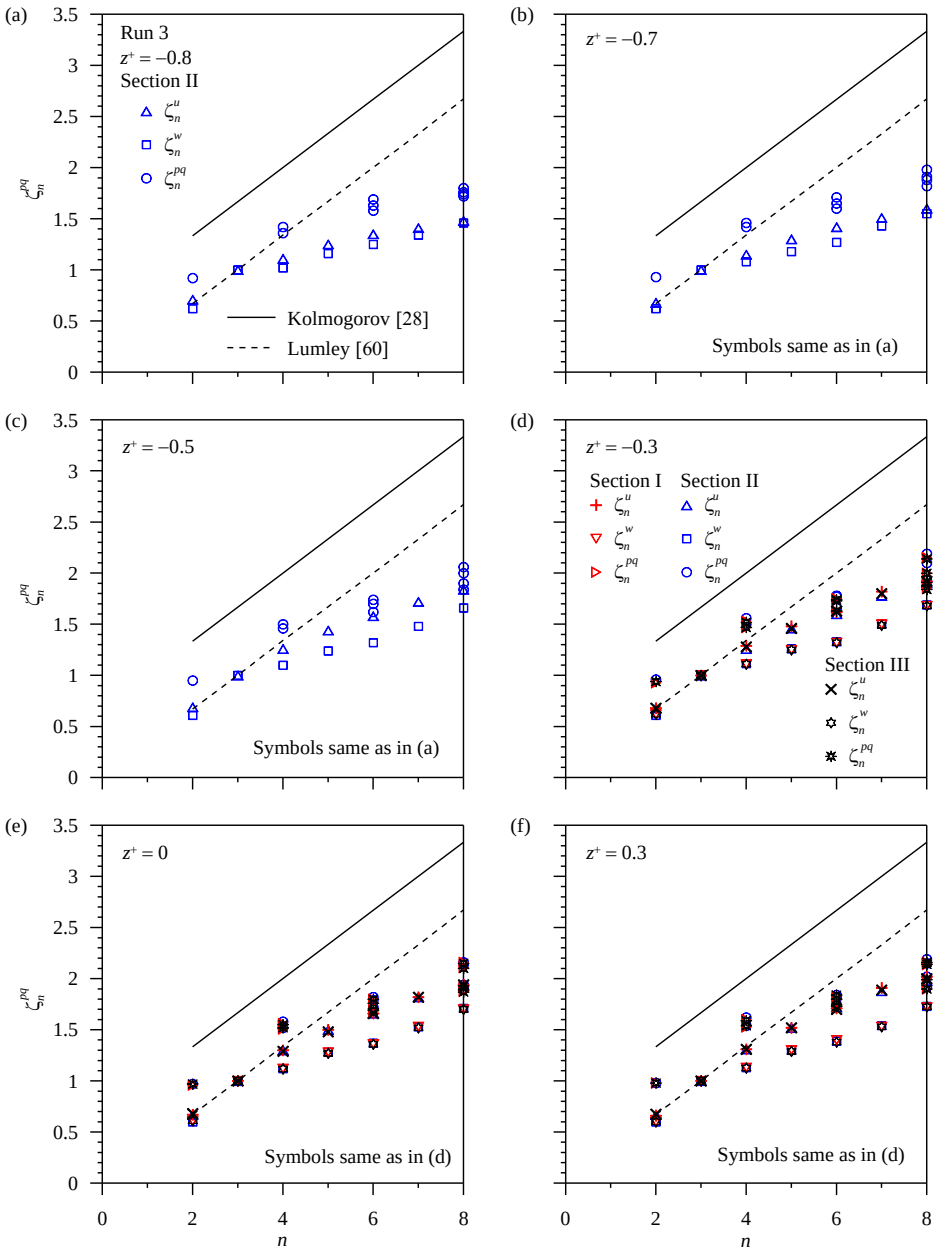

Figure 5.21: Scaling exponents of anisotropic and isotropic (u and w) sectors at z^+ = –0.8, –0.7, –0.5, –0.3, 0 and 0.3 of Section II for Run 3.

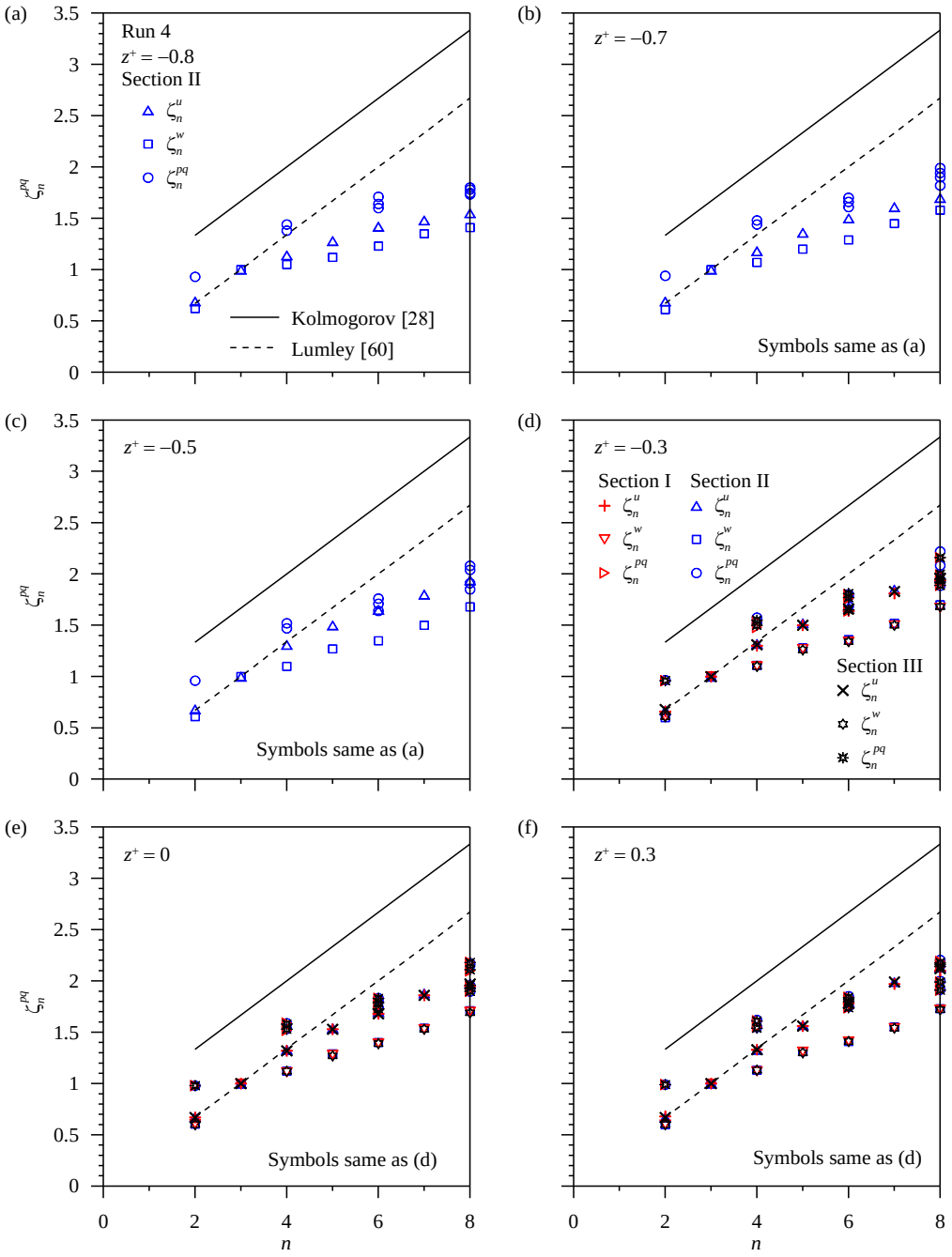

Figure 5.22: Scaling exponents of anisotropic and isotropic (u and w) sectors at z^+ = –0.8, –0.7, –0.5, –0.3, 0 and 0.3 of Section II for Run 4.

Now at z^+ = –0.5 at Section II of Run 4, for eighth-order structure functions, the corresponding scaling exponents are increasing, from 1.85 of S_8^{17} which was w-dominated to 2.11 of S_8^{71} which was u-dominated, also have intermediate value 1.91 of

S_8^{35} partially *w*-dominated and 2.04 of S_8^{53} partially *u*-dominated. Similar patterns of scaling exponents were achieved for all others order mixed structure functions, namely for the fourth- and sixth-orders. Also, for all other points with different vertical distances, the anisotropic exponents value maintained same pattern, although the values of exponents of the points situated at maximum degradation depth are small, and then with the vertical distance, the values of exponent are increasing at a specific order *n* of corresponding mixed structure function.

From Figures 5.21 – 5.22, it was also observed that the anisotropic scaling exponents are always greater than isotropic exponent within lower values of *n* (*n* = 2, 4), although for higher values of *n* (*n* = 6, 8) some of the anisotropic exponents are lower than isotropic exponents which was in confirmation with Warhaft and Shen (2002). As an example, at $z^+ = -0.5$ for Run 4 at Section II for eighth-order, ζ_8^{pq} value ranges within 1.85 and 2.11, whereas ζ_8^{u} and ζ_8^{w} values are 1.94, 1.68 respectively.

The resulting anisotropic exponents are consitently larger then those known as isotropic parts at all orders. This strongly suggest that anisotropic effects decrease with decreasing scale. However, the general behavior of ζ_n^{pq} was quite similar to the findings of Warhaft and Shen (2002). With respect to the degradation, it was quite evident from the figure that the more one moves towards the vicinity of the degraded depth, the more ζ_n^{pq} deviates from Kolmogorov (1941) and Lumley (1967), although as *n* increases ζ_n^{pq} tend to those of ζ_n maintaining $\zeta_n^{pq} > \zeta_n$ irrespective of the location.

Table 4 given below presents a comparison of the scaling exponents obtained at different sections for Runs 1–4 from higher order mixed structure functions with Warhaft and Shen (2002). It was quite clear from the data that in the vicinity of the degraded bed, the values of the scaling exponents differ more than that above the bed-level in the present study from Warhaft and Shen (2002) irrespective of the experimental runs performed here. It can therefore be concluded that the anisotropic scaling exponents also divert more from the values available in the literature.

Table 4: Comparison of the scaling exponents obtained from higher order mixed structure functions with Warhaft and Shen (2002)

For Run 1:

Section	n	z^+ = –0.8	z^+ = –0.7	z^+ = –0.5	z^+ = –0.3	z^+ = 0	z^+ = 0.3	Warhaft and Shen(2002)
I	2	–	–	–	0.93	0.96	0.98	1.05
I	4	–	–	–	1.48	1.51	1.58	1.56
I	4	–	–	–	1.43	1.48	1.52	1.42
I	6	–	–	–	1.68	1.77	1.83	2.02
I	6	–	–	–	1.64	1.74	1.79	1.89
I	6	–	–	–	1.50	1.66	1.70	1.71
I	8	–	–	–	2.04	2.12	2.17	2.33
I	8	–	–	–	1.97	2.06	2.13	2.22
I	8	–	–	–	1.90	1.93	1.97	1.99
I	8	–	–	–	1.80	1.85	1.90	1.80
II	2	0.92	0.93	0.94	0.95	0.97	0.99	1.05
II	4	1.43	1.46	1.50	1.56	1.59	1.60	1.56
II	4	1.40	1.43	1.45	1.50	1.53	1.54	1.42
II	6	1.70	1.68	1.74	1.82	1.83	1.84	2.02
II	6	1.63	1.65	1.69	1.78	1.80	1.81	1.89
II	6	1.60	1.59	1.63	1.65	1.73	1.75	1.71
II	8	2.00	2.02	2.10	2.16	2.18	2.19	2.33
II	8	1.95	1.96	2.00	2.10	2.10	2.14	2.22
II	8	1.86	1.89	1.90	1.95	1.96	1.99	1.99
II	8	1.84	1.78	1.84	1.89	1.90	1.91	1.80
III	2	–	–	–	0.94	0.97	0.98	1.05
III	4	–	–	–	1.47	1.52	1.59	1.56
III	4	–	–	–	1.44	1.49	1.53	1.42
III	6	–	–	–	1.68	1.78	1.84	2.02
III	6	–	–	–	1.618	1.75	1.80	1.89
III	6	–	–	–	1.51	1.67	1.72	1.71
III	8	–	–	–	2.00	2.10	2.15	2.33
III	8	–	–	–	1.96	2.021	2.09	2.22
III	8	–	–	–	1.92	1.94	1.98	1.99
III	8	–	–	–	1.84	1.86	1.92	1.80

For Run 2:

Section	n	z^+ = –0.8	z^+ = –0.7	z^+ = –0.5	z^+ = –0.3	z^+ = 0	z^+ = 0.3	Warhaft and Shen (2002)
I	2	–	–	–	0.93	0.95	0.96	1.05
I	4	–	–	–	1.46	1.56	1.59	1.56
I	4	–	–	–	1.42	1.48	1.50	1.42
I	6	–	–	–	1.72	1.78	1.82	2.02
I	6	–	–	–	1.66	1.77	1.78	1.89
I	6	–	–	–	1.59	1.65	1.70	1.71
I	8	–	–	–	1.98	2.16	2.16	2.33
I	8	–	–	–	1.96	2.00	2.06	2.22
I	8	–	–	–	1.87	1.90	1.96	1.99
I	8	–	–	–	1.82	1.87	1.90	1.80
II	2	0.9	0.91	0.93	0.94	0.96	0.96	1.05
II	4	1.4	1.45	1.48	1.55	1.57	1.61	1.56
II	4	1.35	1.4	1.44	1.48	1.50	1.52	1.42
II	6	1.68	1.70	1.73	1.77	1.80	1.83	2.02
II	6	1.62	1.64	1.68	1.76	1.78	1.79	1.89
II	6	1.56	1.58	1.60	1.64	1.70	1.72	1.71
II	8	1.78	1.96	2.00	2.17	2.15	2.17	2.33
II	8	1.71	1.90	1.98	2.04	2.12	2.13	2.22
II	8	1.75	1.86	1.89	1.92	1.92	2.00	1.99
II	8	1.72	1.80	1.83	1.86	1.89	1.90	1.80
III	2	–	–	–	0.92	0.93	0.95	1.05
III	4	–	–	–	1.47	1.57	1.60	1.56
III	4	–	–	–	1.43	1.14	1.51	1.42
III	6	–	–	–	1.73	1.79	1.83	2.02
III	6	–	–	–	1.67	1.78	1.8	1.89
III	6	–	–	–	1.60	1.66	1.71	1.71
III	8	–	–	–	1.99	2.15	2.15	2.33
III	8	–	–	–	1.97	1.98	2.00	2.22
III	8	–	–	–	1.88	1.92	1.97	1.99
III	8	–	–	–	1.83	1.88	1.92	1.80

For Run 3:

Section	n	$z^+ =$ –0.8	$z^+ =$ –0.7	$z^+ =$ –0.5	$z^+ =$ –0.3	$z^+ =$ 0	$z^+ =$ 0.3	Warhaft and Shen (2002)
I	2	–	–	–	0.93	0.96	0.98	1.05
I	4	–	–	–	1.53	1.56	1.60	1.56
I	4	–	–	–	1.47	1.51	1.53	1.42
I	6	–	–	–	1.75	1.80	1.83	2.02
I	6	–	–	–	1.74	1.77	1.80	1.89
I	6	–	–	–	1.63	1.68	1.72	1.71
I	8	–	–	–	2.15	2.16	2.16	2.33
I	8	–	–	–	2.00	2.11	2.14	2.22
I	8	–	–	–	1.90	1.92	2.00	1.99
I	8	–	–	–	1.85	1.88	1.90	1.80
II	2	0.92	0.93	0.95	0.96	0.97	0.98	1.05
II	4	1.42	1.46	1.50	1.56	1.58	1.62	1.56
II	4	1.36	1.42	1.46	1.50	1.52	1.54	1.42
II	6	1.69	1.71	1.74	1.78	1.82	1.84	2.02
II	6	1.63	1.65	1.70	1.77	1.79	1.81	1.89
II	6	1.58	1.60	1.62	1.66	1.72	1.74	1.71
II	8	1.80	1.98	2.06	2.19	2.16	2.19	2.33
II	8	1.72	1.91	2.00	2.10	2.14	2.15	2.22
II	8	1.76	1.88	1.90	1.93	1.94	2.02	1.99
II	8	1.73	1.83	1.84	1.88	1.90	1.92	1.80
III	2	–	–	–	0.94	0.97	0.98	1.05
III	4	–	–	–	1.52	1.55	1.59	1.56
III	4	–	–	–	1.47	1.52	1.54	1.42
III	6	–	–	–	1.74	1.80	1.84	2.02
III	6	–	–	–	1.73	1.76	1.80	1.89
III	6	–	–	–	1.63	1.69	1.73	1.71
III	8	–	–	–	2.14	2.15	2.16	2.33
III	8	–	–	–	2.00	2.10	2.14	2.22
III	8	–	–	–	1.91	1.93	1.99	1.99
III	8	–	–	–	1.84	1.87	1.90	1.80

For Run 4:

Section	n	$z^+ =$ –0.8	$z^+ =$ –0.7	$z^+ =$ –0.5	$z^+ =$ –0.3	$z^+ =$ 0	$z^+ =$ 0.3	Warhaft and Shen (2002)
I	2	–	–	–	0.96	0.98	0.99	1.05
I	4	–	–	–	1.54	1.59	1.61	1.56
I	4	–	–	–	1.48	1.52	1.55	1.42
I	6	–	–	–	1.80	1.83	1.84	2.02
I	6	–	–	–	1.76	1.79	1.81	1.89
I	6	–	–	–	1.64	1.72	1.74	1.71
I	8	–	–	–	2.16	2.18	2.19	2.33
I	8	–	–	–	1.99	2.10	2.14	2.22
I	8	–	–	–	1.94	1.96	1.99	1.99
I	8	–	–	–	1.89	1.90	1.91	1.80
II	2	0.93	0.94	0.96	0.97	0.98	0.99	1.05
II	4	1.44	1.48	1.52	1.57	1.59	1.62	1.56
II	4	1.38	1.44	1.47	1.52	1.53	1.55	1.42
II	6	1.71	1.70	1.76	1.80	1.83	1.85	2.02
II	6	1.64	1.66	1.71	1.78	1.80	1.82	1.89
II	6	1.60	1.61	1.64	1.68	1.74	1.75	1.71
II	8	1.80	1.99	2.08	2.22	2.17	2.20	2.33
II	8	1.73	1.94	2.04	2.08	2.15	2.15	2.22
II	8	1.78	1.90	1.91	1.94	1.95	2.00	1.99
II	8	1.74	1.82	1.85	1.89	1.90	1.92	1.80
III	2	–	–	–	0.96	0.98	0.99	1.05
III	4	–	–	–	1.55	1.58	1.61	1.56
III	4	–	–	–	1.50	1.53	1.54	1.42
III	6	–	–	–	1.81	1.83	1.84	2.02
III	6	–	–	–	1.77	1.79	1.80	1.89
III	6	–	–	–	1.65	1.73	1.74	1.71
III	8	–	–	–	2.16	2.18	2.18	2.33
III	8	–	–	–	2.00	2.11	2.14	2.22
III	8	–	–	–	1.95	1.96	1.99	1.99
III	8	–	–	–	1.89	1.90	1.92	1.80

Now, in order to find the trend of anisotropic scaling exponents with order n, it may be interesting to determine the ratio of anisotropic exponents to isotropic exponents.

However, while performing so there arise some difficulties as was experienced by Warhaft and Shen (2002) because of $\zeta_n^u \neq \zeta_n^w$ or, more specifically $\zeta_n^u > \zeta_n^w$. Also, in principle, ζ_n^{pq}/ζ_n cannot be less than unity as in the anisotropic sector there remain correlation between *u* and *w* components that must unravel with decreasing scale. However, ζ_n^{pq}/ζ_n to be less than unity, these correlations should increase with decreasing scale, indicating more organized *u* and *w* fluctuations as the scale decreases. Now, for instance, at $z^+ = -0.5$ Section II for Run 4 data set for eighth order, we have ζ_8^{17}/ζ_8^u = 1.85/1.94 less than unity, and which is in consistence with $\zeta_8^w \leq \zeta_8^u$. However, it is important to mention that if one uses ζ_8^w instead of ζ_8^u that would be more appropriate as ζ_8^{17} is *w* dominated. To avoid this difficulty, in the ratio, arithmetic mean of two isotropic exponents was used as denominator, as $\left(l\zeta_{l+m}^u + m\zeta_{l+m}^w\right)/(l+m)$, where *l* and *m* are two positive integers and *n* (= *l* + *m*) is the order of the mixed structure functions.

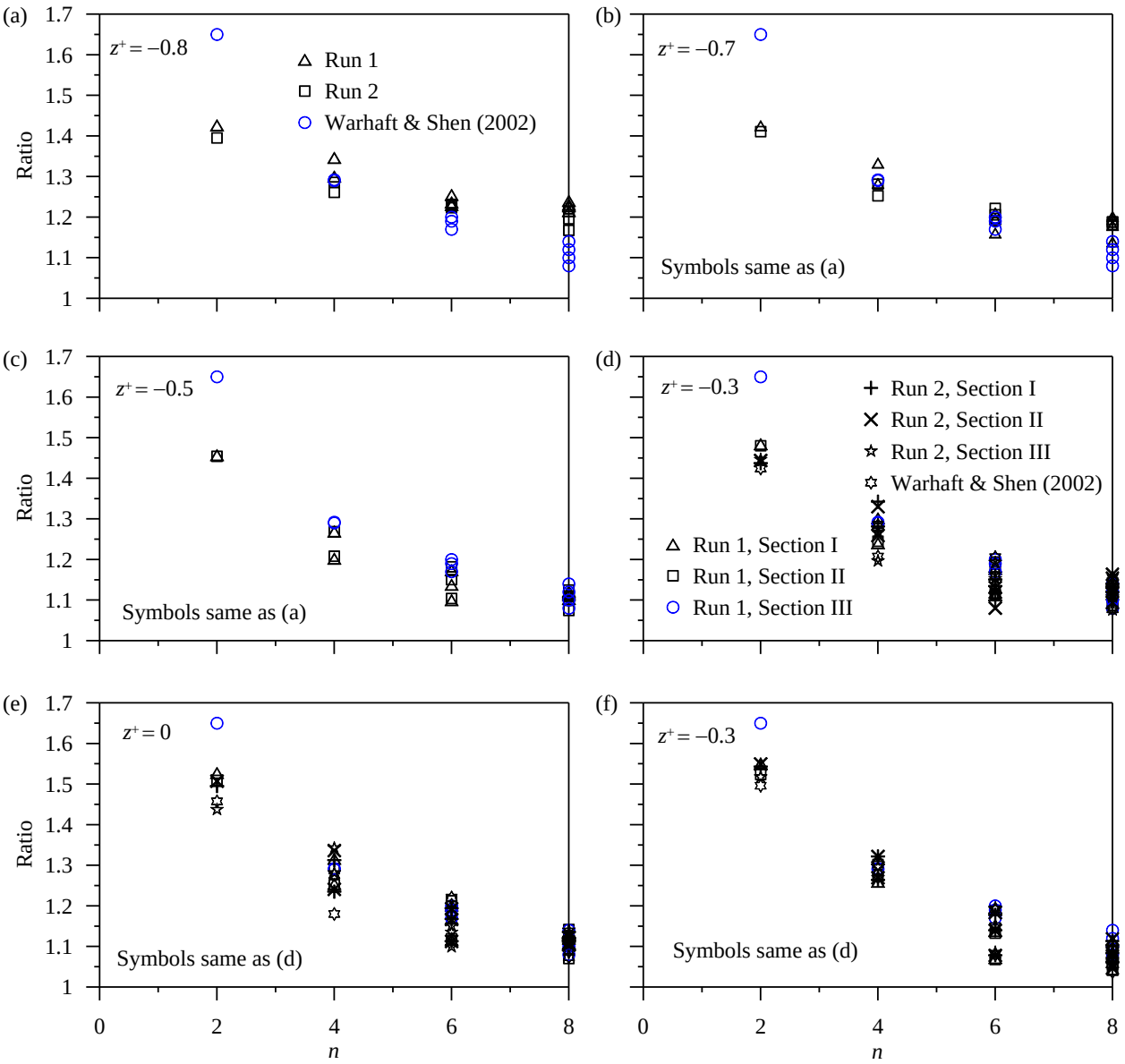

Figure 5.23: Ratio of the anisotropic scaling exponent to the arithmetic mean of isotropic scaling exponent with order n, at $z^+ = -0.8$, -0.7, -0.5, -0.3, 0 and 0.3. Data were plotted for Runs 1 and 2.

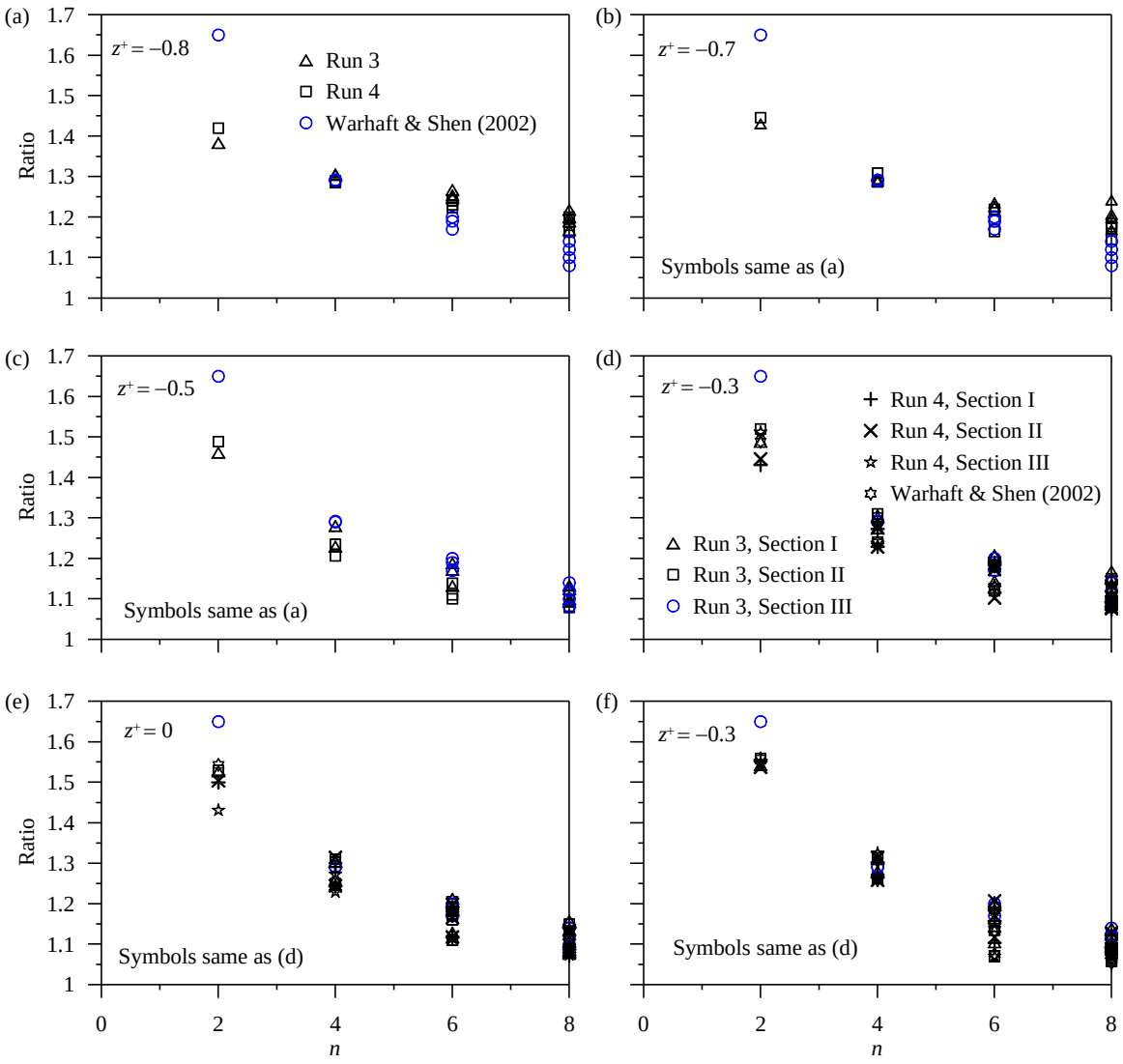

Figure 5.24: Ratio of the anisotropic scaling exponent to the arithmetic mean of isotropic scaling exponent with order n, at $z^+ = -0.8$, -0.7, -0.5, -0.3, 0 and 0.3. Data were plotted for Runs 3 and 4.

Figures 5.23 and 5.24 show the ratio of anisotropic scaling exponents to the arithmetical mean (general form was defined above) of two isotropic scaling exponents at different vertical distances within the maximum degraded depth at different vertical distances and sections for Run 1 and Run 2; and Run 3 and Run 4, respectively. A clear downward trend was observed from the data with order n, and for a particular value of n, they show

good collapse within a band. Here, we have also observed that the similar downward trend for the all data of different vertical distances. A continuing downward trend of the ratio indicated at higher order the anisotropic contribution is as dominant as the isotropic. This inequality becomes methodically weaker with increase in n suggesting anisotropy even in higher-order of structure functions. In case of upper zones of degraded bed, the curve tend to be more closer to unity than lower zones of the degraded region irrespective of the Sections and experimental runs. The possible reason behind this is that, in the maximum degradation region the influence of anisotropy on the scaling exponents of corresponding mixed structure function is more intense than in the upper region. Moreover, very little changes in the values of the ratio of the anisotropic scaling exponent for uniform and bimodal degraded beds were found. Based on the present experimental results, it can be concluded that within the maximum depth of degradation, the vertical distance from the bed-level was the most instrumental factor that controls the ratio of the scaling exponents. This observation gives the clear understanding about the influence of anisotropy on the corresponding scaling exponents due to bed degradation.

5.10 Anisotropy angle

In this section, the anisotropy angle has been measured at different vertical distances at the location of the maximum degraded depth for bimodal sedimentary bed to estimate the level of anisotropy as a function of scales r. Mathematically it is expressed as:

$\theta(r) = \arctan\sqrt{2\frac{S_2(r,0)}{S_2(0,r)}}$, where $S_2(r,0)$ is the second-order structure functions in the streamwise direction and $S_2(0, r)$ is the second-order structure functions in the vertical direction. For the isotropy of the flow, the value of angle $\theta \approx 54.74°$. Any value other than this indicates anisotropy. The idea of structure functions based anisotropy angle was first introduced by Shebalin et al. (1983) for the magnetized plasma turbulence and its structure functions version was anticipated by Milano et al. (2001). In fluvial hydrodynamics, it was used and fully understood by Coscarella et al. (2020) to observe the turbulence anisotropy and intermittency in open-channel flows over rough beds.

In the vicinity of the degradaed bed ($z^+ = -0.8$), θ starts with a value quite larger than 54.74° at lower values of r, which goes on increasing and becomes ≈ 55.5° as r decreases slighly and with increase in r values, it again increases so sharply and moves vertically upward with θ values much larger than 54.74° (≈ 60°). Beyond that θ increases assymptotically with an incraese in r values. As the vertical distance z^+ increases (($z^+ = -0.3, 0, 0.3$), θ starts with values closer to 54.74° and becomes more closer with increase in the values of r. However, beyond $\in [-0.04; 0.04]$, the values of θ increase and goes above ≈ 56.5° indicating more anisotropy in turbulence. It was therefore observed that the turbulence becomes isotropy as one moves vertically upward and is measured within lower magnitude of the incremental vector r. The present results are in agreement with Coscarella et al. (2020) who found for $\in [-0.04; 0.04]$, the values of θ varies of ±2.5% with respect to the isotropy value and when the spatial increment increases further, the θ trends to increases and attain values larger than 56° for flow above the vicinity of the rough beds [zone 2 according to Coscarella et al. (2020)]. However, it is improtatnt to mention that the anisotropy angle was calculated for the bimodal degraed bed-data only.

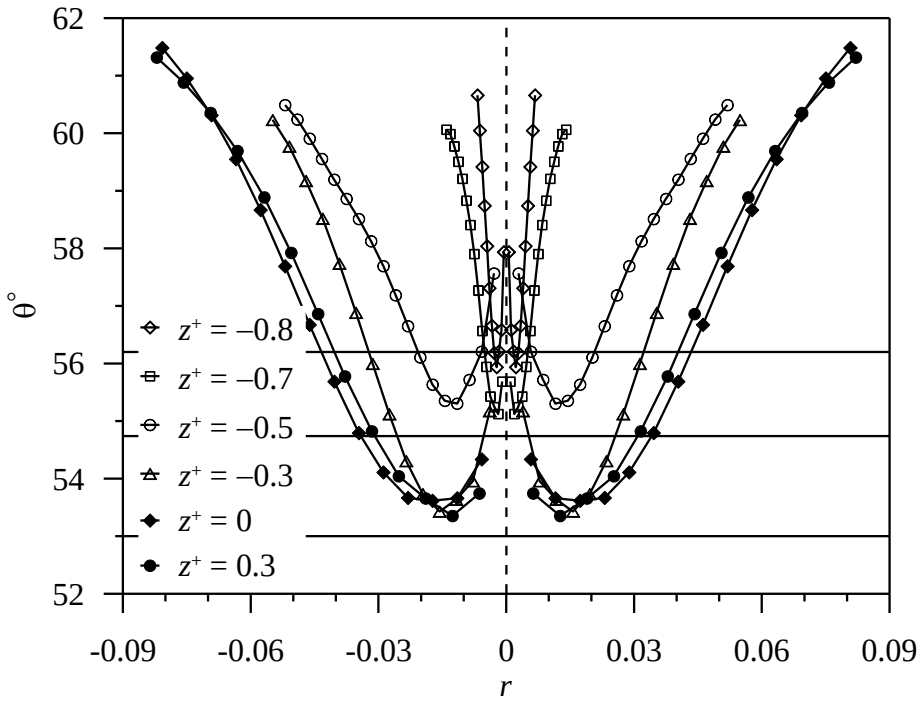

Figure 5.25: Anisotropic angle at different vertical distances.

5.11 Concluding remarks

The report presents the results of an experimental study of turbulent flow over a bimodal degraded bed. The instantaneous velocity components were captured by using an ADV *Vectrino plus* probe at different vertical distances at a location of the maximum degraded depth and its upstream and downstream. The main aim of the paper was to observe the anisotropy and intermittency in the vicinity of the degraded bed, along with the velocity vectors, correlation lengths and Taylor microscale and Kolmogorov length scales. The main findings of the present study are summarized below:

The spatial distributions of the longitudinal and vertical components of the velocity vectors show a clear indication of the flow retardation in the vicinity of the maximum equilibrium degraded depth which goes on decreasing with the increase in streamwise distance. The vicinity of the maximum degraded depth is mostly affected by the local turbulence. As one moves further downstream the turbulence indication become less, indicating an effort of regaining the plane-bed turbulence characteristic.

The length scales attain the least value in the vicinity of the degraded bed and they increase with increase in the vertical distance. However, above the bed-level their values go on increasing indicating turbulence at plane rough-bed. The higher order structure functions of streamwise velocity components indicated the existence of the inertial subrange within lower values of the separation distances. At higher order (seventh and above), the structure functions data show little bit of lacunarity. In the vicinity of the maximum degraded depth, the scaling exponents estimated by ESS divert maximum from the theoretical values indicating maximum intermittency that goes on decreasing with increase in the vertical distance. The effect of anisotropy in the scaling exponents becomes maximum in the vicinity of the bed, although anisotropy in scaling exponents is present throughout the depth. As the order of scaling increases, the effect of anisotropy decreases. Also, anisotropy angle analysis demonstrated that the effect of anisotropy in the degraded region below the initial bed level is much higher than that above. Within the depth of degradation, both the bimodal and uniform sediments beds show almost similar characteristics of the turbulence and scaling parameters studied here, they hold little differences in the values.

Finally, it can be concluded that as the present problem handled here has numerous practical applications in open channel flow, further explorations are required to understand the problem more scientifically. There remain some limitations in the present study mostly due to the experimental setup and instrumentations. The use of a PIV (Particle Image Velocimtery) or LDA (laser Doppler anemometer) could be more appropriate to capture the profiles thoroughly and could have given data with more accuracy in the near-bed. In addition, to have a clear idea of the effects of a bimodal sediment distribution, different proportions of sand and gravel could be considered, and results compared with the uniform sediment case. The bed roughness has important role to play to characterize the turbulence structures that could be well-explained by using some sophisticated ranging system or bed scanner with high precision. Data of the present study may also be useful for numerical simulation under the similar bed conditions and for comparison with that of uniform sedimentary bed conditions.

Chapter 6

Quadrant analysis of Turbulence over a Degraded Channel Bed

6.1 General

This works presented in this chapter investigates the turbulence characteristics in a flow through a degraded channel bed containing a mixture of two sediment sizes. After establishing an equilibrium scour condition in a laboratory setting, three components of instantaneous velocity were recorded using a Vectrino velocimeter over a sufficient duration, with vertical profiles measured at three stream-wise locations along the flume axis. The study employed two different conditional averaging approaches: total- and quadrant-averaging, and compared their results.

Natural open channels have loose boundaries, which make them susceptible to several morphologic phenomena like bed degradation, erosion and deposition of sediments, and local scouring, among others. The study of the mutual interplay between turbulent flow and morphologic changes is a matter of common interest to the researchers working in the fields of fluid mechanics, mathematics, physics, and geology. Among many morphologic processes encountered in channels, in this work we focus on two-dimensional local scour leading to the formation of a degraded bed. This may happen downstream of control structures, frequently in combination with a transition from non-erodible to erodible bed and has significant implications that motivated extensive research, from the earlier studies of Nik Hassan and Narayanan (1985) and Chatterjee et al. (1994) to many following ones (e.g., Dey and Sarkar 2006, Tregnaghi et al. 2007, Dodaro et al. 2016).

In most practical situations, natural channels may carry mixtures of gravel and sand (Smith 1996). A bimodal sedimentary bed is, therefore, closer to the practical aquatic environment than one with uniform sediment. Bimodal sedimentary beds started receiving attention of the scientific community earlier in the twentieth century. For example, Shvidchenko and Pender (2001), Wilcock et al. (2001), Grams and Wilcock

(2007), and Wren et al. (2011) have done significant work on this topic. Furthermore, studying the turbulent properties of a flow field is a mean towards explaining the complex interactions between the fluid and the bounding bed (Dey and Ali 2020). Jain et al. (2015) were probably the pioneers in working with the turbulence characteristics for degraded channel beds; they found significant differences compared to a uniform bed in the stream-wise velocity, Reynolds shear and normal stresses (RSS, RNS) and bursting events at different locations. This was later reconfirmed by Sarkar et al. (2021). Imitating the experimental thought of Jain et al. (2021), Sarkar et al. (2021) and Sarkar and Sarkar (2023) further studied the turbulence characteristics for such a bed. In their study, Sarkar et al. (2021) explored the scaling laws of turbulence and turbulent kinetic energy (TKE) dissipation rates using structure functions, and the turbulence anisotropy, highlighting significant differences also in these turbulence characteristics. Later, Sarkar and Sarkar (2023) extended the study of Sarkar et al. (2021) to high-order structure functions and intermittency in the scaling exponents for flow through bimodal degraded beds. Scaling laws in fluvial processes, particularly for scoured bed, were also studied by Ali and Dey (2017), Ali and Dey (2018) and Dey and Ali (2024).

The literature provides many examples of studying turbulence by dividing velocity fluctuations in four quadrants depending on their sign combinations, using the technique popularly known as the quadrant analysis. Due to pressure or velocity differences in a fluid flow, low-speed fluid streaks intrude into a high-speed fluid domain through the so-called flow ejections. Conversely, in sweeps, high-speed fluid parcels rush down toward the bed. This sequence is known as the sweep-ejection process, whose study was pioneered by Lu and Willmarth (1973). According to the method, the first and third quadrants are referred to as outward and inward interactions, whereas the second and fourth quadrants are called ejection and sweeps, respectively. Among many, Nezu and Nakagawa (1993), Padhi et al. (2020), Dey et al. (2020) found that sweeps and ejections are the predominating events, whereas inward and outward interactions have lower occurrence in an open-channel flow. Importantly, the quadrant analysis introduced by Lu and Willmarth (1973) was primarily used in the conditional statistics of RSS by several researchers to understand the fluid flow in an open channel. Later, the conditional statistics were employed to observe the conditional time-averaged velocity, RSS,

turbulence intensities, etc. Some of the notable works in this direction were conducted by García et al. (1996), Cellino and Lemmin (2004) , Hurther et al. (2007), Pokrajac et al. (2007), among others, using the time-averaged values. Later, Mignot et al. (2009) performed the conditional analysis for spatially-averaged RSS and vertical TKE flux, for flow over a spatially heterogeneous gravel bed. They found that the net spatially-averaged RSS profile is the cumulative sum of the contributions from the ejection and sweeps and the net vertical TKE flux approximately equals the difference between the contributions from the ejection and sweeps. Mohajeri et al. (2016) used the upward and downward velocity fluctuations to quantify the net temporal and advective vertical momentum flux in a gravel-bed flow. The conditional statistics were further explored by Padhi et al. (2019) and Dey et al. (2020) who showed the time-averaged turbulence characteristics in a spatial flow domain for both water-worked and screeded gravel beds. Based on three-dimensional velocity readings captured by using a micro-acoustic Doppler velocimeter, Duan et al. (2011) observed that, for flow over spur dikes under scouring conditions, ejections and sweeps are prevalent before the local scour is initiated, and then outward interactions are dominant after the scour hole is formed.

John et al. (2023) investigated the effect of the busting events in open channel under different vegetation spacing within as submerged vegetation patch. A comparison was made between locations without-vegetation and those under vegetation. The effect of vegetation was maximum within two thirds of vegetation height. The outward interactions dominated near the bed under vegetation, whereas sweeps became proactive for near-bed region without vegetation. It was also observed that the changes in the density of the vegetation changed the percentage contributions of the bursting events.

The brief review above indicates that the conditional statistics have a significant role in describing the turbulence behavior of a fluid flow. Identifying a gap in prior literature, the present manuscript is focused on a quadrant analysis of the flow field over an equilibrium degraded bed with two-size sediment. We argue that conditional properties need a thorough definition; in this manuscript we adopt a definition framework with two averaging options, namely total-averaging and quadrant-averaging. The total-averaged quantities, which have always the total sample size at the denominator, have the advantage that their sum for the four quadrants equals an investigated mean quantity

before conditioning. On the other hand, they are not representative of what happens in a certain quadrant that may be more significant in relation to the interactions between the flow and other bodies (this second aspect possibly stimulating the use of quadrant-averaged quantities). The literature furnished examples of both approaches. Cellino and Lemmin (2004) performed quadrant analysis using conditional averages of turbulent characteristics such asvelocity, stream-wise and vertical fluctuations and TKE fluxes and performed quadrant-based averaging only for velocity, while for the other quantities total-averaging was used, in a mixed approach. Sarkar and Dey (2010), Dey et al. (2011), Sarkar (2016) performed quadrant analysis of RSS using the total-averaging method. Padhi et al. (2019) explored the contributions of bursting events to the total turbulent characteristics in water-worked and screeded gravel bed flows using the quadrant-based averaging. Dey et al. (2020) demonstrated the effectiveness of bursting events in flow over a series of two-dimensional dunes using the quadrant-based averaging for stream-wise velocity, Reynolds shear and normal stresses and TKE fluxes. In summary, different researchers used different averaging methods, not always with a clear definition framework; this is also a gap that the present manuscript intends to fill.

The paper is organized as follows: The experimental methodology and data acquisition are described in section 2; Section 3 presents the definitions of the turbulence properties under investigation; the results are shown in section 4; Section 5 provides a discussion of phenomenological relevance of the results and an extended definition framework for conditional means using a “hole” to filter turbulence events, finally proposing some prospects for further research; Section 6 concludes the study.

6.2 Experimental Methodology

The experimental procedures relevant for this study are the same as those of Sarkar et al. (2021) and Sarkar and Sarkar (2023). However, the main parts of the experimental setup are briefly explained below for the self-sufficiency of the present article. The schematic of the experimental setup is shown in Figure 6. 1(a).

The experiment was carried out in a rectangular flume located in the Fluvial Mechanics laboratory of the Indian Statistical Institute, Kolkata, India. The flume is 20-m long, 0.5-m wide and 0.5-m high. The side walls are made up of Perspex which offers good visual

observation of the flow. The experimental run was performed with a bimodal sediment bed: a mixture was made with two different uniform (uniformity coefficient < 1.4) sediment samples of $(d_{50})_1$ = 0.25mm and gravel with $(d_{50})_2$ = 3.5 mm in 1:1 proportion by weight. Hence, the mean size of the sediment was d_{50} = 1.875 mm while a uniformity coefficient could be quantified as $\sigma_g = [(d_{50})_2/(d_{50})_1]^{0.5}$ = 3.7. The ratio between the larger and lower sediment size used in the present experiment is equal to 14. This condition

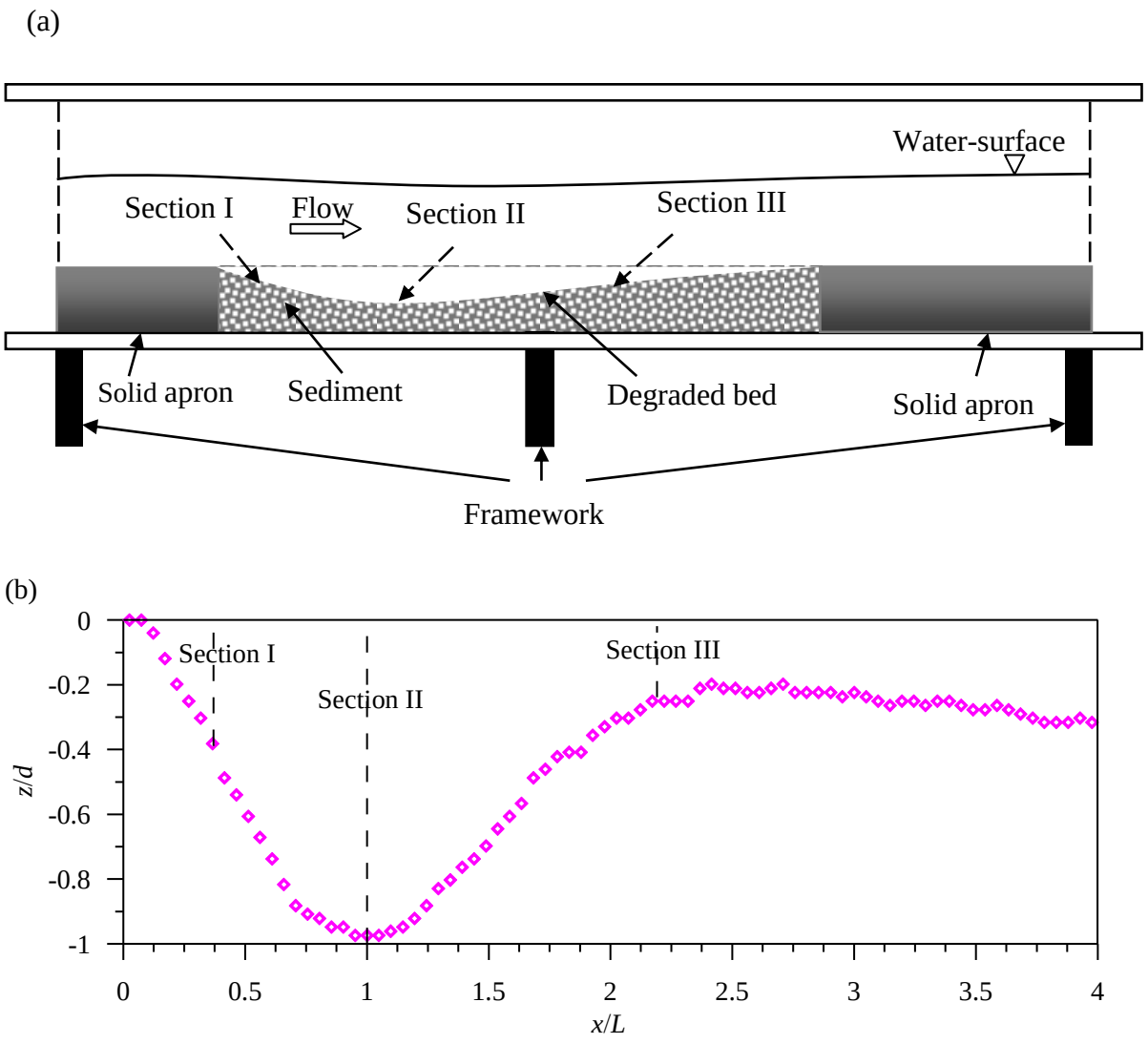

Figure 6.1: (a) Schematic of the test-section for the experiments at the fluvial mechanics laboratory of the Indian Statistical Institute, Kolkata, India. (b) Measured scour profile at the end of the experiment.

reduces a tendency to segregation that could generate streambed armoring, enabling the formation of an equilibrium scour condition with a regular shape.

Two aprons, each of 1 m × 0.2 m × 0.5m in dimensions, were placed upstream and downstream of the test section whose size was 6 m × 0.2 m × 0.5 m. Based on several trials and errors of the experimental configurations, a 20-cm thick sediment bed was prepared with a uniform slope by laying the sediment freely over the floor of the flume. After the bed preparation, water was applied gradually with a centrifugal pump, at a very low velocity to drench the bed completely for a significant time. The water was then drained out completely and the necessary action was taken to fill up the void spaces, if there were any, and necessary adjustment was done to achieve the desired bed-slope. Once the initial bed condition was satisfactory, the discharge for the experiment was applied gradually. Once the predetermined discharge was reached, it was maintained constant for the entire experiment duration. Table 1 shows the initial experimental parameters based on the conditions before the degradation took place. The relative density was s = 2.65 and u_* is the shear velocity calculated from the bed slope before the degradation took place, whereas u_{*c} is the critical shear velocity according to the Shields diagram (Shields 1936, Van Rijin 1984, Dey 2014). The values of the shear velocity and threshold shear velocity indicate that a live-bed regime would have been present in the experiments if a loose bed had not been replaced with an apron. The Reynolds (R) and Froude numbers (F) were calculated as described below Table 1.

Table 6.1: Experimental parameters based on the initial conditions of the experiments

Q (m^3/s)	d_{50} (mm)	d (m)	h (m)	S	$\overline{U}$ (m/s)	u_* (m/s)	u_{*c} (m/s)	F	R	L (m)
0.036	1.875	0.076	0.12	0.0045	0.61	0.073	0.035	0.56	292800	0.39

In Table 1, Q is the discharge, d_{50} = mean sediment size of the bimodal sediment mixture is equal to the mean of $(d_{50})_{sand}$ and $(d_{50})_{gravel}$, Froude number F [= $\overline{U}/(gh)^{0.5}$, where $\overline{U}$ = depth-averaged velocity, g = acceleration due to gravity, h = depth of water above bed-level], Reynolds number R [= $4\overline{U}h/\upsilon$, υ = kinematic viscosity of water =10^{-6} for water at 20°C]. In the above, u_* is the shear velocity calculated from the bed slope before the degradation took place and u_{*c} is the critical shear velocity obtained from the Shields diagram.

Due to the flow, the detachment of the sediment particles started immediately downstream of the first apron. After a significant time, a scour hole (or degraded bed) was created. Figure 6.1(b) shows the measured degraded bed profile at the end of the experiment. The maximum depth of degradation with respect to time was recorded; after a duration of 12 to 14 hours, no more sediment was being eroded indicating achievement of an equilibrium condition. The maximum depth of degradation under such condition was, therefore, considered as the equilibrium depth of degradation.

After reaching equilibrium scour, the three-dimensional velocity components were recorded at three locations (Section I: within the upstream slope of the degraded zone, Section II: at the maximum equilibrium depth of degradation, Section III: in the downstream portion of the degraded zone, see Figure 6.1(b). Three-dimensional velocity was measured using an acoustic Doppler velocimeter, commercially named Vectrino. The Vectrino performs with a rate of acoustic frequency of 10 MHz. Relying upon previous practices, the Vectrino was operated with a data sampling rate of 100 Hz, minimum signal-to-noise ratio of 18, minimum correlation coefficient of 70, and sampling volume with a height of 1–4 mm and diameter of 5 mm. The experimental data were further tested for the uncertainty following the procedure prescribed by Dey et al. (2020) and also adopted by Khan et al. (2021). According to uncertainty estimations, the average of maximum percentage error was within ±5%. These values are within the ranges of acceptability of the measured samples prescribed by Dey et al. (2020). To achieve a time-unbiased average value of the velocity, data were recorded for 180 sat a point. The data used in this manuscript are mostly the untreated raw data to preserve the natural turbulence. However, at some locations the instrument captured a significant amount of spurious data, requiring the application of an appropriate filter (Khan et al. (2021), Pandey et al. (2017)). The acceleration thresholding method (Goring and Nikora) was applied for the data filtering. The identified spurious data were then replaced with values interpolated between neighboring ones. In the present manuscript, the stream-wise, lateral, and vertical velocity components are designated as u, v, and w, while the corresponding coordinates are x, y, and z, respectively.

6.3 Definition framework for total and conditional averaging

This section clarifies how the statistics presented in the manuscript were obtained. We start from a temporal record of (u, v, w) velocity components at one measuring point, for which a single measurement at any instant is then $(u, v, w)_i$. The statistical result from different averaging methods applied to the data. A mean velocity (the stream-wise and vertical components are used here) is:

$$\overline{u} = \frac{\sum_i u_i}{N_{tot}} \text{ and } \overline{w} = \frac{\sum_i w_i}{N_{tot}} \tag{6.1}$$

(note that, unless differently specified, all the sums along i are from 1 to N_{tot}). Velocity fluctuations are instead defined, following the well-known Reynolds decomposition, as:

$$u'_i = u_i - \overline{u} \text{ and } w'_i = w_i - \overline{w} \tag{6.2}$$

6.3.1 Clipping function for quadrant and quadrant relative occurrence

We define a clipping function to label any velocity vector to pertain to a quadrant:

$$\lambda_i^q = 1 \text{ if} (u, w)_i \text{ is} \in \text{quadrant } q, \lambda_i^q = 0 \text{ otherwise} \tag{6.3}$$

As known, an event is in a certain quadrant if it complies with the following definitions: Quadrant 1 (i. e., q= 1) signifies outward interactions where u', w'> 0; Quadrant 2 signifies ejections where u'< 0, w'> 0; Quadrant 3 signifies inward interactions where u', w'< 0; eventually, Quadrant 4 signifies sweeps where u'> 0, w'< 0as shown in Figure 6.2. Our use of a clipping function is analogous to prior ones made in conditional analyses to discriminate the values that shall be considered in an average and those that shall not. For example, Cellino and Lemmin (2004) and Dey et al. (2020) introduced a discriminating function that took a value of 1 if any velocity fluctuation product was in a certain quadrant and exceeded a threshold magnitude. Here we indeed take a similar approach, not imposing a magnitude threshold at this stage (the use of a hole will be treated systematically in the second part of the manuscript, extending the definition framework).

After determining the clipping function, we define a percentage occurrence for a quadrant as:

$$p^q = \frac{\sum_i \lambda_i^q}{N_{tot}} \tag{6.4}$$

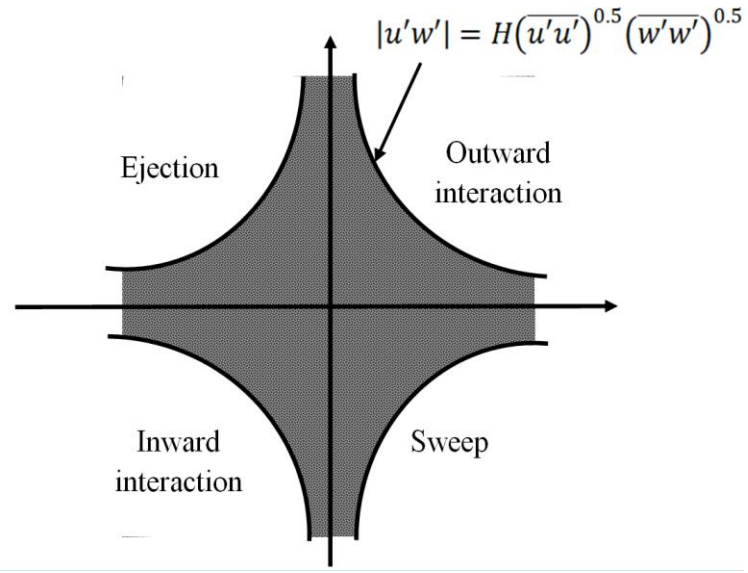

Figure 6.2: Definition sketch of the quadrant analysis. Redrawn from Lu and Willmarth (1973)

This definition implies that$\sum_q p^q = 1$ (where the sum along q is from 1 to 4).

6.3.2 Duration and frequency of events

The relative occurrence of events in any quadrant, just defined, represents the total time for which, within a certain duration, an event in that quadrant occurs. Here the term 'event' is used for a single measurement of instantaneous velocity; events in a certain quadrant may persist for sometime (which would be represented by clusters of consecutive 1 value in the clipping functions). We, therefore, define a mean duration of a cluster of events in a same quadrant. In order to determine this duration, we need to pass from observing the flow events instantaneously to observing their transitions. Naming e^q the number of times in which the λ^q function switches from 0 to 1, the mean time duration of a cluster of events in a certain quadrant is computed as:

$$d^q = \frac{T \times p^q}{e^q} \tag{6.5}$$

where T is the duration of the observation. Furthermore, the appearance of a cluster of events in a certain quadrant may be more or less frequent. Therefore, we also define a frequency that is the inverse of the mean time between two successive switches of the velocity fluctuations to a certain quadrant. This frequency is quantified as:

$$f^q = \frac{e^q}{T} \tag{6.6}$$

leading to $d^q \times f^q = p^q$.

6.3.3 Conditional mean velocity

We define two conditional mean velocities, depending on the denominator one uses to normalize a sum of measured values. The first mean is:

$$\overline{u}^q_{tot} = \frac{\sum_i u_i \lambda_i^q}{N_{tot}} \tag{6.7}$$

The second mean is instead:

$$\overline{u}^q_{quad} = \frac{\sum_i u_i \lambda_i^q}{\sum_i \lambda_i^q} = \frac{\sum_i u_i \lambda_i^q}{p^q N_{tot}} = \frac{\overline{u}^q_{tot}}{p^q} \tag{6.8}$$

Since$p^q < 1$, it will be $\overline{u}^q_{quad} > \overline{u}^q_{tot}$. The two means have different conceptual meaning; the $\overline{u}^q_{tot}$ is a 'total-averaged conditional mean' (that considers the entire duration of the measurement), while the $\overline{u}^q_{quad}$ is a 'quadrant-averaged conditional mean' (that corresponds to the mean velocity one has in a quadrant considering just the period for which events in that quadrant occur). The mean from eq. (6.7) was used, for example, by Dey et al. (2011), while that from eq. (6.8) was employed, for example, by Padhi et al. (2019) and Dey et al. (2020). This applies to all the following distinctions between total-averaged and quadrant-averaged conditional quantities.

Similarly, we define the two conditional mean velocities in the vertical direction as:

$$\overline{w}^q_{tot} = \frac{\sum_i w_i \lambda_i^q}{N_{tot}} \tag{6.9}$$

and

$$\overline{w}^q_{quad} = \frac{\sum_i w \lambda_i^q}{\sum_i \lambda_i^q} = \frac{\sum_i w_i \lambda_i^q}{p^q N_{tot}} = \frac{\overline{w}^q_{tot}}{p^q} \tag{6.10}$$

6.3.4 Reynolds stresses and conditional Reynolds stresses

A Reynolds stress (here we discard $-\rho$ as a multiplying constant) results from a time average of a product of velocity fluctuations. The Reynolds normal stress (RNS) in the stream-wise direction is:

$$\overline{u'u'} = \frac{\sum_i (u\prime u\prime)_i}{N_{tot}} \tag{6.11}$$

As for velocity, also for stream-wise Reynolds normal stress we can define two conditional means:

$$\overline{u'u'}^q_{tot} = \frac{\sum_i (u\prime u\prime)_i \lambda_i^q}{N_{tot}} \tag{6.12}$$

$$\overline{u'u'}^q_{quad} = \frac{\sum_i (u\prime u\prime)_i \lambda_i^q}{\sum_i \lambda_i^q} = \frac{\sum_i (u\prime u\prime)_i \lambda_i^q}{p^q N_{tot}} = \frac{\overline{u\prime u\prime}^q_{tot}}{p^q} \tag{6.13}$$

Again, it will be that $\overline{u'u'}^q_{quad} > \overline{u'u'}^q_{tot}$. Keeping the same denominator in (6.11) and (6.12) implies that $\sum_q \overline{u'u'}^q_{tot} = \overline{u'u'}$. Therefore, conceptually the use of a total-averaged conditional Reynolds stress is supported by the fact that the sum of the conditional stresses equals the unconditional stress; on the other hand, the quadrant-averaged Reynolds stress represents the actual stress magnitude one has during occurrence of events in a certain quadrant.

Analogously, the RNS in the vertical direction is:

$$\overline{w'w'} = \frac{\sum_i (w\prime w\prime)_i}{N_{tot}} \tag{6.14}$$

and the conditional mean for the vertical RNS can be defined as:

$$\overline{w'w'}^q_{tot} = \frac{\sum_i (w\prime w\prime)_i \lambda_i^q}{N_{tot}} \tag{6.15}$$

$$\overline{w'w'}^q_{quad} = \frac{\sum_i (w\prime w\prime)_i \lambda_i^q}{\sum_i \lambda_i^q} = \frac{\sum_i (w\prime w\prime)_i \lambda_i^q}{p^q N_{tot}} = \frac{\overline{w\prime w\prime}^q_{tot}}{p^q} \tag{6.16}$$

Finally, the Reynolds shear stress (RSS) is:

$$\overline{u'w'} = \frac{\sum_i (u\prime w\prime)_i}{N_{tot}} \tag{6.17}$$

with two conditional means defined as follows:

$$\overline{u'w'}^q_{tot} = \frac{\sum_i (u\prime w\prime)_i \lambda_i^q}{N_{tot}} \tag{6.18}$$

$$\overline{u'w'}^{q}_{quad} = \frac{\sum_i (u\prime w\prime)_i \lambda_i^q}{\sum_i \lambda_i^q} = \frac{\sum_i (u\prime w\prime)_i \lambda_i^q}{p^q N_{tot}} = \frac{\overline{u\prime w\prime}^{q}_{tot}}{p^q} \tag{6.19}$$

6.3.5 Kinetic energy fluxes

We introduce the sum of the product of squared velocity fluctuations:

$$k' = 0.5 \times [(u'u') + (v'v') + (w'w')] \tag{6.20}$$

The stream-wise flux of turbulent kinetic energy (TKE) is thus:

$$\overline{k'u'} = \frac{\sum_i (k\prime u\prime)_i}{N_{tot}} \tag{6.21}$$

As for velocity and Reynolds stress, again we can define two conditional means changing the denominator:

$$\overline{k'u'}^{q}_{tot} = \frac{\sum_i (k\prime u\prime)_i \lambda_i^q}{N_{tot}} \tag{6.22}$$

$$\overline{k'u'}^{q}_{quad} = \frac{\sum_i (k\prime u\prime)_i \lambda_i^q}{\sum \lambda_i^q} = \frac{\sum_i (k\prime u\prime)_i \lambda_i^q}{p^q N_{tot}} = \frac{\overline{k\prime u\prime}^{q}_{tot}}{p^q} \tag{6.23}$$

Again, it will be that $\overline{k'u'}^{q}_{quad} > \overline{k'u'}^{q}_{tot}$ and that the sum along q of the means from (6.22) equals the value from (6.21).

Analogously for vertical flux of kinetic energy is:

$$\overline{k'w'} = \frac{\sum_i (k\prime u\prime)_i}{N_{tot}} \tag{6.24}$$

and the conditional means are:

$$\overline{k'w'}^{q}_{tot} = \frac{\sum_i (k\prime w\prime)_i \lambda_i^q}{N_{tot}} \tag{6.25}$$

$$\overline{k'w'}^{q}_{quad} = \frac{\sum_i (k\prime w\prime)_i \lambda_i^q}{\sum \lambda_i^q} = \frac{\sum_i (k\prime w\prime)_i \lambda_i^q}{p^q N_{tot}} = \frac{\overline{k\prime w\prime}^{q}_{tot}}{p^q} \tag{6.26}$$

6.4 Results and discussion

6.4.1 Average flow field

The vertical profiles of the time-averaged stream-wise velocity component computed by Eq. (1) are shown in Figure 6.3(a-f), together with other quantities that will be discussed later, for the three different sections (Sections I, II, III). The vertical distance z was made dimensionless by maximum depth of degradation d under the equilibrium condition (with $z = 0$ at the initial bed level); the velocity values were divided by the friction velocity, even if this parameter is a constant since we are presenting one experiment. Interestingly, for $z/d > 0.2$, the stream-wise velocity component was quite similar at sections I and III, since these sections were close to the upstream and downstream edges of the degraded zone. At section II, the stream-wise velocity component for $z/d > 0.2$ is slightly less than at the other sections (due to flow expansion), but still similar (as if a jet was present in the upper layer of the flow and the length of the scour hole was insufficient for full mixing). Since velocity needs to be zero at the contact with the sediment, the velocity gradient for $z/d < 0$ was largest at section III and lowest at section II. The stream-wise velocity component took a slightly negative value only close to the sediment bed at section I, evidencing a small recirculation after a flow separation from the upstream edge of the scour hole.

The time-averaged vertical velocity component, depicted in Figure 6. 4(a-f), was negative at all elevations and sections, even though close to the surface its magnitude at section III was lower than at sections I and II, indicating that at section III the flow was reasonably recovering from the effect of degradation. The magnitudes of $\overline{w}$ were, however, much lower than those of $\overline{u}$.

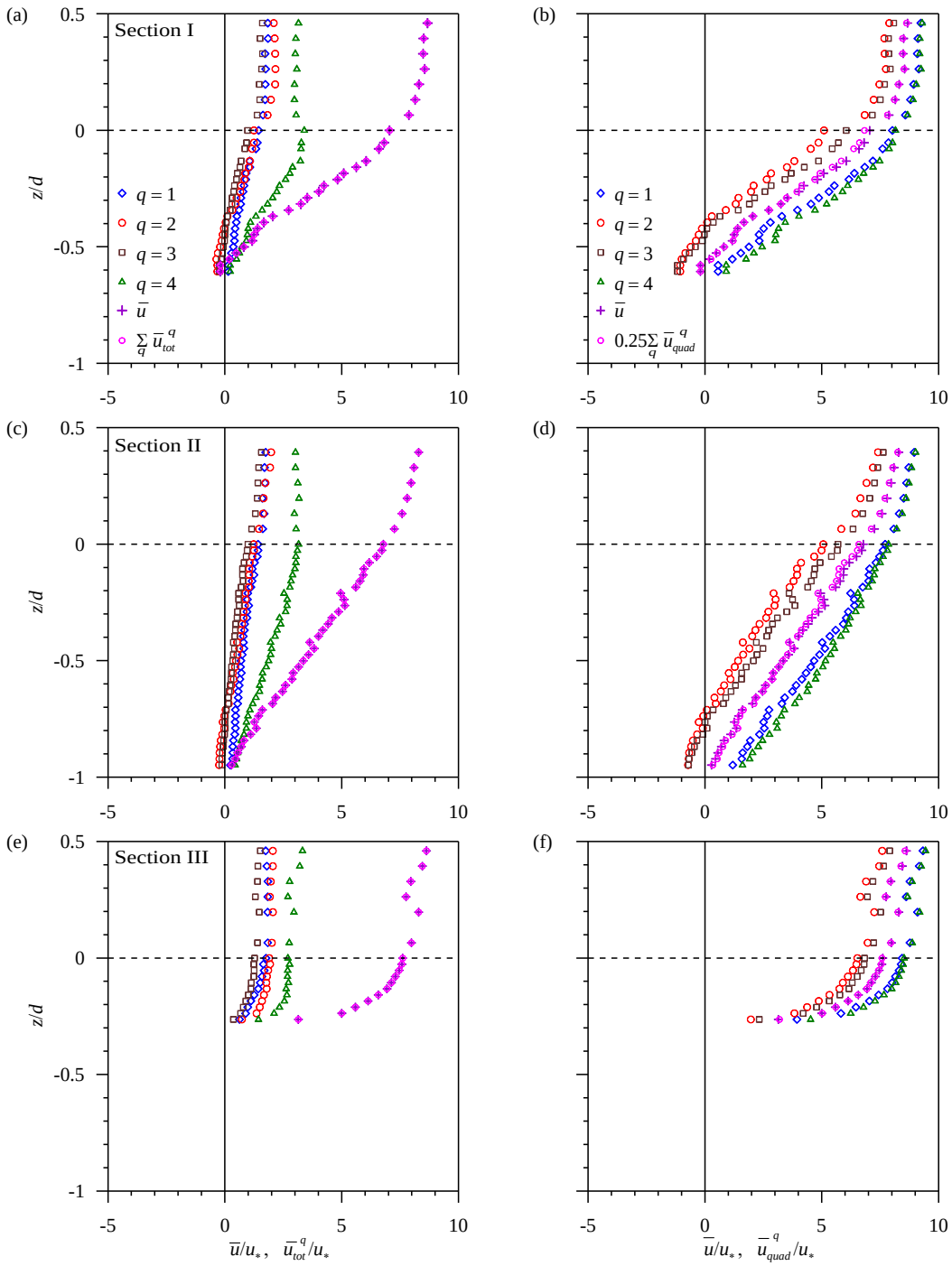

Figure 6.3: (a-f) Vertical distributions of unconditional and conditional stream-wise velocity components using Equations (6.7) and (6.8), respectively.

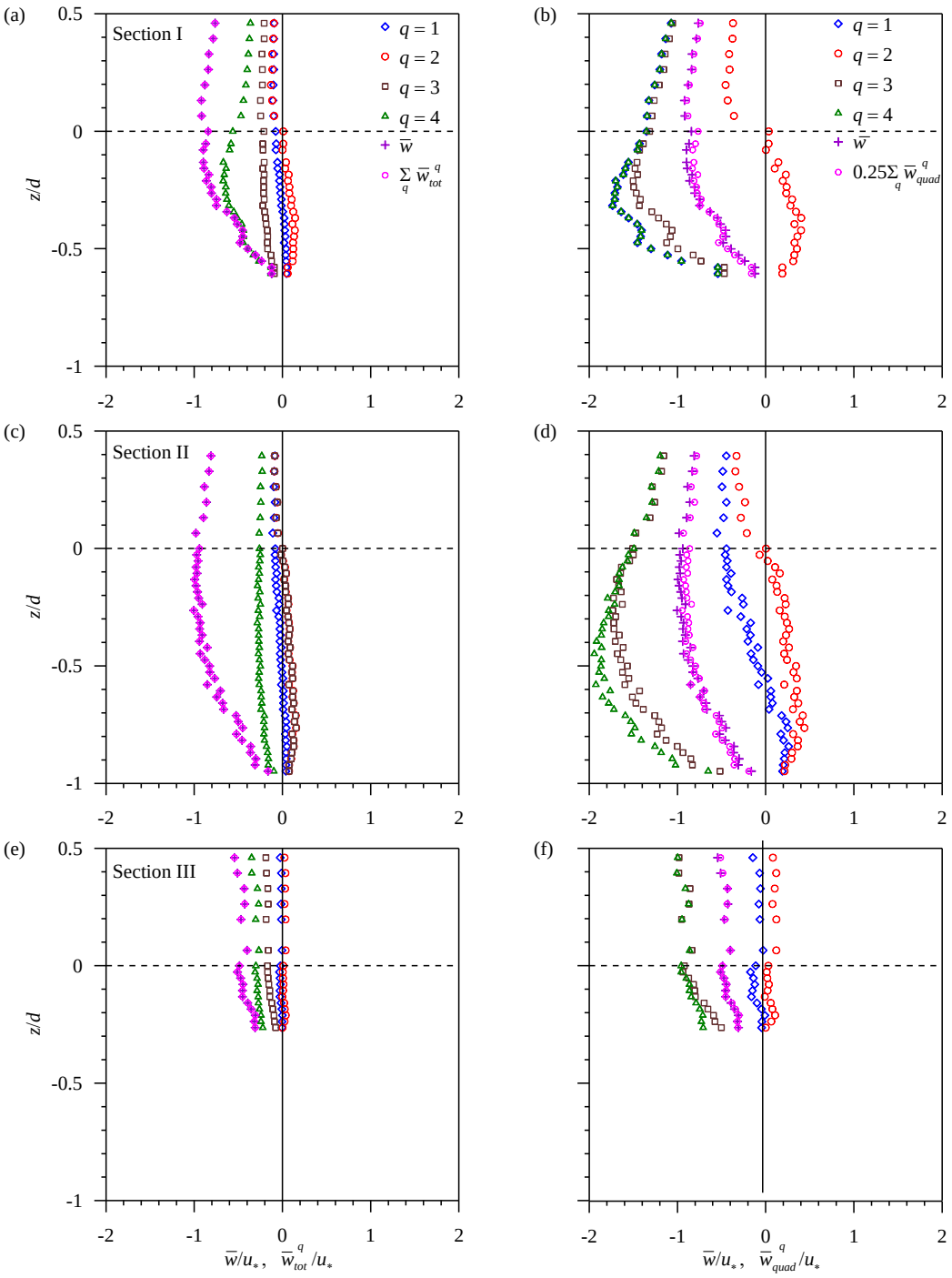

Figure 6.4: (a-f) Vertical distributions of unconditional and conditional vertical velocity components using Equations (6.9) and (6.10), respectively.

6.4.2 Percentage occurrence of events in the quadrants

Figure 4. 5 depicts the vertical profiles of quadrant percentage occurrence as determined by Eq. (4). For the highest elevations, the percentages were similar at sections I to III, with outward and inward interactions at around 20%, ejections between 25 and 30%, sweeps between 30 and 35%. Generally, ejection and sweep events mainly compose the bursting events and were significantly more occurring than outward and inward interactions. At sections I and II and just below the original bed elevation, a peak in the percentage occurrence of sweeps (that were the most frequent events with a percentage occurrence of up to almost 45%) was consistent with the penetration of the upper flow into the scour hole. Close to the sediment bed, instead, ejection events were the most occurring ones (again, particularly at sections I and II), with percentage occurrences of up to 35–40%. A cross-over in the sweep and ejections took place at z/d = -0.3 and -0.6 at sections I and II, respectively. The profiles of the occurrence of inward and outward interactions were more uniform than those of sweeps and ejections.

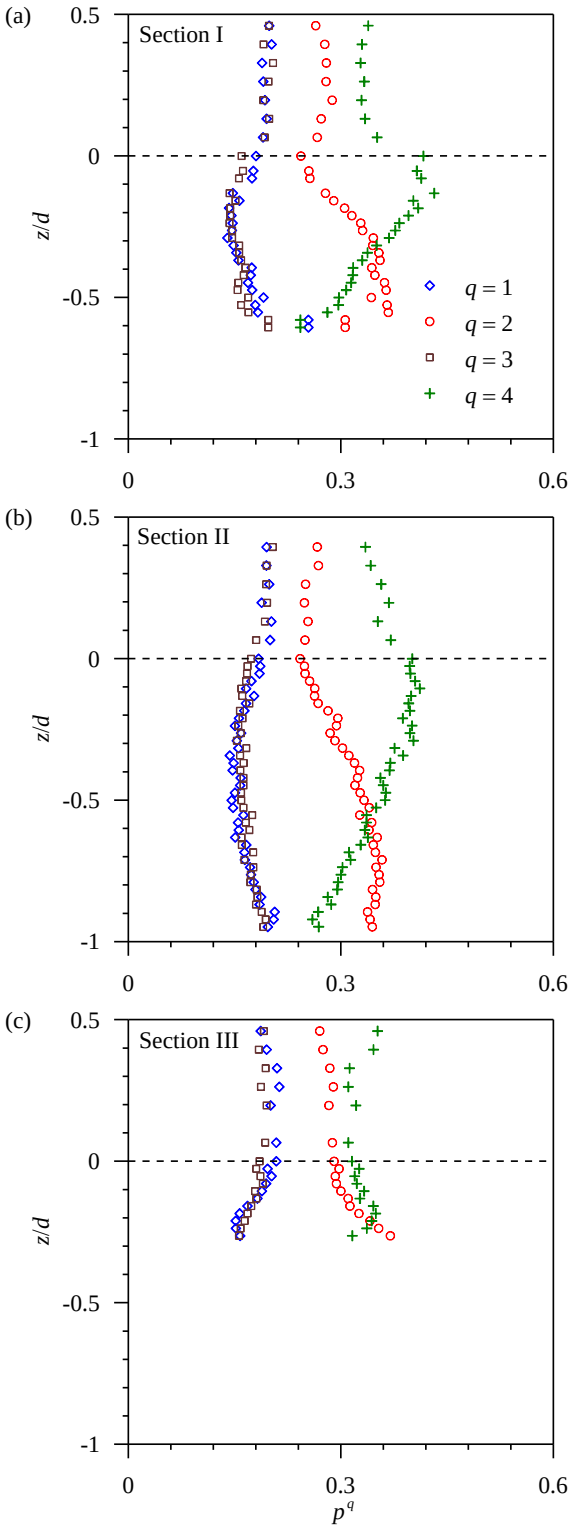

Figure 4.5: Percentage occurrence of the events in any quadrant for the three sections using Equation. (6.4).

6.4.3 Mean duration and frequency of event clusters

Vertical profiles of the mean duration of clusters of flow events, computed as per eq. (6.5), are depicted in Figure 6.6(a,c,e). From the plot it results that sweep and ejection events were not only characterized by larger relative occurrence, but their clusters were also lasting longer than those of the other events (in other words, sweeps and ejections presented a larger temporal coherence than outward and inward interactions). The mean duration of sweeps and ejections was between 0.03 and 0.07 s for the sections at which the flow was measured in this study.

Figure 6.6(b,d,f) presents instead the frequency of occurrence of a transition of the flow to a certain event, as determined by Eq. (6.6). Differently from what happened for the percentage occurrence and the mean duration presented above, the vertical profiles of the frequency were similar for all the events, corresponding to the frequency of the burst cycle at any certain location. For sections I and II the frequency was lower close to the bed and increasing for progressively higher elevation, while for the section III the behavior was the opposite. Characteristic frequencies were in the order of some Hz, indicating that the sampling frequency adopted in the present study (100 Hz) was high enough to observe the succession of burst cycles.

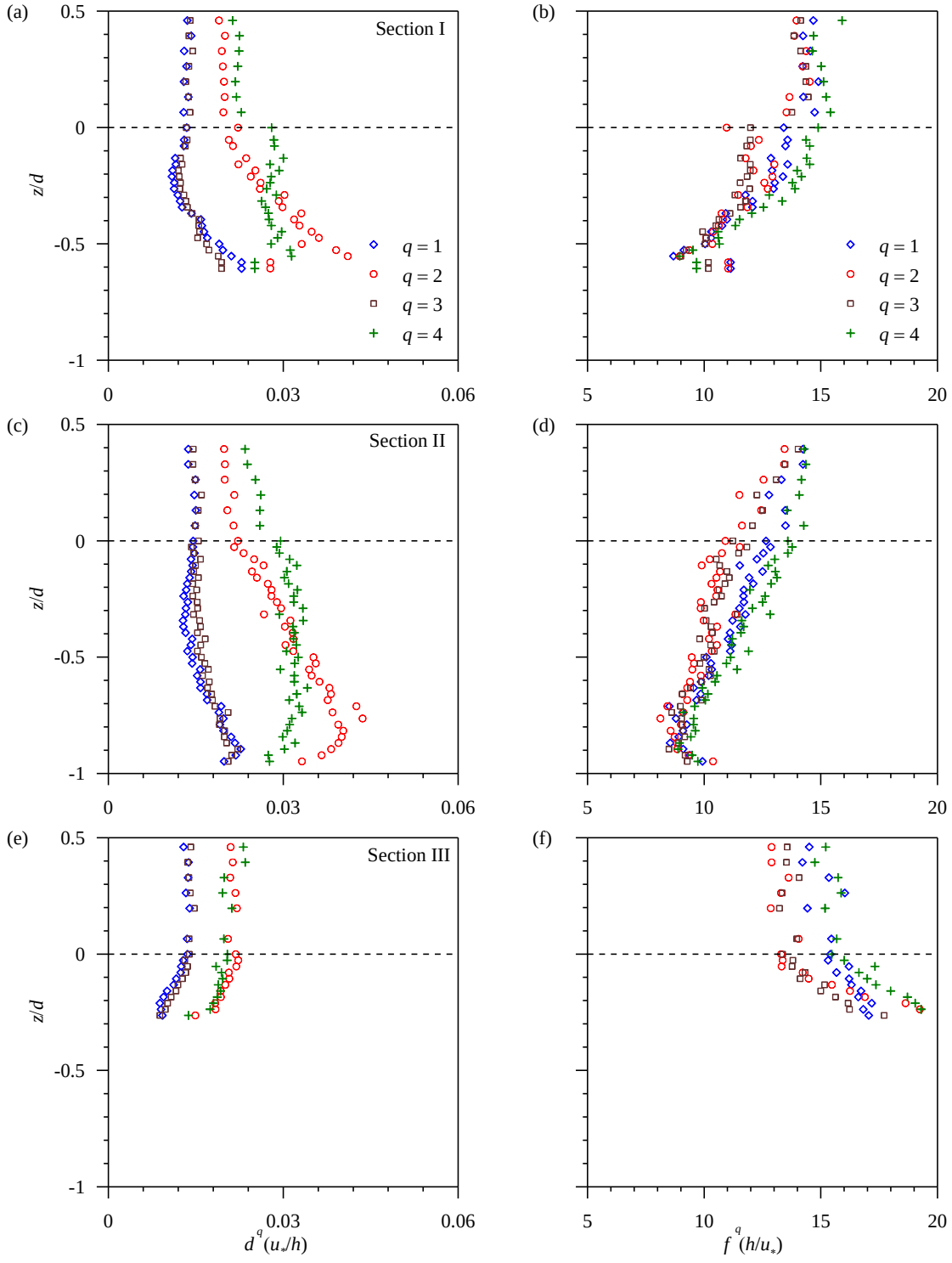

Figure 6.6: Mean duration and frequency of the event clusters in any quadrant for the three sections using Equations (6.5) and (6.6), respectively.

6.4.4 Total-averaged and quadrant-averaged conditional velocity components

Figure 6.3(a–f), already presented above to describe the average flow field, also includes the vertical profiles of the conditional stream-wise velocity computed by (6.7), that is the total-averaged conditional mean $\overline{u}_{tot}^{q}$, and (6.8), that is the quadrant-averaged conditional mean$\overline{u}_{quad}^{q}$.

We first use the results at section I to clarify how the different averaging methods work. In panel (a), the conditional means are generally lower than the total mean $\overline{u}$, with the exception of the lowest locations where negative values for $\overline{u}_{tot}^{2}$ and $\overline{u}_{tot}^{3}$ are compensated by values larger than $\overline{u}$ for $\overline{u}_{tot}^{1}$ and $\overline{u}_{tot}^{4}$ (since, as mentioned above, by definition the sum of the total-averaged conditional means equals the total mean, as checked with the last depicted series).

In panel (b), instead, $\overline{u}_{quad}^{1}$ and $\overline{u}_{quad}^{4}$ are by definition larger than $\overline{u}$, the opposite happening for $\overline{u}_{quad}^{2}$ and $\overline{u}_{quad}^{3}$. The total mean velocity is further compared to the arithmetic mean of the four quadrant-averaged conditional means; the two quantities are similar but not the same (because the total mean velocity is actually equal to a weighted mean of the quadrant-averaged conditional means, the weight being the percentage occurrence of the events in any quadrant); for first moments, like average velocities, the difference between the total mean and the mean of the conditional means is not large. The use of one or the other conditional mean may reveal different relationships between the events in close quadrants: for example, in panel (a) $\overline{u}_{tot}^{4}$ is much larger than $\overline{u}_{tot}^{1}$, because sweeps are more numerous than outward interactions; by contrast, in panel (b) $\overline{u}_{quad}^{4}$ and $\overline{u}_{quad}^{1}$ are quite similar to each other, because the different percentage occurrence of the events in the two quadrants is accounted for.

For the highest elevations, the stream-wise conditional velocity components are quite similar at all the sections, as already mentioned for the total mean. Furthermore, the quadrant-averaged conditional means return, at all sections and locations, $\overline{u}_{quad}^{4}>\overline{u}_{quad}^{1}>\overline{u}_{quad}^{3}>\overline{u}_{quad}^{2}$, indicating that sweeps and ejection events take place with

the highest and lowest stream-velocity, respectively. These results are consistent with, among others, the experimental findings of Cellino and Lemmin (2004) in suspended sediment flow, Dey et al. (2020) for flow over dunes and Padhi et al. (2019) for water-worked and screeded bed flow. In addition, at sections I and II, close to the sediment bed, $\overline{u}^2_{quad}$ and $\overline{u}^3_{quad}$ (also $\overline{u}$ at section I, as already mentioned above) take negative values, clearly demonstrating a flow reversal that can be a strong contribution to vortex formation. Figure 6.3(b,d,f) also show that, at all the sections, all the quadrant-averaged conditional means have a vertical profile similar to that of the mean velocity $\overline{u}$. This also agrees with the findings of Cellino and Lemmin (2004), Padhi et al. (2020) and Dey et al. (2020). The magnitudes of the stream-wise velocity at Section III are higher than those at Sections I and II when considered at a particular vertical distance. This finding indicates that the decaying of the jet-like flow and bed degradation is taking place with increasing of stream-wise distances from the maximum degraded bed (Jain et al. 2015, Sarkar et al. 2021).

The profiles of the vertical velocity component are shown in Figure 6.4(a–f) for the three measuring sections. The considerations made above for the different trends returned using the total-averaged and the quadrant-averaged conditional mean are valid also for *w*. For example, panels (a) and (b) show that passing from the total-averaged conditional mean to the total-averaged one largely reduces the difference between the conditional vertical velocity for sweeps and inward interactions, as discussed with reference to the stream-wise velocity component for sweeps and outward interactions.

For the highest elevations, the conditional mean velocity components were similar at sections I and II, while they were generally higher at section III. Since the general flow pattern indicates a down-flow at all the section and elevations, the vertical velocity component for outward interactions and ejections might be also negative. The traditional interpretation given for one-directional boundary layers over a flat bed, according to which events in quadrants 1 and 2 imply an upward momentum transfer, may be not extended to some portions of the present flow field. However, close to the sediment bed the outward interactions and the ejections presented positive values for the vertical velocity component. Differently from what happened for the stream-wise component, the profiles of the conditional mean velocity components were not similar in shape to that of

the mean velocity component; particularly at sections I and II, they presented a peak in absolute value, at variable distance from the bed.

6.4.5 Reynolds stresses

We first report the results for the normal, stream-wise RNS, then move to the vertical one and finally to the RSS in the *x*-*z* plane.

The vertical distributions of the stream-wise RNS at Sections I, II and III are shown in Figure 6.7(a–f). The panels on the left show the total-averaged conditional RNS; summing the values for the four quadrants again returns $\overline{u'u'}$. The panels on the right instead show the quadrant-averaged conditional RNS, whose mean value over the quadrants is close to $\overline{u'u'}$. At sections I and II, the RNS profiles attained a peak below the initial bed level. Ejections and sweeps were the events with largest RNS, with the former presenting a higher peak value (for example, 7.51 and 5.63) at section II) at higher elevation (for example, at z/d of around -0.3 and -0.6 at section II) than the latter. The vertical profiles at section III were different from those at the previous sections, since here the flow was getting back towards a non-eroded bed; at section III a weak peak was attained a bit closer to the initial bed level (but this may be due to the fact that the bed degradation is much lower than that at the other sections), and the RNS values were significantly lower than those at the other sections (also confirming higher turbulence for decelerating than for accelerating flows). Owing to the influence of bed degradation, strong turbulence mixing amplified the velocity perturbation that enhanced the stream-wise RNS below the initial bed level. Above the latter, decaying of the turbulence mixing became responsible in decreasing the stream-wise perturbation and dampened the conditional and total stream-wise RNS. For the highest elevations, the stream-wise RNS was generally small and similar at all the measuring sections.

Near the bed, the high-speed fluid streaks moved from upstream toward the wall, sweeping away the slowly moving fluid left from the preceding ejections. On the other hand, at higher elevations, the low-speed fluid streaks were ejected from the near-wall and entered into the fluid zone. Close to the sediment bed, sweeps were the events

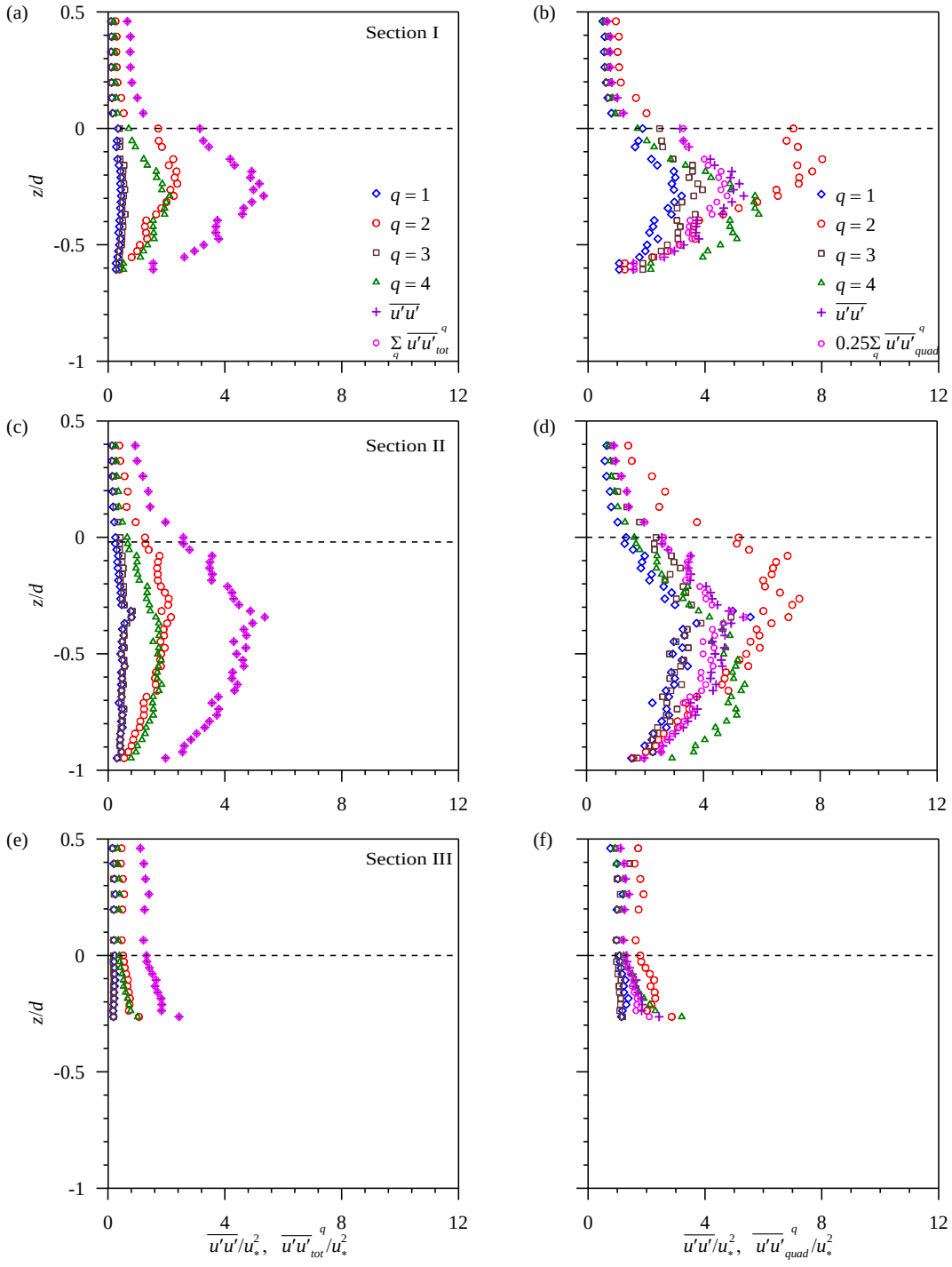

Figure 6.7: (a–f) Vertical distributions of unconditional and conditional Reynolds stream-wise stresses using Equations (6.12) and (6.13), respectively.

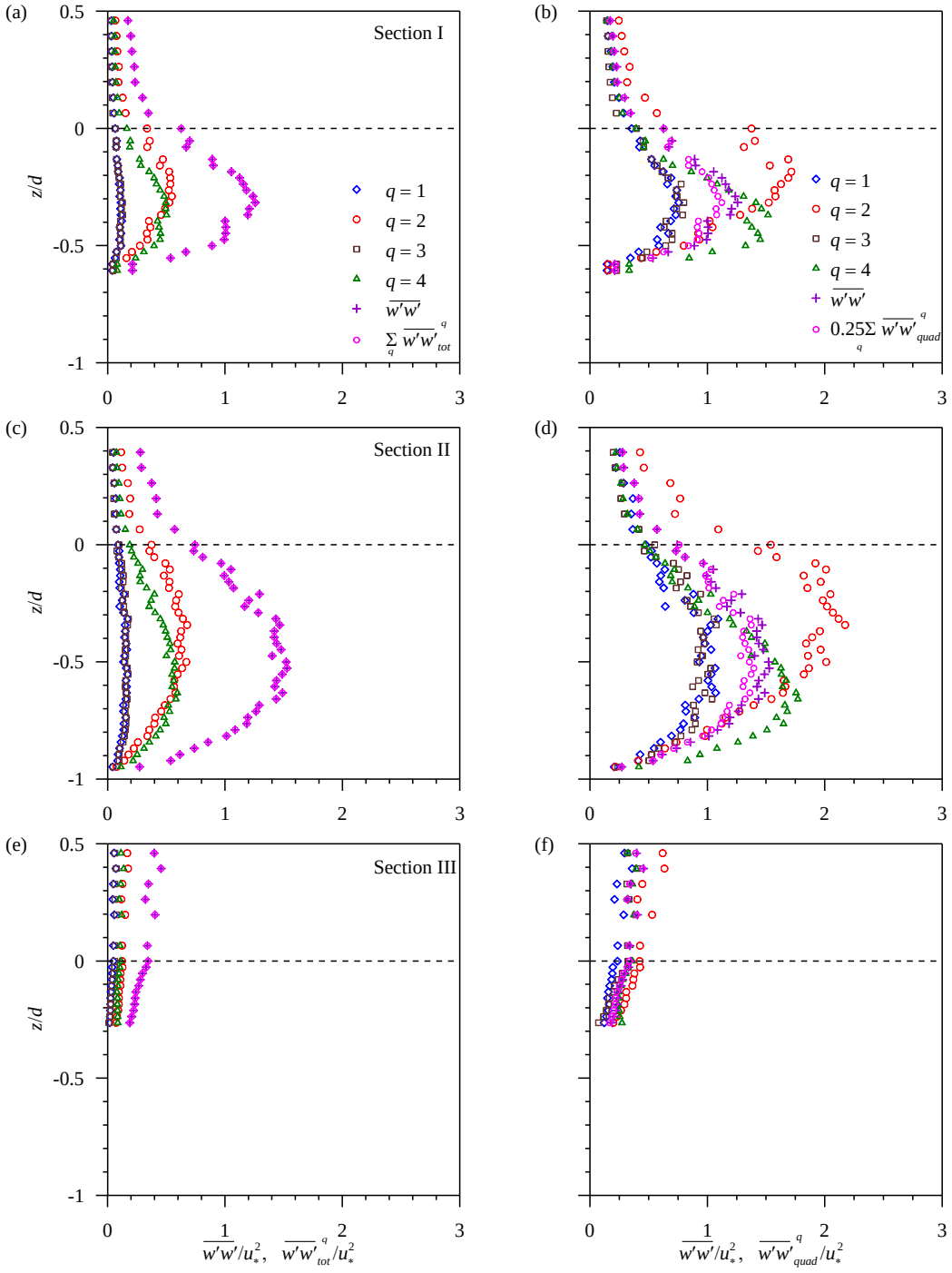

Figure 6.8: (a–f) Vertical distributions of unconditional and conditional Reynolds vertical stresses using Equations (6.15) and (6.16), respectively

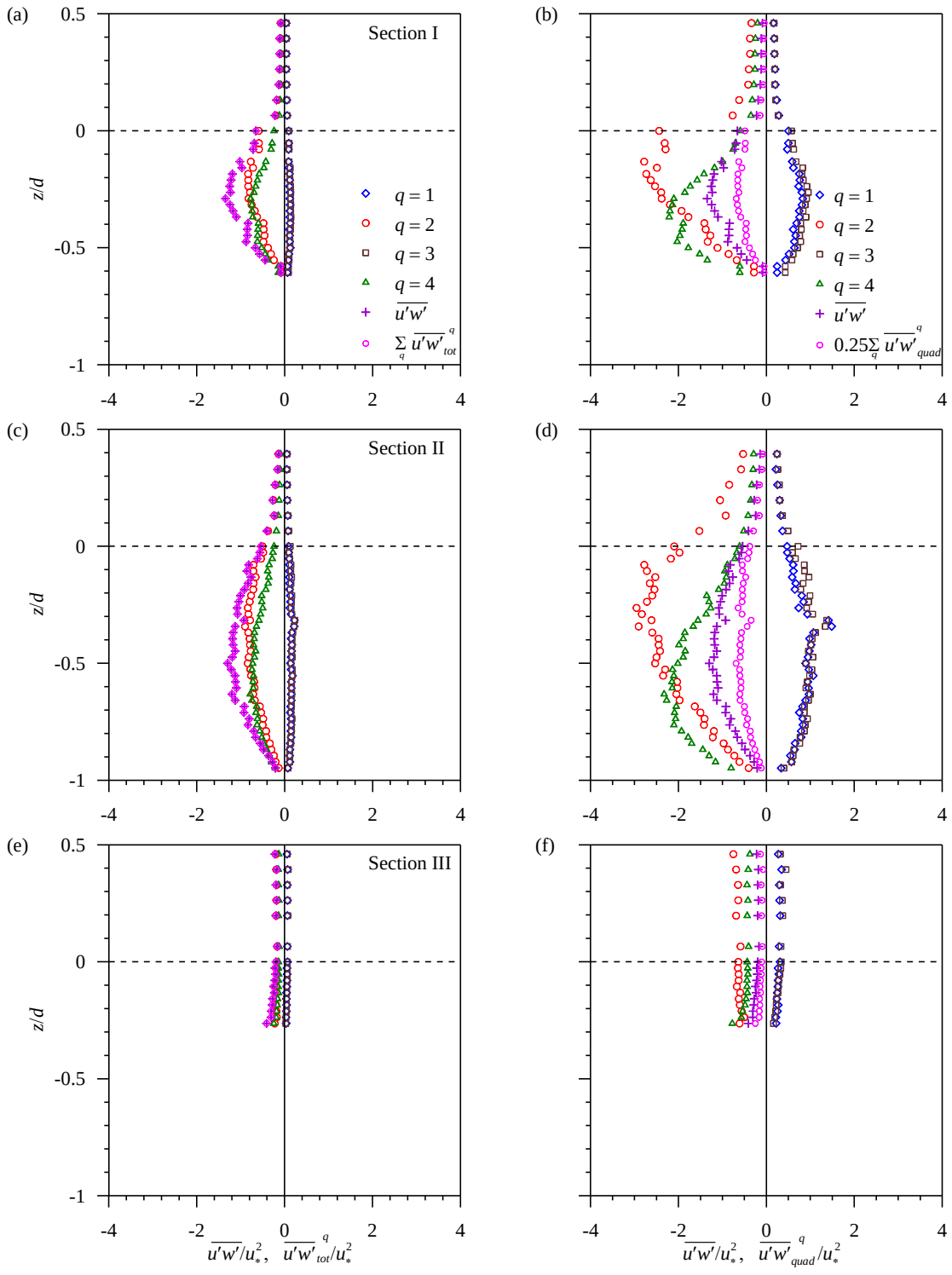

Figure 6.9: (a–f) Vertical distributions of unconditional and conditional Reynolds shear stresses using Equations (6.18) and (6.19), respectively.

determining the highest conditional stream-wise RNS. The near-bed region where sweeps were stronger than ejection had a thickness (in terms of z/d) of around 0.3 and around 0.5 at sections I and II, respectively. The larger thickness at section II was related to the lower bed elevation at that section.

Figure 6.8(a–f) depicts the profiles of the vertical RNS at the measuring sections. At sections I and II the profiles of the vertical RNS were similar in shape to those of the stream-wise RNS, but the values were about 4 times lower. Instead, the profiles at section III differed from the corresponding ones for the stream-wise RNS (the vertical RNS was larger for increasing elevation), even though also for the vertical RNS section III returned completely different profile and values compared to I and II, given a reduced influence of degraded region. Close to the bed, also for the vertical RNS sweeps were the dominant events at sections I and II, ejections prevailing for increasing distance from the bed. This result shows consistency with those of Padhi et al. (2019).

Lastly, the vertical distributions of the RSS are shown in Figure 6.9(a–f). The RSS is the first quantity for which we detected a significant difference between the mean of the quadrant-averaged conditional stresses and the total mean, due to this stress involving velocity fluctuations along two directions. At sections I and II the stress profiles attained a peak below the initial bed elevation; in fact, in the degraded region nearby or slightly below the initial bed level occurrences of strong turbulence mixing enlarged the magnitude of u' and w' in agreement with Dey and Ali (2019). The peak values were lower than those for the stream-wise RNS and larger than those for the vertical RNS (for example, for ejection at section II the peak value was around 7.51 for the stream-wise RNS, 2.81 for the RSS and less than 1.88 for the vertical RNS), consistently with the prevailing direction of motion. The profiles at section III were again markedly different from those at the other sections.

Ejection and sweep events were those with the highest RSS values. As it was for the RNS components, close to the bed the sweep events were the strongest ones, with ejections instead prevailing for increasing distance from the bed. This result shows consistency with those of Mignot et al. (2009), Padhi et al. (2019), and Dey et al. (2020). Also, at

sections I and II, $\overline{u'w'}^4_{quad}$ and $\overline{u'w'}$ took very similar values from slightly below the initial bed level to the highest elevations. This is quite different from the findings of Padhi et al. (2019) and Mignot et al. (2009) . The RSS production within this region was dominated by the bed degradation and the ejections.

6.4.6 Turbulent kinetic energy fluxes

Figure 6.10(a–f) depicts the profiles of the dimensionless stream-wise and vertical TKE fluxes obtained at Section I, II and III. After clarifying for the previous quantities how the plots change applying total-averaging and quadrant-averaging for conditional means, in this case we show for brevity only the quadrant-averaged conditional fluxes. Obviously, the conditional fluxes cannot change sign along the vertical direction because *k′*, that is not a fluctuation in the sense of the other ones (deviation from a mean value), is inherently positive; therefore, the sign of a conditional TKE flux corresponds to that of the considered velocity component fluctuation (that is imposed by definition). By contrast, the signs of the unconditional fluxes computed by (6.21) and (6.24) typically change with elevation.

For example, from Figure 6.10(a,c,e) one sees that at sections I and II the stream-wise fluxes were mostly related to ejections and sweeps, with ejections reaching larger peaks than sweeps (in absolute value). Peak values for ejections and sweeps at sections I and II were similar, but they were detected at different elevations. First, passing from section I to section II the peaks were at lower *z*/*d* for a same quadrant, due to a higher scour depth; second, in any section the peak elevation for sweeps was lower than that for ejections. As a result, the profile for the total fluxes took a sinuous shape, containing both peaks: close to the degraded bed (at section I and II) the stream-wise TKE flux was positive, while it became negative for larger distance from the bed. Furthermore, the profiles for $\overline{k'u'}^1_{quad}/u_*^3$ and $\overline{k'u'}^3_{quad}/u_*^3$ almost mirrored each other, suggesting that inward and outward interactions had minimal contribution to the total flux. The result is totally agreeing with those presented above for the RSS. Finally, the profiles at section III clearly demonstrated the decaying influence of bed degradation with stream-wise distances.

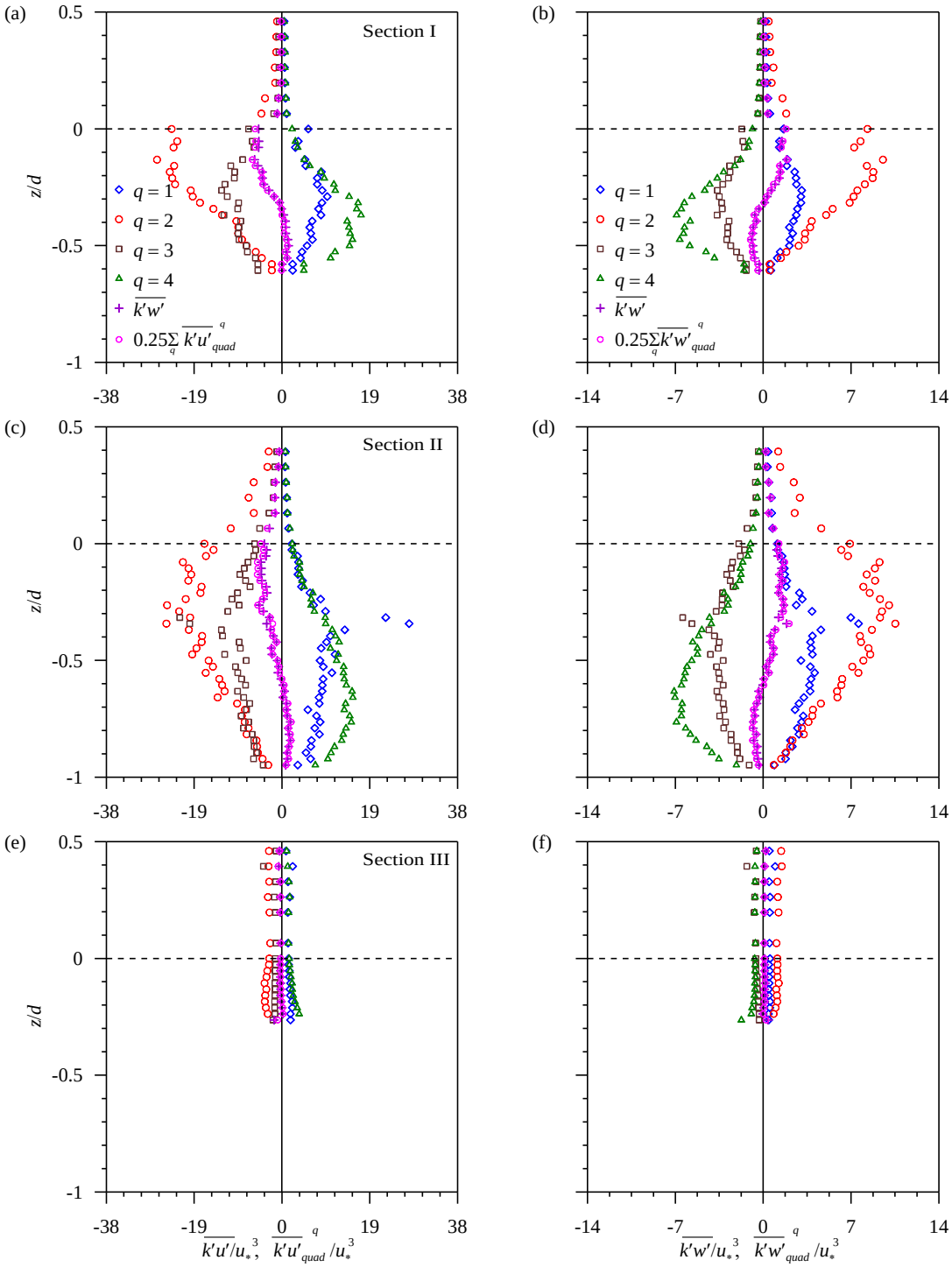

Figure 6.10: (a–f) Vertical distributions of unconditional and conditional (quadrant-averaged) stream-wise TKE fluxes using Equation (6.23) and vertical TKE fluxes using Equation (6.26).

Figure 6.10(b, d, f) shows corresponding results for the vertical TKE flux, indicating similar features to those reported for the stream-wise component. At sections I and II the vertical TKE flux was negative close to the bed and positive for higher elevations. Also for the vertical TKE flux, the profiles for inward and outward interactions mirrored each other and the magnitudes at section III were much lower than those at the other sections. The magnitudes of the vertical TKE flux were, expectedly, much lower than those of the stream-wise flux.

6.5 Relevance of conditional analysis with different averaging approaches

The general characteristics revealed for the flow under investigation are as follows: an upper layer ($z > 0$) is present with similar properties at all sections, probably resembling the properties of the incoming flow; a mixing layer is located a little below the initial bed level, where ejections are the prevailing events, possibly in relation to entrainment of low-momentum fluid into upper layers; close to the bed, sweep events dominate; the flow is highly turbulent in the expansion portion (sections I and II), recovering to low turbulence in the contraction portion (section III). Furthermore, total-averaged and quadrant-averaged means return the expected relationships with the global turbulence indicators: as mentioned, total-averaged ones, that have always the total sample size at the denominator, equal the total quantity once summed but, on the other hand, they are not representative of what actually happens in a certain quadrant; conversely, quadrant-averaged properties correspond to the real magnitude these events have on average, and are similar to the global quantities once a mean is computed over the quadrants. Unconditional and (total- or quadrant-averaged) conditional indicators may be more or less significant in relation to the interactions between the flow and other bodies. One could consider, for example, fish, plants, and sediment.

In recent years, several studies on flow-fish interaction have been performed considering the turbulence of the flow, mostly in relation to fishways (e.g., Alexandre et al. 2013, Ben Jebria et al. 2023, Farzadkhoo et al. 2023 Qiao et al. 2023). Fish seem to prefer locations with lower TKE and non-negligible velocity. These studies typically consider the

unconditional properties of turbulence, presumably because a fish is a relatively large body that will perform some spatio-temporal averaging of the fluctuations it receives. We are not aware of studies applying conditional turbulence analysis for this fauna. Similar considerations apply to studies of turbulence-vegetation interaction (e.g., Vettori and Nikora 2018, Caroppi and Järvela 2022).

A sediment particle (sand/silt) is smaller than a fish or plant, and its lower Stokes number will make it more reactive to the fluctuations of the flow field. For sediment, someprior literature argued that the different quadrants may have different weight in determining particle entrainment. For instance, Drake et al. (1988), Dey et al. (2011) and Radice et al. (2013) attributed a major role to sweep events towards particle entrainment or activity. Rashidi et al. (1990) and Niño and García (1996) indicated instead that ejections seem to be dominant for finer particles. Nelson et al. (1995) analyzed sediment transport downstream of a step and hypothesized a double role of sweeps and outward interactions as events related to higher stream-wise velocity. Furthermore, Sechet and Le Guennec (2000) argued a coupled mechanism of ejections and sweeps. The comprehensive reviews of Dey and Ali (2018) resumed and discussed prior observations; in particular, a dominating role of sweeps in particle entrainment was attributed to a pressure distribution and strong lift induced by these events on bed particles. Finally, very recently, Matsumoto et al. (2021) associated the entrainment of fine sediment in the vicinity of larger boulders to a sweep-ejection succession.

6.6 On applying of a hole in quadrant analysis

Some literature studies dealing with quadrant analysis have applied a hole to consider only the burst events exceeding a threshold magnitude, and showed monotonic decrease of the conditional quantities for increasing hole size (e.g., Dey et al. 2011). A hole was not applied in the results presented above. It is, furthermore, noticed that, when a hole is applied, the conditional averaging procedures become more complicated, as formalized below. We introduce another clipping function to represent if a velocity fluctuation is out of the hole (considering the stream-wise/vertical plane):

$$\lambda_i^H = 1\text{if}\frac{|(u\prime w\prime)_i|}{\left(\overline{u'u'w'w'}\right)^{0.5}} > H \tag{6.27}$$

When we introduce the hole, we can define two unconditional Reynolds stresses. The first one again uses the total sample for the denominator:

$$\overline{u'w'}_{tot}^{H} = \frac{\sum_i (u'w')_i \lambda_i^H}{N_{tot}} \tag{6.28}$$

while the second one uses just the sample of values out of the hole and is:

$$\overline{u'w'}_{hole}^{H} = \frac{\sum_i (u'w')_i \lambda_i^H}{\sum \lambda_i^H} = \frac{\sum_i (u'w')_i \lambda_i^H}{p^H N_{tot}} = \frac{\overline{u'w'}_{tot}^{H}}{p^H} \tag{6.29}$$

with a percentage of values out of the hole as:

$$p^H = \frac{\sum_i \lambda_i^H}{N_{tot}} \tag{6.30}$$

Note that, for $H = 0$, we have λ^H identically equal to 1, $p^H = 1$, and both (6.28) and (6.29) give the value we would obtain with an equation analogous to (6.17). With an increase in H, p^H will obviously decrease and $\overline{u'w'}_{tot}^{H}$ will also decrease. Instead, the behavior of $\overline{u'w'}_{H}^{H}$ will not be obvious because this quantity is the ratio of two decreasing functions.

Now, let us finally move to conditional means applying a hole. We can define four conditional means, depending on the denominator we use. Equations are as follows:

$$\overline{u'w'}_{tot}^{q,H} = \frac{\sum_i (u'w')_i \lambda_i^q \lambda_i^H}{N_{tot}} \tag{6.31}$$

$$\overline{u'w'}_{quad}^{q,H} = \frac{\sum_i (u'w')_i \lambda_i^q \lambda_i^H}{\sum_i \lambda_i^q} = \frac{\sum_i (u'w')_i \lambda_i^q \lambda_i^H}{p^q N_{tot}} = \frac{\overline{u'w'}_{tot}^{q,H}}{p^q} \tag{6.32}$$

$$\overline{u'w'}_{hole}^{q,H} = \frac{\sum_i (u'w')_i \lambda_i^q \lambda_i^H}{\sum_i \lambda_i^H} = \frac{\sum_i (u'w')_i \lambda_i^q \lambda_i^H}{p^H N_{tot}} = \frac{\overline{u'w'}_{tot}^{q,H}}{p^H} \tag{6.33}$$

$$\overline{u'w'}_{quad,hole}^{q,H} = \frac{\sum_i (u'w')_i \lambda_i^q \lambda_i^H}{\sum_i \lambda_i^q \lambda_i^H} = \frac{\sum_i (u'w')_i \lambda_i^q \lambda_i^H}{p^{H,q} \sum_i \lambda_i^q} = \frac{\sum_i (u'w')_i \lambda_i^q \lambda_i^H}{p^{q,H} \sum_i \lambda_i^H} \tag{6.34}$$

where:

$$p^{H,q} = \frac{\sum_i \lambda_i^q \lambda_i^H}{\sum_i \lambda_i^q} \tag{6.35}$$

tells us how many values in a quadrant are out of the hole and:

$$p^{q,H} = \frac{\sum_i \lambda_i^q \lambda_i^H}{\sum_i \lambda_i^H} \tag{6.36}$$

is the percentage of values out of the hole that are in a certain quadrant. Obviously, the numerators of (6.35) and (6.36) are equal to each other, since they are the number of

values out of the hole in a certain quadrant. The sum of the values of (6.34) for the four quadrants

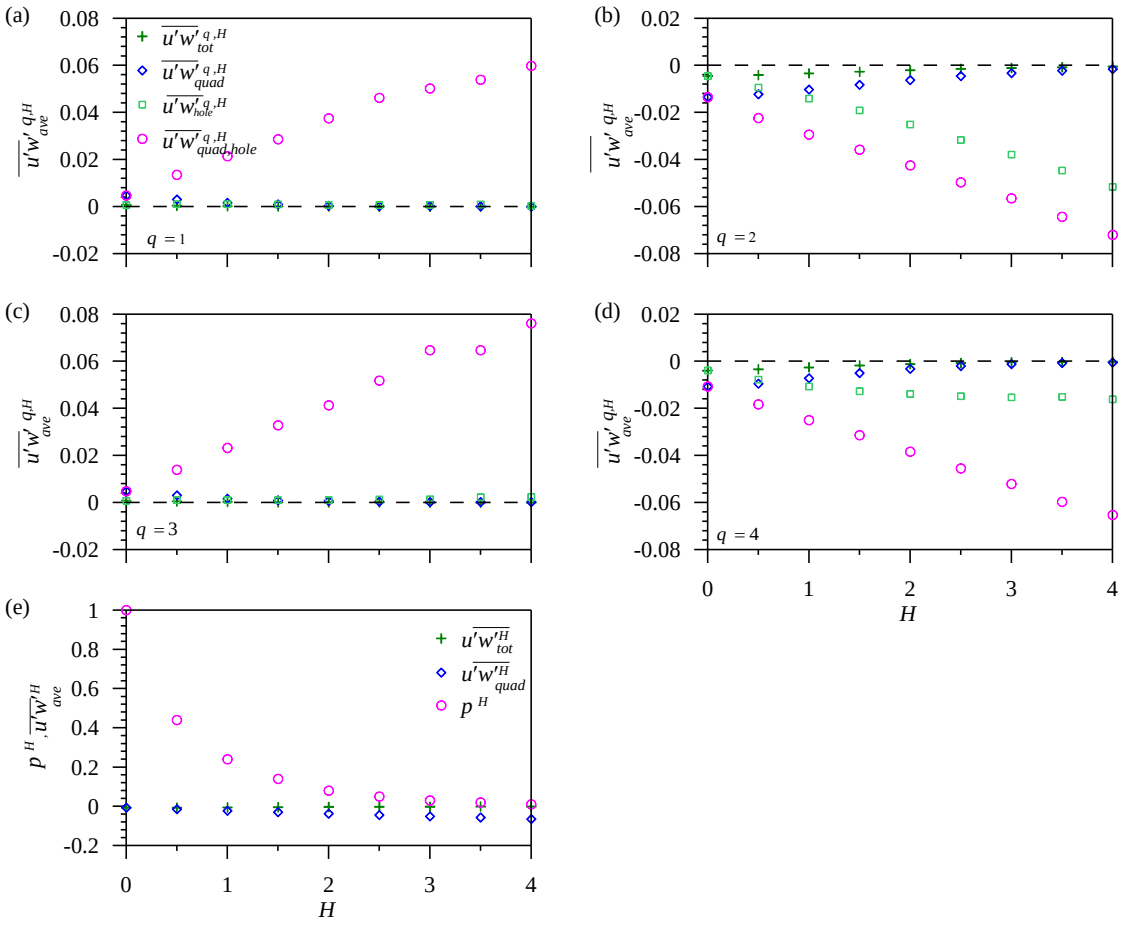

Figure 6.11: (a–e) Variation of properties with H at a single measuring point using Equations (28-30).

will equal the value from (6.29), that is $\sum_q \overline{u'w'}^{q,H}_{hole} = \overline{u'w'}^{H}_{hole}$.Note that when there is no hole ($H = 0$) eq. (6.31) and (6.33) will give the same result as (6.18), while eq. (6.32) and (6.34) will return the same result as (6.19). The discriminating functions used by Lu and Willmarth (1973), Cellino and Lemmin (2004) and Dey et al. (2020) are equal to the product $\lambda_i^q \lambda_i^H$. In our framework, we have in fact used two clipping functions in relation to either a quadrant and the hole. This enabled four conditional means to be defined in a complete framework.

Now let us explore how the defined means vary with the hole size. The mean from (6.31), that is the one typically used in the literature studies discussing hole-size variations, obviously decreases because, increasing H, the numerator of the equation decreases

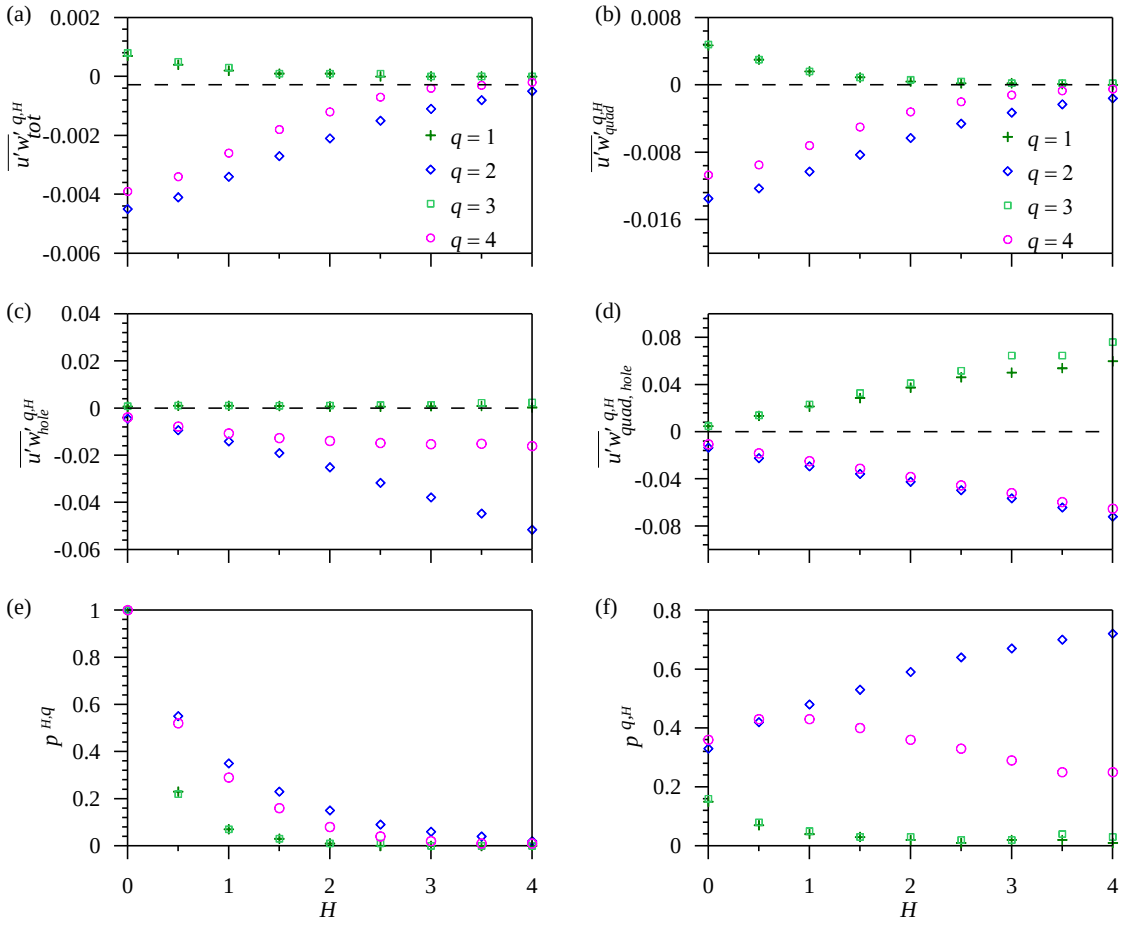

Figure 6.12: (a–f) Variation of properties with H at a single measuring point using Eq. (6.31-6.36).

(because we sum fewer values) while the denominator is a constant. Same for (6.32) that is (6.31) times a hole-independent constant. The trend of the mean from (6.33) will not be obvious because both the numerator and denominator decrease for increasing H.

In principle, it could be the same for the mean from (6.34), but here we note that we keep progressively larger fluctuations and then we expect this mean to increase. For (6.35) we expect it to decrease with H and for (6.36) it is impossible to predict, since also in this case the numerator and denominator will have the same tendency. As a support to the

previous formalization, Figure 6.11 – 6.12 show how mean properties change with reference to the measurements taken at one point. The means from (6.31) present regular trends that are, unfortunately, trivial and not representative of the actual flow in a certain quadrant. The means from (6.32) also have regular trends but do not keep track of the hole in the sample size. The means from (6.33) keep, conversely, no track of the quadrant in the sample size. Finally, the means from (6.34) are the most capable of showing the flow properties in a certain quadrant but return non-monotonic trends. Due to these reasons, for the time being we preferred to show results without the application of a hole.

6.7 Prospects for future research and applications

The framework for definition proposed in this manuscript builds upon earlier analyses based on quadrant decomposition and provides a variety of averaging options in a structured manner. In this way, the present formalization offers different ways to describe the turbulent bursting process, towards progressively more refined phenomenological description. In particular, any study applying a hole seems to need a very clear description of how it is performed, to make evident which kind of average is performed. However, with reference to the scour process under specific consideration in this work (scour downstream of an apron), the variability of the turbulence indicators defined in this work for different experimental configurations can be investigated to interpret the variability of the resulting scour patterns.

In this context, it is noted that the prior studies on quadrant-sediment interaction have been mostly related to indicators of event occurrence, and have not explored quantitative relationships of sediment motion with total-averaged or quadrant-averaged conditional properties. Exploring and finding quantitative relationships between turbulence indicators and, for example, particle entrainment will give merit to the definition and use of such flow properties.

Stability analysis for the present experimental conditions may also be useful for further advancement in the degraded-bed hydrodynamics following some important studies in this direction by Ali et al. (2021), Ali and Dey (2021) and Dey et al. (2009).

The present study has been focused on vertical profiles of conditional properties of the flow field. This depiction hides the fact that the flow events are not in the same quadrant

at a same time. A spatio-temporal variability of actual quadrant was not investigated in this work because the measurements, though extensive and highly time-consuming, were too loose in space for that purpose. For example, recently Matsumoto et al. (2021) presented maps of the spatio-temporal distribution of velocity fluctuations, that were preliminarily used to infer observations on the spatio-temporal coherency of velocity fluctuations. Due to the inherent burden of performing extremely detailed measurements, numerical simulations may help in this kind of analysis

The data presented in this manuscript offer the possibility to validate numerical simulations of the flow field for the same conditions (geometry of the scour hole, flow depth, inlet velocity, roughness height) applied in the experiments. Furthermore, they can also serve as an intermediate step for validation of numerical simulations of the scour process. Earlier models of this kind, either implementing bulk equations as in Dodaro et al. (2016) or incorporating a numerical solution of the flow field as in Amoudry et al. (2009), have been validated by comparing the scoured bed profiles obtained in experiments and model predictions. The availability of turbulent flow data enables, as said, an intermediate step of validation for the part of the model that simulates the scouring flow field.

6.8 Concluding remarks

In this study, we examined the turbulent flow field in a degraded bed made of two-size sediment. The present manuscript integrates previous insight provided by Sarkar et al. (2021) and Sarkar and Sarkar (2023) who investigated the hydrodynamics and the scaling properties of turbulence; in this study attention has been focused on the conditional properties of the flow field, employing the so-called quadrant analysis.

A rigorous definition framework that was produced as a support to the work clarified how conditional properties can be computed and included two conditional means, namely the total- and quadrant-averaging means. These have been sometimes used in prior literature; the framework proposed in the present work clarified that they are related to each other through the percentage occurrence of events in any quadrant. According to the total-averaging method, the conditional quantities are less than an unconditional one, their sum

equaling the latter. Instead, the quadrant-averaged quantities may be more or less than the unconditional one, their mean being more or less similar to the latter.

The study investigated a number of quantities (stream-wise and vertical velocity components, normal and shear Reynolds stresses in the axis plane, stream-wise and vertical fluxes of turbulent kinetic energy. Altogether the findings returned a consistent representation of the flow pattern. In the first two measuring locations (with expanding flow and at maximum scour depth) the flow was highly turbulent; ejection events had the highest percentage occurrence close to the bed, while sweeps were more present towards the original bed elevation where a mixing layer was present; in terms of the contribution to Reynolds stresses, sweeps were most relevant close to the bed and sweeps at higher elevation (particularly for the quadrant-averaged conditional stresses that are inversely proportional to the percentage occurrence); differently from Reynolds stresses, the TKE fluxes have opposite sign for sweeps and ejections, thus the vertical profiles of the unconditional TKE fluxes were sinuous reflecting the elevation ranges where sweeps and ejections prevailed; the duration of clusters of events in a certain quadrant was different (with, again, clusters of sweeps and ejections lasting more than those of the other events) but the frequency was similar for all the event types, reflecting the general frequency of the burst cycle with values in the order of some Hz. At the third location (close to the downstream end of the scour hole) the flow was less turbulent and clearly converging back to a situation without scour.

The present data can be used as benchmark for numerical simulations and as a basis for interpretation of the interactions between the flow and immersed bodies (with presumably increasing relevance of conditional analysis for decreasing size of the bodies).

The extension of the definition framework to cases applying a hole returned four possible ways of obtaining conditional averages, whose variability with H is not straightforward. This is an original development of the present study that, to the best of our knowledge, was not given complete formalization in the past. Further research on quadrant analysis may take the challenge of investigating in more detail the relevance of conditional averages applying a hole, again, particularly emphasizing the most important ones for investigation of flow interactions.

Chapter 7

Summary and Conclusions

7.1 Hydrodynamics of flow through a degraded channel bed

7.1.1 Summary

The hydrodynamics behaviors of turbulent characteristics in flows over a degraded channel bed were extensively studied to understand the influence of degraded regions on fluid turbulence under the equilibrium conditions. In open channel flow, detachment of the sedimentary bed materials takes place due to the erosional process. As a result, these naturally deformed beds are referred to as degraded bed in the field of geology, hydrology, and sediment transport phenomena, which is a very common event in natural river systems, man-made canals and coastal regions etc. The study was focused on near-bed turbulence statistics, specifically in the degraded regions over degraded bed. An acoustic doppler velocimeter (ADV) was used to capture the three dimensional velocity components at different spatial locations over degraded bed under equilibrium conditions. Turbulent characteristics such as time averaged streamwise velocity, Reynolds shear and normal stresses, turbulent kinetic energy (TKE), TKE fluxes and TKE budget are comprehensively studied. Furthermore, Laws of turbulence was discussed thoroughly and used them to estimated TKE dissipation rate. TKE budget was observed along with this dissipation rate. Finally, the nature and degree of turbulent anisotropy were observed using anisotropic invariant map (AIM) and anisotropy invariant functions (AIF).

7.1.2 Conclusions

The analysis of the turbulent flow velocity data, measured by a Vectrino velocimeter, demonstrated the turbulent flow characteristics in degraded region over a degraded channel bed under equilibrium state by different experimental conditions. Our findings of the study are summarized as follows:

- Negative streamwise velocity was observed at the vicinity of the bed surface, indicating flow reversal phenomena, which likely plays a significant role in the

formation of vortex structures. Additionally, the lowest velocities, recorded at the initial sections of the degraded bed, suggest that the greatest retardation of streamwise velocity occurred near the upstream of the region corresponding to the maximum equilibrium depth of degradation. Although the influence of bed degradation is minimal above and beyond the region, their effects are highly significant within the degraded zones.

- The Reynolds shear stress (RSS) profile, deviated from the conventional gravity line generally, observed in shear stress distribution that was shifted above the initial bed level. The initial bed level was measured before the detachment of bed materials. Turbulent mixing was found to be more intense in the upstream section of the degraded bed compared to the middle and downstream sections. Furthermore, the maximum shear stress values near the initial bed level highlight the occurrence of strong turbulent mixing in this region.
- Different magnitude of the Reynolds normal stresses clearly indicates the flow was strongly anisotropy throughout the vertical distance. This is also supported by the result that the ratio of vertical to longitudinal normal stress was less than unity.
- Strong mixing which takes place due to disorganized structure of flow fluctuation bearing the turbulent kinetic energy, is associated with turbulent eddies per unit mass, exhibited near the initial bed level. This is indeed responsible to detach the bed materials from the bed and its influence minimizes as the bed starts to be free from detachment of the materials.
- Turbulent kinetic energy fluxes suggest that sweep is the most dominating event at the vicinity of the degraded bed whereas ejection event predominates the flow as vertical distance increases.
- Second, third, and mixed third order structure functions clearly exhibit the existence of inertial subrange flowing the Kolmogorov's 4/3, Kolmogorov's 4/5, and Monin-Yaglom 4/3-laws respectively.

- The TKE dissipation rate estimated using Kolmogorov's 4/5-law is higher than the value derived from Monin-Yaglom's 4/3-law within the degraded region, below the initial bed level. This difference is attributed due to the strong flow anisotropy in this region.
- Within the degraded regions TKE dissipation rate shows greater value than the TKE production rate and they cross each other slightly below the initial bed level where strong mixing occurs. Furthermore, pressure diffusion possesses largest negative value whereas turbulent diffusion is the lowest throughout the depth, balancing the total TKE budget parameters.
- As we moved from the vicinity of the bed, the anisotropy was found to be diminished, approaching two-dimensional isotropy as the data plots moved closer to the left-curved boundary. As the vertical distance increased, the data plots exhibit a shift toward the bottom cusp, suggesting a progression toward three-dimensional isotropy. This suggests that anisotropy initially aligns with a two-dimensional state, evolves toward a three-dimensional isotropic state with an increase in depth above the initial bed level.

7.2 High-order structure functions of turbulence through a degraded channel bed

7.2.1 Summary

This study was performed to investigate the turbulence intermittency and anisotropy in flows over degraded channel beds, consisting of uniform and bimodal sediment particles. Three-dimensional velocity components were measured using an acoustic doppler velocimeter across the depth at three distinct streamwise locations along the degraded bed. The velocity data were analyzed to assess the spatial distribution of longitudinal and vertical velocity components in vector form, along with turbulence indicators and length scales at various positions. To comprehensively evaluate the impact of bed degradation under equilibrium condition on turbulence intermittency and anisotropy in higher-order scaling exponents, the high-order structure functions approach was employed. The extended self-similarity (ESS) technique was utilized to calculate scaling exponents from

higher-order structure functions of the streamwise velocity component. An intermittency parameter was introduced to characterize the behaviour of flow intermittency based on these scaling exponents. Furthermore, both the isotropic and anisotropic parts of the scaling exponents were estimated using higher-order mixed structure functions. The SO(3) symmetry decomposition method was applied to distinguish between isotropic and anisotropic contributions to the scaling exponents. The findings reveals that anisotropic scaling exponents, derived from mixed structure functions exceeded their isotropic counterparts. While comparing uniform and bimodal sediment beds, no significant differences in scaling exponents or intermittency were observed. Finally, the study is examined the ratio of anisotropic to isotropic scaling exponents across different orders, revealing the influence of anisotropy in flows over degraded channel beds.

7.2.2 Conclusions

The study is aimed to understand the flow behaviour over a degraded bed made of two types of sediment particles, focusing on anisotropy and intermittency. It also explored velocity vector field, turbulent indicator and the length-scale of flow structures, such as the integral length scale, Taylor microscale and Kolmogorov's length scales. The key findings from our study are summarized below:

- The spatial distribution of longitudinal and vertical velocity components reveals the flow retardation in the vicinity of the maximum degraded depth below the initial bed level under equilibrium condition. However, the velocity distributions gradually recover as the streamwise distance increases downstream from the degraded regions.
- Below the initial bed level, although turbulence levels are extremely high, these persist within a small distance through the degraded region. In contrast, above the initial bed level, turbulence decreases significantly, indicating medium to low level of turbulence. Some variations were observed in turbulence indicators between uniform and bimodal beds, which can be attributed to differences in flow and sediment characteristics. The study concludes that bed degradation significantly enhances the local turbulence behaviour of sedimentary beds.

- The vertical distributions of the integral length scales, Taylor microscale, and Kolmogorov dissipation scale exhibit similar patterns, differing only in magnitude. These scales reach their smallest values near the maximum degraded depth, below the initial bed level and increase with vertical distance. However, above the initial bed level, they become nearly constant with vertical variation. Additionally, their values are significantly influenced where bed degradation initiate. Notably, in the vicinity of the maximum degraded depth, these scales drop significantly across all the cases.
- The structure functions exhibit three distinct regions such as scaling, transition, and saturation. Near the maximum equilibrium depth of degradation, the inertial subrange is notably narrow. This range expands with increasing vertical distance until it becomes constant above the initial bed level. These findings highlight a significant narrowing of the inertial subrange caused by bed degradation.
- Using the Extended Self-Similarity (ESS) technique within the inertial subrange, the scaling exponents of the higher-order structure functions were estimated. Near the maximum degraded depth, these scaling exponents show the maximum deviation from Kolmogorov theoretical values, indicating the highest level of intermittency. This intermittency decreases progressively with increasing vertical distance.
- The mixed high-order structure functions also exhibit the existence of inertial subrange where the anisotropic scaling exponents were estimated from the compensated form of the mixed higher-order structure functions and differentiate them from isotropic scaling exponents using SO(3) decomposition.
- The influence of anisotropy on the scaling exponents is strongest near the degraded bed and gradually weakens with increasing vertical distance above the initial bed level. This is evident from the decreasing value of the ratio of anisotropic scaling exponents to isotropic scaling exponents as vertical distance increases. This result is strongly supported by the anisotropy angle analysis using second order structure functions.

7.3 Quadrant analysis of turbulence over a degraded channel bed

7.3.1. Summary

In this study we have investigated the conditional turbulence characteristics in flow over a degraded channel bed with bimodal sediment. Laboratory experiments were conducted until equilibrium scour conditions were achieved, after which three components of instantaneous velocity were recorded over a sufficient duration using a Vectrino velocimeter. Vertical profiles of streamwise and normal velocity were obtained at three streamwise positions along the centre line of flume axis. The conditional statistics, focusing on streamwise and vertical velocity components, Reynolds shear and normal stresses, turbulent kinetic energy fluxes are comprehensively explored along with quadrant-based metrics such as percentage occurrence, mean duration and frequency of flow events. Notably, the study provided a framework for defining various conditional means. Two distinct approaches, total averaging and quadrant averaging, were employed, and their results were systematically compared. Furthermore, the definition framework was expanded to incorporate the concept of a "hole" enabling the definition of four conditional means and performed the analysis and discussed contributions to generate Reynolds shear stress explicitly. The variation of these means with hole size demonstrated complex, non-linear trends.

7.3.2. Conclusion

This study is investigated for the conditional turbulence characteristics of flow over a degraded bed composed of a bimodal sediment mixture, using velocity components measured with a Vectrino velocimeter. The analysis focused on conditional flow properties, including streamwise and vertical velocities, Reynolds shear and normal stresses, and turbulent kinetic energy fluxes, utilizing the quadrant analysis approach. The results of the study are summarized in the context of turbulent flow characteristics in flows in a degraded region.

- A comprehensive definition framework was developed to support this study, providing clarity on the computation of conditional properties and incorporating two types of conditional means: total averaging and quadrant averaging.

- Total-averaged quantities, which consistently use the total sample size as the denominator, have the advantage that their sum across all four quadrants equals the mean value of the investigated quantity before conditioning. However, they may not adequately represent the dynamics within a specific quadrant, which could be more relevant to understanding interactions between the flow and external bodies. This limitation highlights the potential usefulness of quadrant-averaged quantities which consistently use the number of elements within each quadrant as the denominator.
- In the total-averaging method, conditional quantities are always less than the unconditional value, with their sum equal to the latter. In contrast, quadrant-averaged quantities can be either greater or smaller than the unconditional value, with their average approximating the latter to varying degrees.
- At the first two measurement locations, characterized by expanding flow and maximum degraded depth, the flow exhibited high turbulence. Near the maximum degraded depth ejection events had the highest percentage occurrence, while sweeps were more prevalent around the original bed elevation, where a mixing layer was observed.
- The duration of event varied across quadrants, with sweeps and ejections forming longer-lasting clusters compared to other events. However, all event types shared similar frequencies, are consistent with the burst cycle frequency.
- Regarding the contribution to Reynolds shear and normal stresses, sweeps were most significant near the bed, while ejections were more prominent at higher elevations, especially for quadrant-averaged conditional stresses, which are inversely related to the percentage occurrence. The total Reynolds shear and normal stresses align with those obtained from the total averaging approach, although the quadrant-averaged results differ significantly. Despite this, both approaches exhibit similar overall behavior.
- The TKE fluxes for sweeps and ejections have opposite signs, causing the vertical profiles of the streamwise and vertical TKE fluxes to be sinuous, reflecting the elevation ranges where sweeps and ejections dominate.

- At the third location, near the downstream end of the degraded region, the flow became less turbulent and showed a clear tendency to return to a smooth boundary layer flow, resembling a situation without disturbances.
- Expanding the definition framework to include cases with a hole resulted in four possible methods for calculating conditional averages, with their variability in relation to hole size being complex and not straightforward. The variation of contributions to the conditional Reynolds shear stress with hole size exhibited intricate, non-linear patterns.

7.4 Future Scope of Studies

Turbulent flow is highly connected to nature, the environment, and society, playing a crucial role in various practical applications. Turbulence in open-channel flow is one of the most natural phenomena, occurring in rivers, canals, dams, coastal regions, and various natural and engineering systems. Researchers from different regions of the world have been studying turbulence since the 17th century, and it continues to be an active area of research. Several fundamental aspects, such as energy distribution, intermittency, velocity gradient behavior, and extreme events, are still being explored. Turbulent flow in rivers and coastal regions remains a subject of ongoing investigation. Specifically, turbulence in natural vegetation under various conditions, upstream and downstream of aggraded and degraded beds, and through movable rigid and flexible bodies is frequently observed in natural rivers and coastal systems. Exploring turbulent characteristics in these flows presents significant opportunities for future research.

Collecting data from an ADV can sometimes be challenging. We must avoid regions where there is insufficient space to insert the ADV, and capturing data at every specific location in the longitudinal and vertical directions with fine spacing is a time-consuming process. Using PIV, we could minimize these issues related to both time and spatial resolution. Additionally, we can analyze advanced statistical turbulence characteristics including structure functions methodologies, proper orthogonal decomposition, and multifractality.

Beyond high Reynolds number turbulence (inertial turbulence), we could also explore turbulence at low Reynolds numbers, such as bacterial turbulence, cytoskeletal turbulence, self-propelled colloids and active droplets, plasma and astrophysical systems (active turbulence), turbulence dominated by elastic stress depending on the Weissenberg number (elastic turbulence), and magnetohydrodynamic (MHD) turbulence.

References

Aberle, J., Nikora, V. (2006). Statistical properties of armored gravel bed surfaces. Water *Resources Research*, 42(11).

Alexandre, C. M., Quintella, B. R., Silva, A. T., Mateus, C. S., Romão, F., Branco, P., Almeida, P. R. (2013). Use of electromyogram telemetry to assess the behavior of the Iberian barbel (Luciobarbus bocagei Steindachner, 1864) in a pool-type fishway. *Ecological Engineering*, 51, 191-202.

Ali, S. Z., Dey, S., Mahato, R. K. (2021). Mega riverbed-patterns: linear and weakly nonlinear perspectives. *Proceedings of the Royal Society A*, 477(2252), 20210331.

Ali, S. Z., Dey, S. (2021). Interfacial instability of sand patterns induced by turbulent shear flow. *International Journal of Sediment Research*, 36(4), 449-456.

Ali, S. Z., Dey, S. (2021). Linear stability of dunes and antidunes. *Physics of Fluids*, 33(9).

Ali, S. Z., Dey, S. (2021). Instability of large-scale riverbed patterns. *Physics of Fluids*, 33(1).

Ali, S. Z., Dey, S. (2017). Origin of the scaling laws of sediment transport. *Proceedings of the Royal Society A: Mathematical, Physical and Engineering Sciences*, 473(2197), 20160785.

Ali, S. Z., Dey, S. (2018). Impact of phenomenological theory of turbulence on pragmatic approach to fluvial hydraulics. *Physics of Fluids*, 30(4).

Amoudry, L. O., Liu, P. F. (2009). Two-dimensional, two-phase granular sediment transport model with applications to scouring downstream of an apron. *Coastal Engineering*, 56(7), 693-702.

Antonia, R. A., Ould-Rouis, M., Anselmet, F., Zhu, Y. (1997). Analogy between predictions of Kolmogorov and Yaglom. *Journal of Fluid Mechanics*, 332, 395-409.

Anselmet, F., Gagne, Y., Hopfinger, E. J., Antonia, R. A. (1984). High-order velocity structure functions in turbulent shear flows. *Journal of Fluid Mechanics*, 140, 63-89.

Arenas, A., Chorin, A. J. (2006). On the existence and scaling of structure functions in turbulence according to the data. *Proceedings of the National Academy of Sciences*, 103(12), 4352-4355.

Arenas, A., Chorin, A. J. (2006). On the existence and scaling of structure functions in turbulence according to the data. *Proceedings of the National Academy of Sciences*, 103(12), 4352-4355.

Arad, I., Dhruva, B., Kurien, S., L'vov, V. S., Procaccia, I., Sreenivasan, K. R. (1998). Extraction of anisotropic contributions in turbulent flows. *Physical Review Letters*, 81(24), 5330.

Banerjee, S., Krahl, R., Durst, F., Zenger, C. (2007). Presentation of anisotropy properties of turbulence, invariants versus eigenvalue approaches. *Journal of Turbulence*, 8, N32.

Basse, N. T. (2017). Turbulence intensity and the friction factor for smooth-and rough-wall pipe flow. *Fluids*, 2(2), 30.

Benzi, R., Ciliberto, S., Baudet, C., Chavarria, G. R., Tripiccione, R. (1993). Extended self-similarity in the dissipation range of fully developed turbulence. *Europhysics letters*, 24(4), 275.

Benzi, R., Ciliberto, S., Baudet, C., Chavarria, G. R. (1995). On the scaling of three-dimensional homogeneous and isotropic turbulence. *Physica D: Nonlinear Phenomena*, 80(4), 385-398.

Ben Jebria, N., Carmigniani, R., Drouineau, H., De Oliveira, E., Tétard, S., Capra, H. (2023). Coupling 3D hydraulic simulation and fish telemetry data to characterize the behaviour of migrating smolts approaching a bypass. *Journal of Ecohydraulics*, 8(2), 144-157.

Bertin, S., Friedrich H. (2018). Effect of surface texture and structure on the development of stable fluvial armors. *Geomorphology*, 306, 64-79.

Bigillon, F., Nino, Y., Garcia, M. H. (2006). Measurements of turbulence characteristics in an open-channel flow over a transitionally-rough bed using particle image velocimetry. *Experiments in Fluids*, 41, 857-867.

Boschung, J., Hennig, F., Denker, D., Pitsch, H., Hill, R. J. (2017). Analysis of structure function equations up to the seventh order. *Journal of Turbulence*, 18(11), 1001-1032.

Buffin-Bélanger, T., Rice, S., Reid, I., Lancaster, J. (2006). Spatial heterogeneity of near-bed hydraulics above a patch of river gravel. *Water Resources Research*, 42(4).

Caroppi, G., Järvelä, J. (2022). Shear layer over floodplain vegetation with a view on bending and streamlining effects. *Environmental Fluid Mechanics*, 22(2), 587-618.

Cellino, M., Lemmin, U. (2004). Influence of coherent flow structures on the dynamics of suspended sediment transport in open-channel flow. *Journal of Hydraulic Engineering*, 130(11), 1077-1088.

Chatterjee, S. S., Ghosh, S. N., Chatterjee, M. (1994). Local scour due to submerged horizontal jet. *Journal of Hydraulic Engineering*, 120(8), 973-992.

Chin, C. O., Melville, B. W., Raudkivi, A. J. (1994). Streambed armouring. *Journal of Hydraulic Engneering*, 120(8), 899-918.

Cooper, J. R., Tait, S. J. (2009). Water-worked gravel beds in laboratory flumes–a natural analogue? *Earth Surface Processes and Landforms*, 34(3), 384-397.

Cooper, J. R., Tait, S. J. (2010). Spatially representative velocity measurement over water-worked gravel beds. *Water Resources Research*, 46(11).

Coscarella, F., Servidio, S., Ferraro, D., Carbone, V., Gaudio, R. (2017). Turbulent energy dissipation rate in a tilting flume with a highly rough bed. *Physics of Fluids*, 29(8).

Coscarella, F., Penna, N., Servidio, S., Gaudio, R. (2020). Turbulence anisotropy and intermittency in open-channel flows on rough beds. *Physics of Fluids*, 32(11).

Davidson, P. (2015). Turbulence: An Introduction for Scientists and Engineers. *Oxford Academic*.

De Karman, T., Howarth, L. (1938). On the statistical theory of isotropic turbulence. *Proceedings of the Royal Society of London. Series A-Mathematical and Physical Sciences*, 164(917), 192-215.

Dey, S., Das, R., Gaudio, R., Bose, S. K. (2012). Turbulence in mobile-bed streams. *Acta Geophysica*, 60, 1547-1588.

Dey, S., Sarkar, S., Solari, L. (2011). Near-bed turbulence characteristics at the entrainment threshold of sediment beds. *Journal of Hydraulic Engineering*, 137(9), 945-958.

Dey, S., Paul, P., Ali, S. Z., Padhi, E. (2020). Reynolds stress anisotropy in flow over two-dimensional rigid dunes. *Proceedings of the Royal Society A*, 476(2242), 20200638.

Dey, S., Paul, P., Fang, H., Padhi, E. (2020). Hydrodynamics of flow over two-dimensional dunes. *Physics of Fluids*, 32(2).

Dey, S., Ravi Kishore, G., Castro-Orgaz, O., Ali, S. Z. (2019). Turbulent length scales and anisotropy in submerged turbulent plane offset jets. *Journal of Hydraulic Engineering*, 145(2), 04018085.

Dey, S., Das, R., Gaudio, R., Bose, S. K. (2012). Turbulence in mobile-bed streams. *Acta Geophysica*, 60(6), 1547e1588.

Dey, S., & Sarkar, A. (2006). Scour downstream of an apron due to submerged horizontal jets. *Journal of hydraulic engineering*, 132(3), 246-257.

Dey, S., Sarkar, S., & Solari, L. (2011). Near-bed turbulence characteristics at the entrainment threshold of sediment beds. *Journal of Hydraulic Engineering*, 137(9), 945-958.

Dey, S., Raikar, R. V. (2007). Characteristics of horseshoe vortex in developing scour holes at piers. *Journal of Hydraulic Engineering*, 133(4), 399-413.

Dey, S., Paul, P., Fang, H., Padhi, E. (2020). Hydrodynamics of flow over two-dimensional dunes. *Physics of Fluids*, 32(2).

Dey, S., Paul, P., Ali, S. Z., Padhi, E. (2020). Reynolds stress anisotropy in flow over two-dimensional rigid dunes. *Proceedings of the Royal Society A*, 476(2242), 20200638.

Dey, S. (2014). Fluvial Hydrodynamics: Hydrodynamic and Sediment Transport Phenomena, Springer, Berlin.

Dey, S., Sarkar, S. (2020). Turbulent length scales and Reynolds stress anisotropy in wall-wake flow downstream of an isolated dunal bedform. *In Recent Trends in Environmental Hydraulics: 38th International School of Hydraulics* (1-21). Springer International Publishing.

Dey, S., Sarkar, A. (2006). Scour downstream of an apron due to submerged horizontal jets. *Journal of hydraulic engineering*, 132(3), 246-257.

Dey, S., Ali, S. Z. (2020). Fluvial instabilities. *Physics of Fluids*, 32(6).

Dey, S., Ali, S. Z. (2024). The universal two-fifths law of pier scour. *Physics of Fluids*, 36(4).

Dey, S., Paul, P., Padhi, E. (2020). Conditional spatially averaged turbulence and dispersion characteristics in flow over two-dimensional dunes. *Physics of Fluids*, 32(6).

Dey, S., Ali, S. Z. (2019). Bed sediment entrainment by streamflow: State of the science. *Sedimentology*, 66(5), 1449-1485.

Dey, S., Ali, S. Z. (2018). Advances in modeling of bed particle entrainment sheared by turbulent flow. *Physics of Fluids*, 30(6).

Dey, S., Mahato, R. K., Ali, S. Z. (2022). Linear stability of sand waves sheared by a turbulent flow. *Environmental Fluid Mechanics*, 22, 429-446.

Dhruva, B., Tsuji, Y., Sreenivasan, K. R. (1997). Transverse structure functions in high-Reynolds-number turbulence. *Physical Review E*, 56(5), R4928.

Dodaro, G., Tafarojnoruz, A., Sciortino, G., Adduce, C., Calomino, F., Gaudio, R. (2016). Modified Einstein sediment transport method to simulate the local scour evolution downstream of a rigid bed. *Journal of Hydraulic Engineering*, 142(11), 04016041.

Drake, T. G., Shreve, R. L., Dietrich, W. E., Whiting, P. J., Leopold, L. B. (1988). Bedload transport of fine gravel observed by motion-picture photography. *Journal of Fluid Mechanics*, 192, 193-217.

Duan, J., Li, H., Wang, G., Fu, X. (2011). Turbulent burst around experimental spur dike. *International Journal of Sediment Research*, 26(4), 471-523.

Eckert, M. (2013). Arnold Sommerfeld: Science, Life and Turbulent Times 1868-1951. Springer Science & Business Media.

Farzadkhoo, M., Kingsford, R. T., Suthers, I. M., Felder, S. (2023). Flow hydrodynamics drive effective fish attraction behaviour into slotted fishway entrances. *Journal of Hydrodynamics*, 35(4), 782-802.

Ferraro, D., Servidio, S., Carbone, V., Dey, S., Gaudio, R. (2016). Turbulence laws in natural bed flows. *Journal of Fluid Mechanics*, 798, 540-571.

Frohnapfel, B., Lammers, P., Jovanović, J., Durst, F. (2007). Interpretation of the mechanism associated with turbulent drag reduction in terms of anisotropy invariants. *Journal of Fluid Mechanics*, 577, 457-466.

Frisch, U. (1995). *Turbulence: the legacy of AN Kolmogorov*. Cambridge university press.

Garcia, M., Nino, Y., Lopez, F. (1996). Laboratory observations of particle entrainment into suspension by turbulent bursting. *Coherent flow structures in open channels*, Wiley, New York, 63–84.

Gaudin, E., Protas, B., Goujon-Durand, S., Wojciechowski, J., Wesfreid, J. E. (1998). Spatial properties of velocity structure functions in turbulent wake flows. *Physical Review E*, 57(1), R9.

Goring, D. G., Nikora, V. I. (2002). Despiking acoustic Doppler velocimeter data. *Journal of hydraulic engineering*, 128(1), 117-126.

Grams, P. E., Wilcock, P. R. (2007). Equilibrium entrainment of fine sediment over a coarse immobile bed. *Water Resources Research*, 43(10).

Han, X., He, G. J., Fang, H. W. (2017). Double-averaging analysis of turbulent kinetic energy fluxes and budget based on large-eddy simulation. *Journal of Hydrodynamics*, 29(4), 567-574.

Hinze, J. O. (1959). The Effect of Compressibility on the Turbulent Transport of Heat in a Stably Stratified Atmosphere. In *Proc. Symposium on Atmospheric Diffusion and Air Pollution*, Academic Press, 6, 229.

Hurther, D., Lemmin, U. (2000). Shear stress statistics and wall similarity analysis in turbulent boundary layers using a high-resolution 3-D ADVP. *IEEE journal of oceanic engineering*, 25(4), 446-457.

Hurther, D., Lemmin, U., Terray, E. A. (2007). Turbulent transport in the outer region of rough-wall open-channel flows: the contribution of large coherent shear stress structures (LC3S). *Journal of Fluid Mechanics*, 574, 465-493.

Irwin, H. P. A. (1973). Measurements in a self-preserving plane wall jet in a positive pressure gradient. *Journal of Fluid Mechanics*, 61(1), 33-63.

Jain, R. K., Kumar, A., Kothyari, U. C. (2015). Turbulence statistics of flow through degraded channel bed of sand-gravel mixture. *Journal of Hydro-environment Research*, 9(4), 508-518.

Jiménez, J. (1998). Small scale intermittency in turbulence. *European Journal of Mechanics-B/Fluids*, 17(4), 405-419.

John, C. K., Pu, J. H., Guo, Y., Hanmaiahgari, P. R., Pandey, M. (2023). Flow turbulence presented by different vegetation spacing sizes within a submerged vegetation patch. *Journal of Hydrodynamics*, 35(6), 1131-1145.

Khan, M. A., Sharma, N., Pu, J., Aamir, M., Pandey, M. (2021). Two-dimensional turbulent burst examination and angle ratio utilization to detect scouring/sedimentation around mid-channel bar. *Acta Geophysica*, 69(4), 1335-1348.

Kirkil, G., Constantinescu, G. (2010). Flow and turbulence structure around an in-stream rectangular cylinder with scour hole. *Water Resources Research*, 46(11).

Kolmogorov, A. N. (1941). The local structure of turbulence in incompressible viscous fluid for very large Reynolds. Numbers. *In Dokl. Akad. Nauk SSSR*, 30, 299-303.

Kolmogorov, A. N. (1941). Dissipation of energy in the locally isotropic turbulence. *In Dokl. Akad. Nauk. SSSR*, 32, 19-21.

Kolmogorov, A. N. (1962). A refinement of previous hypotheses concerning the local structure of turbulence in a viscous incompressible fluid at high Reynolds number. *Journal of Fluid Mechanics*, 13(1), 82-85.

Krogstadt, P. Å., Antonia, R. A. (1999). Surface roughness effects in turbulent boundary layers. *Experiments in fluids*, 27(5), 450-460.

Krogstadt, P. Å., Antonia, R. A. (1999). Surface roughness effects in turbulent boundary layers. *Experiments in fluids*, 27(5), 450-460.

Kurien, S., Sreenivasan, K. R. (2000). Anisotropic scaling contributions to high-order structure functions in high-Reynolds-number turbulence. *Physical Review E*, 62(2), 2206.

Kurien, S., Sreenivasan, K. R. (2000). Anisotropic scaling contributions to high-order structure functions in high-Reynolds-number turbulence. *Physical Review E*, 62(2), 2206.

Landau, L. D. (1959). Em lifshitz, fluid mechanics, *Course of theoretical physics*, 6, Pergamon, London.

Lopez, F., García, M. H. (1999). Wall similarity in turbulent open-channel flow. *Journal of engineering mechanics*, 125(7), 789-796.

Lu, S. S., Willmarth, W. W. (1973). Measurements of the structure of the Reynolds stress in a turbulent boundary layer. *Journal of Fluid mechanics*, 60(3), 481-511.

Lumley, J. L., Newman, G. R. (1977). The return to isotropy of homogeneous turbulence. *Journal of Fluid Mechanics*, 82(1), 161-178.

Lumley, J. L. (1967). Similarity and the turbulent energy spectrum. *Physics of fluids*, 10(4), 855-858.

Marion, A., Tait, S. J., McEwan, I. K. (2003). Analysis of small-scale gravel bed topography during armoring. *Water Resources Research*, 39(12).

Mao, L., Cooper, J. R., Frostick, L. E. (2011). Grain size and topographical difference between static and mobile armour layers. *Earth Surface Processes and Landforms*, 36(10), 1321e1334.

Matsumoto, K., Okamoto, T. A., Sanjou, M. (2024). Particle entrainment by bursting phenomena in open-channel flow over rough bed. *Environmental Fluid Mechanics*, 24, 1-28.

Mätzler, C. (2002). Relation between grain-size and correlation length of snow. *Journal of Glaciology*, 48(162), 461-466.

Mignot, E., Barthélemy, E., Hurther, D. (2009). Double-averaging analysis and local flow characterization of near-bed turbulence in gravel-bed channel flows. *Journal of Fluid Mechanics*, 618, 279-303.

Mignot, E., Hurther, D., Barthelemy, E. (2011). Double-averaging turbulence characteristics in flows over a gravel bed. *Journal of Hydraulic Research*, 49(5), 703-704.

Mignot, E., Hurther, D., Barthélemy, E. (2009). On the structure of shear stress and turbulent kinetic energy flux across the roughness layer of a gravel-bed channel flow. *Journal of Fluid Mechanics*, 638, 423-452.

Milano, L. J., Matthaeus, W. H., Dmitruk, P. and Montgomery, D. C. (2001). Local anisotropy in incompressible magnetohydrodynamic turbulence. *Physics of plasmas*, 8, 2673–2681 .

Monin AS, and Yaglom AM. (1975). *Statistical Fluid Mechanics*. MIT Press.

Mohajeri, S. H., Righetti, M., Wharton, G., Romano, G. P. (2016). On the structure of turbulent gravel bed flow: Implications for sediment transport. *Advances in Water Resources*, 92, 90-104.

Nelson, J. M., Shreve, R. L., McLean, S. R., Drake, T. G. (1995). Role of near-bed turbulence structure in bed load transport and bed form mechanics. *Water resources research*, 31(8), 2071-2086.

Nezu, I., Nakagawa, H. (1993). *Turbulence in open-channel flows*. Rotterdam, Netherlands, Balkema A A.

Nikora, V., Goring, D. (2000). Flow turbulence over fixed and weakly mobile gravel beds. *Journal of Hydraulic Engineering*, 126(9), 679-690.

Nikora, V., Walsh, J. (2004). Water-worked gravel surfaces: High-order structure functions at the particle scale. *Water Resources Research*, 40(12).

Niño, Y., García, M. (1998). Using Lagrangian particle saltation observations for bedload sediment transport modelling. *Hydrological Processes*, 12(8), 1197-1218.

Nik Hassan, N. M. K., Narayanan, R. (1985). Local scour downstream of an apron. *Journal of Hydraulic Engineering*, 111(11), 1371-1384.

Obukhov, A. (1941). On the distribution of energy in the spectrum of turbulent flow. *In Dokl. Akad. Nauk SSSR*, 32, 22-24

Obukhov, A. M. (1962). Some specific features of atmospheric turbulence. *Journal of Geophysical Research*, 67(8), 3011-3014.

O'Neill, P. L., Nicolaides, D., Honnery, D., Soria, J. (2004). Autocorrelation functions and the determination of integral length with reference to experimental and numerical data. *In 15th Australasian fluid mechanics conference*, 1, (1-4), University of Sydney, Sydney, NSW, Australia.

Padhi, E., Penna, N., Dey, S., Gaudio, R. (2019). Near-bed turbulence structures in water-worked and screeded gravel-bed flows. *Physics of Fluids*, 31(4).

Padhi, E., Penna, N., Dey, S., Gaudio, R. (2018). Spatially averaged dissipation rate in flows over water-worked and screeded gravel beds. *Physics of Fluids*, 30(12).

Padhi, E., Penna, N., Dey, S., Gaudio, R. (2018). Hydrodynamics of water-worked and screeded gravel beds: A comparative study. *Physics of Fluids*, 30(8).

Padhi, E., Dey, S., Penna, N., Gaudio, R. (2020). Conditional turbulence characteristics in water-worked and screeded gravel-bed flows. *Journal of Hydraulic Engineering*, 146(2), 04019052.

Pandey, M., Lam, W. H., Cui, Y., Khan, M. A., Singh, U. K., Ahmad, Z. (2019). Scour around spur dike in sand–gravel mixture bed. *Water*, 11(7), 1417.

Padhi, E., Penna, N., Dey, S., Gaudio, R. (2019). Near-bed turbulence structures in water-worked and screeded gravel-bed flows. *Physics of Fluids*, 31(4).

Pandey, M., Sharma, P. K., Ahmad, Z., Singh, U. K., Karna, N. (2018). Three-dimensional velocity measurements around bridge piers in gravel bed. *Marine Georesources & Geotechnology*, 36(6), 663-676.

Penna, N., Padhi, E., Dey, S., Gaudio, R. (2020). Structure functions and invariants of the anisotropic Reynolds stress tensor in turbulent flows on water-worked gravel beds. *Physics of Fluids*, 32(5).

Penna, N., Padhi, E., Dey, S., Gaudio, R. (2022). Response of Reynolds stresses and scaling behavior of high-order structure functions to a water-worked gravel-bed surface and its implication on sediment transport. *International Journal of Sediment Research*, 37(1), 1-13.

Penna, N., Padhi, E., Dey, S., Gaudio, R. (2021). Statistical characterization of unworked and water-worked gravel-bed roughness structures. *Journal of Hydraulic Research*, 59(3), 420-436.

Penna, N., Coscarella, F., D'Ippolito, A., Gaudio, R. (2020). Anisotropy in the free stream region of turbulent flows through emergent rigid vegetation on rough beds. *Water*, 12(9), 2464.

Pokrajac, D., Campbell, L. J., Nikora, V., Manes, C., McEwan, I. (2007). Quadrant analysis of persistent spatial velocity perturbations over square-bar roughness. *Experiments in fluids*, 42, 413-423.

Protas, B., Goujon-Durand, S., Wesfreid, J. E. (1997). Scaling properties of two-dimensional turbulence in wakes behind bluff bodies. *Physical Review E*, 55(4), 4165.

Qiao, J., Bennett, S. J., Atkinson, J. F. (2023). Simultaneous Measurement of Turbulent Surface Velocities and Fish Movement in an Open Channel Flow with Implications for Agent-Based Models. *Journal of Hydraulic Engineering*, 149(9), 04023035.

Radice, A., Nikora, V., Campagnol, J., Ballio, F. (2013). Active interactions between turbulence and bed load: Conceptual picture and experimental evidence. *Water Resources Research*, 49(1), 90-99.

Rashidi, M., Hetsroni, G., Banerjee, S. (1990). Particle-turbulence interaction in a boundary layer. *International Journal of Multiphase Flow*, 16(6), 935-949.

Rathore, V., Penna, N., Dey, S., Gaudio, R. (2022). Response of open-channel flow to a sudden change from smooth to rough bed. *Environmental Fluid Mechanics*, 22(1), 87-112.

Reynolds, O. (1983). Papers on mechanical and physical subjects. *CUP* Archive.

Rott, N. (1990). Note on the history of the Reynolds number. *Annual Review of Fluid Mechanics*, 22, 1.

Rotta, J. C. (1951). Statistische theorie nichthomogener turbulenz. *Zeitschrift für Physik*, 129, 547-572.

Russo, F., Basse, N. T. (2016). Scaling of turbulence intensity for low-speed flow in smooth pipes. *Flow Measurement and Instrumentation*, 52, 101-114.

Sambrook Smith, G. H. (1996). Bimodal fluvial bed sediments: origin, spatial extent and processes. *Progress in Physical Geography*, 20(4), 402-417.

Sarkar, M., Maurya, S. K., Gopmandal, P. P., Sarkar, S. (2021). Hydrodynamics of flow through a degraded channel bed. *Journal of Turbulence*, 22(12), 814-842.

Sarkar S, Dey S. Reply by the Authors. (2011). *Journal of Hydraulic Research*, 49(5), 704-705.

Sarkar, S., Papanicolaou, A. N., Dey, S. (2016). Turbulence in a gravel-bed stream with an array of large gravel obstacles. *Journal of Hydraulic Engineering*, 142(11), 04016052.

Sarkar, S., Dey, S. (2015). Turbulent length scales and anisotropy downstream of a wall mounted sphere. *Journal of Hydraulic Research*, 53(5), 649-658.

Sarkar, S., Dey, S. (2015). Turbulence anisotropy in flow at an entrainment threshold of sediment. *Journal of Hydraulic Engineering*, 141(7), 06015007.

Sarkar, S., Ali, S. Z., Dey, S. (2019). Turbulence in wall-wake flow downstream of an isolated dunal bedform. *Water*, 11(10), 1975.

Sarkar, S., Dey, S. (2015). Turbulent length scales and anisotropy downstream of a wall mounted sphere. *Journal of Hydraulic Research*, 53(5), 649-658.

Sarkar, S., Papanicolaou, A. N., Dey, S. (2016). Turbulence in a gravel-bed stream with an array of large gravel obstacles. *Journal of Hydraulic Engineering*, 142(11), 04016052.

Sarkar, M., Sarkar, S. (2023). Structure functions of turbulence through a degraded channel bed. *European Journal of Mechanics-B/Fluids*, 98, 292-318.

Sarkar, S., Dey, S. (2010). Double-averaging turbulence characteristics in flows over a gravel bed. *Journal of Hydraulic Research*, 48(6), 801-809.

Sarkar, S. (2016). Time-averaged turbulent flow characteristics over a highly spatially heterogeneous gravel-bed. *Acta Geophysica*, 64, 1797-1824.

Séchet, P., Le Guennec, B. (1999). Bursting phenomenon and incipient motion of solid particles in bed-load transport. *Journal of Hydraulic Research*, 37(5), 683-696.

Shebalin, J. V. Matthaeus, W. H. and Montgomery, D. (1983). Anisotropy in MHD turbulence due to a mean magnetic field. *Journal of Plasma Physics*, 29, 525–547.

Shields, A. (1936). Application of similarity principles and turbulence research to bed-load movement. *Soil Conservation Service*, 26, 5–24 (in German).

Shvidchenko, A. B., Pender, G. (2001). Macroturbulent structure of open-channel flow over gravel beds. *Water Resources Research*, 37(3), 709-719.

Shen, X., Warhaft, Z. (2002). Longitudinal and transverse structure functions in sheared and unsheared wind-tunnel turbulence. *Physics of fluids*, 14(1), 370-381.

Singh, A., Howard, K. B., Guala, M. (2014). On the homogenization of turbulent flow structures in the wake of a model wind turbine. *Physics of Fluids*, 26(2).

Sreenivasan, K. R. (2019). Turbulent mixing: A perspective. *Proceedings of the National Academy of Sciences*, 116(37), 18175-18183.

Sukhodolov, A., Thiele, M., Bungartz, H. (1998). Turbulence structure in a river reach with sand bed. *Water Resources Research*, 34(5), 1317-1334.

Tregnaghi, M., Marion, A., Gaudio, R. (2007). Affinity and similarity of local scour holes at bed sills. *Water Resources Research*, 43(11).

Trush, A., Pospíšil1, S. Kozmar, H. (2022). Comparison of turbulence integral determination methods. *In Advances in Fluid Mechanics XIII*, Edited By: S. Hernández, University of A Coruña, Spain, 24-26 May, Tallinn, Estonia.

Van Rijn, L. C. (1984). Sediment transport, part I: bed load transport. *Journal of hydraulic engineering*, 110(10), 1431-1456.

Van de Water, W., Herweijer, J. A. (1999). High-order structure functions of turbulence. *Journal of Fluid Mechanics*, 387, 3-37.

Vettori, D., Nikora, V. (2018). Flow–seaweed interactions: a laboratory study using blade models. *Environmental Fluid Mechanics*, 18, 611-636.

Wan, M., Servidio, S., Oughton, S., Matthaeus, W. H. (2010). The third-order law for magnetohydrodynamic turbulence with shear: Numerical investigation. *Physics of Plasmas*, 17(5), 052307.

Warhaft, Z., Shen, X. (2002). On the higher order mixed structure functions in laboratory shear flow. *Physics of Fluids*, 14(7), 2432-2438.

Wilcock, P. R., Kenworthy, S. T., Crowe, J. C. (2001). Experimental study of the transport of mixed sand and gravel. *Water Resources Research*, 37(12), 3349-3358.

Wren, D. G., Langendoen, E. J., Kuhnle, R. A. (2011). Effects of sand addition on turbulent flow over an immobile gravel bed. *Journal of Geophysical Research: Earth Surface*, 116(F1).

Yaglom, A. M. (1949). On the local structure of a temperature field in a turbulent flow. *In Dokl. akad. nauk sssr*, 69(6), 743-746.

Zanchi, B., Radice, A. (2021). Celerity and height of aggradation fronts in gravel-bed laboratory channel. *Journal of Hydraulic Engineering*, 147(10), 04021034.

Zanchi, B., Zucchi, M., Radice, A. (2019). On the relationship between experimental and numerical modelling of gravel-bed channel aggradation. *Hydrology*, 6(1), 9.

Zhu, W., Van Hout, R., Luznik, L., Kang, H. S., Katz, J., Meneveau, C. (2006). A comparison of PIV measurements of canopy turbulence performed in the field and in a wind tunnel model. *Experiments in fluids*, 41, 309-318.

Paper Written from the Thesis

Sarkar, M., Maurya, S. K., Gopmandal, P. P., Sarkar, S. (2021). Hydrodynamics of flow through a degraded channel bed. *Journal of Turbulence*, 22(12), 814-842.

Sarkar, M., Sarkar, S. (2023). Structure functions of turbulence through a degraded channel bed. *European Journal of Mechanics-B/Fluids*, 98, 292-318.

Sarkar, M., Radice, A., Gopmandal, P. P., Sarkar, S. (2024). Quadrant analysis of turbulence over a degraded channel-bed of bimodal sediment, with a definition framework for averaging methods. *Environmental Fluid Mechanics*, 1-33.